

In-situ Investigations of Molecular Self-Assembly Using Microfluidics

DOCTORAL THESIS
(Dissertation)

Accepted by the University of Bayreuth (Germany)
in consideration of the academic grade of
Doctor rerum naturalium (Dr. rer. nat.)
and The University of Melbourne (Australia)
in fulfilments of the requirements of the degree of
Doctor of Philosophy (PhD)
in agreement with a joint-degree-arrangement

submitted by

Susanne Ingrid Seibt, M.Sc.

from Hof, Germany

ORCID: 0000-0001-5634-7271

March 2018

The work described in this thesis was carried out at the Department of Physical Chemistry I within the Bayreuth School of Mathematical and Natural Sciences (BayNAT) at the University of Bayreuth and the Nanoscience Laboratory, School of Chemistry at the University of Melbourne from October 2014 to March 2018 under the supervision of Prof. Dr. Stephan Förster and Prof. Dr. Paul Mulvaney as a Joint PhD degree within the DAAD Bayreuth-Melbourne Polymer/Colloid Network.

Thesis submitted	29. March 2018
Date of scientific colloquium	29. June 2018

Doctoral committee

Prof. Dr. Stephan Förster	(1st Examiner)
Prof. Dr. Paul Mulvaney	(2nd Examiner)
Prof. Dr. Anna Schenk	(3rd Examiner)
Prof. Dr. Peter Strohsriegl	(Chair)

Abstract

Despite their small size, nanomaterials have a big impact on the scientific world, as well as our daily lives. To date, well-described reaction mechanisms for the syntheses or self-assembly processes of most of these nanomaterials remain a mystery. New reaction platforms are needed to gain insights about reaction kinetics and structural arrangements of these systems, particularly when dealing with fast kinetics. Microfluidics in this regard has become a powerful tool with great impact in many scientific fields of modern biology and chemistry. The fastest and most efficient techniques are based on hydrodynamic flow-focusing where a central reacting stream in a channel is confined, and focused, by outer enveloping streams. This can be used for investigating the nucleation and growth of nanoparticles as well as the self-assembly of macromolecules in real time with both high spatial and temporal resolution. A broad range of techniques can be used to probe reactions in microfluidic channels from optical measurements of absorption and fluorescence microscopy and spectroscopy, to structure analysis methods like Raman spectroscopy and X-ray scattering is available.

In this work, the growth kinetics of nanoparticles, self-assembly processes of hydrogelators and polymers as well as the flow-orientated alignment of anisotropic particles was studied. This was enabled by the combination of highly optimised microfluidic devices with material-dependent analytical methods, including optical spectroscopy, fluorescence microscopy and X-ray scattering. In particular, this thesis focuses on the *in-situ* kinetic investigations of processes occurring during the reactions.

The first part of the presented work deals with the slow reaction kinetics of the seed-induced growth of gold nanorods. The hydroquinone-based synthesis method used provided insights into a new reaction process, starting from spherical seeds to spherical capped cylinders following a double-sigmoidal growth. The shape transition from a cuboctahedral single-crystal seed to an ellipsoidal-shaped intermediate before the formation of the final spherical capped cylinder could be assigned to facet growth rates in dependency of the amount of free gold in solution. These highly uniform gold nanorod samples could then be used to investigate the alignment behaviour in structural and orientational distributions of anisotropic particles with different axial ratios. To perform the experiments, a liquid microjet setup was used to generate a stable stream of particles for X-ray scattering measurements with low background signal. The monitored parallel and perpendicular alignment could then be related to the torque which depended on the aspect ratio of each sample.

The second part of this thesis deals with faster reactions: the nucleation and growth of nanocrystals in addition to hydrogel fibres and polymer self-assembly. These systems presented two unique challenges: Firstly, the entire reaction volume needed to avoid contact with the wall of the microfluidic channel to avoid artefacts from heterogeneous nucleation and growth. Secondly, the high scattering background of PDMS needed to be minimized to enable measurements of the self-assembly process of hydrogelators via X-ray scattering.

The first problem was overcome via a computationally and experimentally optimized mixing cross sections providing lateral and vertical hydrodynamic focusing. These microfluidic platforms were then used to follow the pH-induced fiber formation of a fluorescent hydrogelator, the solvent exchange induced self-assembly of a watersoluble fluorescent conjugated polymer and the fast reaction kinetics of nucleation and growth of CdS nanoparticles. These reactions could be followed by fluorescence microscopy and confocal laser scanning microscopy.

In combination with X-ray scattering and Raman spectroscopy, the all-PDMS device was replaced by a PDMS-glass hybrid device to ensure a lower background signal from the glass as channel environment and therefore overcome the second problem. As the structural evolution of the gel fibre formation via supramolecular assembly could be followed, this proves that investigations of fast structural rearrangements can be followed *in-situ* by microfluidics combined with microfocus X-ray scattering.

Zusammenfassung

Ungeachtet ihrer kleinen Ausmaße haben Nanomaterialien einen großen Einfluss auf die wissenschaftliche Welt und unser alltägliches Leben. Bis heute sind gut beschriebene Reaktionsmechanismen in Synthese und Selbst-Anordnungsprozessen dieser Nanomaterialien jedoch oft ein Mysterium. Neue Reaktionsumgebungen werden benötigt um Einblicke in Reaktionskinetik und Strukturanordnungen zu erhalten. Mikrofluidik entwickelte sich in dieser Hinsicht zu einem leistungsfähigen Werkzeug mit großem Einfluss auf viele wissenschaftliche Felder moderner Biologie und Chemie. Die schnellsten und effizientesten Techniken basieren auf hydrodynamischer Flussfokussierung, in welcher ein zentraler Strom im Kanal von äußeren umgebenden Strömen abgegrenzt und fokussiert wird. Diese können zur Untersuchung von Nanopartikel Nukleations und Wachstums Prozessen, sowie der Selbstanordnung von Makromolekülen in Echtzeit mit hoher Orts- und Zeitaufösung genutzt werden. Für die eigentlichen Messungen während dieser Reaktionen steht eine große Auswahl an Techniken zur Verfügung, welche von optischem Equipment für Absorptions- und Fluoreszenz-Mikroskopie und -Spektroskopie bis zu Strukturanalysemethoden wie Ramanspektroskopie und Röntgenstreuung reichen.

In dieser Arbeit wurde die Wachstumskinetik von Nanopartikeln, Selbstanordnungsprozessen von Hydrogelbildnern und Polymeren sowie die Flussorientierung von anisotropen Partikeln untersucht. Dieses wurde durch die Kombination von optimierten Mikrofluidik Bauteilen mit materialeigenschaftsspezifischen, analytischen Methoden, einschließlich optischer Spektroskopie, Fluoreszenzmikroskopie und Röntgenstreuung ermöglicht. Diese Doktorarbeit fokussiert sich auf die Kinetik Untersuchungen welche *in-situ* während der Reaktion erhalten wurden.

Der erste Teil der vorliegenden Arbeit beschäftigt sich mit der langsamen Reaktionskinetik des keiminduzierten Gold Nanostäbchen Wachstums. Die angewendete Hydrochinonbasierte Synthesemethode lieferte Einblicke in einen neuen Reaktionshergang, welche startend von sphärischen Keimen bis hin zu sphärisch gekappten Zylindern einem doppelsigmoidalen Wachstumsratenverlauf folgt. Die einzelnen Formveränderungsschritte von einem kuboktahedrischen Einkristall über einen ellipsoidalen Zwischenzustand zu dem finalen sphärisch gekappten Zylinder konnten einzelnen Facettenwachstumsraten zugeordnet werden, welche abhängig von der Menge an zur Verfügung stehendem Gold in der Lösung sind. Diese Proben mit höchst einheitlichen Gold Nanostäbchen konnten anschließend für eine umfangreiche Studie des Ausrich-

tungsverhaltens in Struktur- und Orientierungsverteilung von anisotropen Partikeln mit verschiedenen Achsen Verhältnissen genutzt werden. Zur Durchführung dieser Experimente wurde ein Flüssigkeits-Mikrostrahl Aufbau verwendet, um einen stabilen Partikelstrom für Röntgenstreuungsmessungen mit geringem Hintergrundsignal zu erzeugen. Die beobachtete parallele und senkrechte Ausrichtung konnte folgend den Rotationskräften in Abhängigkeit vom Aspekt Verhältnis jeder Probe zugeordnet werden.

Der zweite Teil dieser Arbeit beschäftigt sich mit schnelleren Reaktionskinetiken: der Nukleation und Wachstum von Nanokristallen sowie Hydrogelfasern und Polymer Selbstanordnung. Diese Systeme stellten zwei einzigartige Probleme dar: Erstens musste das gesamte Reaktionsvolumen Wandkontakt mit den Wänden des Mikrofluidikkanals verhindern um Artefakten aus heterogener Nukleation und Wachstum vorzubeugen. Zweitens musste das hohe Streuhintergrundsignal des verwendeten PDMS minimiert werden um Messungen des Selbstanordnungsprozesses von Hydrogelbildnern und Polymeren mit Röntgenstreuung und Raman Spektroskopie zu ermöglichen.

Das erste Problem wurde beseitigt durch rechnerische und experimentelle Optimierung der Mischkreuzregion durch Bereitstellung von lateraler und vertikaler hydrodynamischer Flussfokussierung. Dieser mikrofluidische Aufbau wurde anschließend benutzt zur Untersuchung der pH induzierten Faserformation eines fluoreszierenden Hydrogelbildners, der Lösungsmitteltausch-induzierten Selbstanordnung eines wasserlöslichen fluoreszierenden konjugierten Polymers und der schnellen Reaktionskinetik der Nukleation und Wachstum von CdS Nanopartikeln. Diese Reaktionen konnten mittels Fluoreszenz- und Konfokalmikroskopie verfolgt werden.

In Kombination mit Röntgenstreuung und Ramanspektroskopie wurden die ausschließlich PDMS basierten Bauteile von PDMS-Glas Hybrid Bauteilen ersetzt, um ein geringeres Hintergrundsignal vom umgebenden Kanal zu gewährleisten und das zweite Problem zu beheben. Da die strukturelle Entwicklung der Gelfaserformierung durch supramolekulare Anordnung verfolgt werden konnte, dient dies als ein erster Beweis, dass die Untersuchung von schnelle Strukturänderungen *in-situ* mit einer Kombination aus Mikrofluidik und Mikrofokus-Röntgenstreuung verfolgt werden kann.

Eidesstattliche Erklärung

§4 Abs.1 Nr. 2 PromO

Ich habe die Dissertation nicht bereits zur Erlangung eines akademischen Grades anderweitig eingereicht und habe auch nicht bereits diese oder eine gleichartige Doktorprüfung nicht bestanden.

§4 Abs.1 Nr. 4 PromO

Hiermit erkläre ich, dass keine Tatsachen vorliegen, die mich nach den gesetzlichen Bestimmungen über die Führung akademischer Grade zur Führung eines Doktorgrades unwürdig erscheinen lassen.

§8 Nr. 3 PromO (§9 Nr. 3 BayNAT PromO)

Hiermit erkläre ich eidesstattlich, dass ich die Dissertation selbstständig verfasst und keine anderen als die von mir angegebenen Quellen und Hilfsmittel benutzt habe. Ich erkläre außerdem, dass ich die Dissertation nicht bereits zur Erlangung eines akademischen Grades eingereicht habe und auch nicht bereits diese oder eine gleichartige Doktorprüfung endgültig nicht bestanden habe.

§8 Nr. 4 PromO (§9 Nr. 4 BayNAT PromO)

Hiermit erkläre ich, dass ich keine Hilfe von gewerblichen Promotionsberatern bzw. -vermittlern oder ähnlichen Dienstleistern in Anspruch genommen habe und auch künftig nicht nehmen werde.

§8 Nr. 7 PromO (§9 Nr. 7 BayNAT PromO)

Hiermit erkläre ich mich damit einverstanden, dass die elektronische Fassung meiner Dissertation unter Wahrung meiner Urheberrechte und des Datenschutzes einer gesonderten Überprüfung hinsichtlich der eigenständigen Anfertigung der Dissertation unterzogen werden kann.

§8 Nr. 8 PromO (§9 Nr. 8 BayNAT PromO)

Hiermit erkläre ich mich damit einverstanden, dass bei Verdacht wissenschaftlichen Fehlverhaltens Ermittlungen durch universitäre Organe der wissenschaftlichen Selbstkontrolle stattfinden können.

Bayreuth, 29.03.2018

Susanne Seibt

Declaration

This is to certify that:

- (i) the thesis comprises of only my original work towards the PhD except where indicated otherwise,
- (ii) due acknowledgement has been made in the text to all other material used,
- (iii) the thesis is less than 100.000 words in length, exclusive of tables, maps, bibliographies and appendices.

Bayreuth, 29.03.2018

Susanne Seibt

- For Sebastian -

My everlasting idol, greatest support and beloved brother.

Preface

Refereed Journal Publications

During the course of this PhD project, several peer-review publications have been made, which are based on the work presented in Chapter 3, Chapter 4, Chapter 5, Chapter 6 and Chapter 7. They are listed here for reference in the actual publication status.

Schlenk, M.; Hofmann, E.; Seibt, S.; Rosenfeldt, S.; Schrack, L.; Drechsler, M.; Rothkirch, A.; Ohm, W.; Breu, J.; Gekle, S.; Förster, S. Parallel and perpendicular alignment of anisotropic particles in free liquid micro-jets and emerging micro-droplets. *Langmuir*, **2018**, *34*, 4843-4851.

Seibt, S.; With, S.; Bernet, A.; Schmidt, H.-W.; Förster, S. Hydrogelation kinetics measured in a microfluidic device with in-situ X-ray and fluorescence detection. *Langmuir*, **2018**, *34*, 5535-5544.

Seibt, S.; Zhang, H.; Mudie, S.; Förster, S.; Mulvaney, P. Growth Kinetics of Gold Nanorods: A SAXS Study. *Manuscript ready for submission*.

Seibt, S.; Mulvaney, P.; Förster, S. Millisecond CdS nanocrystal nucleation and growth studied by microfluidics with in-situ spectroscopy. *submitted to Colloids and Surfaces A*.

Seibt, S.; Johnson, B.; Schmidt, M.; Thelakkat, M.; Mulvaney, P.; Förster, S. Diffusion-limited self-assembly in microfluidics as a platform for structural analysis of anionic conjugated polyelectrolytes. *Manuscript in progress*.

Contents

Abstract	III
Zusammenfassung	V
Eidesstattliche Erklärung	VII
Declaration	IX
Preface	XIII
1. Introduction	1
1.1. Nanoparticles	1
1.1.1. Metal Nanoparticles	5
1.1.2. Semiconductor Nanoparticles	9
1.1.3. Synthesis Methods	12
1.2. Microfluidics	17
1.2.1. Microfluidic devices	18
1.2.2. Device design	21
1.2.3. Fluid dynamics	23
1.2.4. Convection	29
1.3. Self-Assembly	34
1.4. Thesis Outline	38
References	41
2. Experimental Methods	49
2.1. Materials	49
2.2. Microfluidic device fabrication	49
2.2.1. Photolithography	49
2.2.2. Soft lithography	50
2.2.3. Device handling	51
2.3. Instrumentation	51
2.3.1. UV-Vis spectrometry	51
2.3.2. Photoluminescence spectrometry	52
2.3.3. Confocal Laser Scanning Microscopy (CLSM)	52
2.3.4. Transmission Electron Microscopy (TEM)	53
2.3.5. Small angle X-ray scattering (SAXS)	55
References	60

3. Growth Kinetics of Gold Nanorods: A SAXS Study.	63
3.1. Abstract	64
3.2. Introduction	64
3.3. Experimental Methods	66
3.4. Results and Discussion	68
3.5. Conclusion	94
References	95
4. Parallel and perpendicular alignment of anisotropic particles in free liquid micro-jets and emerging micro-droplets.	97
4.1. Abstract	98
4.2. Introduction	98
4.3. Experimental Section	99
4.4. Results and Discussion	102
4.5. Conclusion	116
References	118
5. Hydrogelation kinetics measured in a microfluidic device with in-situ X-ray and fluorescence detection.	121
5.1. Abstract	122
5.2. Introduction	122
5.3. Experimental Section	124
5.4. Results and Discussion	128
5.5. Conclusion	140
References	141
6. Millisecond CdS nanocrystal nucleation and growth studied by microfluidics with in-situ spectroscopy.	145
6.1. Abstract	146
6.2. Introduction	146
6.3. Experimental Methods	148
6.4. Results and Discussion	150
6.5. Conclusion	156
References	158
7. Diffusion-limited self-assembly in microfluidics as a platform for structural analysis of anionic conjugated polyelectrolytes.	161
7.1. Abstract	162

7.2. Introduction	162
7.3. Experimental Methods	164
7.4. Results and Discussion	165
7.5. COMSOL Simulations	175
7.6. Conclusion	179
References	180
Concluding Remarks	183
Scientific Contributions	187
Acknowledgements	191
Appendix	193
A. SI: Growth Kinetics of Gold Nanorods: A SAXS Study	193
B. SI: Parallel and perpendicular alignment of anisotropic particles in free liquid micro-jets and emerging micro-droplets.	211
C. SI: Hydrogelation kinetics measured in a microfluidic device with in-situ X-ray and fluorescence detection.	227
D. SI: Millisecond CdS nanocrystal nucleation and growth studied by microfluidics with in-situ spectroscopy.	240
E. SI: Diffusion-limited self-assembly in microfluidics as a platform for structural analysis of anionic conjugated polyelectrolytes.	245

Chapter 1

1. Introduction

1.1. Nanoparticles

"Nanos" - from the Greek word for dwarf, is commonly used as a unit prefix, meaning one billionth. In science, the term "nanoparticle", describes particles made up of hundreds to thousands of atoms, with dimensions between 1-100 nm. Different shaped particles can be classed under the term nanoparticle, including platelets, disks and sheets with one dimension in this range, wires and rods with two dimensions in the nanometre range and spheres, stars, cubes or prisms with all three dimensions smaller than 100 nm. The chemical and physical properties of these nanoparticles distinguish them clearly from the corresponding macroscopic material. Size dependent characteristics are influenced by mainly 2 effects - the fraction of atoms at the surface and the quantum confinement effect.^[1,2]

Surface effects

With decreasing particle size, the ratio of surface to core atoms increases. Hence, this so called dispersion F is much higher than in the bulk material and is, for cubic particles, given by equation 1.1. For larger particles, F approximately follows a $N^{-1/3}$ scaling law.

$$F = \frac{6n^2 - 12n + 8}{n^3} = \frac{6}{N^{1/3}} \left(1 - \frac{2}{N^{1/3}} + \frac{8}{6N^{2/3}} \right) \approx \frac{6}{N^{1/3}} \quad (1.1)$$

Here n is the number of atoms along a cube edge and $N = n^3$ is the total number of atoms. To display this relationship, F as a function of n is shown in Figure 1.1, where for $n = 2$ the dispersion equals 1, due to every atom being at the surface. A similar trend for the dispersion can be found for spheres, as the volume scales with radius³.

The atoms at the surface of the cluster are less stable than the ones in the core, because of their lower coordination number and fewer bonds. The least stable atoms are the corner atoms, which have the lowest saturation of neighbours, followed by edge and in-plane surface atoms. At thermodynamic equilibrium the sphere is the most stable geometry, lacking corner and edge atoms and containing the highest volume to surface ratio.^[1]

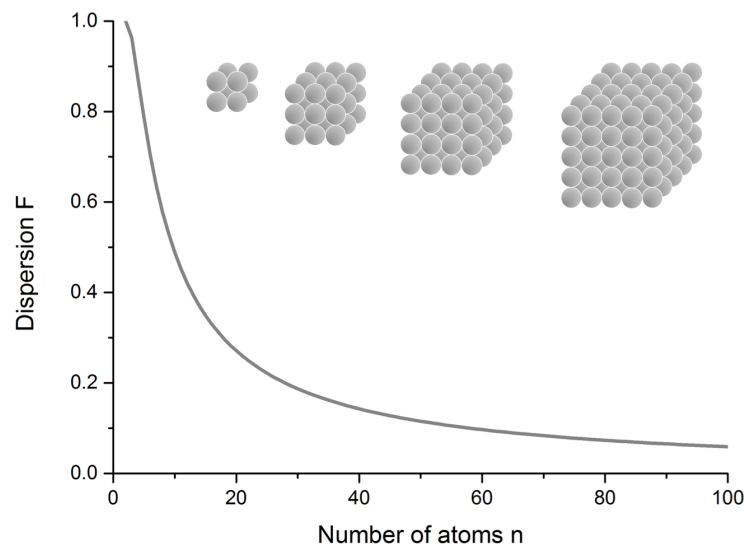


Figure 1.1: Dispersion F as a function of the total number of atoms n for cubic clusters up to 100 atoms. The structure of the first 4 clusters is displayed.

Another effect of the decreased stabilisation of surface atoms is a lower material melting point. This was described by W. Thomson in 1871, leading to the widely known Gibbs-Thomson equation^[3]

$$\frac{T_m - T_m^*}{T_m^*} = \frac{\Delta T_m}{T_m^*} = -\frac{2V_{m,l}\gamma_{sl}}{\Delta H_m r} \quad (1.2)$$

where T_m is the melting point of the cluster with radius r , T_m^* is the melting point of the bulk material, $V_{m,l}$ the molar volume of the liquid, γ_{sl} the interfacial tension between the solid and the liquid surface and ΔH_m the bulk latent heat of melting.

In general, equation 1.2 results in a linear dependency of the melting point with the inverse diameter, extrapolating to the melting point of the bulk material. The behaviour of these endotherms typically includes a broadened melting temperature that is characteristic for nanomaterials.^[1]

Quantum effects

The rules for classical physics are not sufficient to describe the properties of nanoparticles, therefore the laws of quantum-mechanics are needed. A fundamental aspect of quantum mechanics is the wave-particle duality after de Broglie. With decreasing volume of a material, approaching the dimension of the de Broglie wavelength of the charge carrier, the carrier's mobility becomes limited, leading to an energy level quantisation, i.e. quantisation is due to spatial restriction of the charge carrier. Size dependent optical properties are the consequence of this quantum confinement ef-

fect. To explain this phenomenon, two theoretical models can be used: the "linear combination of atomic orbitals" (LCAO) theory^[4,5] or the "Particle in a Box" model.^[6] The significant difference between these two approaches is the particle size. While the LCAO uses a large particle assumption, the "Particle in a Box" model describes nanoparticle energy levels in terms of a size correction to the bulk properties.

The electrons in atoms can move, within the bounds of their probability density, unhindered in their atomic orbitals (AO). Those orbitals are stacked around the atomic core and cannot be exactly calculated analytically. However, using approximations such as the Hartree-Fock-Method^[7] it is possible to describe atomic orbitals, leading to a distribution of discrete energy levels. In molecules, those AOs combine to form molecular orbitals (MO), divided into bonding and anti-bonding orbitals. Electrons fill the energetically lower MOs first, up to the "highest occupied molecular orbital" (HOMO), whereas the first empty level is the "lowest unoccupied molecular orbital" (LUMO).^[4,5]

In macroscopic bulk material, MOs combine periodically, leading to a higher density of states (DOS). Degeneracy of the single energy levels build into energy bands, within the charge carrier can be delocalised.^[1] The occupied energy levels up to the HOMO form the so-called valence band, while the unoccupied levels down to the LUMO degenerate to the conduction band. The energy difference between HOMO and LUMO is called the bandgap (BG). The bandgap energy determines many of the properties of a material, from metals (no BG), semiconductors (small BG) and insulators (large BG). Nanoparticles are the transition size regime between atoms or molecules and macroscopic bulk material, and as such they still have discrete energy levels, however the energy spacing is much lower than for the MOs of molecules.

The quantisation of the energy levels only influences the properties of metal nanoparticles with less than 100 atoms. Regarding the transition of molecules to nanoparticles, the energy levels form at the centre of the energy bands. For metals, this is the level of the Fermi edge. The emerging valence and conduction bands already form with just a few metal atoms, without a bandgap (see Figure 1.2). For gold, the transition from molecule to nanoparticle is determined at a cluster size of 55 gold atoms Au_{55} . Therefore, the size confinement effect is especially distinctive in metal nanoparticles larger than one nanometer.^[8]

In semiconducting nanoparticles however, quantisation affects the edge of the energy bands, leading to an increasing bandgap in comparison to the bulk material through discretisation. This defines and modifies the optical and electrical properties of the material.^[9]

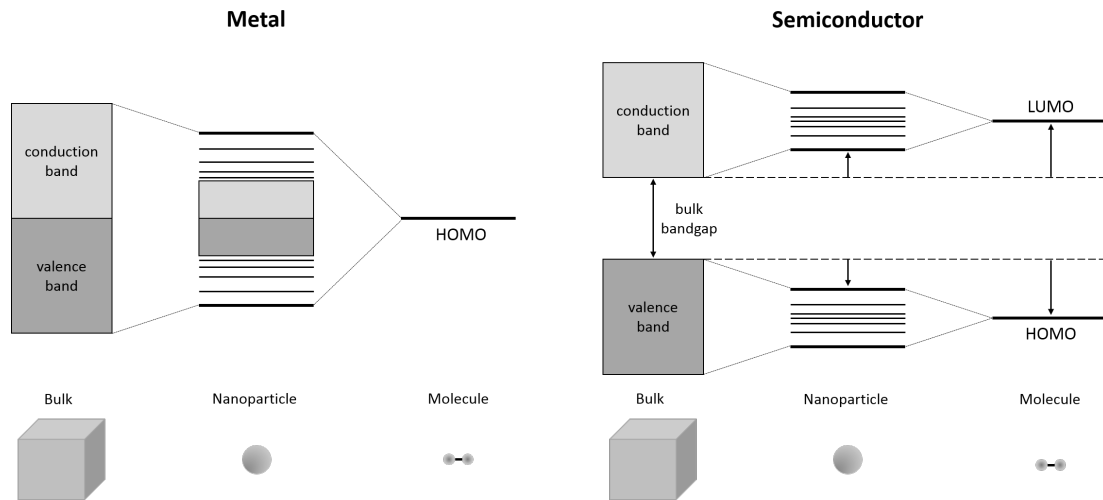


Figure 1.2: Schematic diagram of the density of states (DOS) in metal (left) and semi-conducting material (right). Transition of the conduction and valence band to discrete energy levels from a bulk material, to nanoparticles, to molecules.

The "Particle in a Box" model describes the charge carriers as particles in a box with a well-defined width and infinite height, in which the particle can move unhindered. The nanoparticle is represented by the box, whilst an electron-hole pair (exciton) serves as the particle. Due to electrostatic attraction, the electron and the hole in this exciton exist at a certain separation, known as the Bohr-radius. For a nanoparticle with a size smaller than this Bohr-radius, the electron starts to feel the restrictions of the walls. Therefore, the one dimensional potential is given by

$$E = \frac{n^2 h^2}{8mL^2} \quad (1.3)$$

with h the Planck constant, m the mass of the particle, L the width of the box, n is the quantum number and is a positive integer. As the walls are infinitely high, the particle cannot leave the box and L must be an even multiple of a half wavelength of the box. The Brus equation (see equation 1.4) defines the change in the bandgap energy as a function of the nanoparticle size for spherical particles.

$$\Delta E = \frac{h^2}{8R^2} \left(\frac{1}{m_e} + \frac{1}{m_h} \right) - \frac{1.8e^2}{4\pi\epsilon\epsilon_0 R} \quad (1.4)$$

h is the Planck constant, R the particle radius, m_e the mass of the electron and m_h the mass of the hole, e the electron charge, ϵ the permittivity and ϵ_0 the permittivity in vacuum. This equation features an approximately inverse square relation between particle size and bandgap, $\Delta E \propto R^{-2}$.^[6]

1.1.1. Metal Nanoparticles

Gold - the metal of kings - is known in our macroscopic world as a gold coloured, soft material.^[5] Gold nanoparticles, also known as colloidal gold, are however red in colour. They have been used since medieval times to dye glass and ceramics red or purple.^[10] Glass makers since the 4th century produced these particles for window colours by reducing certain metal salts during the glass manufacture.^[11] The chemical examination of these colloids was hindered for a long time however due to the noble character of gold, which makes the use of strongly oxidising liquids (e.g. aqua regia) or complexing agents (e.g. cyanides) necessary to get it to dissolve in solution under air.^[2,8,12]

The syntheses of metal nanoparticles have been intensively refined in the past years. The development from the early Turkevich (20 nm gold spheres)^[13] and Frens (16 nm - 147 nm gold spheres)^[14] methods has led to precisely controlled reaction conditions for the production of well-defined particles. Those metal nanoparticles with different sizes and shapes show various properties and find more and more applications in fields of modern nanotechnology, such as sensing,^[15,16] waveguiding,^[17] medicine,^[18,19] catalysis,^[20] and coating materials.^[21]

Optical properties

Metal nanoparticles have been the centre of attention for a long time because of their unique optical properties. Especially for silver and gold nanoparticles, size and shape play a key role in determining the absorption and scattering properties of the material.^[22] When such nanocrystals are irradiated with light, the electric field of the incoming light interacts with the free electrons on the particle surface. Hence, the surface electrons start to oscillate collectively as an electron cloud around the metal nanoparticle. This oscillation phenomenon is called a plasmon.^[23] At an interface between a metal nanoparticle and a dielectric material, a so-called surface plasmon resonance (SPR) occurs. These can either propagate as surface plasmon polaritons or be spatially confined as a localised surface plasmon resonance (LSPR), which is shown in Figure 1.3.^[22,23]

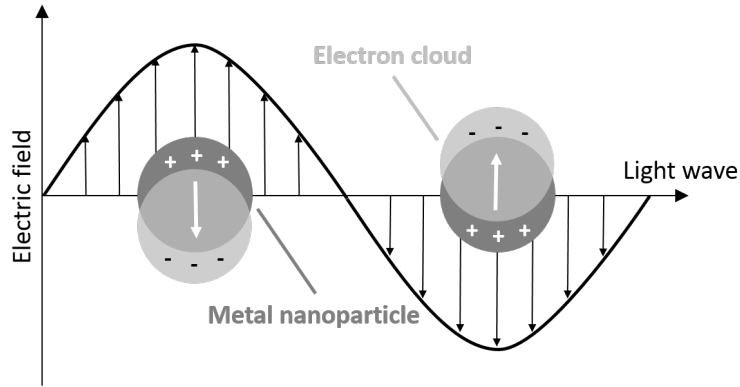


Figure 1.3: Schematic drawing of the light-matter interaction. The electric field of an incoming light wave interacts with the resonant condition of a nanoparticle in a dielectric medium. The free conduction electrons on the particle surface couple with the light wave and oscillate collectively. This oscillating electron cloud around the nanocrystal is called the localised surface plasmon resonance (LSPR).

To describe the optical properties of spherical nanoparticles, the Mie theory is used. Gustav Mie published in 1908 a complete theoretical explanation of absorption and scattering effect of electromagnetic radiation by an arbitrary sphere by solving Maxwell's equations.^[24] The absorption A of a dilute nanoparticle solution is given by

$$A = \log \left(\frac{I_0}{I_d} \right) = \frac{NC_{ext}d}{2.303} \quad (1.5)$$

where I_0 is the intensity of the incoming light, I_d the intensity of the outgoing light over a pathlength d , N is the number of particles per unit volume and C_{ext} is the extinction cross-section.^[22,25]

The extinction cross-section C_{ext} for spherical particles with a wavelength dependent dielectric function $\epsilon = \epsilon' + i\epsilon''$ which are in a medium with a dielectric function ϵ_m can be written as

$$C_{ext} = \frac{2\pi}{k^2} \sum_{n=0}^{\infty} (2n+1) \text{Re}\{a_n + b_n\} \quad (1.6)$$

with $k = 2\pi\frac{\sqrt{\epsilon_m}}{\lambda}$ and a_n and b_n as Mie scattering coefficients. The latter are a function of the particle radius R and the wavelength λ described by the Ricatti-Bessel function. In case of metal spheres below 30 nm, where $kR \ll 1$, only dipole oscillation contributes significantly to the total extinction and Mie's theory can therefore be reduced to the dipole approximation - known as the Rayleigh approximation. Thus, the extinction cross-section at a certain wavelength λ can be written as

$$C_{ext} = \frac{24\pi^2 R^3 \epsilon_m^{3/2}}{\lambda} \frac{\epsilon''}{(\epsilon' + 2\epsilon_m)^2 + \epsilon''^2} \quad (1.7)$$

Mie theory can be used to predict the position of the extinction maximum of resonant metal nanoparticles. However, the actual line shape of an extinction spectrum cannot be predicted by these equations, as they don't include all the physical processes occurring in nanoparticles and their interaction in solutions.^[26]

To describe the dielectric response, the Drude model is used, which has a real and imaginary part for the dielectric function, shown in equations 1.8 and 1.9. However, the free electron behaviour can only be used for metal particles whose frequencies are lower than the bulk plasma value.

$$\epsilon'(\lambda) = \epsilon(0) - \frac{\lambda^2}{\lambda_p^2} \quad (1.8)$$

$$\epsilon''(\lambda) = \frac{\lambda(\lambda^2 + \lambda_d^2)}{\lambda_p^2 \lambda_d} \quad (1.9)$$

$\epsilon(0)$ is the short wavelength dielectric constant, accounting for all UV absorption bands, λ_d is the conduction electron damping constant, λ_p is the bulk plasma wavelength, which can be described by the following:

$$\lambda_p = \frac{2\pi c}{\omega_p} = \sqrt{\frac{4\pi^2 c^2 m \epsilon_0}{N e^2}} \quad (1.10)$$

where m is the effective electron mass, ω_d is the damping frequency, ϵ_0 the permittivity in vacuum, N the electron density and e the electron charge.

Hence, following equation 1.7, the surface plasmon band will appear for a small ϵ'' when

$$\epsilon' = -2\epsilon_m \quad (1.11)$$

The Mie theory in combination with the Drude model show the dependency between absorption peak, size of the particle, inherent properties and the dielectric constant of the surrounding medium. With an increasing particle size, higher order terms start to dominate in this regime and the position of the absorption peak shifts to higher wavelength.^[27,28]

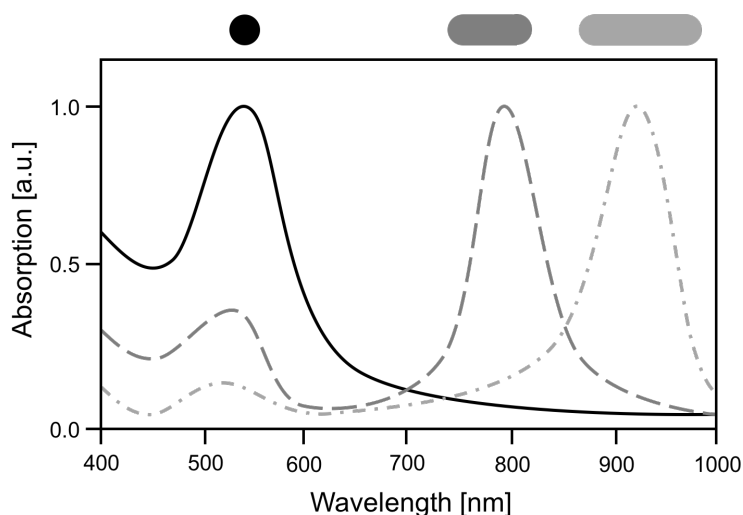


Figure 1.4: Peak-normalised extinction spectra of gold spheres and nanorods in aqueous solution with varying aspect ratio. A red-shift of the LSPR with increasing aspect ratio can be seen.

A representative absorption spectrum of gold spheres is shown in Figure 1.4 (black solid line). A characteristic surface plasmon band could be observed around 520 nm. Non-spherical particles however show multiple LSPR modes, which are displayed in Figure 1.4 as dashed lines in grey for various aspect ratios of rodshaped gold nanocrystals. The equations formulated by Gustav Mie predict very precisely the absorption of spheres of various sizes, though his model does not include other shapes and morphologies. To predict the optical properties of ellipsoidal shaped particles, Richard Gans extended Mie's equation by broadening the dipole approximation (see equation 1.7).^[29,30]

As described earlier, two LSPR modes can be seen in the absorption spectra of gold nanorods, shown in Figure 1.4. These two plasmon resonances, commonly known as transverse and longitudinal modes, correspond to the oscillations along the rod axes. The transverse band of gold nanorods appears as an absorption peak around 520 nm, which is similar to the extinction of spherical gold particles. It corresponds to the oscillations across the short axis of the nanorod. The longitudinal band can be found at higher wavelength and red-shifts with increasing aspect ratio (AR, nanorod length L divided by nanorod width D ; $AR = L/D$). It corresponds to the oscillation across the long axis, the length, of the nanorod and the width and intensity of the peak is strongly influenced by surface scattering and radiation damping.

The polarisability α of ellipsoidal nanorods can be described by

$$\alpha = \frac{4\pi abc (\epsilon_{Au} - \epsilon_m)}{3\epsilon_m + 3L_{xyz} (\epsilon_{Au} - \epsilon_m)} \quad (1.12)$$

where a , b and c are the dimensions of the ellipsoid along the x -, y - and z -axis. Thereby the condition $a > b = c$ applies. L_{xyz} is the polarisation factor along the corresponding axis, described by

$$L_x = \frac{1 - e^2}{e^2} \left(-1 + \frac{1}{2e} \ln \frac{1 + e}{1 - e} \right) \quad (1.13)$$

$$L_{y,z} = \frac{(1 - L_x)}{2} \quad (1.14)$$

with e the rod ellipticity, given by $e^2 = 1 - \left(\frac{b}{a}\right)^2$. To calculate the position of the longitudinal plasmon resonance of rod-shaped gold nanocrystals, the Gans-Drude theory can be used.^[25]

$$\lambda^2 = \lambda_p^2 \left(\epsilon^0 + \epsilon_m \left(\frac{1}{L} - 1 \right) \right) \quad (1.15)$$

Equation 1.15 reveals the strong dependence of the surface plasmon resonance energy on both the solvent refractive index and the particle shape.

1.1.2. Semiconductor Nanoparticles

Semiconducting nanoparticles - widely referred to as quantum dots (QDs) have gained interest over the last two decades because of their unique chemical and physical properties, which, like metal nanoparticles, show a strong dependence on size and shape of the nanocrystal.^[31-35] However, the origin of the size dependence is quite different. When the nanoparticle size becomes comparable to the Bohr radius of excitons in the bulk material, a strong confinement effect arises.^[31,36] The electronic, optical and chemical properties of QDs can therefore be tailored by their size and surface composition for various fields of application.^[37,38]

Quantum dots can be built up from a huge variety of semiconducting materials^[39], however this thesis will focus on II-IV semiconductor particles, such as cadmium sulfide (CdS). CdS nanoparticles are of special interest due to their wide band gap of 2.4 eV and their good optical transmittance.^[40,41] The access to tunable photoluminescence across the visible spectrum has led to wide applications in solar cells, photodetectors, light-emitting diodes or biological labelling.^[42]

Optical properties

In general, the physical phenomenon of quantum confinement results from changes in the density of electronic states. These can be explained by the relationship between momentum and position of free carriers and their confinement in nanoparticles. If a particle in a solid bulk material is considered as a free particle, the crystal momentum and the energy can be precisely defined, whilst the position is undefined. In nanoparticles, a more localised state exists, where the energy remains defined, whereas the positional uncertainty decreases. This causes the momentum to be no longer precisely defined, leading to a transition of the discrete energy of the bulk material eigenfunctions to superpositions of bulk momentum states. In semiconducting nanoparticles, this causes photon absorption/emission of a certain energetic width occurring in bulk material, to be narrowed by the quantum confinement to a single, more intense transition.^[31] The DOS is dependent on the size of the semiconducting material (Figure 1.5 A) and its dimension (Figure 1.5 B).

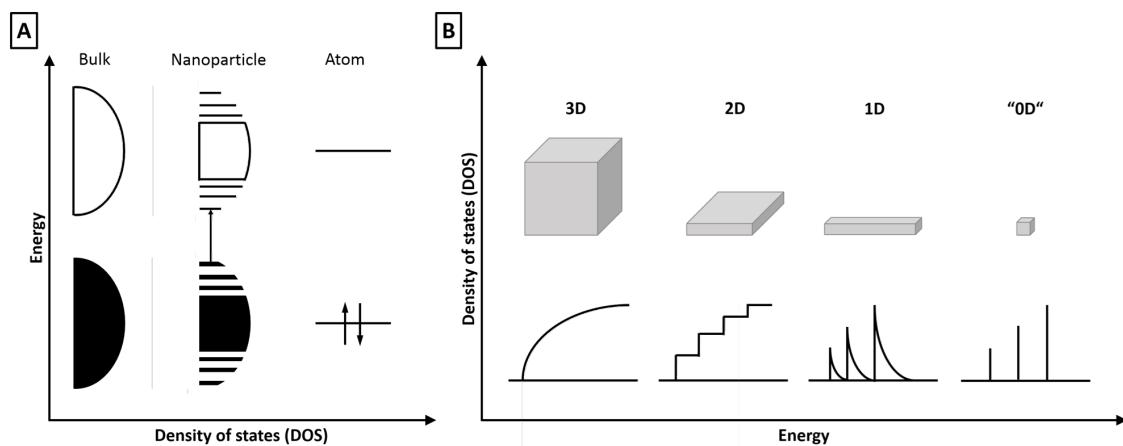


Figure 1.5: (A) Density of electronic states shown for a semiconductor material in bulk, nanoparticle and atom. (B) Semiconductor DOS in one band displayed as a function of dimension. Reproduced from reference^[31]

If a photon of incident light has a higher or equal energy to that of the bandgap of the semiconducting material it is impinging on, an electron can be excited from the valence band to the conduction band. As described in Chapter 1.1, Quantum effect, this excited electron leaves a positively charged hole in the valence band. The electron and hole can be seen as two separate particles with effective masses m_e^* and m_h^* respectively, described as a fraction of the electron rest mass m_0 . The electron-hole pairs, so called excitons, are bound together by Coulomb forces with an effective mass of $m^* = \frac{(m_e^* m_h^*)}{m_e^* + m_h^*}$. The Bohr radius a_B defines the area in which those excitons are localised by

$$a_B = \frac{4\pi\epsilon_r\epsilon_0\hbar^2}{m^*m_0e^2} = 5.29 \cdot 10^{-11}m \quad (1.16)$$

where ϵ_r is the relative permittivity of the material, ϵ_0 the vacuum permittivity, \hbar the reduced Planck constant and e the elemental charge of an electron.^[43]

Considering the electron and hole as individual particles in a spherical potential well of infinite height (see chapter 1.1), Brus described the origin of size-dependent electron and hole energy levels as discrete atom-like energies by

$$E_{n,l} = \frac{\hbar^2\alpha_{n,l}^2}{2m_{e/h}^*m_0r^2} \quad (1.17)$$

with $n = 1,2,3,\dots$ and $l = s,p,d,\dots$ as quantum numbers, $\alpha_{n,l}^2$ is the n th zero of the l th order spherical Bessel function, $m_{e/h}^*$ is the effective mass of electron or hole and r is the radius of the sphere (QD).^[43,44]

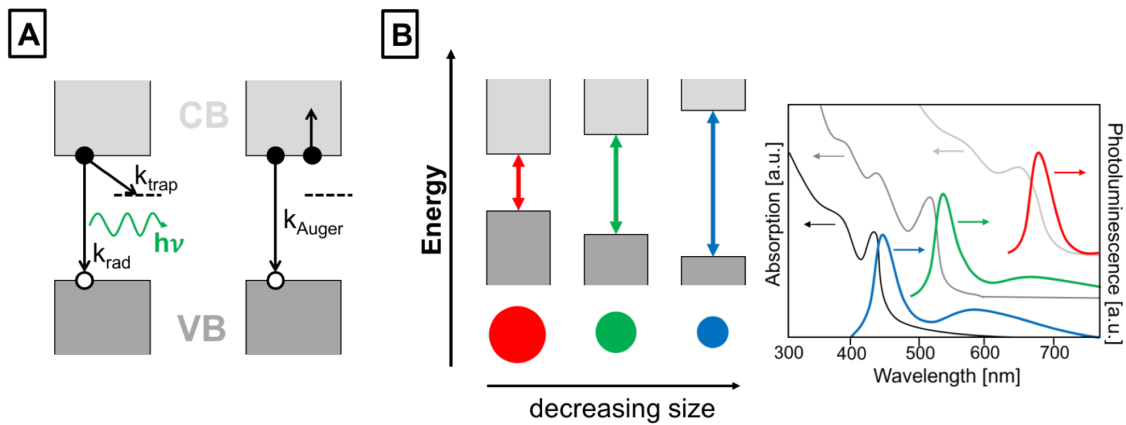


Figure 1.6: (A) Schematic illustration of the processes leading to the decay of an exciton: radiative recombination (k_{rad}), trapping of the electron (k_{trap}) followed by non-radiative or radiative recombination and Auger recombination (k_{Auger}). (B) Size-dependent bandgap energies displayed for three different particle sizes schematically (left). Characteristic absorption and emission spectra according to the three different sized quantum dots (right).

There are several processes occurring, which lead to the decay of an exciton, shown schematically in Figure 1.6 A. The first process is the radiative decay by direct recombination of electron and hole whilst emitting a photon with the same energy as the bandgap energy ($h\nu$). In Figure 1.6 this is labelled with the reaction rate constant k_{rad} . The direct recombination process can be observed in photoluminescence spectra (see Figure 1.6 B) as a sharp fluorescence peak, which shows a redshift with increasing particle size.

Another process is the two-step recombination over a trap-state (k_{trap}). The electrons

or holes can be trapped in a mid-gap energy state and then recombine from that energy level radiatively or non-radiatively. If the recombination occurs radiatively, a lower-energy photon is emitted, leading to the broadened emission band at higher wavelength in the photoluminescence spectra, shown in Fig. 1.6 B.^[45]

The third possibility is the so-called Auger recombination (k_{Auger}). Thereby, an electron and hole recombine by transferring their energy to an extra electron or hole in the same quantum dot. Hence, this effect can only occur in the presence of multiple electrons and holes. The excited charge carrier then loses the transmitted energy by collisions with the particle lattice.^[46]

1.1.3. Synthesis Methods

There are several techniques, which can be used for the synthesis of nanoparticles. In general, they can be split into two main approaches - the "top-down" and the "bottom-up" method.

The synthesis of nanoparticles following the "top-down" method is a destructive approach and is carried out by size-reduction of macroscopic particles from the bulk-phase. Thereby, the application of energy, with which the lateral dimension is reduced, is essential to form nanoparticles. Techniques for this method are milling, grinding, atomisation, high pressure homogenisation, shearing, agitation, ultrasonic treatment or phase inversion. The advantages of all these methods are their easy implementation in laboratories and the large amount of sample which can be produced. However, the "top-down" method is rarely used due to the highly variable influence of the energy application, involving huge technical effort and costs, as well as the difficulty in controlling synthetic conditions, leading to sample polydispersity.^[47-49]

The "bottom-up" method in contrast is a constructive approach, usually following the two-step mechanism of nucleation and growth. This process is thermodynamically controlled and mainly produces nanoparticles from molecular precursors by chemical approaches. Besides the common batch synthesis in solution, thermal decomposition, sol-gel-processes and aerosol procedures are typical techniques used for this method. All techniques provide precise control over reaction conditions and surface protection, leading to highly monodisperse samples of the desired size, and therefore precisely tuned properties. However, the resulting small batch size and the extensive and complex synthesis and purification steps are disadvantages of this method.^[47-49]

Nucleation of nanoparticles

Nucleation of particles generally occurs in two ways - homogeneous or heterogeneous. Homogeneous nucleation describes the statistical constructive conjunction of molecules without external forces, whereas heterogeneous nucleation is initiated on an existing surfaces, especially in the presence of defects.

The key results from classical nucleation theory are described by the Gibbs-Thomson relation, in terms of the surface energy of a solid particle with diameter r , which is in equilibrium with a concentration of a soluble monomer unit of the composite material, $[C]_e$ (see equation 1.18).

$$[C]_e = [C]_\infty \exp \left\{ \frac{2\gamma V_m}{rRT} \right\} \quad (1.18)$$

$[C]_e$ is the concentration of the monomer C , which is in equilibrium with the particle of diameter r , $[C]_\infty$ is the concentration of the monomer in equilibrium with a surface of infinite curvature, such as a flat surface, γ is the surface energy, T the Temperature, R the ideal gas constant and V_m the molar volume. This equation predicts that, if the concentration of monomer in the bulk of the solution $[C]_b$ decreases, smaller particles will preferentially dissolve. The ratio of monomer in the bulk to $[C]_\infty$ is defined as the supersaturation of monomer S , with $S = \frac{[C]_b}{[C]_\infty}$.^[50]

Entropically, as well as energetically, it is unfavourable for a system to form nuclei, and thus increase the surface. Thermodynamically this is explained by the free energy ΔG in the solution, which is described by

$$\Delta G = \Delta G_{bulk} + \Delta G_{surface} = \frac{4}{3}\pi r^3 \Delta G_\nu + 4\pi r^2 \gamma \quad (1.19)$$

where ΔG_ν is the free energy per unit volume of the material. This is highly dependent on the supersaturation S , expressed by

$$\Delta G_\nu = \frac{-RT \ln S}{V_m} \quad (1.20)$$

The free energy ΔG_ν of the bulk term in equation 1.19 is negative until the concentration reaches the point of saturation. The dependency of the free energy in solution ΔG from the radius r leads to a critical radius r^* , which is shown in Figure 1.7. Below this critical radius, particles decrease their local free energy by dissolving in solution, whereas above this nuclei size, formed particles are stable and able to grow.^[51-53]

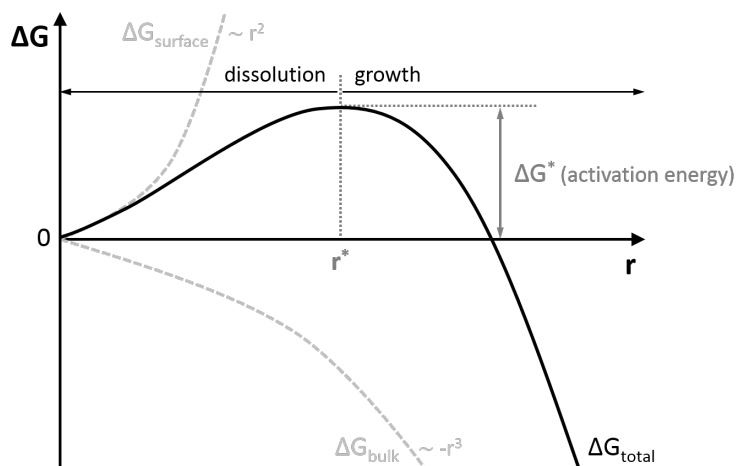


Figure 1.7: Free Energy ΔG in solution as a function of the nuclei radius r using 1.19.

The critical radius r^* can be calculated by differentiating equation 1.19 and setting ΔG equal to zero, leading to the following expression:

$$r^* = \frac{2\gamma V_m}{RT \ln S} \quad (1.21)$$

Equation 1.21 shows the dependency of the critical radius r^* from the supersaturation S in the solution. This predicts the process of particle ripening, widely known as Ostwald-ripening, in which at a later time in the reaction the supersaturation of monomer is low enough that r^* becomes larger than the radius of the smallest nuclei in the solution. This forces the latter to dissolve in solution (see Figure 1.7) in favour of bigger particles growing further, leading to a broadened size distribution of particles in the solution.^[51-53] Furthermore, the critical radius is strongly influenced by the temperature T and the surface energy γ . The latter can be precisely controlled by the type and concentration of ligand, which is chosen for each reaction.

Growth of nanoparticles

For the growth of a colloidal particle, two processes are important: the diffusion of the monomer towards the nuclei surface and the reaction of those monomers at the surface. Figure 1.8 displays the situation for a nuclei with radius r , where $[C]_b$ is the bulk concentration of monomer, $[C]_i$ the concentration of monomer at the interface, and $[C]_e$ describes the solubility of the particle as a function of the radius. δ is the thickness of the diffusive layer around the particle and can be described as a function of the hydrodynamic shear coming from the Brownian motion of the particle.^[51] The monomer diffuses towards the nuclei in solution with the diffusion coefficient D and the reaction rate of the monomer with the particle surface is labeled as k .

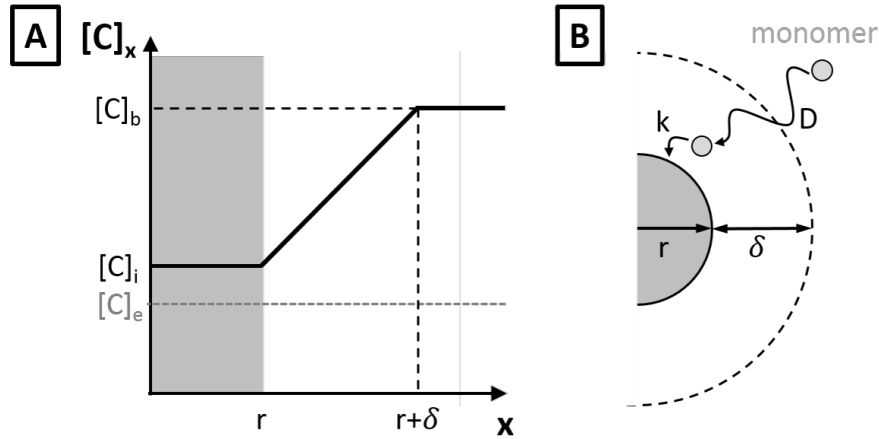


Figure 1.8: (A) Radial averaged monomer concentration $[C]_x$ distribution in the diffusion layer around the particle. (B) Schematic of the particle cross-section in a growth solution containing a monomer gradient δ . The monomer is diffusing through the diffusion layer of width δ with a Diffusioncoefficient D and reacts with the particle surface with the reaction rate k .

In general, the growth of nanoparticles can be diffusion-limited and reaction-limited. Therefore two different growth rates can be derived. If the particle growth would be purely diffusion-limited, monomer and surface react instantly, which leads to $[C]_i \simeq [C]_e$. In pure reaction-limited growth, the diffusion layer concentration will be in equilibrium with the bulk monomer concentration, hence $[C]_i \simeq [C]_b$. Sugimoto first derived separate equations for the respective growth rate using these limiting conditions in combination with Fick's law.^[51] The diffusion-limited growth rate in relation to the radius r and critical radius r^* is therefore described by

$$\frac{dr}{dt} = \frac{2\gamma V_m^2 [C]_\infty D}{RT} \left(\frac{1}{r^*} - \frac{1}{r} \right) \quad (1.22)$$

and the reaction-limited growth rate by

$$\frac{dr}{dt} = \frac{2\gamma V_m^2 [C]_\infty k}{RT} \left(\frac{1}{r^*} - \frac{1}{r} \right) \quad (1.23)$$

Figure 1.9 A shows the reaction rate as a function of the particle radius for diffusion-limited growth. The growth rate there shows a maximum peak at $2r^*$. This would broaden the particle size distribution due to the faster growth of larger particles compared to smaller ones. When a crystal size of $2r^*$ is achieved, the growth of the bigger particles slows down until it is slower than the smaller particle growth and the size distribution begins to get narrower. Ostwald-ripening processes will compete in this case with size focusing at the late stages of the reaction, when the supersaturation

of the monomer is decreasing. However, reaction-limited growth predicts that larger particles constantly grow faster than smaller particles, showing a consistent increase in reaction rate. A more and more broadened particle size distribution results.^[51,53]

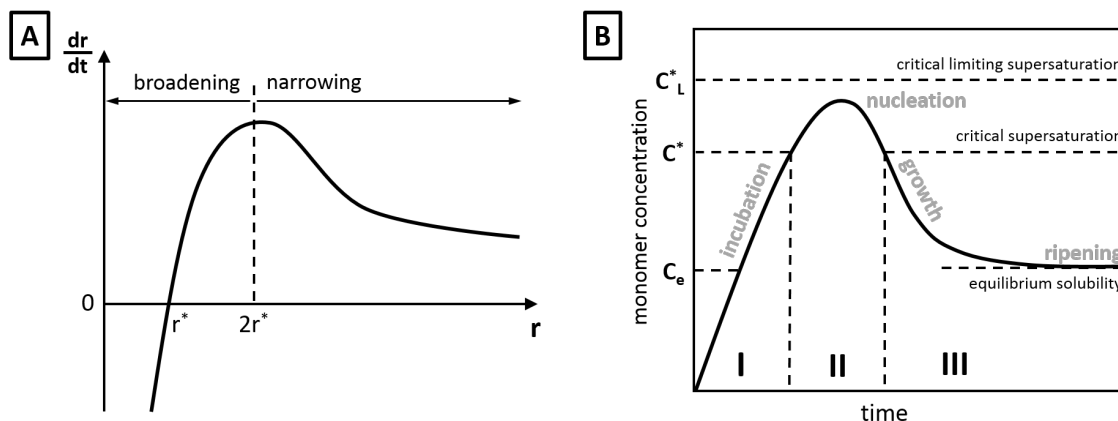


Figure 1.9: (A) Growth rate as a function of the particle radius r in the case of diffusion-limited growth (equation 1.22). (B) Plot of the monomer concentration as a function of reaction time following the theory of LaMer and Dinegar.^[54]

To synthesise monodisperse nanoparticles, the size distribution should be as narrow as possible. Therefore, LaMer and Dinegar^[54] provided the key theory by dividing the reaction into three regions, shown in Figure 1.9 B.

Phase I is the so-called incubation period. The reactions of the precursor in solution increase the concentration of the monomer until it reaches a critical concentration C^* . At this point, a metastable condition exists and the system becomes heterogeneous by starting to nucleate. The second phase (II) displays the fast nucleation, at which the concentration of monomer decreases through the formation of nuclei until it is below C^* . Finally, phase III in which the slower growth of nanoparticles takes place through diffusion and reaction of monomer. When the concentration of monomer reaches the equilibrium solubility, these formed particles gain slowly in size by a ripening process. LaMer^[54] states that the final size distribution is determined by the critical first phase (nucleation), defined by the time and nucleation rate. However, recent studies have shown, that a strict separation between nucleation, growth and ripening stage may not be valid for the general growth of nanoparticles in solution generally.^[50]

The study of nucleation in bulk solutions has proven to be incredibly difficult. A new approach uses microfluidics to create a continuous nucleating system.

1.2. Microfluidics

Microfluidics - as the name already reveals, is a multidisciplinary field of science concerned with the behaviour and manipulation of gases and liquids in dimensions between $10\ \mu\text{m}$ and $100\ \mu\text{m}$. These can be fundamentally different from macroscopic systems, as in micro-dimensions certain effects become dominant that are irrelevant in classical fluid dynamics. Most importantly, inside a microfluidic channel, no turbulent mixing occurs, as shown in Figure 1.10. If liquids are brought together in a microfluidic device, the present laminar flow present means they can only mix by diffusion. On the other hand, this has the advantage of allowing prediction of the exact movement of a particle by calculation, as no chaotic mixing needs to be considered.^[55]

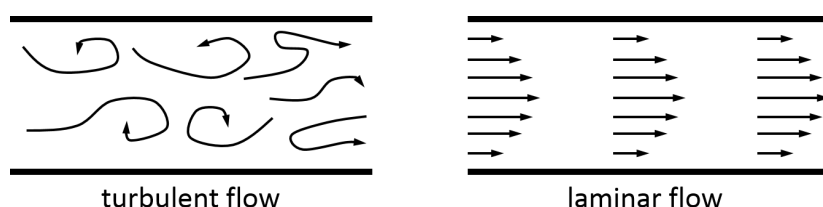


Figure 1.10: Schematic illustration of turbulent and laminar flow of a fluid in a microfluidic channel.

The applications of microfluidics can be found in various fields, such as analytics, biology, chemistry, medicine, and technology. The most important benefit of microfluidics is its ability to perform quantitative and qualitative analysis with high sensitivity and resolution, whilst microfluidic devices only need small amounts of substances. Furthermore, it is a low cost method for fast analysis, which is, in combination with the low sample quantity needed, highly efficient and useful when working with toxic, valuable or low volume samples.^[56]

Historically, the beginning of microfluidics as a scientific method was in the 1970s^[57], as miniaturisation became more and more developed. However, the significant increase in real applications came with the development of *rapid prototyping*, a combination of photolithography, soft lithography and commercial printing, making the fast and efficient construction and fabrication of microfluidic devices with customised designs possible.^[58] The analysis of aqueous solutions in different ways using microfluidics was first introduced by Manz^[59,60], Harrison^[61], Ramsey^[62] and Mathies^[63] in the 1990s, originating from microelectronics.^[58]

In general, two fundamental experiments (excluding any droplet methods) can be differentiated - stopped flow and continuous flow (see Figure 1.11). Microfluidic devices

for stopped flow experiments provide a temporal resolution from hours down to microseconds. Due to their easy setup and design, stopped flow cells are the ideal choice for *in-situ* measurements of slow reactions which take a long time to reach the final product stage.^[64] As there is no more change in the investigated sample volume after the cell is filled and the flow stopped, it is guaranteed that the same part of the solution is investigated over time. However, this can lead to damage by the probe beam, influencing the observed reaction. Furthermore, agglomeration of reacting sample on the walls can influence the measurement quality and due to the ongoing reaction, only small windows of each reaction step can be detected once before the experiment has to be repeated.

Continuous flow experiments on the other hand have many advantages. They have time-resolution down to nanoseconds, depending on design and flow velocity and there is no dead time between the start of the reaction and the first measurements, as the on-point can be precisely controlled and shifted in the scannable region of the microfluidic device. In addition, the reaction is spread out along the channel, providing steady conditions at each position, which can be scanned as long and as often as necessary. As a result of continuous flow, no beam damage has to be considered, as there is a continued supply of fresh material.^[65]

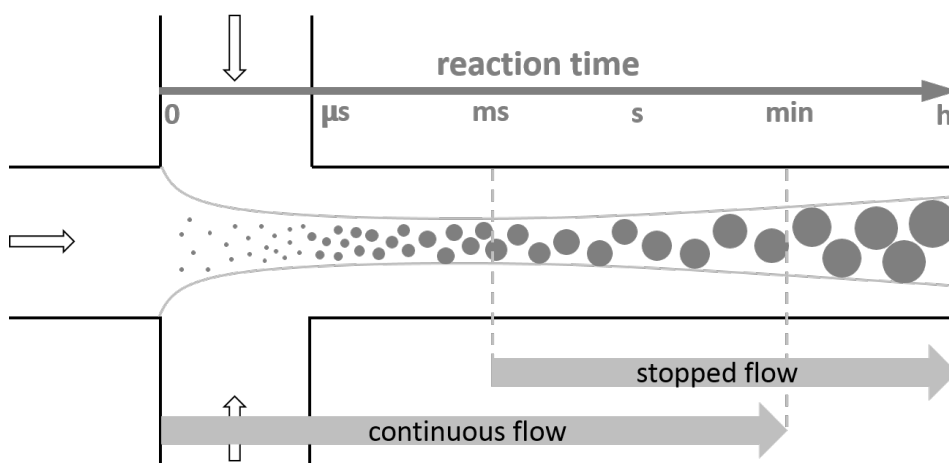


Figure 1.11: Schematic comparison of the provided time scales in continuous and stopped flow microfluidic devices.

1.2.1. Microfluidic devices

The fabrication of microfluidic devices in glass or silica is very time-consuming and cost-intensive. Therefore, new methods had to be found prioritising production and evaluation speed, customisable design, and availability of necessary components.^[58] Polymers quickly turned out to be excellent materials for this approach, as they are

low-cost and can easily be formed in the desired shape by molding or embossing, and also sealed thermally or with the help of adhesives. However, they show low resistance against most common solvent chemicals and high temperature.^[66-69]

The widely used polymer poly(dimethylsiloxane) (PDMS) is an excellent device material for aqueous systems as it is optically transparent, non-toxic, even for biological samples, and curable at low temperatures. It can be deformed reversibly and it can be sealed reversibly to itself or glass substrates and it can form replicas by moulding with structures down to the micron scale.^[58]

Rapid prototyping

For the fabrication of polymer-based microfluidic devices, the manufacturing process of *rapid prototyping* is used.^[70] The full cycle is shown in Figure 1.12^[71], starting with designing the CAD model of a conceived device structure before it is printed on UV semi-transparent masks. These masks form the basis of the photolithographic process for the production of silicon masters. Another important component is the photosensitive, highly functionalised epoxy monomer EPON SU-8, dissolved in 69% γ -Butyrolacetone, which can undergo photoinduced cross-linking in a solution containing 3.3% triaryl sulfonium hexafluoro antimonate in propylene carbonate (4-Methyl-1,3-diokol-2-one).^[72] The latter functions as a cationic photoinitiator and forms, in the presence of photo-donors, a strong Lewis acid.^[73,74] During the above described photocatalysis, several byproducts are produced, especially if the photoresist is overexposed with UV-light. For this reason, this initiator is not available for the epoxy cross-linking anymore.^[73]

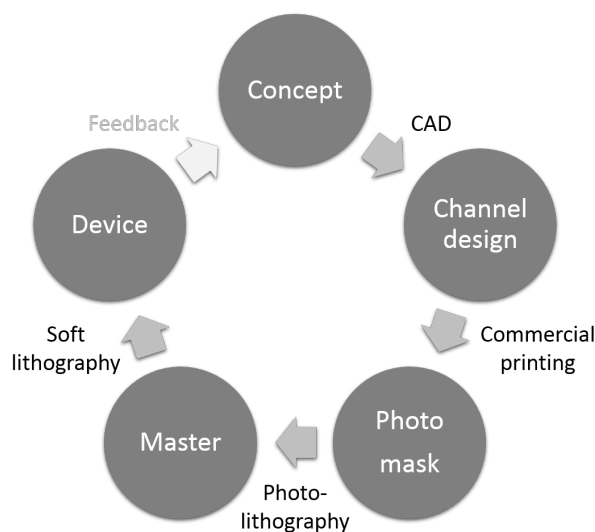


Figure 1.12: Schematic illustration of the cyclic process of *rapid prototyping*, describing the 24h design-feedback-loop, which enables fast microfluidic device optimisation.

Acid-induced cross-linking of the photoresist by several heating steps is called *post exposure bake*. The desired structures can be achieved by covering parts of the wafer with the spin-coated photoresist layer with the previously designed mask. The latter has different UV-permeability whereby the covered parts of the SU-8 stay uncured. Hence, the cross-linked and uncured areas on the wafer can be separated by development in a mr-DEV 600 (80-100% 2-Methoxy-1-methylethylacetate solution) bath.^[74]

For the soft lithographic replication of the formed channel structure^[71,75], in the main two materials were used throughout this work, PDMS, in form of the two component system Sylgard® 184, and Norland Optical Adhesive (NOA) 81, which is a UV curable polymer mixture. The detailed preparation procedure was carried out according to literature methods and can be found in the experimental methods in chapter 2.2.

The most obvious advantages of PDMS as a microfluidic device material were already discussed in chapter 1.2.1. It is ideal for various solvents, although it shows considerable swelling behaviour when in contact with most organic solvents.^[76] Therefore, the surface of PDMS can be modified. One way to do this is by glass coatings *via* sol-gel methods. Unfortunately, these are very brittle compared to the flexible PDMS, which causes cracks through which the solvent can penetrate into the PDMS. Another, more promising method uses poly(p-xylylene) chemical vapour deposition coatings.^[77] These layers with approximately 4 μm thickness turned out to be very resilient and last for the duration of several experiments. The most significant disadvantage occurs when using PDMS devices for small angle X-ray scattering (SAXS) experiments.^[78] PDMS shows strong background scattering, due to the high density of silicon in the molecular backbone.^[79] Thus, for SAXS experiments during this work, hybrid chips with an inserted glass capillary^[80] or NOA devices were used.

NOA 81, which is a commercially available, UV-curable adhesive, finds common applications for optics. As the exact composition is not clearly defined, FT-Raman and NMR studies revealed allyl- and thiol-based components, which react in a UV-induced radical polymerisation reaction.^[81] It has a much lower scattering background, leading to better implementation in SAXS experiments.^[82] It also stays flexible after sealing and shows a higher resistance against organic solvents than PDMS.

Microfluidic channels were chosen as reactor vessels or platforms for kinetic investigations due to their enabling of the investigation of fast nucleation and growth as well as assembly processes. At dedicated synchrotron beamlines, micrometer sized focussing of the X-ray beams is possible. In combination with microfluidics, these novel techniques open up possibilities to follow the structural evolution of nanomaterials in

microchannels with excellent temporal and spatial resolution.^[80]

1.2.2. Device design

To successfully investigate reaction kinetics in microfluidic devices, the channel design has to be carefully adapted to the requirements of each application. The main features of microfluidic mixing, which can be customised to adapt to each reaction condition, are displayed in Figure 1.13.

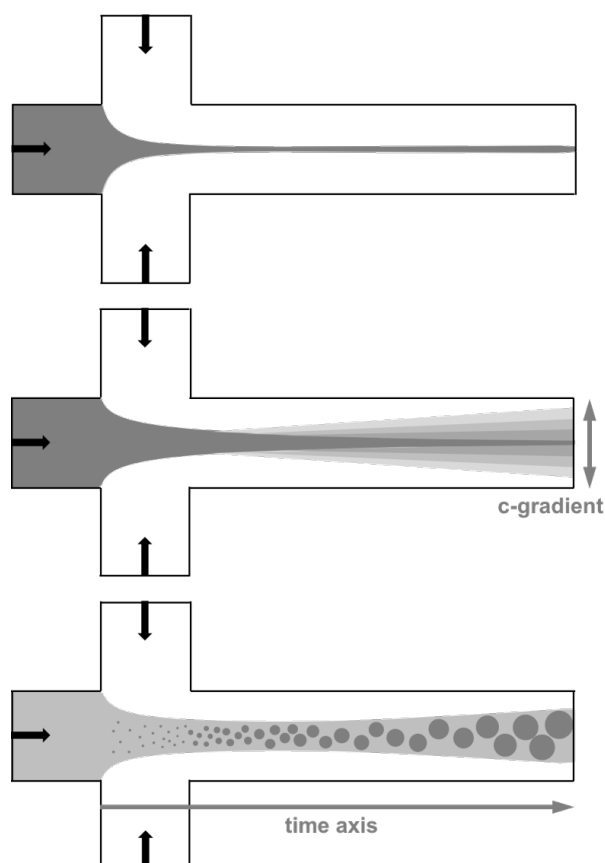


Figure 1.13: Scheme of microfluidic features for kinetic investigations in flow in a cross shaped mixer. Top: Hydrodynamically narrow focused center stream for fast mixing experiments. Middle: Mapping of concentration gradient across and along the channel through interdiffusion of the different liquids from main and side channel. Bottom: Nucleation and growth or self-assembly processes of nanomaterials as a function of time for kinetic investigations along the outlet channel.

All experiments thus require careful planning and consideration of the simultaneous use of analysis, separation, mixing, and cleaning equipment due to the small dimensions of the microfluidic devices in general.

Since there is only diffusion occurring in continuous flow devices, due to laminar flow

conditions, the complete mixing of reactants takes much longer than in turbulent flow conditions and can become very difficult with decreasing channel dimensions.^[83] Hence, various approaches for channel design and optimisation were considered, to reach homogeneous mixing without integrating specific mixing regions before the actual measurement part.^[84] Microfluidic devices with hydrodynamic focusing can be divided in two main categories: coaxial tube and planar on-chip devices. Only the latter were used in this work, due to their simple fabrication and easy adjustable cross design.^[85] On-chip devices with hydrodynamic flow focusing can be two or three dimensional as shown in Figure 1.14. The simplest geometry for a two dimensional chip is a Y-shaped design, in which mixing occurs by diffusion only (Fig. 1.14 A). The cross sectional diffusion is broadened at the channel walls in comparison to the centre, which was first observed by Ismagilov et al. in the early 2000s.^[86] However, this design is highly limited when it comes to parameter variations in the actual experiment. Therefore, the use of cross-shaped geometries is preferred. In these devices, the central flow is focused from both incoming side channels, which provides good control over the actual thickness of the center stream. Furthermore, this also allows a well-defined sample composition, which can be adapted by variation of the volume flow of each inlet individually.^[87] For multi-step synthesis, where a certain flow focusing area is necessary^[88], several side channels for introducing additional reactants can be added, as shown in Figure 1.14 C for a design with two side channels.^[89]

For kinetic investigations, the above-described channel geometries can be disadvantageous when chemical reactions or self-assembly processes are involved. In the two dimensional devices, the interface of reacting solutions is in contact with the channel walls, which leads to sticking and agglomeration of formed particles or macromolecules to the channel surface. Although this does not disturb the laminar flow conditions, it interferes with analytical investigations, as they have to be performed through the adsorbed materials, and in the worst case leads to completely blocked channels. To prevent this contact between the reactive liquid interface and channel walls, a new three dimensional channel geometry was developed, which completely encloses the focused central stream by introducing the hydrodynamic focusing from both sides as well as the top and the bottom through a three dimensional cross design.^[90-93] Such three-dimensional hydrodynamic focusing devices build ideal platforms for small angle X-ray scattering (SAXS) investigations, which was impressively shown with RNA folding by Russell et al.^[94]

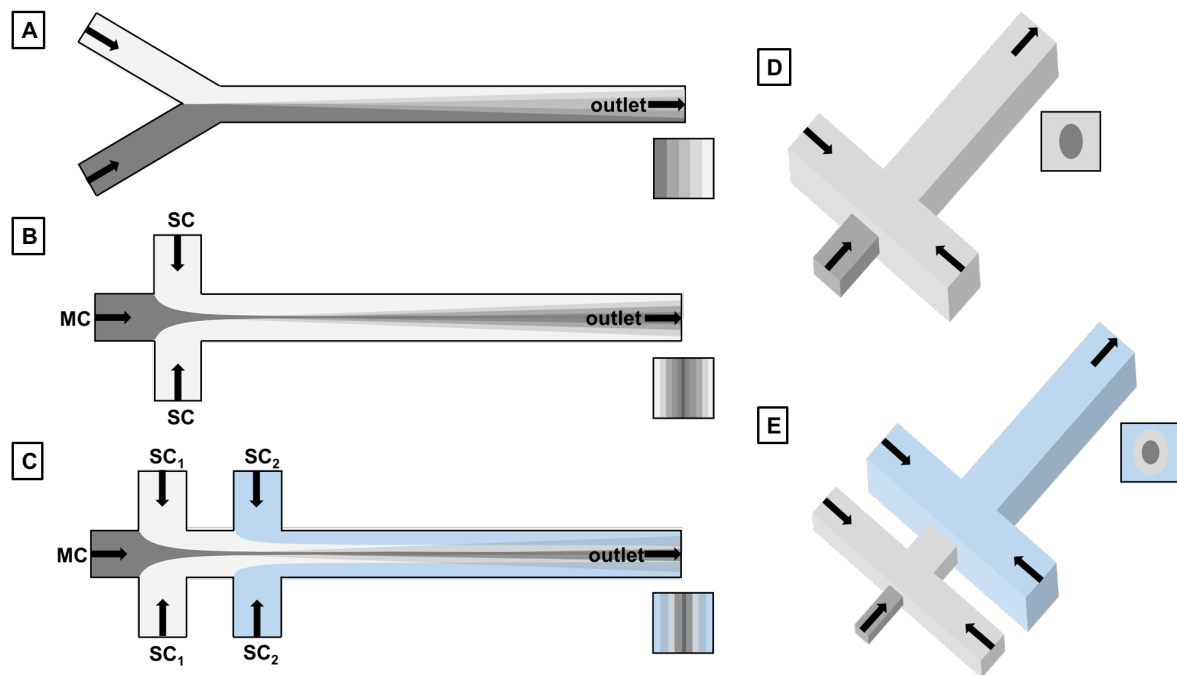


Figure 1.14: Schematic illustration of microfluidic devices with various channel cross designs with the corresponding cross-sections through the outlet channel. (A) Y-shaped design, where mixing is solely based on diffusion. (B) Cross-shaped geometry at the inlets for hydrodynamic focusing experiments. (C) Channel design with two cross-sections, also known as double-focus devices. Thereby, three different solutions can be introduced into the channels, whereas the flow in the first side channel (SC_1) acts as a buffer layer and prevents the immediate contact of the solution in main channel (MC) stream and second side channel (SC_2) stream. (D) and (E) Multilayer designs of the geometries displayed in (B) and (C), respectively, avoiding contact between the central stream and the channel walls.

Figure 1.14 D and E display example structures for three-dimensional microfluidic devices, according to the 2D geometries in Fig. 1.14 B and C. With the introduction of additional layers for out-of-plane focusing, the central stream introduced through the main channel can be focused precisely in the middle of the outlet channel without any wall contact.^[95,96]

1.2.3. Fluid dynamics

As the complexity of microfluidic devices increases steadily, simulations for the fluid flow become more and more important to enable an efficient device design. The standard tool for modeling the flow behaviour of fluids in microfluidic channels is computational fluid dynamics (CFD), which uses numerical methods to solve partial differential equations (PDEs). These describe the transport of mass, momentum and energy in moving fluids.^[97]

Various methods for approximating PDEs by discretisation of the respective problem in fluid dynamics have been published. Hence, the most common are the following: the finite element method (FEM), the finite difference method (FDM) and the finite volume method (FVM).^[98-100] CFD has been dominated by FDM and FVM, whilst modern computer progress enables FEM to be a powerful simulation tool. It enables high-accuracy modeling and is therefore used in this work in the form of *COMSOL Multiphysics*.

Navier-Stokes equations

To describe the exact motion of continuum materials like fluids mathematically, the Navier-Stokes equation is used. This derives from Newton's second law of motion ($\vec{F} = m\vec{a}$) applied to fluids^[101] and is a set of two PDEs.^[100,102] For an incompressible, Newtonian fluid, the Navier-Stokes equation is defined as:

$$\rho \left[\frac{\partial u}{\partial t} + (u \cdot \nabla) u \right] = \eta \nabla^2 u - \nabla p + F \quad (1.24)$$

where ρ is the density and η the viscosity of the fluid, p the pressure, u is the vector of the fluid flow, ∇ is the Nabla-Operator and F stands for additional forces, which are directed on the fluid (e.g. centrifugal or gravitational forces). Internal accelerations appear on the left side of equation 1.24, whereas forces are shown on the right.^[101] The term $\eta \nabla^2 u - \nabla p$ formulates the stress force per unit volume, which results from a pressure gradient ∇p and the viscosity $\eta \nabla^2 u$.

In microfluidic flow, body forces are negligible, leading to a simplification of equation 1.24 to the linear Stokes equation^[102]

$$\eta \nabla^2 u = \nabla p \quad (1.25)$$

which includes the requirements for mass conservation

$$\frac{\partial \rho}{\partial t} + \rho \nabla \cdot u = 0 \quad (1.26)$$

Using the assumption that a liquid is incompressible and treating it as a continuum as described earlier, the Navier-Stokes equation can be expressed as the so-called continuity equation:

$$\nabla \cdot u = 0 \quad (1.27)$$

implying that the liquid under consideration is flowing slowly and with nearly constant density. Figuratively, this only means that a liquid mass, which is filling a finite volume

over a certain period of time, has to flow in this volume the same way as it flows out of this volume. In addition, equation 1.27 is time-independent, restricting fluid flow in microfluidic channels to be symmetric in time.^[102]

Dimensionless numbers in fluid dynamics

As already described earlier in this chapter, the physics of fluids on the macro-scale are significantly different from those of hydrodynamics in microfluidic devices. To be able to describe and compare phenomena at different scales, several dimensionless numbers were introduced. The Reynolds number (Re), which shows the relation of internal and viscous forces of a fluid, is thereby the most important dimensionless number for microfluidic applications.^[101] It is described by

$$Re \equiv \frac{\text{inertial forces}}{\text{viscous forces}} = \frac{|\rho(u \cdot \nabla)u|}{|\eta \nabla^2 u|} = \frac{\rho \nu}{\eta} d \quad (1.28)$$

where ν is the flow velocity and d is the characteristic length of the system, in this case the diameter of the channel.^[103,104] With decreasing size of the system, the Reynolds number becomes smaller, leading to viscous forces becoming more important, as they describe the resistance of a fluid which experiences shear stress.^[105] The result is liquid behaviour contrary to our day-to-day experience, dominated by high Reynolds numbers. The most important examples are the absence of turbulences in flow, a higher influence of surface tension and an increased evaporation rate on exposed surfaces.^[102] Reynolds numbers in microfluidic devices can be estimated for water, as the typically-used solvent, where flow velocities in the range of 0.1 mm/s to 100 mm/s and channel dimensions around several 100 μm lead to Reynolds numbers between 0.01 and 10. These low values of Re result in laminar flow, where the mixing of liquids is only diffusion-limited.^[101] For the transition to turbulent flow, Reynolds numbers of $Re = 2040 \pm 10$ have to be achieved.^[106]

The Weber number (We), describing the relation of the fluid surface tension to its inertia, follows the same calculations as the Reynolds number, only using the surface tension γ instead of the viscosity. It is described by

$$We \equiv \frac{\rho u^2 \nu}{\gamma} d \quad (1.29)$$

In numerous applications of microfluidics, materials, such as polymers are dissolved in the flowing liquid. Thus, the flow behaviour of the fluid in the channel changes, due to

the added elastic components. To describe these effects, the Weissenberg number (Wi) and the Deborah number (De) were introduced. Both describe the polymer relaxation time τ_P within a fluid, but at different time ranges.

The Weissenberg number sets the polymer relaxation rate τ_P in terms of either the inverse shear rate time $\dot{\gamma}^{-1}$ or the inverse extension rate time \dot{e}^{-1} and can be written by

$$Wi \equiv \tau_P \dot{\gamma} = \tau_P \dot{e} \quad (1.30)$$

For small Wi , the polymer is able to relax before it gets deformed significantly. This changes when Wi reaches 1, as the polymer does not have enough time to relax anymore and the deformation becomes significant.^[101]

The Deborah Number on the other hand compares τ_P to the flow time τ_{flow} and is therefore expressed by

$$De \equiv \frac{\tau_P}{\tau_{flow}} \quad (1.31)$$

De is used to describe a fluid response to stimuli of a given duration, e.g. changes of channel geometries.^[107] With increasing flow velocity u , elastic effects become more and more important, leading to an increase in De and Wi . However, Re increases similarly, leading to a stronger influence of inertial effects. This relation is expressed by the Elasticity number (EI):

$$EI \equiv \frac{De}{Re} = \frac{\tau_P \eta}{\rho h^2} \quad (1.32)$$

with h being the shortest dimension setting the shear rate. EI is flow velocity-independent, as it only depends on geometry and the material properties.^[101]

In the case of gas flows instead of liquids, molecules move ballistically, hence colliding only rarely. Nevertheless, the mean free path between collisions can be calculated by

$$\lambda_f \sim \frac{1}{na^2} \quad (1.33)$$

where n is the number density of molecules with radius a . With decreasing device dimensions, λ_f plays an increasingly important role, leading to the Knudsen number (Kn), which expresses the relationship between mean free path and the macroscopic length scale L .^[101]

$$Kn \equiv \frac{\lambda_f}{L} \quad (1.34)$$

The last important dimensionless number in this section is the Péclet number, which will be described in detail in section 1.2.4. All these dimensionless numbers enable us to decide for each system geometry which forces dominate and allow us in computations to ignore some terms, that play only a minor role.

Non-slip condition and resulting flow profile

Microfluidic channel systems have in general a high surface-to-volume ratio. Hence, the impact of surface properties on flow resistance and the velocity profile is significant. The definition of suitable boundary conditions is therefore necessary to simulate the fluid flow in microfluidic devices. Universally, the Navier boundary condition applies to describe the interaction of a flowing liquid and a solid surface. Navier^[108] described the flow velocity tangential to the surface ν_x as proportional to the shear stress at the surface by

$$\nu_x = \lambda \frac{d\nu_x}{dy} \quad (1.35)$$

with λ as the slip length, also known as Navier length.^[109] This length is the distance between an imaginary point inside the channel walls and the surface, where the velocity is zero, as shown in Figure 1.15 A. In the case of $\lambda = 0$ it is the "no-slip" condition, which is used to describe the interaction between fluid and wall.

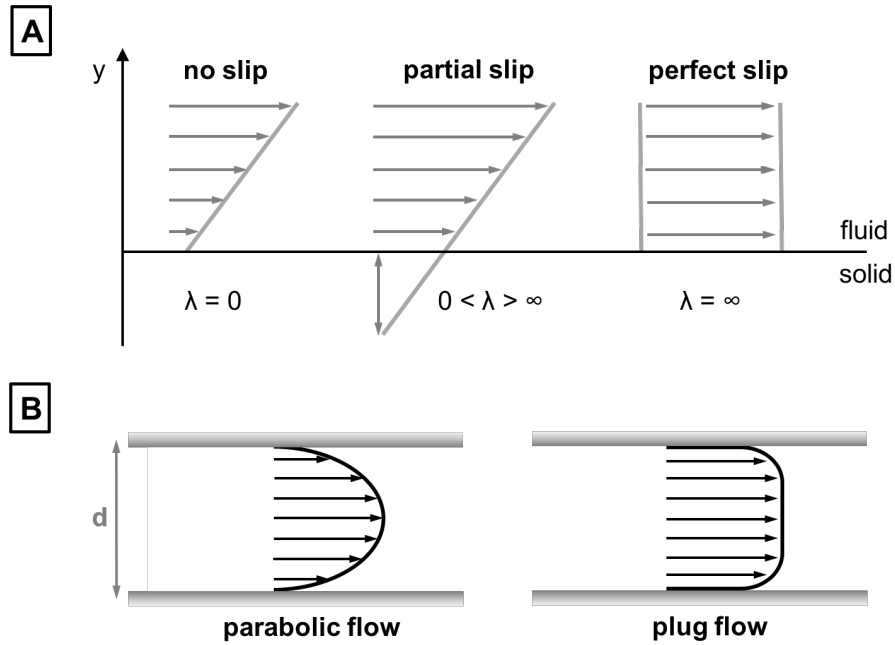


Figure 1.15: (A) Schematic illustration of the Navier length λ for no slip (left), partial slip (middle) and perfect slip (right) condition. (B) Flow velocity profiles for parabolic (left) and plug (right) flow.

Assuming "no-slip" conditions at the channel walls, the idealised plug flow model will change to a parabolic flow profile with a highest velocity in the middle of the channel, whilst it decreases parabolically to the walls until it finally reaches 0 (illustrated in Figure 1.15).^[110,111] For circularly shaped channels, the volumetric flow rate Q can be calculated using the Poiseuille equation

$$Q = \frac{\pi d^4 \Delta p}{128 \eta L} \quad (1.36)$$

and the maximum flow velocity by

$$v_{max} = \frac{d^2 \Delta p}{16 \eta L} \quad (1.37)$$

where d is the diameter of the pipe and η is the fluid viscosity. Δp describes the difference in pressure along a channel with a length L .^[112] Another consequence of the "no-slip" condition can be formulated as the fluidic resistance R of the microchannel as

$$R = \frac{Q}{\Delta p} \quad (1.38)$$

Therefore, the mean flow velocity is half of the maximum velocity, as calculated for the Poiseuille regime.^[102]

1.2.4. Convection

Convection can take place in two ways - through diffusion or advection. This is important, as mixing at the macroscopic scale is supported by "chaotic advection" or turbulence, whereas on the micron-scale, and inside microfluidic channels, it is driven by diffusion. In general, every biological process and every chemical reaction is limited by the converging and mixing of the two or more reactants involved.^[113] From the mathematical point of view, solving the Navier-Stokes equation numerically for turbulent flow is very difficult, almost impossible. For flow applications, this implies that it is hardly possible to predict the exact outcome of any turbulent mixing experiment, defining turbulent flow as irreversible, as opposed to laminar, diffusion-limited flow.^[101]

Fick's first law of Diffusion

Diffusion specifies the migration of particles along a concentration gradient. Thereby, matter always moves from an area of high concentration to an area of lower concentration. This migration is measured by its flux J , which describes the number of particles passing through a unit area per unit time.^[4] The proportionality constant in this relation is defined by Fick's first law of diffusion^[4,114]:

$$J \propto \frac{dc}{dx} = -D \frac{\partial c}{\partial x} \quad (1.39)$$

This equation can be solved, determining the spatial and time dependency of the concentration, for adequate boundary conditions. The constant D , introduced in equation 1.39, is the so-called diffusion coefficient. It can be described for spherical particles with radius r in low Re numbers by the Stokes-Einstein relation^[4]:

$$D = \frac{k_B T}{6\pi\eta r} \quad (1.40)$$

where k_B is the Boltzmann constant, T the temperature and η the solvent viscosity. Diffusion is a nonlinear process, in which two particles need a certain amount of time to diffuse into each other. The average of this diffusion time t_{diff} can be derived by the Einstein-Schmoluchowski equation^[4,102]:

$$D = \frac{d^2}{2t_{diff}} \quad \longrightarrow \quad t_{diff} = \frac{d^2}{2D} \quad (1.41)$$

with d as the characteristic length for the diffusive process. However, in the case of advection-based mixing time, an exclusive dependency on the flow velocity ν exists^[102], described by

$$t_{adv} = \frac{d}{\nu} \quad (1.42)$$

Comparing the times required for diffusion (equation 1.41) and advection (equation 1.42), it is clear that diffusion, scaling quadratically with distance, is a much slower process. However, in microfluidics this value for distance is decreased due to the device geometry, decreasing the required time for diffusion and thus making diffusive processes more and more relevant.^[115]

Péclet number

The last dimensionless number of importance for microfluidic experiments is the Péclet number (Pe). It describes the relation between advection and diffusion for mass transport by

$$Pe \equiv \frac{\text{advection}}{\text{diffusion}} = \frac{\nu d}{D} \quad (1.43)$$

High Pe numbers, meaning the numerator advection predominates equation 1.43, leads to turbulent mixing in flow. In microfluidic devices, this only occurs further down the outlet channel. The typical flow velocities (e.g. $\nu = 10$ mm/s) and dimensions (e.g. $L = 100$ μm) lead to higher Péclet numbers (around 1000) along the flow direction. Diffusion therefore has an insignificant contribution to the convection downstream. Nevertheless, a different situation prevails perpendicular to this flow, across the channel. In this regime, lower Pe numbers exist as the denominator gets more important. The mixing across microfluidic channels therefore occurs only by diffusion.^[101,115]

Fick's second law of Diffusion

To relate the change of concentration to its spatial variation at any point obtained by diffusion, it is necessary to solve Fick's second law of diffusion. This is derived from Fick's first law of diffusion (equation 1.39) combined with mass conservation principles by

$$\frac{\partial c}{\partial t} = D \frac{\partial^2 c}{\partial x^2} = D \cdot \nabla^2 c \quad (1.44)$$

In equation 1.44 the diffusivity D can be different for various sorts of diffusion, depending on the systems. In homogeneous or binary systems, self-diffusivity occurs, whereas intrinsic diffusivity or interdiffusivity exist as well, changing the form of equation 1.44. The simplest of all these is in the case of a constant D , whilst it can also be a function of direction, concentration or time. Direction-dependent diffusivity occurs in

anisotropic materials. The most common dependency is a function of concentration, especially in the case of high concentration gradients, which is advantageous for mixing experiments with a large concentration difference between the solutions involved.^[4,116] Equation 1.44 can also be seen as a linear PDE, containing two spatial and one time derivative. For solving this equation, initial and boundary conditions are necessary. These are for an interface ($x = 0$) between two phases of material A and material B (thickness $0 \leq x \leq \infty$) with step-function initial conditions described as:

1. For every position x at time $t = 0$, the initial uniform concentration c_0 is similar:

$$c(x, t = 0) = c_0.$$
2. At every time, the concentration at position $x = 0$ is constant:

$$c(x = 0, t) = c_s.$$
3. For every time, the concentration at infinity equals the initial concentration:

$$c(x = \infty, t) = c_0.$$

The analytical solution for Fick's second law of diffusion following these boundary conditions and constant diffusivity is then described by

$$\frac{c(x, t) - c_s}{c_0 - c_s} = \text{erf} \left(\frac{x}{\sqrt{4Dt}} \right) \quad (1.45)$$

with the corresponding error function:

$$\text{erf}(z) = \frac{2}{\sqrt{\pi}} \int_0^z e^{-u^2} du \quad \text{with } z = \frac{x}{\sqrt{4Dt}} \quad (1.46)$$

The function shown in equation 1.46 has the properties $\text{erf}(0) = 0$, $\text{erf}(\infty) = 1$ and $\text{erf}(-z) = -\text{erf}(z)$. The one-dimensional diffusion along x on a one dimensional line from a step-functional concentration condition is described by equation 1.45. It describes the one-dimensional diffusion from a step function in a two-dimensional plane for the case of particles per unit area, and for a three dimensional volume in the case of particles per unit volume.^[116]

There are numerous methods to solve the diffusion equation. In the linear case, a sum of the solutions is also a valid solution, so the equation can be expressed in terms of a superposition of error-functions. As the solutions describe the diffusion from an initial step function into an infinite domain, the superpositions of both is Δx and the step functions are

$$c(x, t = 0) = \begin{cases} 0 & -\infty < x < 0 \\ c_0 & 0 < x < \infty \end{cases} \quad (1.47)$$

and

$$c(x, t = 0) = \begin{cases} 0 & -\infty < x < \Delta x \\ -c_0 & \Delta x < x < \infty \end{cases} \quad (1.48)$$

Similar to equation 1.46, both of these step functions evolve in the form of error functions. Hence, their superposition can be written as

$$\begin{aligned} c(x, t) &= \frac{c_0}{2} + \frac{c_0}{2} \frac{2}{\sqrt{\pi}} \int_0^{\frac{x}{\sqrt{4Dt}}} e^{-\zeta^2} d\zeta - \frac{c_0}{2} - \frac{c_0}{2} \frac{2}{\sqrt{\pi}} \int_0^{\frac{(x-\Delta x)}{\sqrt{4Dt}}} e^{-\zeta^2} d\zeta = \\ &= \frac{c_0}{\sqrt{\pi}} \int_{\frac{(x-\Delta x)}{\sqrt{4Dt}}}^{\frac{x}{\sqrt{4Dt}}} e^{-\zeta^2} d\zeta \end{aligned} \quad (1.49)$$

A simple solution of this can be derived for "thin-films", where $\Delta x \ll x$, meaning the actual diffusion distance Δx is small compared to the overall diffusion distance x . This is a result of overlapping of the superposed functions, leading to

$$c(x, t) = \frac{c_0 \Delta x}{\sqrt{4\pi Dt}} e^{-\frac{x^2}{4Dt}} = \frac{n_d}{\sqrt{4\pi Dt}} e^{-\frac{x^2}{4Dt}} \quad (1.50)$$

with n_d as the source strength, a constant, defined by the number of particles or atoms at the source at $x = 0$.^[116-118] Using equation 1.50, the diffusion in one direction can be followed, resulting in an initial concentration a factor of 2 larger and described by

$$c(x, t) = \frac{n_d}{\sqrt{\pi Dt}} e^{-\frac{x^2}{4Dt}} \quad (1.51)$$

However, for a two-directional diffusion with the source at $x = 0$ and the boundary condition $-\infty < x < \infty$ the concentration function is symmetric around 0 in the form of a Gaussian shape.

Diffusion-limited Micromixers

Convection in microfluidics can be achieved in different ways.^[119] In this work, we focus on diffusion based designs, like the simple Y- or T-shaped cross channel, as previously described in detail in section 1.2.2. In all those described geometries two reactant solutions are introduced in the channel design, respectively, forming an interface where mixing of the liquids occurs by diffusion. One step further are the developed cross-shaped geometries, which allow the formation of a thickness-controlled middle layer. The diffusive mixing for kinetic experiments can then be described by the following

equations:

$$\frac{d_1}{d_2} = \frac{\eta_1 Q_1}{\eta_2 Q_2} \quad (1.52)$$

$$\frac{d_{MC}}{d_{SC_1} + d_{SC_2}} = \frac{\eta_{MC}}{\eta_{SC_1} + \eta_{SC_2}} \frac{Q_{MC}}{Q_{SC_1} + Q_{SC_2}} \quad (1.53)$$

where d is the thickness of the relevant layer, η the viscosity and Q the volume flow. These equations apply for flow experiments if following assumptions are fulfilled:

1. The microchannel provides a steady and laminar flow.
2. All fluids are Newtonian.
3. The density and viscosity of all fluids is the same in all inlet and outlet channels, and do not change during the experiment.
4. The used channel geometry of the microfluidic device is rectangular and all inlet and outlet channels have the same height.

Equation 1.52 applies for Y-shaped channels, in which layer 1 and layer 2 are equivalent to the space which two introduced liquids in the inlet channel occupy. It shows the hydrodynamic relation of the two merging liquid streams to their viscosity and volume flow rate. Furthermore, it is possible to calculate the viscosity of one of the solutions, if all other parameters are known.^[115]

Flow in cross-shaped channel geometries on the other hand, given the viscosities and flow rates in both side channels (SC_1 and SC_2) are identical, hydrodynamically focusing a main channel (MC), follows equation 1.53.^[120,121] Schematic illustrations of these hydrodynamic channel geometries are shown in Figure 1.14.

The interdiffusion in cross-shaped three-dimensional microfluidic channels shows two adjacent streams at the central stream interface.^[80] This results from the diffusion of the solvent or reactant of the side streams into the main channel stream, as the diffusion of these components is much slower. As this represents a non-ideal situation, the Gaussian shape distribution across the channel no longer applies. Hence, the above-derived equations have to be adjusted, as they are not sufficient to describe the asymmetrical shape.

Adjuvant in this case is the use of exponentially-modified Gaussian (EMG) functions^[122,123], which can be written as:

$$F(t) = \frac{h_G \cdot \sigma}{\tau} \sqrt{\frac{\pi}{2}} \cdot e^{\left(\frac{\mu-t}{\tau} + \frac{\sigma^2}{2\tau^2}\right)} \cdot \operatorname{erfc} \left[\frac{1}{\sqrt{2}} \left(\frac{\mu-t}{\sigma} + \frac{\sigma}{\tau} \right) \right] \quad (1.54)$$

with h_G and σ as Gaussian height and Gaussian sigma, μ as the position of the unmodified Gaussian and τ as the relaxation time parameter of the exponent used to modify the Gaussian. Additionally, the corresponding error function $\operatorname{erfc}(z)$ can be defined as

$$\operatorname{erfc}(z) = 1 - \operatorname{erf}(z) \quad (1.55)$$

An application for an EMG fit to determine the diffusivity of a trisamide-based hydrogelator is shown in chapter 5.

1.3. Self-Assembly

A fundamental principle in nature and technology is the formation of ordered structures of particles or components of a system out of chaotic arrangements without external forces. This autonomous organisation is called self-assembly.^[124] It can be found on all length scales in life.^[2] In general one can differentiate between two types of self-assembly - the static self-assembly, as occurring in systems who are in global or local equilibrium and don't dissipate energy, and the dynamic self-assembly, forming patterns by competition between reaction and diffusion while dissipating energy.^[124] The most common material to build up superstructures by self-assembly are amphiphilic molecules. Their name derives from the Greek words $\alpha\mu\phi\iota\sigma$ - *amphis* meaning "both" and $\phi\iota\lambda\iota\alpha$ - *philia* for "love", describing their physicochemical character of both lipophilic and hydrophilic properties. Macromolecular chemistry offers a huge variety of these materials, where already simple molecules can self-organise into numerous complex structures. This transition of forming order from a disordered state can be described by the order parameter η , which is per definition $\eta = 0$ in the disordered phase and $\eta = 1$ in the ordered phase.^[125]

Block copolymers are defined as macromolecules with two or more different immiscible blocks of varying monomer composition, which are radially and/or linearly arranged. They form the largest group of artificial molecules for self-assembly processes. Furthermore, these block copolymers can be functionalised, resulting in an extended range of possible new materials in fields like medicine, catalysis, ceramics or photoelectrics.^[126,127]

It is inevitable for the building of superstructures that both short-range attraction and

long-range repulsion are present at the same time. As shown in Figure 1.16 for a block copolymer consisting of molecules A and B, they are affected by long range repulsive forces, while additionally be forced to stay attached by short range attractive forces, as in this case binding.

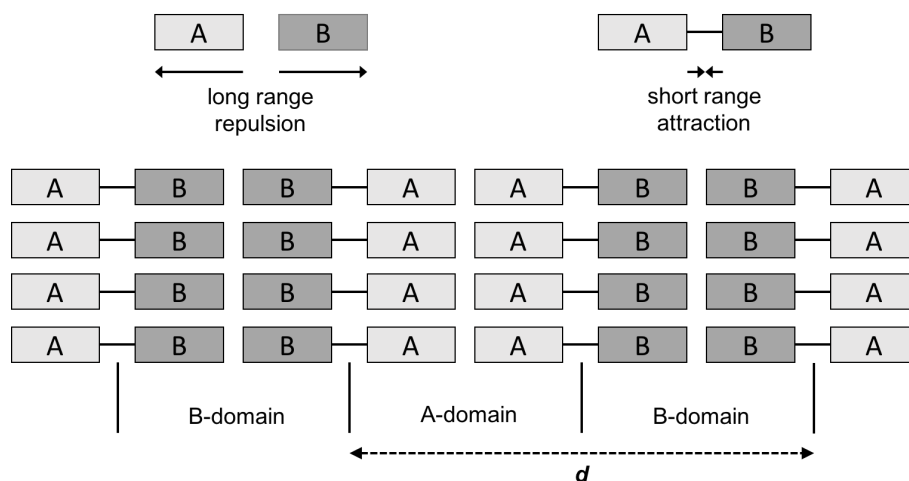


Figure 1.16: Scheme of long range repulsive and short range attractive forces between building blocks A and B of an amphiphilic molecule. d is the periodic length of the structure.^[125]

As a consequence of the balance of these forces, A/B components as illustrated in Figure 1.16 will undergo an assembly process, aiming to minimise the contact area between A- and B-blocks while maximising the organisation of blocks of the same molecule in a certain area (domains). The displayed configuration of alternating A- and B-domains is therefore the preferred formation. The periodic length d of these domains can range from 10 nm up to 1 cm, depending on the experimental parameters. Examples for the above-explained pairs of forces are shown in Table 1.1.^[125]

Table 1.1: Pairs of forces for short range attraction and long range repulsion resulting in self-assembly.

Long range repulsion	Short range attraction	Examples
hydrophilic/hydrophobic incompatibility	covalent binding	micelles
Coulomb repulsion	covalent binding	block copolymers
	electroneutrality	ionic crystals

In addition, it is possible to manipulate the interface leading to a forced interfacial curvature, depending on the size and shape of each building block. This curvature can be described by its mean curvature H as well as the Gaussian curvature K , both given by the radii of the curvature R_1 and R_2 (compare Figure 1.17), defined by the following equations:

$$H = \frac{1}{2} \left(\frac{1}{R_1} + \frac{1}{R_2} \right) \quad K = \frac{1}{R_1 R_2} \quad (1.56)$$

The relation between curvature and surfactant packing parameter P is given by

$$P = \frac{V_h}{a_i l_c} = 1 + H l_c + \frac{K l_c^2}{3} \quad (1.57)$$

with V_h as the hydrophobic volume of the copolymer, a_i as the interfacial area and l_c as the chain length normal to the interface.^[128,129] Figure 1.17 also shows the relation of molar fraction f and packing parameter P and curvature. Calculating these values, the characterisation of simple shapes such as spheres, cylinders and bilayers is possible, as shown in Table 1.2.

Table 1.2: Various simple self-assembled shapes with according packing parameter P , mean curvature H and Gaussian curvature K .^[129]

Shape	P	H	K	R_1	R_2
Sphere	1/3	1/R	1/R ²	R	R
Cylinder	1/2	1/(2R)	0	R	$\rightarrow \infty$
Bilayer	1	0	0	$\rightarrow \infty$	$\rightarrow \infty$

In bulk as well as diluted solution the self-organising process is driven by segregation of the immiscible polymer blocks. This leads to a small mixing entropy coupling with an unfavourable mixing enthalpy, whereas the covalent bonding, which is connecting the polymer blocks, prevents a macrophase separation. However, this process results in a microphase separation, described by the following parameters:

1. the volume fraction f . For a diblock copolymer, consisting of molecule A and B, it applies that $f_A + f_B = 1$;
2. the degree of polymerisation N , with $N = N_A + N_B$;
3. the Flory-Huggins parameter χ_{AB} , which defines the degree of incompatibility between the polymer blocks of A and B.

The latter is strongly dependent on the temperature ($\chi \propto T^{-1}$), which is given by

$$\chi_{AB} = \left(\frac{z}{k_B T} \right) \left[\epsilon_{AB} - \frac{1}{2} (\epsilon_{AA} + \epsilon_{BB}) \right] \quad (1.58)$$

with z as the number of nearest neighbours per repeat unit in the final polymer, ϵ_{AB} , ϵ_{AA} and ϵ_{BB} as the interaction energies per repeat unit A-B, A-A and B-B, respectively.^[127,130]

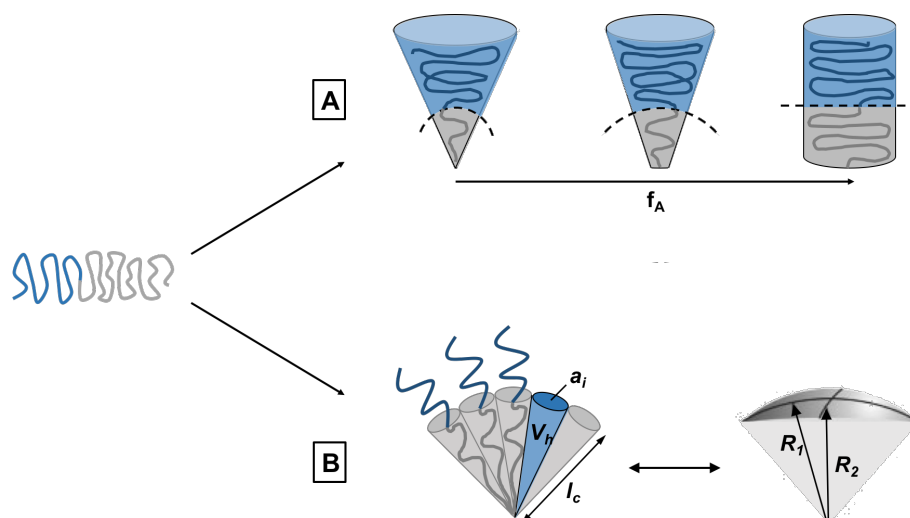


Figure 1.17: Illustration of the relation between (A) the curvature and the molar fraction f ^[127] and (B) the amphiphilic shape and the curvature of the interface.^[129]

To describe the phase behaviour of block copolymers, several theories have been developed. In terms of investigating χN , the self-consistent mean-field (SCMF) theory can be used.^[127,131,132] It involves the weak segregation limit (WSL) in the range of $\chi N < 10$, in which the one dimensional polymer volume fraction profiles feature a periodic Gaussian shape. Additionally the SCMF theory also includes the counterpart, the strong segregation limit (SSL) for $\chi N \gg 10$, in which regime narrow interfaces separate into almost pure polymer block microdomains of each molecule.^[130,133]

Block copolymers in a microphase-separated state can be found in dilute solution as well as in bulk. With varying polymer composition, length and length ratios, different patterns can be assembled. However, in equilibrium the state with lowest energy is always favoured. A collection of formed structures for different packing parameters in dilute solution or bulk is shown in Figure 1.18. The stability of those formed structures can be recapitulated in a phase diagram, derived from the SCMF theory for each single composition describing the bulk behaviour as a function of f . Hence, the formation of specific structures in defined solvent compositions can be predicted.^[125,131]

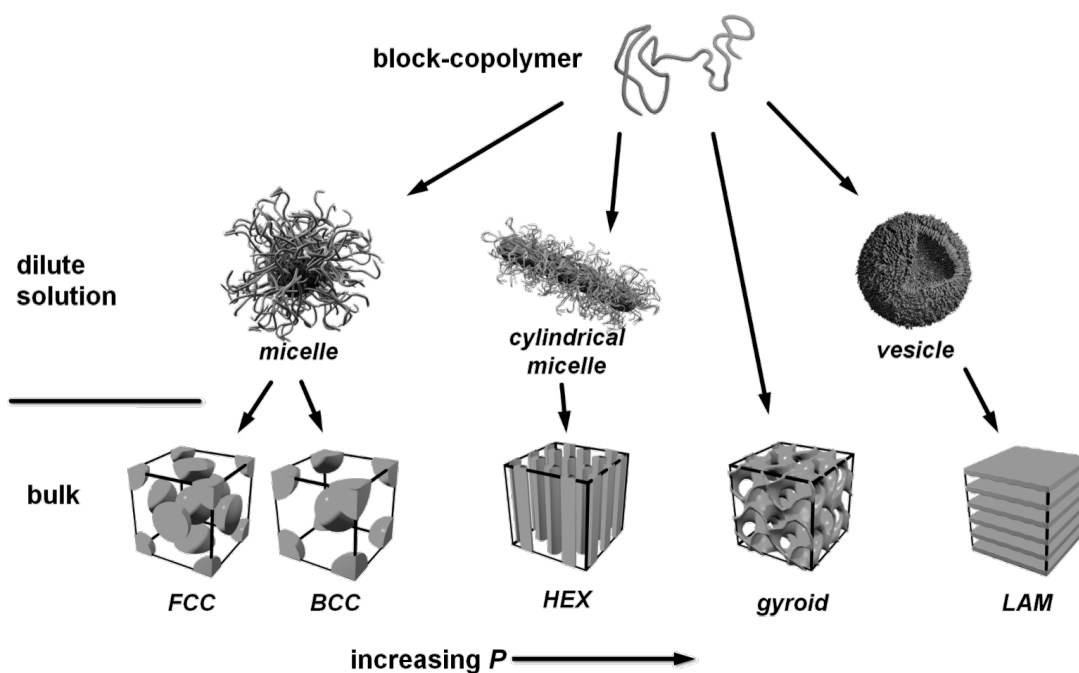


Figure 1.18: Different structures formed by self-assembly of block copolymers in dilute solution and bulk. In latter, complex structures like face centered cubic (FCC), body centered cubic (BCC), hexagonal packed cylinders (HEX), bicontinuous gyroids and lamellar phases (LAM) can be formed.^[125] © S. With^[134]

1.4. Thesis Outline

Over the course of this introductory chapter, a broad range of topics have been discussed. They originate from the idea of performing fast kinetic investigations in highly controlled microfluidic flow devices. By transferring different assembly or growth processes in microfluidic reaction platforms, a standardised design can be developed to access investigations at any time scale. The possibility to follow processes on time scales of microseconds and in the nanometer range is enabled by the combinations of microfluidic techniques with powerful analytical methods, such as X-ray scattering, confocal microscopy and optical spectroscopy.

The understanding of structure-related formation mechanism of nanomaterials is essential for optimisation processes resulting in the improvement of fabrication methods. As X-ray scattering applications are highly sensitive to byproducts and scattering background, the synthesis protocols as well as the device material had to be improved and adapted to the setup respectively.

In **Chapter 3** a hydroquinone based synthesis for the formation of gold nanorods in high yield was optimised to up to 99% purity. It could then be used to follow the

in-situ mechanism of seeded growth using X-ray scattering and optical spectroscopy simultaneously. By systematic variation of precursor concentration, the influence on kinetic and final properties could be investigated.

In the course of investigations in microfluidic environments, fast laminar flow conditions are present transporting molecules through the channel design, as described in section 1.2. Therefore, the question arises, if anisotropic particles such as the synthesised gold nanorods in chapter 3 align when exposed to a highly flow-orientating environment as the described liquid micro-jets. **Chapter 4** shows the aim of using a combination of microfocused X-ray scattering with a microfluidic jet setup to investigate the spatial and orientational distributions in a continuously stable liquid microjet of anisotropic particles with long axial ratios (wormlike micelles and nanoplatelets) towards small axial ratios (gold nanorods).

Faster reaction kinetics, such as the pH-induced self-assembly of trisamide-based hydrogelators presented in **Chapter 5**, made the use of a microfluidic setup with hydrodynamic flow focusing necessary. The fluorescent properties, which are developed by the self-organisation of disk-like molecules by controlled change of pH, were followed. The main challenge in these experiments was the development of a new channel geometry, providing out-of-plane focusing to precisely position the mixing region and prevent wall contact (such hydrogels showed high adsorption properties at the channel walls). The molecular assembly in hybrid chips as a combination of PDMS and glass capillaries could then be followed via confocal fluorescence microscopy and X-ray scattering *in-situ*.

Chapter 6 describes the adaption of an exemplary quantum dot synthesis, aqueous CdS nanoparticle in the case of this thesis, onto microfluidic reaction platforms to follow very fast nucleation and growth kinetics *ab initio*. By systematic variation of the precursor salt concentrations, the influence of every reaction parameter could be investigated and the formation of uniform nanoparticles followed by optical spectroscopy and confocal fluorescence microscopy. The characteristic absorption and emission behaviour of quantum dots enable the exact tracing of structural evolution during the synthesis time.

Finally, **Chapter 7** is about the self-assembly process of water-soluble poly (tetrabutylammonium 6-(thiophen-3-yl) hexane 1-sulfonate), also called PTHS. As a P3HT derivate, this newly developed polymer shows unique fluorescence properties in aqueous solution, which can be quenched by controlled solvent exchange. As this is a case of classical polymer self-assembly, the question about superstructure formation arises. To provide consistent patterns, the application of diffusion-controlled microfluidic channels as reaction vessel was investigated, using confocal fluorescence and Raman mi-

croscopy to examine the assembly process.

Therefore, the key fundamental research questions to be answered in this thesis are:

1. Can we follow the growth kinetics of gold nanorods *in-situ*, using SAXS?
2. How does the axial ratio of anisotropic particles influence the flow alignment in liquid microjets?
3. What is the structural information that lies behind the fast pH-induced self-assembly of 1,3,5-benzene tricarboxamide, when investigated under microfluidic hydrodynamically focused flow?
4. Can we follow the nucleation and growth of CdS nanocrystals by using a microfluidic reactor to slow the kinetics down?
5. Can we control the self-assembly of water-soluble Poly(tetrabutylammonium 6-(thiophen-3-yl) hexane 1-sulfonate) (PTHS) by diffusion-controlled, microfluidically defined solvent mixtures?

References

- [1] Roduner, E. *Chemical Society Reviews* **2006**, *35*, 583–592.
- [2] Cademartiri, L.; Ozin, G. A. *Concepts of Nanochemistry*; Wiley-VCH, 2009.
- [3] Thomson, W. *Philosophical Magazine* **1871**, *42*, 448–452.
- [4] Atkins, P. W.; de Paula, J. *Physical Chemistry*; Wiley-VCH, 2006.
- [5] Schmid, G. *Nanoparticles*; Wiley-VCH, 2010.
- [6] Brus, L. E. *The Journal of Physical Chemistry* **1983**, *79*, 5566–5571.
- [7] Pinna, N.; Weiss, K.; Urban, J.; Pileni, M. P. *Advanced Materials* **2001**, *13*, 261–264.
- [8] Schmid, G.; Corain, B. *European Journal Inorganic Chemistry* **2003**, *17*, 3081–3098.
- [9] Alivisatos, A. P. *The Journal of Physical Chemistry* **1996**, *100*, 13226–13239.
- [10] Hagen, E.; Rubens, H. *Annalen der Physik* **1903**, *316*, 873–901.
- [11] Barber, D. J.; Freestone, I. C. *Archaeometry* **1990**, *32*, 33–45.
- [12] Daniel, M.-C.; Astruc, D. *Chemical Reviews* **2004**, *104*, 293–346.
- [13] Turkevich, J.; Stevenson, P. C.; Hillier, J. *Discussions of the Faraday Society* **1951**, *11*, 55–75.
- [14] Frens, G. *Nature* **1973**, *241*, 20–22.
- [15] Dahlin, A. B.; Zahn, R.; Voeroes, J. *Nanoscale* **2012**, *4*, 2339–2351.
- [16] Zijlstra, P.; Paulo, P. M. R.; Orrit, M. *Nature nanotechnology* **2012**, *7*, 379–382.
- [17] Halas, N. J.; Lal, S.; Chang, W. S.; Link, S.; Nordlander, P. *Chemical Reviews* **2011**, *111*, 3913–3961.
- [18] Kennedy, L. C.; Bickford, L. R.; Lewinski, N. A.; Coughlin, A. J.; Hu, Y.; Day, E. S. *Small* **2011**, *7*, 169–183.
- [19] Kinneer, C.; Moore, T. L.; Rodriguez-Lorenzo, L.; Rothen-Rutishauser, B.; Petri-Fink, A. *Chemical Reviews* **2017**, *117*, 11476–11521.
- [20] Narayanan, R.; El-Sayed, M. A. *The Journal of Physical Chemistry B* **2005**, *109*, 12663–12676.

- [21] Caruso, F. *Advanced Materials* **2001**, *13*, 11–22.
- [22] Mulvaney, P. *Langmuir* **1996**, *12*, 788–800.
- [23] Novotny, L.; Hecht, B. *Principles of Nano-Optics*; University Press, Cambridge, 2006.
- [24] Mie, G. *Annalen der Physik* **1908**, *330*, 377–445.
- [25] Perez-Juste, P.; Pastoriza-Santos, I.; Liz-Marzan, L. M.; Mulvaney, P. *Coordination Chemistry Reviews* **2005**, *249*, 1870–1901.
- [26] Klar, T.; Perner, M.; Grosse, S.; von Plessen, G.; Spirkl, W.; Feldmann, J. *Physical Review Letters* **1998**, *80*, 4249–4252.
- [27] Link, S.; El-Sayed, M. A. *The Journal of Physical Chemistry B* **1999**, *103*, 5410–8426.
- [28] Myroshnychenko, V.; Rodriguez-Fernandez, J.; Pastoriza-Santos, I.; Funston, A. M.; Novo, C.; Mulvaney, P.; Liz-Marzan, L. M.; de Abajo, F. J. G. *Chemical Society Reviews* **2008**, *37*, 1792–1805.
- [29] Gans, R. *Annalen der Physik* **1912**, *342*, 881–900.
- [30] Gans, R. *Annalen der Physik* **1915**, *352*, 270–284.
- [31] Alivisatos, A. P. *Science* **1996**, *271*, 933–937.
- [32] Steigerwald, M. L.; Brus, L. E. *Accounts of Chemical Research* **1990**, *23*, 183–188.
- [33] Weller, H. *Angewandte Chemie International Edition* **1993**, *32*, 41–53.
- [34] Weller, H. *Current opinion in colloid & interface science* **1998**, *3*, 194–199.
- [35] Qi, L.; Coelfen, H.; Antonietti, M. *Nano Letters* **2001**, *1*, 61–65.
- [36] Pal, M.; Mathews, N. R.; Santiago, P.; Mathew, X. *Journal of Nanoparticle Research* **2012**, *14*, 916.
- [37] Kim, T. H.; Cho, K. S.; Lee, E. K.; Lee, S. J.; Chae, J.; Kim, J. W.; Kim, D. H.; Kwon, J. Y.; Amaratunga, G.; Lee, S. Y.; Choi, B. L. *Nature photonics* **2011**, *5*, 176–182.
- [38] Mashford, B. S.; Stevenson, M.; Popovic, Z.; Hamilton, C.; Zhou, Z.; Breen, C.; Steckel, J.; Bulovic, V.; Bawendi, M.; Coe-Sullivan, S.; Kazlas, P. T. *Nature photonics* **2013**, *7*, 407–412.

- [39] Scholes, G. D. *Advanced Functional Materials* **2008**, *18*, 1157–1172.
- [40] Trindade, T.; O'Brien, P.; Pickett, N. L. *Chemistry of Materials* **2001**, *13*, 3843–3858.
- [41] Schiener, A.; Magerl, A.; Krach, A.; Seifert, S.; Steinrueck, H.-G.; Zagorac, J.; Zahn, D.; Wehrich, R. *Nanoscale* **2015**, *7*, 11328–11333.
- [42] Unni, C.; Philip, D.; Gopchandran, K. G. *Spectrochimica Acta Part A* **2008**, *71*, 1402–1407.
- [43] Brus, L. *The Journal of Physical Chemistry* **1986**, *90*, 2555–2560.
- [44] Brus, L. E. *The Journal of Chemical Physics* **1984**, *80*, 4403–4409.
- [45] Efros, A. L.; Rosen, M.; Kuno, M.; Nirmal, M.; Norris, D. J.; Bawendi, M. *Physical Review B* **1996**, *54*, 4843.
- [46] Klimov, V. I.; Mikhailovsky, A. A.; McBranch, D. W.; Leatherdale, C. A.; Bawendi, M. G. *Science* **2000**, *287*, 1011–1013.
- [47] Raab, C.; Simko, M.; Gazso, A.; Fiedeler, U.; Nentwich, M. *Nano trust dossiers* **2008**, *8*, 1–4.
- [48] Mijatovic, D.; Eijkel, J. C. T.; van den Berg, A. *Lab on a Chip* **2005**, *5*, 492–500.
- [49] Park, J.; Joo, J.; Kwon, S. G.; Jang, Y.; Hyeon, T. *Angewandte Chemie International Edition* **2007**, *46*, 4630–4660.
- [50] vanEmbden, J.; Sader, J. E.; Davidson, M.; Mulvaney, P. *The Journal of Physical Chemistry C* **2009**, *113*, 16342–16355.
- [51] Sugimoto, T. *Advances in Colloid and Interface Science* **1987**, *28*, 65–108.
- [52] Peng, X.; Wickham, J.; Alivisatos, A. P. *Journal of the American Chemical Society* **1998**, *120*, 5343–5344.
- [53] Clark, M. D.; Kumar, S. K.; Owen, J. S.; Chan, E. M. *Nano Letters* **2011**, *11*, 1976–1980.
- [54] LaMer, V. K.; Dinegar, R. H. *Journal of the American Chemical Society* **1950**, *72*, 4847–4854.
- [55] Whitesides, G. M. *Nature* **2006**, *442*, 368–373.
- [56] Manz, A.; Harrison, D. J.; Verpoorte, E. M. J.; Fettinger, J. C.; Paulus, A.; Luedi, H.; Widmer, H. M. *Journal of Chromatography* **1992**, *593*, 253–258.

- [57] Terry, S. C.; Jerman, J. H.; Angell, J. B. *IEEE Transactions on Electron Devices* **1979**, *26*, 1880–1886.
- [58] McDonald, J. C.; Duffy, D. C.; Anderson, J. R.; Chiu, D. T.; Wu, H.; Schueller, O. J. A.; Whitesides, G. M. *Electrophoresis* **2000**, *21*, 27–40.
- [59] Manz, A.; Graber, N.; Widmer, H. M. *Sensors and Actuators B* **1990**, *1*, 244–248.
- [60] Kopp, M. U.; deMello, A. J.; Manz, A. *Science* **1998**, *280*, 1046–1048.
- [61] Harrison, D. J.; Fluri, K.; Seiler, K.; Fan, Z.; Effenhauser, C. S.; Manz, A. *Science* **1993**, *261*, 895–897.
- [62] Hadd, A. G.; Raymond, D. E.; Halliwell, J. W.; Jacobson, S. C.; Ramsey, J. M. *Analytical Chemistry* **1997**, *69*, 3407–3412.
- [63] Woolley, A. T.; Mathies, R. A. *Analytical Chemistry* **1995**, *67*, 3676–3680.
- [64] Pontoni, D.; Bolze, J.; Dingenouts, N.; Narayanan, T.; Ballauff, M. *Journal of Physical Chemistry B* **2003**, *107*, 5123–5125.
- [65] Knight, J. B.; Vishwanath, A.; Brody, J. P.; Austin, R. H. *Physical Review Letters* **1998**, *80*, 3863–3866.
- [66] Schuetzner, W.; Kenndler, E. *Analytical Chemistry* **1992**, *64*, 1991–1995.
- [67] Rohlicek, V.; Deyl, Z.; Miksik, I. *Journal of Chromatography A* **1994**, *662*, 369–373.
- [68] Bayer, H.; Engelhardt, H. *Journal of Microcolumn Separations* **1996**, *8*, 479–484.
- [69] McCormick, R. M.; Nelson, R. J.; Alonso-Amigo, M. G.; Benvegna, D. J.; Hooper, H. H. *Analytical Chemistry* **1997**, *69*, 2626–2630.
- [70] Duffy, D. C.; McDonald, J. C.; Schueller, O. J. A.; Whitesides, G. M. *Analytical Chemistry* **1998**, *70*, 4974–4984.
- [71] Xia, Y.; Whitesides, G. M. *Angewandte Chemie International Edition* **1998**, *37*, 550–575.
- [72] Wang, Y.; Pai, J. H.; Lai, H. H.; Sims, C. E.; Bachman, M.; Allbritton, G. P. *Journal of Micromechanics and Microengineering* **2007**, *17*, 1371–1380.
- [73] Wang, Y.; Bachman, M.; Sims, C. E.; Li, G. P.; Allbritton, N. L. *Langmuir* **2006**, *22*, 2719–2725.

- [74] MicroChem, *NANOTM SU-8 Organic Resin Solution*; MSDS, 2001.
- [75] Xia, Y.; Whitesides, G. M. *Annual Review of Materials Research* **1998**, *28*, 153–184.
- [76] Lee, J. N.; Park, C.; Whitesides, G. M. *Analytical Chemistry* **2003**, *75*, 6544–6554.
- [77] Moss, T.; Paulus, I. E.; Raps, D.; Altstaedt, V.; Greiner, A. *e-Polymers* **2017**, *17*, 255–261.
- [78] Weinhausen, B.; Koester, S. *Lab on a Chip* **2013**, *13*, 212–215.
- [79] Koester, S.; Pfohl, T. *Modern Physics Letters B* **2012**, *26*, 1230018.
- [80] Seibt, S.; With, S.; Bernet, A.; Schmidt, H.-W.; Foerster, S. *Langmuir* **2018**, *34*, 5535–5544.
- [81] Carlborg, C. F.; Haraldsson, T.; Oeberg, K.; Malkoch, M.; van der Wijngaart, W. *Lab on a Chip* **2011**, *11*, 3136–3147.
- [82] Brennich, M. E.; Nolting, J.-F.; Dammann, C.; Noeding, B.; Bauch, S.; Herrmann, H.; Pfohl, T.; Koester, S. *Lab on a Chip* **2011**, *11*, 708–716.
- [83] Panine, P.; Finet, S.; Weiss, T. M.; Narayanan, T. *Advances in colloid and interface science* **2006**, *127*, 9–18.
- [84] Shastri, M. C. R.; Roder, H. *Nature Structural Biology* **1998**, *5*, 385–392.
- [85] Lu, M.; Ozcelik, A.; Grigsby, C. L.; Zhao, Y.; Guo, F.; Leong, K. W.; Huang, T. J. *Nano Today* **2016**, *11*, 778–792.
- [86] Ismagilov, R. F.; Stroock, A. D.; Kenis, P. J. A.; Whitesides, G. M.; Stone, H. A. *Applied Physics Letters* **2000**, *76*, 2376–2378.
- [87] Majedi, F. S.; Hasani-Sadrabadi, M. M.; Emami, S. H.; Taghipoor, M.; Dashtimoghadam, E.; Bertsch, A.; Moaddel, H.; Renaud, P. *Chemical Communications* **2012**, *48*, 7744–7746.
- [88] Park, H. Y.; Qiu, X.; Rhoades, E.; Korfach, J.; Kwok, L. W.; Zipfel, W. R.; Webb, W. W.; Pollack, L. *Analytical Chemistry* **2006**, *78*, 4465–4473.
- [89] Koh, C. G.; Zhang, X.; Liu, S.; Golan, S.; Yu, B.; Yang, X.; Guan, J.; Jin, Y.; Talmon, Y.; Muthusamy, N.; Chan, K. K.; Byrd, J. C.; Lee, R. J.; Marcucci, G.; Lee, J. *Journal of Controlled Release* **2010**, *141*, 62–69.

- [90] Kim, Y. T.; Joshi, S. D.; Davidson, L. A.; LeDuc, P. R.; Messner, W. C. *Lab on a Chip* **2011**, *11*, 2182–2188.
- [91] Kennedy, M. J.; Ladouceur, H. D.; Moeller, T.; Kirui, D.; Batt, C. A. *Biomicrofluidics* **2012**, *6*, 044119.
- [92] Sundararajan, N.; Pio, M. S.; Lee, L. P.; Berlin, A. A. *Journal of Microelectromechanical Systems* **2004**, *13*, 559–567.
- [93] Lee, M. G.; Choi, S.; Park, J.-K. *Lab on a Chip* **2009**, *9*, 3155–3160.
- [94] Russell, R.; Millett, I. S.; Tate, M. W.; Kwok, L. W.; Nakatani, B.; Gruner, S. M.; Mochrie, S. G. J.; Pande, V.; Doniach, S.; Herschlag, D.; Pollack, L. *Proceedings of the National Academy of Sciences* **2002**, *99*, 4266–4271.
- [95] Simonnet, C.; Groisman, A. *Applied Physics Letters* **2005**, *87*, 114104.
- [96] Chang, C.-C.; Huang, Z.-X.; Yang, R.-J. *Journal of Micromechanics and Microengineering* **2007**, *17*, 1479–1486.
- [97] Chung, T. J. *Computational Fluid Dynamics*, 2nd ed.; Cambridge University Press, 2002.
- [98] Kaemmel, G.; Franek, H.; Recke, H.-G. *Einfuehrung in die Methode der finiten Elemente*, 2nd ed.; Carl Hanser Verlag, 1990.
- [99] Wesseling, P. *Principles of Computational Fluid Dynamics*, 1st ed.; Springer, 2000.
- [100] Zienkiewicz, O. C.; Taylor, R. L. *The Finite Element Method, Vol. 3: Fluid Dynamics*, 5th ed.; Butterworth Heinemann, 2000.
- [101] Squires, T. M.; Quake, S. R. *Reviews of Modern Physics* **2005**, *77*, 977–1026.
- [102] Brody, J. P.; Yager, P.; Goldstein, R. E.; Austin, R. H. *Biophysical Journal* **1996**, *71*, 3430–3441.
- [103] Reynolds, O. *Philosophical Transactions of the Royal Society of London* **1884**, *174*, 935–982.
- [104] Reynolds, O. *Philosophical Transactions of the Royal Society of London* **1895**, *186*, 123–164.
- [105] Purcell, E. M. *American Journal of Physics* **1977**, *45*, 3–11.

- [106] Avila, K.; Moxey, D.; deLozar, A.; Avila, M.; Barkley, D.; Hof, B. *Science* **2011**, *333*, 192–196.
- [107] Trebbin, M.; Steinhäuser, D.; Perlich, J.; Buffet, A.; Roth, S. V.; Zimmermann, W.; Thiele, J.; Foerster, S. *Proceedings of the National Academy of Sciences* **2013**, *110*, 6706–6711.
- [108] Navier, C. L. M. H. *Memoires de l'Academie des sciences de l'Institut de France* **1823**, *6*, 389–416.
- [109] Neto, C.; Evans, D. R.; Bonaccorso, E.; Butt, H.-J.; Craig, V. S. J. *Reports on Progress in Physics* **2005**, *68*, 2859–2897.
- [110] Bocquet, L.; Barrat, J.-L. *Physical Review Letters* **1993**, *70*, 2726–2729.
- [111] Bocquet, L.; Barrat, J.-L. *Physical Review E* **1994**, *49*, 3079.
- [112] Poiseuille, J. L. *Recherches expérimentales sur le mouvement des liquides dans les tubes de très-petits diamètres.*; Imprimerie Royale, 1844.
- [113] deMello, A. J. *Nature* **2006**, *442*, 394–402.
- [114] Mialdun, A.; Yasnou, V.; Shevtsova, V.; Koeniger, A.; Koehler, W.; de Mezquia, D. A.; Bou-Ali, M. M. *The Journal of Chemical Physics* **2012**, *136*, 244512.
- [115] Capretto, L.; Cheng, W.; Hill, M.; Zhang, X. *Microfluidics*; Springer Berlin Heidelberg, 2011; Chapter Micromixing within microfluidic devices, pp 27–68.
- [116] Balluffi, R. W.; Allen, S.; Carter, W. C. *Kinetics of materials.*; John Wiley & Sons, 2005.
- [117] Crank, J. *The Mathematics of Diffusion*, 2nd ed.; Oxford University Press, 1975.
- [118] Bennett, T. D. *Transport by Advection and Diffusion.*; John Wiley & Sons, 2013.
- [119] Tonhauser, C.; Natalello, A.; Loewe, H.; Frey, H. *Macromolecules* **2012**, *45*, 9551–9570.
- [120] Dambrine, J.; Géraud, B.; Salmon, J.-B. *New Journal of Physics* **2009**, *11*, 075015.
- [121] Gachelin, J.; Mino, G.; Berthet, H.; Lindner, A.; Rousselet, A.; Clément, E. *Physical Review Letters* **2013**, *110*, 268103.
- [122] McWilliam, I. G.; Bolton, H. C. *Analytical Chemistry* **1969**, *41*, 1755–1770.

- [123] Foley, J. P.; Dorsey, J. G. *Journal of Chromatographic Science* **1984**, *22*, 40–46.
- [124] Whitesides, G. M.; Grzybowski, B. *Science* **2002**, *295*, 2418–2421.
- [125] Foerster, S.; Plantenberg, T. *Angewandte Chemie International Edition* **2002**, *41*, 688–714.
- [126] Riess, G. *Progress in Polymer Science* **2003**, *28*, 1107–1170.
- [127] Mai, Y.; Elsenberg, A. *Chemical Society Reviews* **2012**, *41*, 5969–5985.
- [128] Hyde, S. *Journal de Physique Colloques* **1990**, *51*, C7209.
- [129] Antonietti, M.; Foerster, S. *Advanced Materials* **2003**, *15*, 1323–1333.
- [130] Leibler, L. *Macromolecules* **1980**, *13*, 1602–1617.
- [131] Matsen, M. W.; Bates, F. S. *Macromolecules* **1996**, *29*, 1091–1098.
- [132] Matsen, M. W.; Schick, M. *Current Opinion in Colloid & Interface Science* **1996**, *1*, 329–336.
- [133] Foerster, S.; Zisenis, M.; Wenz, E.; Antonietti, M. *The Journal of Chemical Physics* **1996**, *104*, 9956–9970.
- [134] With, S. Microfluidics as a method to follow dynamic assembly of colloidal systems. Ph.D. thesis, University of Bayreuth, 2015.

Chapter 2

2. Experimental Methods

This chapter provides a general description of the experimental methods and instrumentation used throughout the thesis. Experimental details and techniques relevant for specific experiments are described in the according section of each chapter.

2.1. Materials

Gold(III) chloride trihydrate ($\text{HAuCl}_4 \cdot 3\text{H}_2\text{O}$; Alpha Aesar, $\geq 99.9\%$), cetyltrimethylammonium bromide (CTAB; Sigma-Aldrich, 96%), sodium borohydrate (NaBH_4 ; Sigma-Aldrich, $\geq 99.99\%$), silver(I) nitrate (AgNO_3 ; Sigma-Aldrich, $\geq 99.9\%$), hydroquinone (Sigma-Aldrich, $\geq 99\%$), hydrochloric acid (HCl; VWR), Calcium GreenTM-5N (CG5N; hexapotassium-salt, ThermoFisher), Cascade[®] Blue dextran (ThermoFisher), cadmium chloride (CaCl_2 ; Sigma-Aldrich), cadmium nitrate ($\text{Cd}(\text{NO}_3)_2$; Sigma-Aldrich), sodium sulfide (Na_2S ; Sigma-Aldrich), thioglycerol (Sigma-Aldrich) and L-cysteine (Sigma-Aldrich) were used as received without further purification. For the microfluidic device production Polydimethylsiloxane (PDMS; Dow Corning) as the two component kit Sylgard[®] 184 was used as described in section 2.2. The hydrogelater N,N',N''-tris(4-carboxyphenylene)-1,3,5-benzene tricarboxamide (BTA), used in chapter 5, was synthesised by A. Bernet and M. Behr (Macromolecular Chemistry I, University of Bayreuth) and used as received. The poly(tetrabutylammonium 6-(thiophen-3-yl) hexane-1-sulfonate), used in chapter 7, was synthesised by M. Schmidt (Macromolecular Chemistry I, University of Bayreuth) and used as received with a molecular weight of ca. 38.5 kg/mol (according to 79 repeating units). Water was purified using a Milli-Q system (Millipore), leading to a final resistivity of 18 M Ω cm.

2.2. Microfluidic device fabrication

2.2.1. Photolithography

The photolithographic fabrication of Si-masters was carried out in ISO 5 class clean-rooms. Furthermore, amber light was used to ease the handling of UV-sensitive negative-photoresist. Si-wafer (type P/Boron <100>, SI-MAT, diameter 50.0 ± 0.5 mm, thickness 256-306 μm) were cleaned with isopropanol before blow-dried with pressurised air.

The photoresist EPON SU-8 was spincoated in the desired thickness according to the published spincoat velocities^[1] followed by the prebake and softbake. After the exposure with UV light in a mask aligner (Süss MicroTech with Hg lamp, 365 nm), the designed device geometry was hardened in the post exposure bake. The exact process parameters are shown in Table 2.1. For a multi-layered design, each lithography mask with the layer design was placed in the mask aligner and oriented on top of the previously exposed photoresist structures. After all crosslinking steps, the uncured photoresist was washed away in a developer bath (mr-DEV 600; Dow Corning) until no white flowmarks were visible.^[1,2]

Table 2.1: Process parameters for photolithographic fabrication of microstructured microfluidic devices.^[1]

Step	Parameter
thickness	50 μm
spincoat velocity	2000 rpm
prebake (65°C)	10 min
softbake (95°C)	30min
UV exposure	2 · 8s
post exposure bake 1 (65°C)	1 min
post exposure bake 2 (95°C)	10 min
developer	10 min

2.2.2. Soft lithography

The replication of the channel structure by PDMS and the following fabrication of microfluidic devices was carried out in a *Scanlaf* Flowbox, class 2 with laminar suppression flow. For the soft lithographic replication, the PDMS oligomer^[3] Sylgard® 184 was thoroughly mixed with the appropriate crosslinker^[4] in a weight ratio of 10:1 before it was poured into a petri dish with the silicon master. Subsequent, this was degassed in a desiccator for 60 minutes, followed by curing at 75°C for 2 hours.^[5,6] The microstructures could then be cut out with a scalpel and the connections for inlet and outlet were punched out with a hole-puncher (UniCore; 0.75 mm) before the PDMS replica was cleaned with isopropanol and blow dried with pressured air. Both PDMS parts were oxidised in a Plasma Cleaner (*Mini Flecto-PC-MFC*; Plasma technology) for 30 s at 0.5 mbar, 80% capacity and 100% air and aligned with the aid of a drop of filtered water under an optical microscope.^[7,8]

2.2.3. Device handling

The usability of all devices were tested before each experiment. Thereby, the leak tightness of the PDMS-PDMS bonding as well as the tubing connection were tested by pumping water through the channel system.

For creation, control and manipulation of laminar flowprofiles in microfluidic channels, the modular syringe pump system neMESYS®, *New Modular Exptensible Syringe pump System* (Cetoni GmbH) was used. According to the channel geometry in chapter 5 and 6, five dosing units were deployed, whose servomotors could be operated individually via the neMESYS user interface.

For reaction kinetic experiments in microfluidic systems, Hamilton syringes in the sizes 0.5 mL, 1.0 mL, 2.5 mL, 5.0 mL and 10 mL were used. Ahead of every experiment, a reference scan was performed to calibrate each dosing unit and set the origin. The syringes were connected with dialysis tube ends (BBraun) and PE-tubing (Scientific Commodities Inc.) to the microfluidic device inlets and outlet.

2.3. Instrumentation

2.3.1. UV-Vis spectrometry

UV-Vis spectroscopy is an absorption spectroscopy method, which uses electromagnetic waves of the ultraviolet (100 - 400 nm) and visible (400 - 760 nm) part of light to excite molecules by photon radiation. The necessary energy of the photon to excite valence electrons from HOMO to LUMO in the investigated molecules is given by

$$\Delta E = h \cdot \nu = \frac{h \cdot c}{\lambda} \quad (2.1)$$

with ΔE as the energy difference between HOMO and LUMO, h as the Planck constant, c as the speed of light, ν as the frequency and λ as the wavelength of the electromagnetic wave.^[9]

Atoms exhibit precisely defined line spectra, as only single transitions are addressed, which can be assigned to one defined wavelength. Molecules in a liquid state on the other side show broad absorption bands. The intensity of those is thereby proportional to the concentration and can be calculated by the Lambert-Beer law:

$$E_{\lambda} = \lg \left(\frac{I}{I_0} \right) = \epsilon_{\lambda} \cdot c \cdot d \quad (2.2)$$

where E_{λ} is the absorbance of a material for light with the wavelength λ , I_0 is the intensity of the incoming light, I the intensity of the transmitted light, ϵ_{λ} the extinction

coefficient at the wavelength λ , c the substance concentration and d the thickness of the radiated object.^[10]

Thus, UV-Vis spectroscopy is a method ideally suited for kinetical analysis. Following Lambert-Beer law (equation 2.2), structural and optical properties can be gained directly from the collected absorption information (see chapter 1.1.1).^[11,12] In this work, UV-Vis spectra were collected with an Agilent HP 8453 UV-Vis spectrophotometer for static experiments after purification and an Ocean Optics UV-Vis setup, composed of a HR2000 detector in combination with a DH-2000-BAL UV-Vis-NIR lightsource and QP400-2-SR optical fibers for *in-situ* kinetic experiments. PMMA and quartz cuvettes with 1 cm pathlength were used to measure the spectra of purified solution. The *in-situ* detection setup is described in the according chapters.

2.3.2. Photoluminescence spectrometry

Fluorescence spectroscopy is an emission spectroscopy method, which detects the released energy of an electron relaxing from an excited state to the ground state (see chapter 1.1.2).^[13]

The emission spectra in this work were collected with a Horiba Jobin-Yvon Fluorolog-3 spectrometer. The PMT detector was corrected for the background wavelength-dependent response using the in-built correction function by Horiba Jobin-Yvon. In addition, some spectra were detected with a Jasco FP 6500. PMMA and quartz cuvettes for fluorescence spectroscopy were used to measure the spectra of solutions. The excitation wavelength was chosen as described in the according chapters.

2.3.3. Confocal Laser Scanning Microscopy (CLSM)

In the most commonly used confocal microscope, a laser scanning of the sample in a defined pattern is used. This type of microscopy is also known as confocal laser scanning microscopy (CLSM) and is schematically shown in Figure 2.1.

The laser is used to selectively excite a fluorescent dye in the sample. The luminescence produced is imaged through an upstream connected pinhole optically in a point of the focal plane of the objective or in the sample.^[14] The emitted light of the sample then passes apertures in its optical path until it hits the detector. Hence, the surrounding and scattered light outside of the focal plane is suppressed. In contrast to normal microscopy, confocal microscopy has the opportunity to image single slides of a sample without displaying blurred, out-of-focus pictures from different planes of the surrounding sample. By imaging different focal planes of a specimen and then merging

the images with the instrument software, three-dimensional pictures of an object can be created.^[15,16]

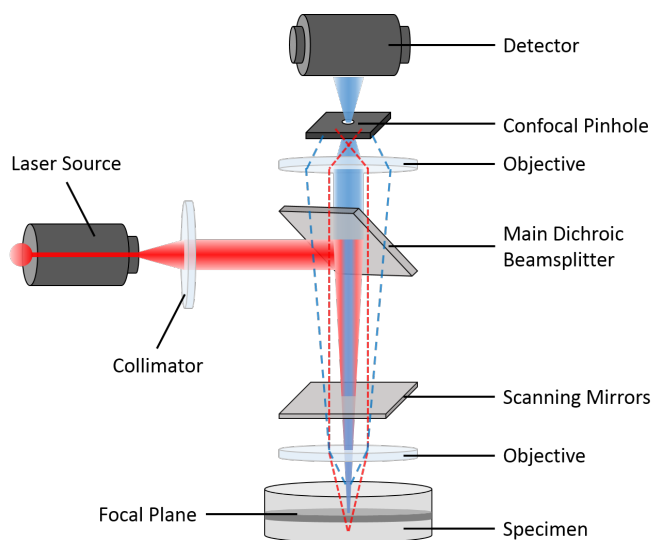


Figure 2.1: Schematic setup of the light beam path in a confocal microscope.

Because a laser provides monochromatic radiation, the chromatic aberration is lower. Furthermore, through the point focused laser beam, less scattered light is detected. These two effects lead to a factor 1.4 higher resolution at similar magnification. In this thesis, confocal measurements were performed using a Leica TCS SP8 in combination with a Leica DMI 6000B microscope and lasers with a wavelength of $\lambda_{max} = 405$ nm and $\lambda_{max} = 514$ nm.

2.3.4. Transmission Electron Microscopy (TEM)

Transmission electron microscopy is a common technique for imaging nanomaterials by using electrons instead of photons. Due to the de Broglie wavelength of high energy accelerated electron being much smaller than those of a photon, a higher magnification can be achieved.

The electron beam is generated by a hairpin cathode, in the case of thermal electronemitter a tungsten or LaB_6 crystal. Thereby, electrons are emitted by thermoionic, Schottky- or fieldemission of the cathode in the electron chamber. These are subsequently bundled by a Wehnelt cylinder and accelerated towards the anode. Hence, an electron microscope needs high vacuum as reactive gases could interact with the heated electron emitter and damage the tungsten filament.^[17-19]

The generated electron beam is concentrated with a condenser lens and projected onto the sample. As the electrons hit the specimen, three different kinds of interaction are possible:

1. the electrons penetrate the sample unhindered.
2. the electrons are deflected by the positively charged atomic cores and loose (almost) no energy, in which case this interaction is called elastic scattering.
3. the electrons of the electron beam interact with the electrons of the atomic shell, whereas the hit electrons are characterised by their energy loss and slight deviation of their path. This effect is known as inelastic scattering.

A schematic transmission electron microscopy beam path is shown in Figure 2.2. In the typical setup of a TEM, the objective aperture of the objective lens is adjusted in a way that only the unscattered and the main part of the inelastic scattered electrons pass it. This leads to a significant increase in contrast. The product of all lenses results in a 100 to 500,000 times magnification and a resolution of 0.2 to 0.5 nm.^[20,21]

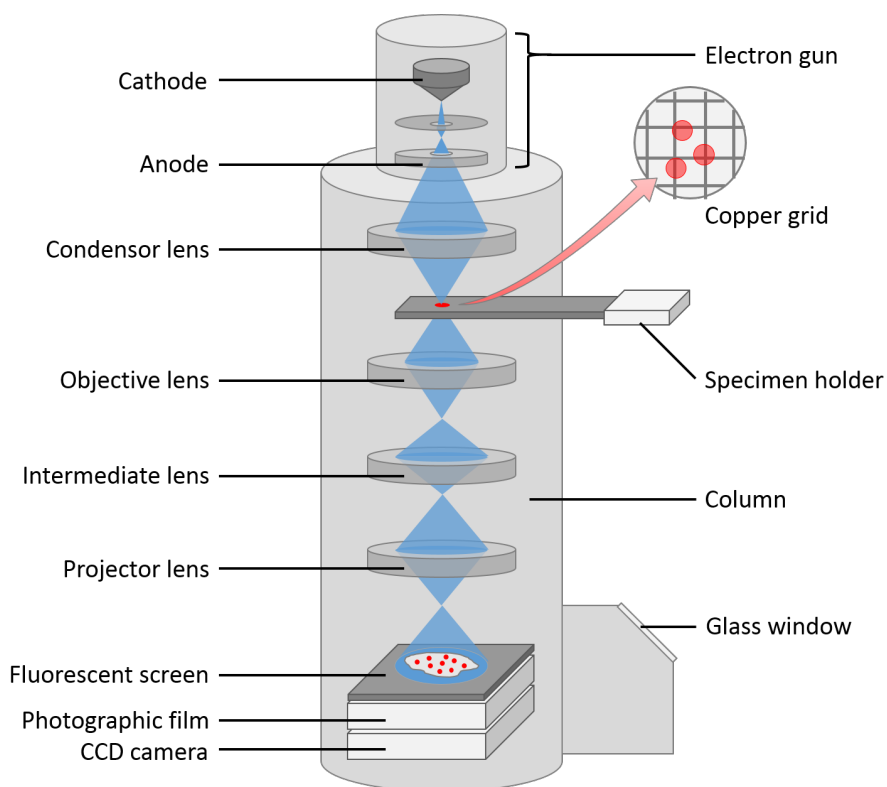


Figure 2.2: Schematic setup of the electron beam path in a transmission electron microscope.

The TEM measurements for this work were carried out on a Zeiss LEO 922 Omega and on a FEI Technai TF20 TEM operating at 200 keV. Samples were prepared by dropping 4 μ L of dilute nanoparticle solution onto a formvar-coated TEM grid (Proscitech) and allowing the excess solvent to evaporate.

2.3.5. Small angle X-ray scattering (SAXS)

Small angle X-ray scattering (SAXS) in general is a method to determine the structure of particle systems. It gives informations about the average particle size and shape. Thereby liquid and solid materials can be investigated, which can contain other solid, liquid or gaseous materials (particles). In this method, X-rays with a typical wavelength between 0.07-0.2 nm are used, resulting in sub-nanometer resolution.^[22] A schematic illustration of the fundamental setup is shown in Figure 2.3.

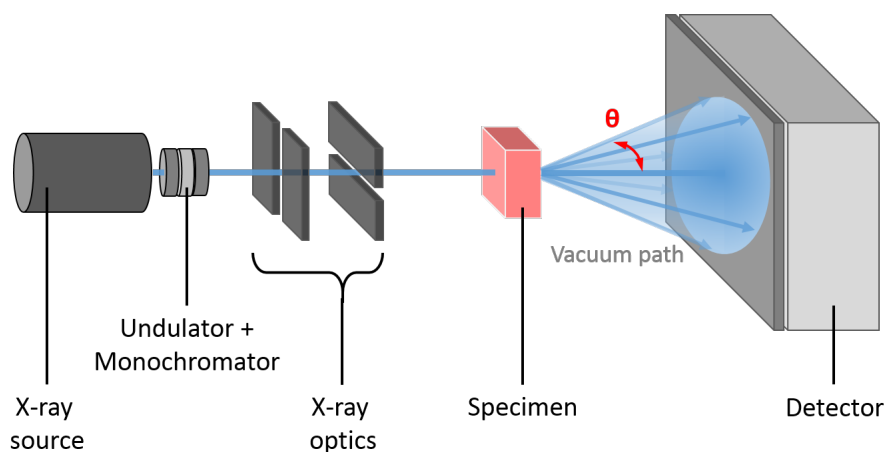


Figure 2.3: Schematic setup of a small angle X-ray scattering experiment.

The X-rays are emitted from the X-ray source (e.g. rotating anode, synchrotron ring source) and pass undulators, monochromators and collimation systems (X-ray optics) before they hit the sample. Thus, the scattering process is considered as elastic because the scattered photons have the same energy as the incoming photons. As the scattered X-rays are coherent, a phase difference between the secondary waves appears originating from different spatial positions of the scattering electrons. The constructive or destructive interference of these phase shifts can be recorded using two-dimensional detectors resulting in a scattering pattern. These are characteristic of the given sample structure and are fundamentally described by Bragg's law (see equation 2.3) for principles of wave interference.

$$2d \sin \theta = n\lambda \quad (2.3)$$

where d is the lattice distance between the scattering electrons, θ is the half scattering angle, n is the positive integer and λ is the wavelength of the used X-rays. The Bragg equation is schematically illustrated in Figure 2.4A, showing the path difference between incoming and reflected X-rays on two scattering planes.^[23]

The two-dimensional scattering pattern recorded by the detector is an angle-dependent

distribution. The detected size range of structures in SAXS experiments lies between 1 nm and 100 nm.^[24]

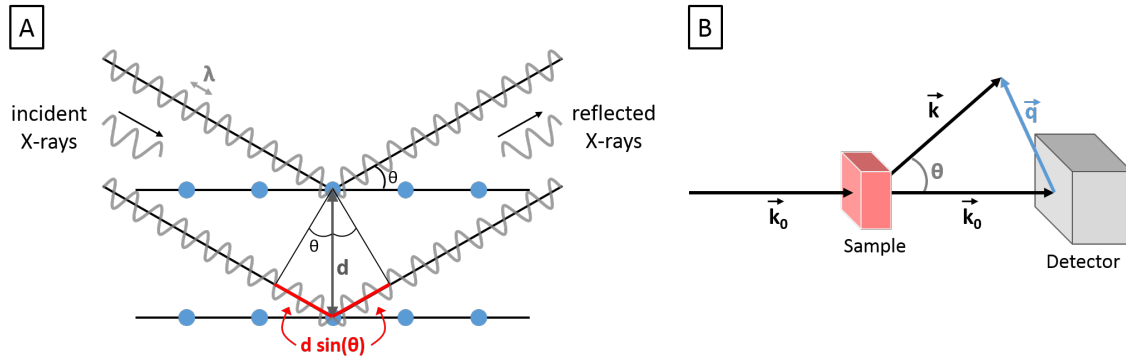


Figure 2.4: (A) Schematic illustration of the Bragg equation with incident and reflected X-rays on two scattering planes, showing the lattice distance d , the half scattering angle θ , the wavelength λ and the path difference defined by Bragg's law. (B) Geometric construction of the scattering vector \vec{q} from the incident wave vector \vec{k}_0 and the scattered wave vector \vec{k} with the half scattering angle θ .

The phase shift ξ between the incident and reflected X-rays can mathematically be described by

$$\xi = -\vec{q} \cdot \vec{r} \quad (2.4)$$

containing the distance between two scattering electrons \vec{r} and the scattering vector \vec{q} . The absolute value of the latter is thereby given by

$$q = |\vec{q}| = |\vec{k} - \vec{k}_0| = \frac{4\pi}{\lambda} \sin\left(\frac{\theta}{2}\right) \quad (2.5)$$

The geometric representation of the scattering vector as a construct of the incident wave vector \vec{k}_0 and the scattered wave vector \vec{k} with the half scattering angle θ is shown in Figure 2.4B.

To describe the interference of the waves, the scattering amplitude $E(\vec{q})$ dependence on the density and position of the scattering centres $\rho(\vec{r})$ in the sample is introduced and described by

$$E(\vec{q}) = \text{const} \cdot \int_V \rho(\vec{r}) \cdot e^{-i\vec{k}\vec{r}} d\vec{r} \quad (2.6)$$

The mathematical form of equation 2.6 is a Fourier transformation, therefore the scattering density function $\rho(\vec{r})$ and the scattering amplitude $E(\vec{q})$ are a pair of Fourier

transforms and link the real space to the reciprocal space. However, $E(\vec{q})$ is experimentally not accessible, as only the scattering intensity $I(\vec{q})$ can be measured. Hence, their relation is defined with $I(\vec{q})$ as the time-averaged square of the absolute value of the scattering amplitude $E(\vec{q})$ as

$$I(\vec{q}) = \langle |E(\vec{q})|^2 \rangle \quad (2.7)$$

In the form of a Fourier transform, $I(\vec{q})$ can also be expressed as

$$I(\vec{q}) = \left\langle \int_V \gamma(\vec{r}) e^{-i\vec{q}\vec{r}} d\vec{r} \right\rangle = 4\pi \int_0^\infty \gamma(r) r^2 \frac{\sin(qr)}{qr} dr = 4\pi \int_0^\infty p(r) \frac{\sin(qr)}{qr} dr \quad (2.8)$$

with $\gamma(\vec{r})$ as the autocorrelation function of a statistically isotropic system without any long range order, given by

$$\gamma(\vec{r}) = \left\langle \int_V \rho(\vec{r}_e) \rho(\vec{r}_e - \vec{r}) d\vec{r}_e \right\rangle \quad (2.9)$$

with \vec{r}_e as the wave vector of the first scattering electron and the pair distribution function $p(\vec{r})$ given by

$$p(\vec{r}) = \vec{r}^2 \cdot \gamma(\vec{r}) \quad (2.10)$$

whereas $p(\vec{r})$ results from the self-convolution of the scattering center density $\rho(\vec{r})$.^[25] To clarify the relations between real and reciprocal space, a graphical illustration of the mathematical operation is shown in Figure 2.5.

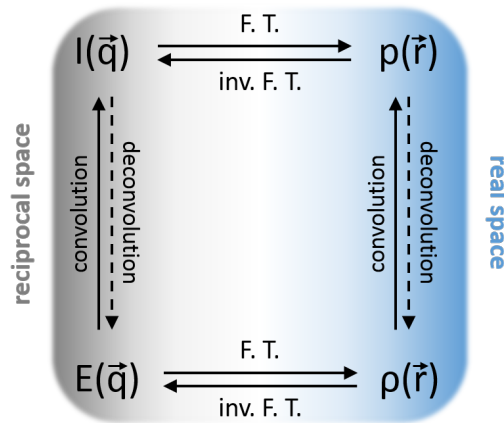


Figure 2.5: Graphical illustration of the relationship between the mathematical operations linking the reciprocal space and the real space for small angle X-ray scattering. The pairs of Fourier transforms scattering intensity $I(\vec{q})$ and pair correlation function $\rho(\vec{r})$ as well as the scattering amplitude $E(\vec{q})$ and scattering density function $\rho(\vec{r})$ are shown.

One approach for obtaining the scattering centre density $\rho(\vec{r})$ is the so-called indirect method. This is based on modeling $\rho(\vec{r})$ using spline functions, which are Fourier transformed into the measurement space and fitted to the scattering curve, leading to the scattering centre density by final deconvolution.^[26-31]

Form factor $P(q)$

Another approach is the model-based, or direct method, which uses a given structure where the scattering centre density function $\rho(\vec{r})$ is known, to describe the scattering curve as a basic function by

$$I(q) = I_0 \cdot P(q) \quad (2.11)$$

where I_0 is the intensity of the incident beam at a 0° angle and $P(q)$ is the form factor.^[32] As the name already explains, the form factor $P(q)$ describes the form and shape of the investigated particles. For spherical particles with radius R , $P(q)$ is given by^[33]

$$P(q) = \rho^2 V^2 \left(3 \frac{\sin(qR) - qR \cdot \cos(qR)}{(qR)^3} \right)^2 \quad (2.12)$$

whereas for cylinders with radius R and length L , the form factor is described by^[34]

$$P(q) = \frac{L\pi}{q} \cdot P_c(q) \quad (2.13)$$

with

$$P_c(q) = 4\rho^2 R^2 \left(\frac{\sin(qR)}{qR} \right)^2 \quad (2.14)$$

Structure factor $S(q)$

The structure factor describes the relationship and interaction between particles, and is important when the solution is more concentrated. In the scattering intensity calculation, the structure factor therefore appears as an additional factor, modifying equation 2.11 to

$$I(q) = I_0 \cdot P(q) \cdot S(q) \quad (2.15)$$

whereas $S(q)$ is derived as

$$S(q) = 1 + \int_0^\infty [g(r) - 1] \frac{\sin(qr)}{qr} 4\pi r^2 dr \quad (2.16)$$

where $g(r)$ is the radial distribution function. For systems with increasing concentration, which form consequently more order, the structure factor $S(q)$ generates peaks that decay exponentially. Indication for structural order is usually evident from a decrease in intensity at low q -values in the scattering pattern, along with the appearance of peaks in the pattern. Dilute systems on the other side, are described solely by the form factor, as the structure factor becomes 1.^[35,36]

The SAXS measurements for this work were carried out with a lab-based setup consisting of a Cu rotating anode (Rigaku), a microfluidic sample stage and an evacuated pinhole camera system (Ganesha SAXS system, SAXSLab) equipped with a 2D-detector (Pilatus 300k, Dectris), as well as the SAXS/WAXS beamline at the Australian Synchrotron, equipped with a Pilatus 1M detector (Dectris).

References

- [1] MicroChem, NANOTM SU-8 Negative Tone Photoresist Formulations 50-100. 2002.
- [2] MicroChem, NANOTM SU-8 Organic Resin Solution; MSDS, 2001.
- [3] Corp., D. C. Sylgard[®] 184 Silicone Elastomer Base.
- [4] Corp., D. C. Sylgard[®] 184 Silicone Elastomer Curing Agent.
- [5] Xia, Y.; Whitesides, G. M. *Annual Review of Materials Research* **1998**, *28*, 153–184.
- [6] Xia, Y.; Whitesides, G. M. *Angewandte Chemie International Edition* **1998**, *37*, 550–575.
- [7] McDonald, J. C.; Duffy, D. C.; Anderson, J. R.; Chiu, D. T.; Wu, H.; Schueller, O. J. A.; Whitesides, G. M. *Electrophoresis* **2000**, *21*, 27–40.
- [8] Whitesides, G. M. *Nature* **2006**, *442*, 368–373.
- [9] Bliefert, C.; Kwiatkowski, J. *Kinetische Analyse mit Hilfe der UV-Vis-Spektroskopie*, 1st ed.; VCH, 1991.
- [10] Demtroeder, W. *Molekuelphysik: Theoretische Grundlagen und experimentelle Methoden.*, 1st ed.; Oldenburg, 2003.
- [11] Prescott, S. W.; Mulvaney, P. *Journal of applied physics* **2006**, *99*, 123504.
- [12] Haiss, W.; Thanh, N. T. K.; Aveyard, J.; Fernig, D. *Analytical Chemistry* **2007**, *79*, 4215–4221.
- [13] Atkins, P. W.; de Paula, J. *Physical Chemistry*; Wiley-VCH, 2006.
- [14] Song, H.; Ismagilov, R. F. *Journal of the American Chemical Society* **2003**, *125*, 14613–14619.
- [15] Tipler, P. A.; Mosca, G. *Physik - Fuer Wissenschaftler und Ingenieure*, 2nd ed.; Springer Verlag, Berlin, Heidelberg, 2007.
- [16] Kilian, U.; Weber, C. *Lexikon der Physik*, 1st ed.; Spektrum Akademischer Verlag, Heidelberg, 2000; Vol. 4.
- [17] Fultz, B.; Howe, J. *Transmission Electron Microscopy and Diffractometry of Materials.*, 4th ed.; Springer, 2012.

- [18] Williams, D.; Carter, C. *Transmission Electron Microscopy: A Textbook for Materials.*, 1st ed.; Plenum Press, 1996.
- [19] Michler, G. H. *Electron Microscopy of Polymers.*, 1st ed.; Springer, 2008.
- [20] Chescoe, D.; Goodhew, P.; Britain, R. M. S. G. *The Operation of Transmission and Scanning Electron Microscopes.*, 1st ed.; Oxford University Press, 1990.
- [21] Reimer, L. *Transmission Electron Microscopy.*, 3rd ed.; Springer, 1993.
- [22] Schnablegger, H.; Singh, Y. *The SAXS Guide. Getting acquainted with the principles.*, 3rd ed.; Anton-Paar GmbH, 2013.
- [23] Lindner, P.; Zemb, T. *Neutrons, X-rays and Light. Scattering Methods applied to Soft Condensed Matter.*, 1st ed.; Elsevier, 2002.
- [24] Guinier, A.; Fournet, G. *Small-Angle Scattering of X-rays.*, 1st ed.; Wiley New York, 1955.
- [25] Debye, P. *Annalen der Physik* **1915**, 351, 809–823.
- [26] Glatter, O. *Journal of Applied Crystallography* **1977**, 10, 415–421.
- [27] Glatter, O. *Journal of Applied Crystallography* **1979**, 12, 166–175.
- [28] Glatter, O. *Journal of Applied Crystallography* **1980**, 13, 577–584.
- [29] Glatter, O. *Journal of Applied Crystallography* **1981**, 14, 101–108.
- [30] Glatter, O.; Hainisch, B. *Journal of Applied Crystallography* **1984**, 17, 435–441.
- [31] Svergun, D. I. *Journal of Applied Crystallography* **1991**, 24, 485–492.
- [32] Dusek, K.; Joanny, J.-F. *Polymer Characterization. Rheology, Laser Interferometry, Electrooptics.*; Springer, 2010.
- [33] Pedersen, J. S. *Physical Review B* **1993**, 47, 657.
- [34] Neugebauer, T. *Annalen der Physik* **1943**, 434, 509–533.
- [35] Brunner-Popela, J.; Glatter, O. *Journal of Applied Crystallography* **1997**, 30, 431–442.
- [36] Weyerich, B.; Brunner-Popela, J.; Glatter, O. *Journal of Applied Crystallography* **1999**, 32, 197–209.

Chapter 3

3. Publication I

Growth Kinetics of Gold Nanorods: A SAXS Study.

Susanne Seibt^{a,b}, Heyou Zhang^b, Stephen Mudie^c, Stephan Förster^{a,*}, Paul Mulvaney^{b,*}

^a*Physical Chemistry I, University of Bayreuth, Universitätsstraße 30, 95447 Bayreuth, Germany.*

^b*Bio21 & School of Chemistry, The University of Melbourne, VIC-3010 Melbourne, Australia.*

^c*SAXS/WAXS Beamline, Australian Synchrotron, 800 Blackburn Road, VIC-3168 Clayton, Australia.*

The results presented in this chapter are prepared as a manuscript, ready for submission.

Individual contribution of involved authors

I performed all experiments and analysed the data. Together with Prof. Stephan Förster and Prof. Paul Mulvaney I wrote the manuscript. Heyou Zhang helped with experiments and data analysis, as well as COMSOL simulations. Dr. Stephen Mudie helped with the SAXS experiments and provided technical support at the synchrotron beamline.

3.1. Abstract

Gold nanorods have a broad range of applications in biology, plasmonics and sensing. Despite several studies of crystallisation dynamics of ascorbic acid-catalysed nanorod synthesis, the anisotropic growth kinetics of hydroquinone-based syntheses are not well-understood. Using simultaneous *in-situ* optical spectroscopy and time-resolved small angle X-ray scattering at the Australian Synchrotron, the seeded growth of highly monodisperse gold nanorods could be directly monitored and the growth parameter for both expanding directions as well as the thickness of the stabilising CTAB layer could be extracted. Hence, direct insights into the reaction using hydroquinone as a reducing agent were obtained for the first time. A novel reaction mechanism for the reduction and oxidation process between hydroquinone / benzoquinone and gold in solution is proposed. In addition, the length and aspect ratio of the synthesised nanorods can be precisely controlled by varying the initial concentration of tetrachloro gold (III) acid and hydroquinone. Finally, we were also able to demonstrate the influence of these changing parameters on the overall size and growth kinetics of the evolving gold nanorods. The newly developed growth model explains and predicts the properties of the gold nanorods and allows well-defined tuning of particle shape and performance.

3.2. Introduction

Gold nanoparticles are of ongoing interest in various fields due to their broad range of applications, reaching from biomedical^[1] and plasmonic^[2] utilisation to their wide use in sensing devices.^[3] The preparation of gold-based nanoparticles has continued to evolve from the original protocols of Turkevich^[4] with ever increasing empirical control over size, polydispersity and shape being reported. Cylindrically-shaped gold nanorods in particular exhibit a very intense longitudinal surface plasmon resonance, whose peak wavelength can be tuned over several hundred nanometres through control of the particle aspect ratio.^[5] Precise control over the morphology of the metallic nanoparticle is necessary. Therefore, a synthesis method separating nucleation and growth phase by overgrowing pre-synthesised seeds, was developed for penta-twinned^[6] and single crystal^[7] gold nanorods. Although both routes result in the growth of rod-shaped nanoparticles, these syntheses were limited in terms of the polydispersity and chemical yield of the final desired product, and both protocols are very sensitive to small changes in the experimental conditions.^[3]

Different paths to improving gold nanorod syntheses were undertaken, primarily via additives to assist well-defined, crystalline growth.^[8] Replacing the widely used ascorbic

acid by an excess of hydroquinone as a weaker reducing agent lead to a high reliability, and high degree of purity synthesis with near quantitative conversion of gold ions to metallic gold during the synthesis.^[9] Further optimisation of this method showed almost no other gold particle shape existed as a side product in solution, while the longitudinal surface plasmon resonance (LSPR) peak could be shifted by size-tuning beyond 1000 nm.^[10]

Recent progress in understanding of the growth mechanism at different stages, including the symmetry breaking step, renewed interest in wet-chemical nanoparticle crystallisation processes.^[11,12] By using different *ex-situ* methods, deeper insight into the symmetry breaking point from a cuboctahedral seed to an anisotropic rod was gained. Additionally, the influence of different parameter changes in the initial synthesis solution, also during the growth stage, was widely investigated.^[11,13] Nevertheless, employing ascorbic acid as reducing agent still produced several side products and a less reproducible synthesis due to faster reaction kinetics.

A more detailed insight into the growth of nanocrystals can be provided by *in-situ* observations. The time-dependent optical properties of growing gold nanorods can be easily analysed using absorption spectroscopy.^[7,14] *In-situ* investigations of structural evolution are more challenging, but were used recently to study the seeded growth of gold nanorods, using CTAB-capped seeds to grow single-crystal rod-shaped nanoparticles following ascorbic acid protocols.^[15-17] Using small angle (SAXS) and wide angle (WAXS) X-ray scattering with a strong X-ray source, such as a synchrotron, provides sufficient time resolution to detect single steps of nanoparticle growth in detail and to study the growth kinetics.^[18,19]

The above-mentioned methods for *in-situ* investigation of particle growth using X-ray scattering facilities use setups utilising a syringe-pump for the injection of the seed solutions. These techniques face serious challenges for the homogeneous mixing of the growth and seed solution and, consequently, to the growth of gold nanorods. However, using hydroquinone-based syntheses allows mixing of the prepared growth solution with the altered seeds prior to insertion of the reaction solution in the measurement capillary, without missing the important early stages of the growth kinetics.

Here we state for the first time a novel growth process for hydroquinone-based seeded-growth of gold nanorods. The studied synthesis in aqueous CTAB solution shows a double-sigmoidal growth, which can be linked to the reaction speed of single gold crys-

tal facettes. We find this optimised synthesis route as highly reproducible method resulting in monodisperse gold nanorods without significant side products. The slower growth kinetics of this synthetic route allows the use of simultaneous absorption spectroscopy and small angle X-ray scattering at a synchrotron source to follow the growth mechanism. From the spectral and scattering data, we can explain for the first time the growth reaction mechanism of the hydroquinone-based synthesis. Furthermore, the influence of changing the gold acid and hydroquinone precursor concentrations in the initial solution was investigated giving further insights into the nanoparticle growth mechanism.

3.3. Experimental Methods

Gold(III) chloride trihydrate ($\text{HAuCl}_4 \cdot 3\text{H}_2\text{O}$, $\geq 99.9\%$) was purchased from Alpha Aesar and used without further purification. Sodium borohydrate (NaBH_4 , $\geq 99.99\%$), silver(I) nitrate (AgNO_3 , $\geq 99.9\%$), hexadecyltrimethylammonium chloride (CTAB, 96%) and hydroquinone (HQ, $\geq 99\%$) were purchased from Sigma-Aldrich and used without further purification. All solutions were freshly prepared, using Millipore-filtered water.

Synthesis of CTAB-capped Au seeds

Briefly, an equal amount of 5 mL of 0.5 mM aqueous HAuCl_4 solution and 0.2 M aqueous CTAB solution were mixed and stirred for 10 min at room temperature. Next, 600 μL of a freshly prepared 0.01 M NaBH_4 solution was added quickly under vigorous stirring. After 2 min, the stirring was stopped and the seeds were aged for 1 h at room temperature.

Synthesis of single-crystalline Au nanorods

To 2.5 mL of a 0.1 M aqueous CTAB solution, 12.5 μL of HAuCl_4 solution (0.1 M, 0.15 M, 0.2 M) and 0.1 M AgNO_3 solution was added and mixed until everything was homogeneously dissolved. 125 μL of an aqueous HQ solution (0.2 M, 0.4 M, 0.6 M) was then added and the growth solution gently mixed, leading to complete decolourisation. Finally, 100 μL of the aged CTAB-capped Au seeds were added and mixed thoroughly. The Au nanorods were grown undisturbed for 24 h at room temperature. The solution was purified by centrifugation (10 min, 14000 rcf) before being washed with water two times and redispersed in 0.5 mL of millipore water to yield a concentration four times higher than the initial synthesis concentration.

Characterisation

UV-Vis spectra were recorded using an Agilent HP 8453. TEM images were obtained with a LEO 922 OMEGA EFTEM with an acceleration voltage of 200 kV from Zeiss (Germany). Zero-loss filtered images were recorded using a bottom mounted Ultrascan 1000 (Gatan) CCD camera system. Gatan Digital Micrograph 3.9 for GMS 1.4 software was used for image acquisition. For the TEM analysis, 4 μL of the as-prepared solution was dried on a mesh copper grid with carbon foil. For size evaluation, the software ImageJ (version 1.44p, U.S. National Institute of Health) was used.

Kinetic experiment setup

2.5 mL of the growth solution was prepared as described earlier in a vial and the seeds injected, followed by thorough mixing. The solution containing the growing nanoparticles was filled in a 1 mm quartz capillary and placed in a 3D-printed holder in the X-ray beam (shown in Figure 3.1). These experiments were carried out for all 9 combinations of HAuCl_4 and HQ concentration and the total measuring time adjusted until no change in the measured curves could be seen, varying from one to seven hours.

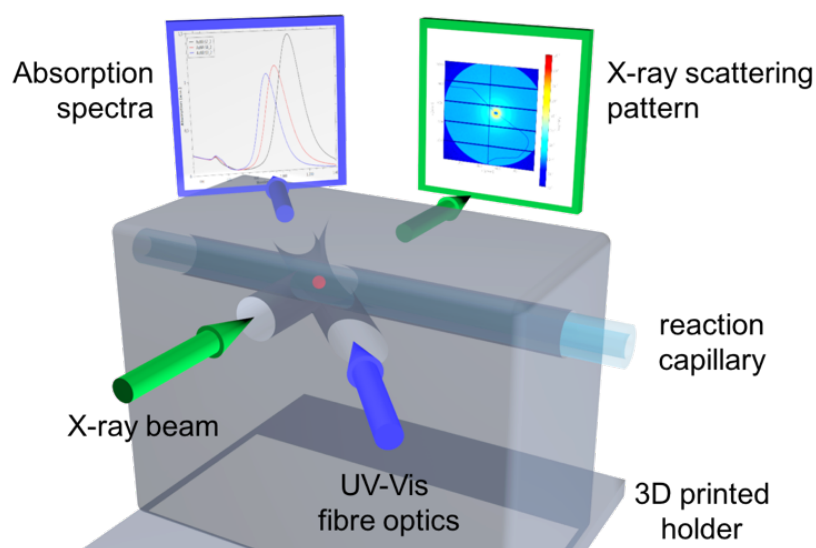


Figure 3.1: Schematic image of the *in-situ* simultaneous SAXS/UV-Vis setup for measuring the growth kinetics of gold nanorods at the Australian Synchrotron.

Simultaneous SAXS / UV-Vis measurements

SAXS experiments were performed at the SAXS/WAXS beamline at the Australian Synchrotron, Melbourne, Australia. An energy of 11.5 keV was used and the detector with flight tube was at 1.6 m distance to the sample. Two-dimensional SAXS patterns were

acquired in 1 min time frames with a PILATUS 1 M detector and radially integrated to yield the SAXS intensity $I(q)$. Therefore, the exposure time was set to 10 s with 50 s delay time, to prevent sample damage through heterogeneous X-ray nucleation. For simultaneous *in-situ* absorption measurements, an OceanOptics UV-Vis setup, composed of a HR2000 detector (detection range 200 – 1100 nm) in combination with a DH-2000-BAL UV-Vis-NIR lightsource (deuterium and halogen lamp, illumination range 215 – 2000 nm) and QP400-2-SR optical fibres (operating range 200 – 1100 nm), was used. The optical fibres were mounted in a 45-degree angle to the position of the capillary. All measurements were background corrected using a capillary filled with 0.1 M CTAB solution.

CV measurements

Cyclic voltammetry was performed using an Autolab model GGSTAT 302 potentiostat. A glassy carbon disk (5 mm diameter) was used as working electrode, the counter electrode was a 1 cm x 1 cm platinum sheet. The working electrode potentials were measured against Ag/AgCl in 0.1 M KCl as reference electrode. The experiments were performed measuring cyclically from -1.0 V to +1.3 V with a scan rate of 100 mV per second, starting from 0 V in positive direction. Measurements were performed at 22°C.

3.4. Results and Discussion

In-situ small angle X-ray scattering experiments need a very monodisperse and pure sample to obtain clear scattering signals, which can be fitted with a certain model for size distributions. Therefore, our first step was the optimisation of the hydroquinone based gold nanorod synthesis to eliminate side products with different shapes during the reaction. It is of critical importance to keep the production of side products to a minimum, as the volume fraction of growing spheres or prisms would obscure the signal of the cylindrical nanorod growth.

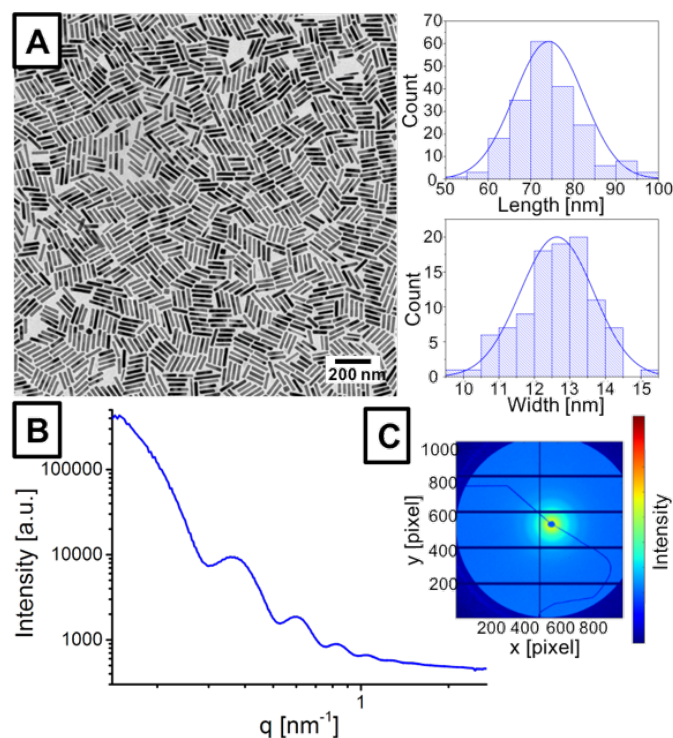


Figure 3.2: (A) TEM image of the final gold nanorod solution without purification, following the hydroquinone based synthesis route. Length and width could be evaluated as monodisperse. (B) Typical X-ray scattering curve for an unpurified gold nanorod solution, showing a cylindrical form factor. (C) 2D-scattering pattern according to the SAXS signal in (B).

Figure 3.2A shows an example of a typical TEM image, obtained by slight improvements of previously published gold nanorod syntheses using hydroquinone as a reducing agent.^[3,10] As displayed, these changes lead to highly monodisperse gold nanorods with up to 99% yield. The growth rate is also suitable for SAXS studies. To validate the suitability for *in-situ* X-ray scattering experiments, a static measurement of the completed synthesis solution was measured beforehand, shown in Figure 3.2B and 3.2C. The signal in both the two-dimensional scattering pattern and radial integrated scattering curve exhibit sufficient intensity and form factor information for a cylindrical fit model.

Influence of precursor concentrations

To investigate the influence of the amount of precursor in the growth solution on the nanorod growth kinetics and the final rod size, the concentration of HAuCl_4 and hydroquinone was varied systematically and the influence studied *ex-situ* with transmission electron microscopy and simultaneous *in-situ* absorption spectroscopy and small angle X-ray scattering.

The exact synthetic parameters are shown in Table 3.1. The added concentration of gold acid was varied between 0.45 mM, 0.68 mM and 0.91 mM, while for hydroquinone the variation range was between 9.09 mM, 18.18 mM and 27.27 mM in the final solution.

Table 3.1: Synthetic parameters for all investigated samples with systematic variation of gold acid and hydroquinone concentrations. Length and width of the resultant nanorods, with error, evaluated from TEM images for every sample are included.

		Hydroquinone		
		9.09 mM	18.18 mM	27.27 mM
Gold(III) acid	0.45 mM	AuNR-S1	AuNR-S2	AuNR-S3
		$L = 43.15 \pm 2.77 \text{ nm}$	$L = 37.16 \pm 1.87 \text{ nm}$	$L = 31.29 \pm 2.01 \text{ nm}$
		$W = 7.64 \pm 0.42 \text{ nm}$	$W = 6.99 \pm 0.36 \text{ nm}$	$W = 7.66 \pm 0.44 \text{ nm}$
	0.68 mM	AuNR-S4	AuNR-S5	AuNR-S6
		$L = 54.02 \pm 2.86 \text{ nm}$	$L = 45.34 \pm 2.18 \text{ nm}$	$L = 39.84 \pm 2.54 \text{ nm}$
		$W = 9.74 \pm 0.37 \text{ nm}$	$W = 7.71 \pm 0.43 \text{ nm}$	$W = 7.48 \pm 0.29 \text{ nm}$
	0.91 mM	AuNR-S7	AuNR-S8	AuNR-S9
		$L = 71.41 \pm 3.28 \text{ nm}$	$L = 51.24 \pm 2.88 \text{ nm}$	$L = 46.38 \pm 2.41 \text{ nm}$
		$W = 10.41 \pm 0.41 \text{ nm}$	$W = 9.70 \pm 0.37 \text{ nm}$	$W = 9.58 \pm 0.58 \text{ nm}$

Typical TEM images of unpurified nanorod samples used for the determination of the length and width of the rod can be seen in Figure 3.3. The first observation is the strong increase in rod length with higher amounts of HAuCl_4 in solution, as well as smaller increases in the rod width. The second observation is a strong decrease in final rod length with increasing hydroquinone concentration. The width decreases slightly but the effect is not pronounced.

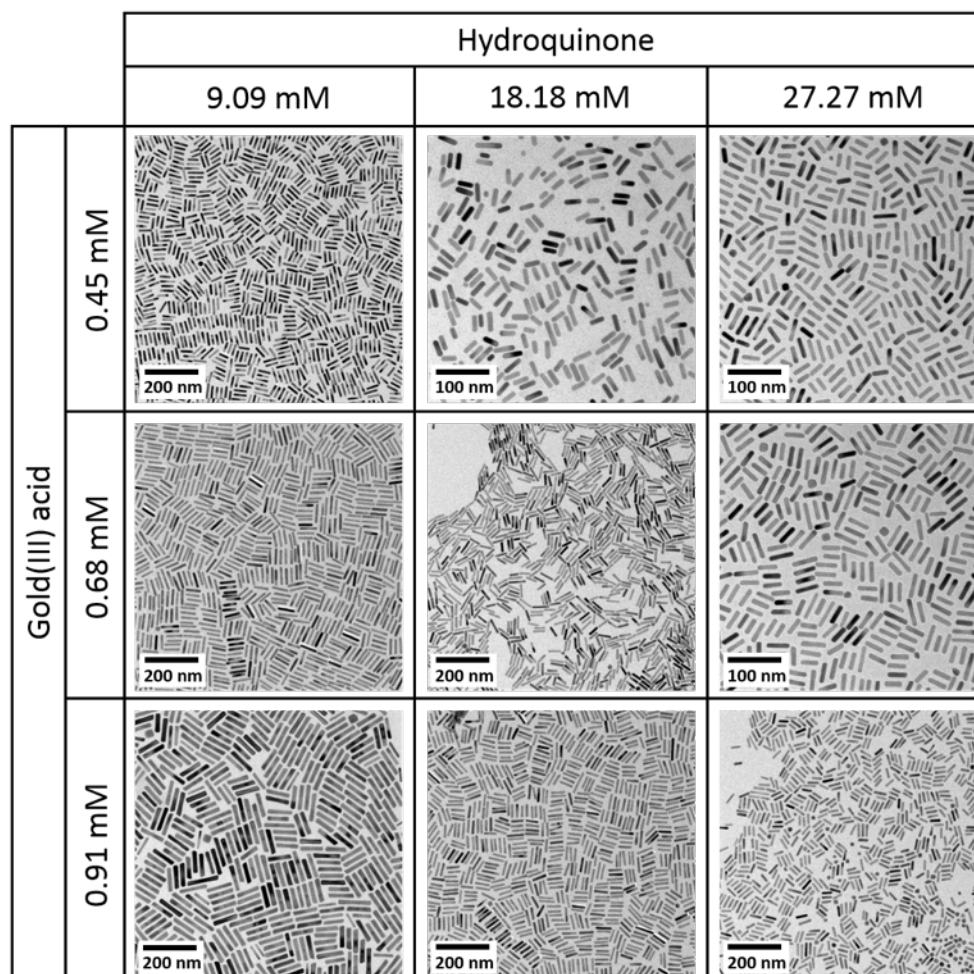


Figure 3.3: TEM images of the final gold nanorod solutions without purification, following the hydroquinone based synthesis route according to Table 3.1. All nanorod solutions show negligible contributions from spheres. Rods prepared on carbon coated grids and images collected at 200kV.

In-situ investigations of gold nanorod synthesis

The slower reaction kinetics of hydroquinone-based syntheses, compared to the use of L-ascorbic acid as a reducing agent, allows a very detailed investigation of the optical properties of the growing nanorods. Hence, the seeded growth process, emanating from a spherical, cuboctahedral seed, resulting in a spherical capped cylinder can be followed by the appearance of the longitudinal surface plasmon resonance (LSPR) peak in the UV-Vis spectrum.

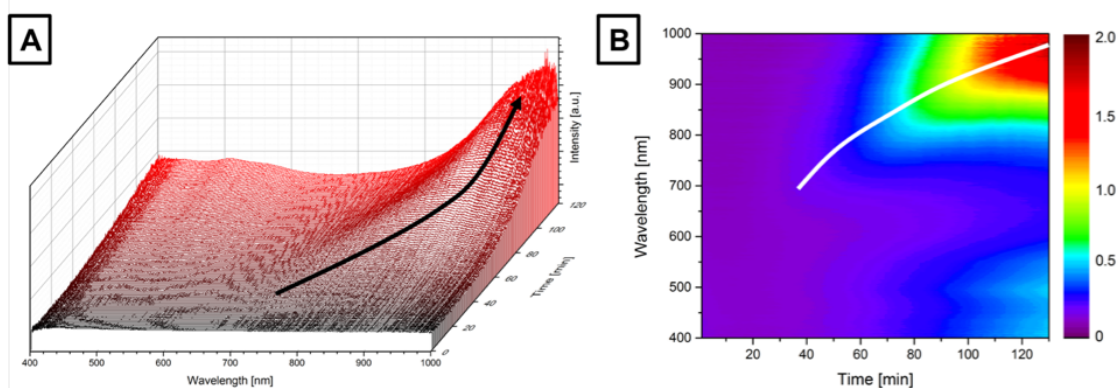


Figure 3.4: (A) *In-situ* absorption spectra of sample AuNR-S4, shown as a time-resolved multi-curve plot. A significant increase in intensity as well as the development of the longitudinal plasmon peak (black arrow) around 800 nm can be seen over a reaction time of 120 minutes. (B) Colour-coded extinction (arbitrary units) shown as a function of time, highlighting the progress of the longitudinal plasmon resonance (white line). The second lower peak at 510 nm corresponds to the transverse plasmon mode, while around 400 nm contributions from interband transitions are evident as the concentration of rods increases.

The *in-situ* collected absorption spectra in Figure 3.4 show the optical evolution of nanorod growth in an initial growth solution containing 0.45 mM chloroauric acid and 9.09 mM hydroquinone (AuNR-S4). The development of the characteristic LSPR peak around 800 nm can clearly be seen, showing an increase in intensity over the reaction time of one hour. Furthermore, the red-shift in wavelength, indicated by the black arrow in Figure 3.4A, signals the growth of gold nanorods in solution and is displayed in more detail in Figure 3.4B by the white line.

The optical evolutions during the reaction of all samples are displayed in Figure 3.5. The respective contour plots can be found in the Supporting Information.

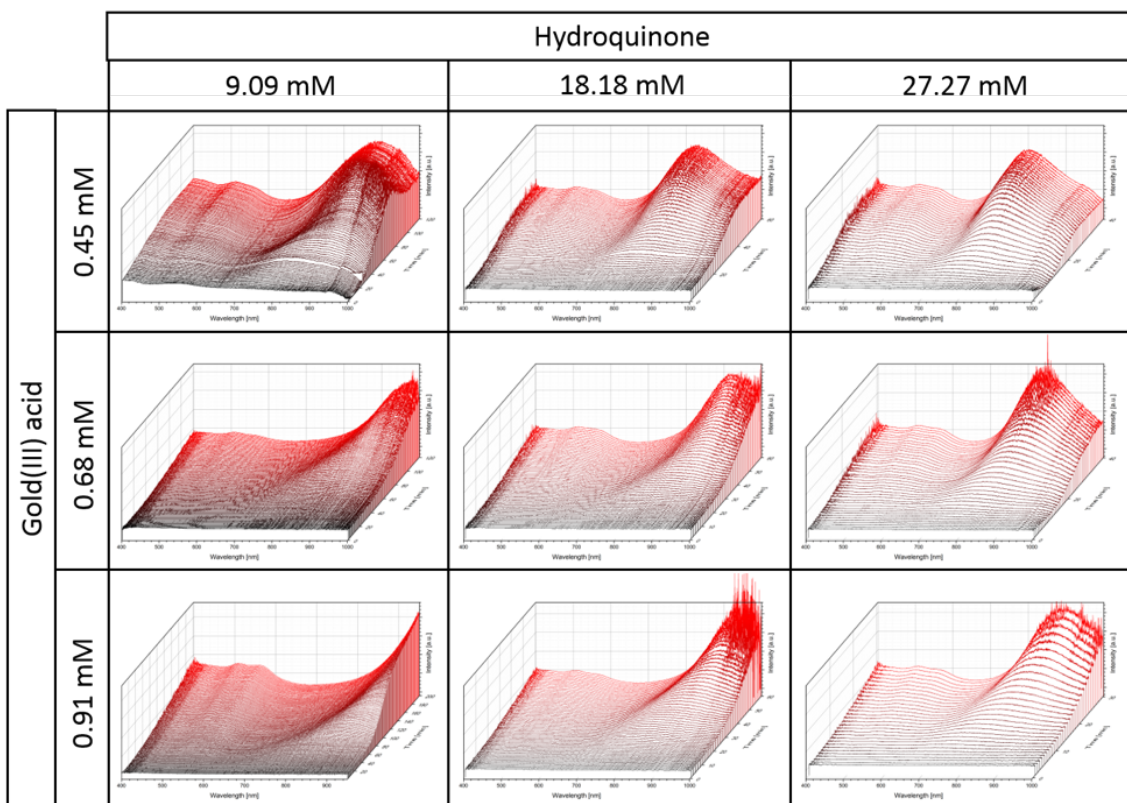


Figure 3.5: *In-situ* absorption spectra of all samples following the hydroquinone based synthesis route according to Table 3.1, shown as a time-resolved multi-curve plot. A significant increase in intensity as well as the development of the longitudinal plasmon peak can be seen over the reaction times. A clear shift of the LSPR maximum wavelength with varying precursor concentration as well as different reaction kinetics can be seen.

To analyse the optical data in Figure 3.5, we convert all the data into plots of the surface plasmon mode peak wavelength vs time, shown in Figure 3.6.

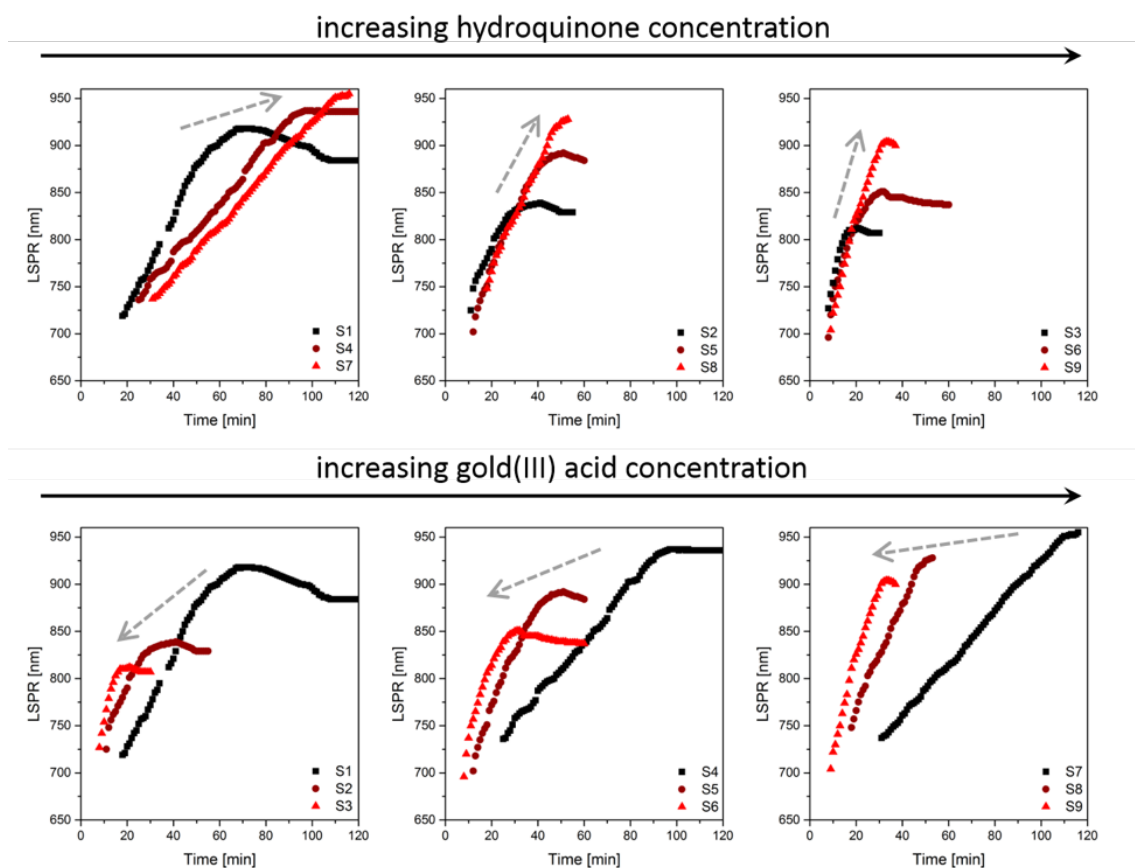


Figure 3.6: Longitudinal surface plasmon resonance peak as a function of time for all varied synthesis parameter according to Figure 3.5. Top row shows the combined graphs for increasing hydroquinone concentration for 3 different gold concentrations each (black squares lowest, dark red circles middle, bright red triangles highest concentration). The growth kinetics slows down with increasing gold acid in the growth solution. The bottom row shows combined graphs for increasing gold acid concentration with 3 different HQ concentrations each. The growth kinetics is getting faster with increasing HQ in the synthesis.

It is evident that the hydroquinone and chloroauric acid concentration both have pronounced effects on the evolution of the SPR peak. In virtually all cases, the shift in the peak is almost linear with time until the reaction is complete. In some cases, a small blue-shift is observed near completion. We see faster peak shifts for higher hydroquinone concentrations implying that rod growth rates increase with increasing [HQ]. Despite this, TEM shows the final rods are shorter at higher [HQ]. Increasing the chloroauric gold acid concentration leads to a final SPR peak at longer wavelengths, consistent with TEM. The growth rate is slower with higher [HAuCl₄].

To investigate the influence of silver(I) nitrate concentration on the reaction, the amount of added silver was varied between four values and the reaction rate measured via *in-*

in situ UV-Vis. The LSPR as a function of time is shown for all four syntheses in Figure 3.7. The added amount of 0.1 M AgNO₃ (equivalent of 0.46 mM in the final solution) is thereby according to the reaction conditions of the previously described nanorod synthesis AuNR-S7 (see Table 3.1). The measured LSPR for these reactions are in very good agreement (red squares and red dots in Figure 3.7), proving again the high reproducibility of the synthesis method.

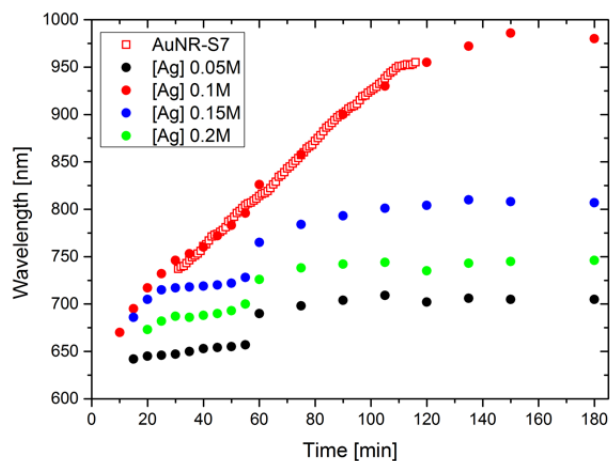


Figure 3.7: Wavelength of the longitudinal surface plasmon resonance as a function of time for gold nanorod synthesis with four different silver(I) nitrate concentrations. The [Ag] for the black dots is 0.23 mM, 0.46 mM for the red dots and therefore identically with the synthesis parameters of synthesis AuNR-S7, shown as red squares. For the blue dots, [Ag] is 0.68 mM and 0.91 mM for the green dots. The typical redshift with growing nanorods can be seen for all four parameters, as well as a jump in the LSPR at 60 min for each synthesis. However, a significant difference of the end LSPR value is found.

Each of the reactions shown in Figure 3.7 show the characteristic redshift of the LSPR wavelength during the gold nanorod growth process. Furthermore, a clear jump in the wavelength can be seen at the 60 min point of the reaction, which also appears in the *in-situ* SAXS investigations of the AuNR-S7 synthesis. This leads to the assumption, that the growth of nanorods is highly dependent on the Au^{III} / Au^{II} ratio and amount in the growth solution, as the silver concentration does not shift this to earlier or later times during the reaction. In addition, the growth rate of each concentration variation as well as the final LSPR wavelength, and thereby the aspect ratio of the final rod, seem to decrease with increasing silver(I) nitrate concentration in solution. These reaction rates are also in agreement with the previously published investigation, that the seed size at which the symmetry breaking point occurs increases with increasing [HAuCl₄]:[AgNO₃] ratio.^[11] However, the experiment with the lowest concentration does

not follow this trend, which can be the consequence of a too low $[Ag]$ in solution for a controlled, well-defined gold nanorod growth.

Because the SPR wavelength is sensitive to particle shape one cannot determine growth rates or particle sizes from the absorption spectroscopy. The extinction coefficient is dependent on both absolute length and width and endcap geometry.^[20,21] However, Small angle X-ray scattering can be used to obtain both length and width as a function of time, provided the morphology is known (compare Figure 3.2B). In turn, this is dependent on the quality of the fitting function employed.

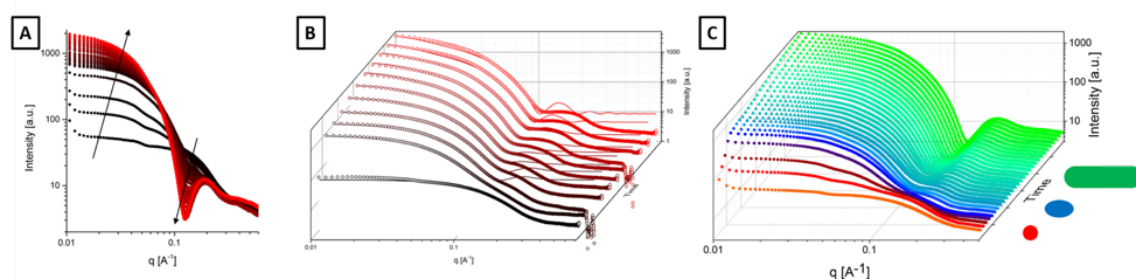


Figure 3.8: Two- (A) and three-dimensional (B) time resolved SAXS Intensity as a function of scattering vector q for sample AuNR-S4. The solid lines in the waterfall plot are fit using a cylindrical form factor. The scattering signal indicates an increasingly defined rod-shaped structure and an increase in volume over time. (C) Waterfall plot showing the shape transition from sphere (red) to ellipsoid (blue) to spherical capped cylinder (green) as a function of the reaction time.

Time resolved SAXS intensity as a function of the scattering vector q is shown in Figure 3.8 in 2 min (left) and 5 min (right) intervals over 120 min (left) and 60 min (right) of reaction time. The intensities increase significantly with reaction time immediately after starting the reaction, indicated by the left black arrow. Furthermore, a dip in the intensity at higher q -values appears after 15 min and becomes more pronounced over time, shown by the right arrow in Figure 3.8A. The corresponding fit using a spherical model in the beginning, evolving through an ellipsoidal shape to a cylindrical model for the final growth of rod-shaped gold particles in length and width is shown in Figure 3.8B respectively. A detailed explanation for the fitting criteria for each shape can be found in Table 3.2 and in the Supporting Information. The SAXS data reveal that there is a well-defined transition from spherical seeds to ellipsoidal geometry and finally to a rod morphology during the reaction. The exact time at which this symmetry breaking occurs depends on the solution conditions. Furthermore, knowing the radius and length as a function of time allows the rate of gold deposition $(d[Au]/dt) = 1/V_m dV/dt$

to be evaluated. However more surprisingly, the SAXS data reveal a second change in growth mechanism about an hour after the reaction commences. At this point, the reaction rate accelerates.

Table 3.2: Evaluated length and width over time from the SAXS fits and the according LSPR from *in-situ* absorption measurements with the respective shape from the fit model (S = sphere, E = ellipsoid, C = spherical capped cylinder) for sample AuNR-S1.

Time [min]	Length [nm]	Width [nm]	AR	LSPR [nm]	S	E	C
2	3.3	3.3	1	n/a	X		
3	5.22	3.6	1.45	n/a		X	
6	7.21	4.36	1.65	n/a		X	
9	7.95	4.7	1.69	n/a		X	
15	8.33	5.44	1.53	n/a		X	
20	8.67	5.9	1.47	728		X	
25	10.3	6.02	1.71	752			X
30	10.7	6.1	1.75	772			X
35	13.5	6.24	2.16	795			X
39	18.3	6.28	2.91	816			X
45	24.8	6.32	3.92	857			X
49	30.2	6.36	4.74	876			X
51	35.6	6.38	5.58	881			X
60	39.6	6.5	6.09	903			X
61	39.8	6.5	6.12	906			X
65	41.2	6.5	6.34	913			X
71	41.2	6.5	6.34	918			X
76	42.5	6.52	6.52	917			X
81	43.2	6.64	6.51	914			X
86	43.3	6.8	6.57	909			X
91	44.7	6.8	6.57	904			X
100	45.2	6.84	6.61	896			X

The evolution of the particle size in length and width with time is shown in Figure 3.9A. The increase in length (black squares) as well as the increase in width (red circles) show a novel double sigmoidal trend over time, which is a common growth phenomena in nature.^[22] In addition, the start point of the second sigmoidal growth curve is at the same time, around 60 minutes for this sample, for both dimensions. This type of growth could be seen in previously published *in-situ* X-ray investigations on L-ascorbic acid-based gold nanorod synthesis^[17], however until now it was never attributed to an actual growth mechanism effect, due to the very fast growth kinetics of these kind of reactions.

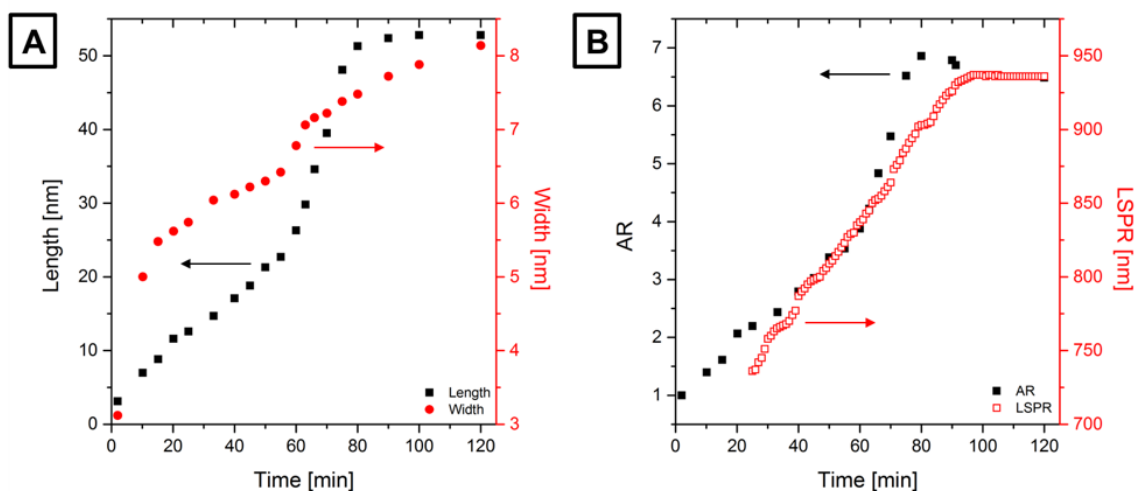


Figure 3.9: (A) Time evolution of the size parameters, length (black squares) and width (red circles), of the gold nanorods during the reaction obtained from the best fits. (B) Time evolution of the aspect ratio AR (solid black squares), calculated from length divided by width, in comparison to the appearance and shift of the absorption maximum of the longitudinal surface plasmon resonance (LSPR) peak (open red squares).

The aspect ratio AR can be calculated by $AR = L/D$, where L is the length of the growing nanorod and D the width, experimentally determined from the fit of the X-ray scattering curves. Hence, the development of the AR against time can be detected, which is displayed in Figure 3.9B (black solid squares). Again, the double sigmoidal growth could be seen as the particle increased in size over time. From the collected optical properties, shown in Figure 3.5 and 3.6, the LSPR can be traced at every absorption spectra according to the point of time during the reaction. Thus, these maxima can then be mapped as a function of time, shown in Figure 3.9B, open red squares. Comparing the experimental data for aspect ratio with the LSPR development, a good agreement between results from SAXS and optical data can be found.

The *in-situ* investigation of length (black squares) and width (red circles) growth is shown in Figure 3.10, and the calculated AR as a function of time is shown in Figure 3.12. Detailed information about the SAXS data and their fit with different model shapes (sphere, ellipsoid, cylinder) can be found in the Supporting Information. The above mentioned, novel double sigmoidal growth of gold nanorods from spherical seeds can be seen for all of the displayed syntheses. Furthermore, the same trend of reaction kinetics as already observed in the absorption spectra can be followed by X-ray scattering. A significant decrease in the reaction time can be seen, until the rods are almost completely evolved and the time-resolved curves for length and width growth reach a

plateau. Only small growth in both directions is happening after this point.

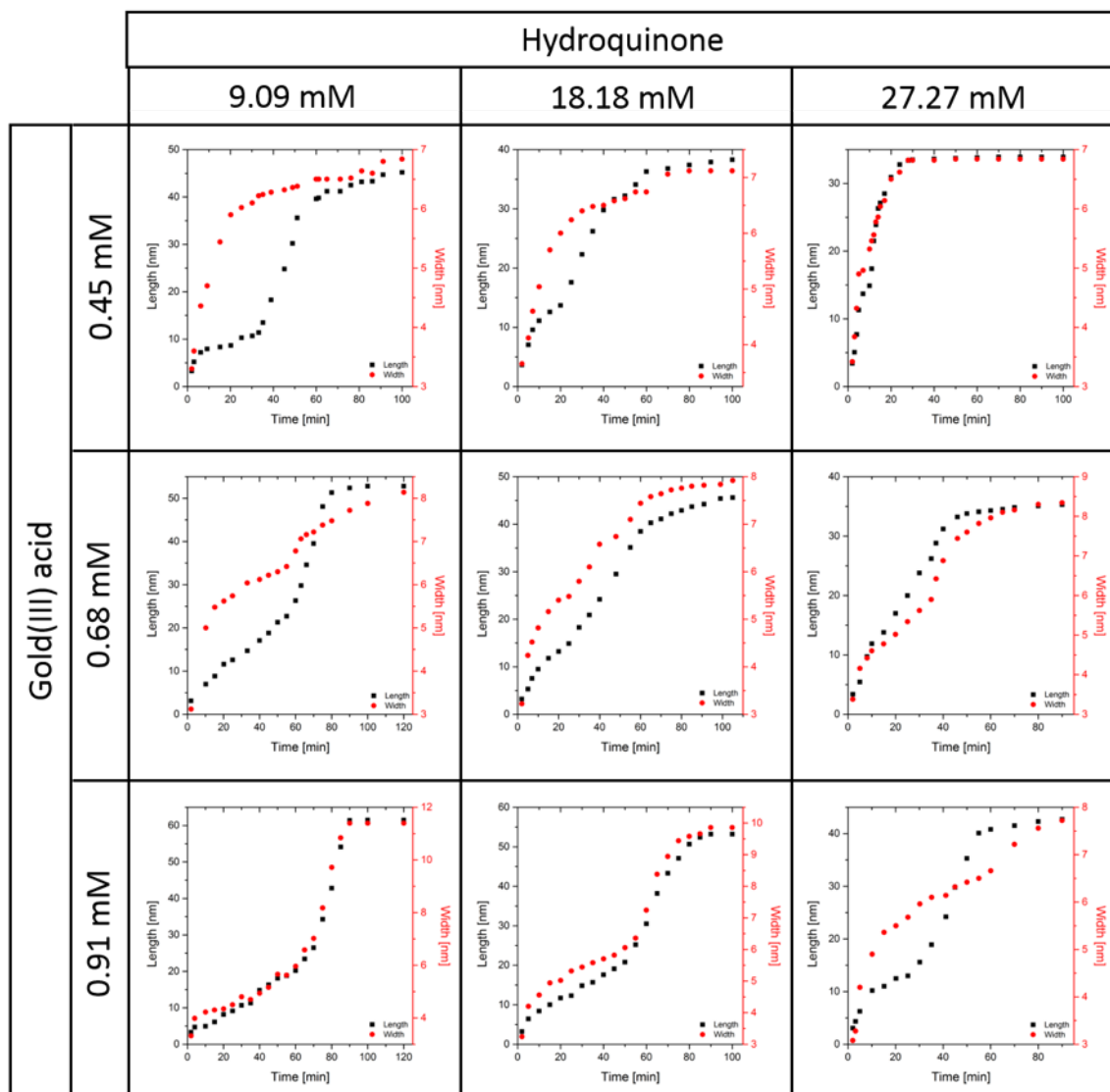


Figure 3.10: Time evolution of the size parameters, length (black squares) and width (red circles), of the gold nanorods during the reaction obtained from the best fits.

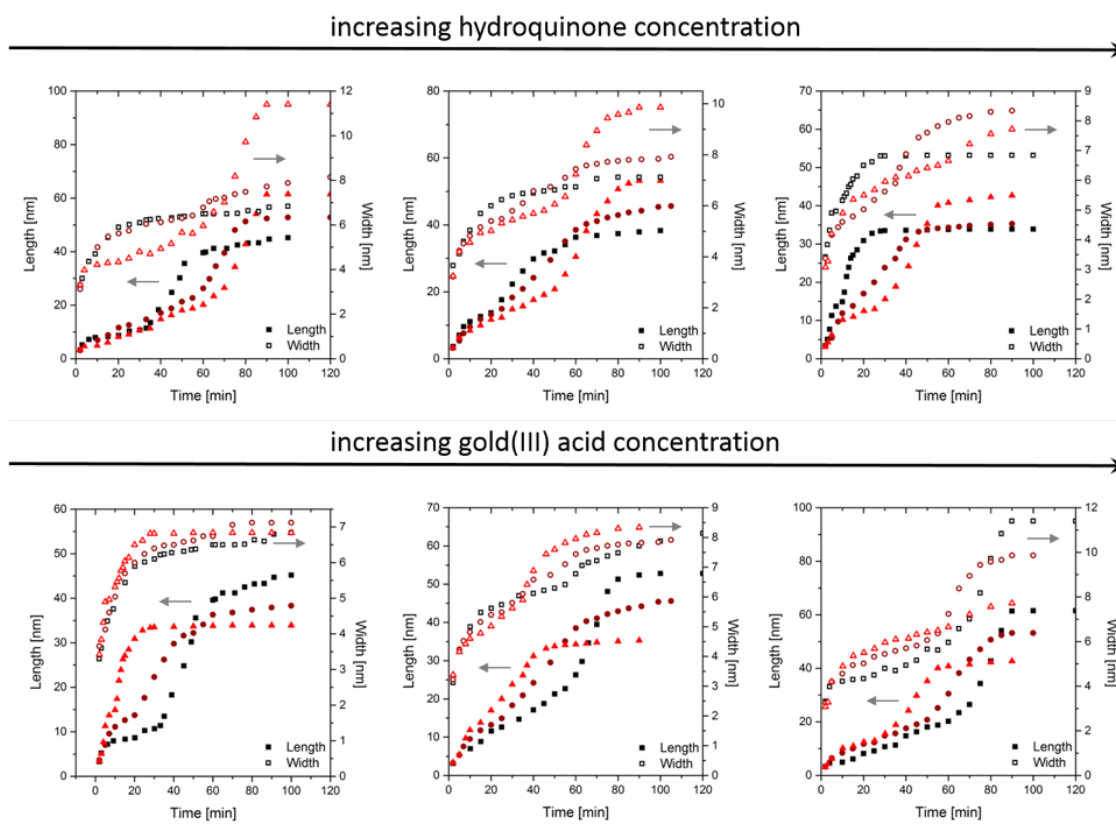


Figure 3.11: Length (solid symbols) and width (open symbols) as a function of time during the nanorod growth synthesis. Top row shows the influence on reaction rate for increasing hydroquinone concentration for three different gold(III) acid concentration from 0.45 mM (black squares) to 0.91 mM (red triangles). Bottom row displays an increase in gold acid for three different [HQ] each, also from 9.09 mM (black squares) to 27.27 mM (red triangles). The double sigmoidal growth can be seen in all experiments, however the reaction rate decreases with increasing gold acid and increases with increasing hydroquinone concentration.

All calculated growth data for length or width showed the same clear trend, starting the second sigmoidal growth at nearly the same values. This could be explained as a form of critical size effect. Apparently, the gold ellipsoid, grown from the spherical seed, needs to reach a certain size in length and width before the second faster growth to the final spherical capped cylinder shape occurs. This size is between 10 nm and 15 nm in length and around 6 nm in width.

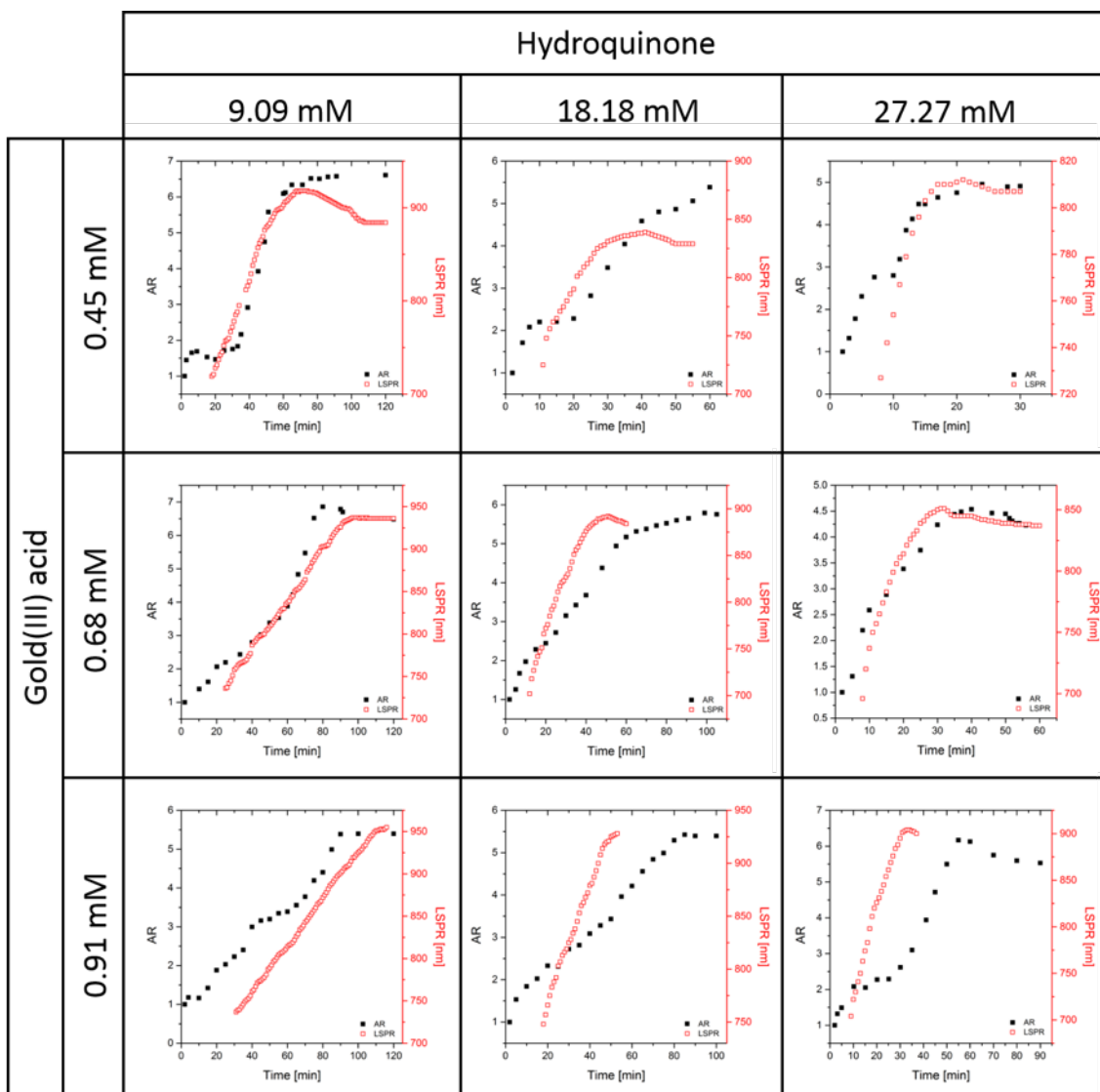


Figure 3.12: Time evolution of the aspect ratio AR (solid black squares), calculated from length divided by width, in comparison to the appearance and shift of the absorption maximum of the longitudinal surface plasmon resonance (LSPR) peak (open red squares).

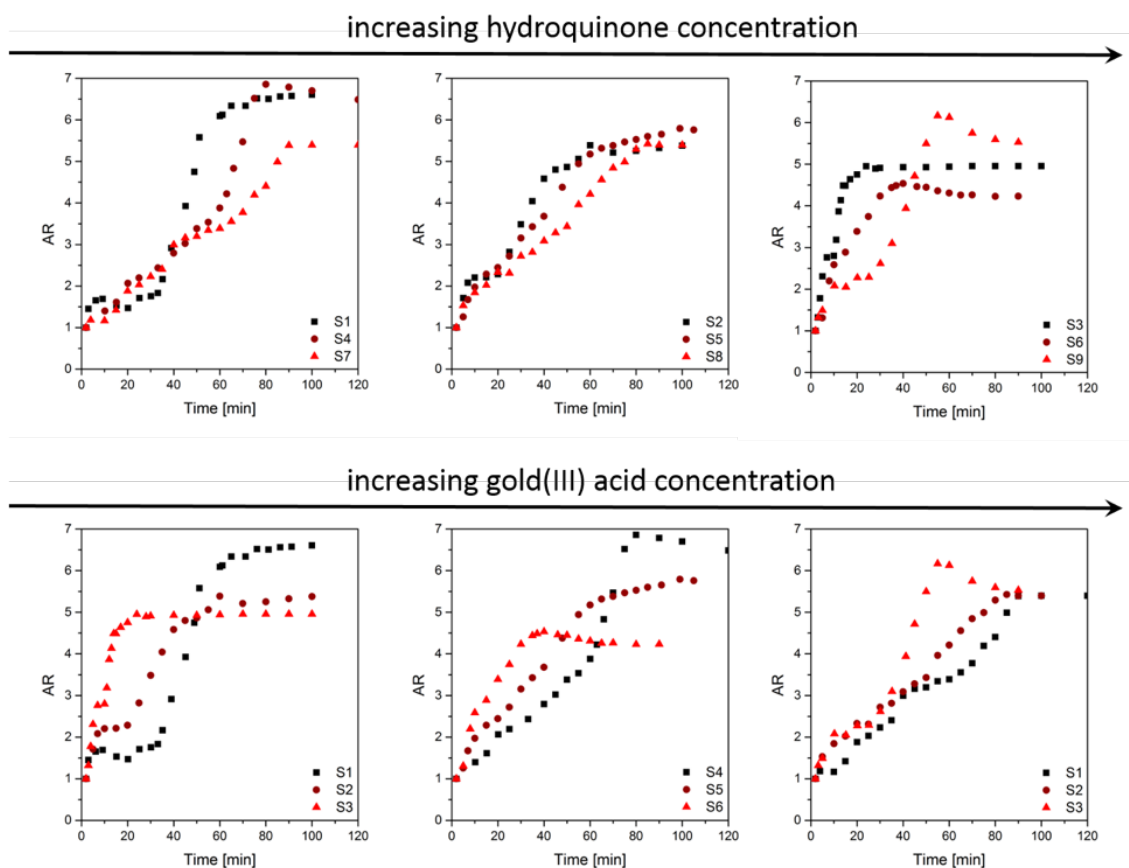


Figure 3.13: Aspect ratio, calculated from length and width for each sample according to Figure 12, for all syntheses in comparison as a function of time. The top row shows analogue to Figure 12 the influence of increasing [HQ] on the reaction rate, the bottom row the increase of [HAuCl₄].

The aspect ratio shows the same double sigmoidal growth for the growth kinetics over time as already seen for length, width and LSPR. Furthermore, a clear increase in the growth rate with increasing [HAuCl₄] and decreasing [HQ] can be seen for all synthesis in Figure 3.13. The simulated LSPR from the length and width / aspect ratio from the SAXS data shows quite a different temporal evolution than the optical data measured during the experiments. This however can be explained with the strong dependency of the LSPR position from the aspect ratio of the particle, which has a certain standard deviation, resulting from standard deviations of length and width in the SAXS fitting. In this standard deviation, the aspect ratio can range at a factor of ± 1 , leading to a significant shift of the corresponding LSPR. Within this dispersity, the optical data and the simulations agree nicely.

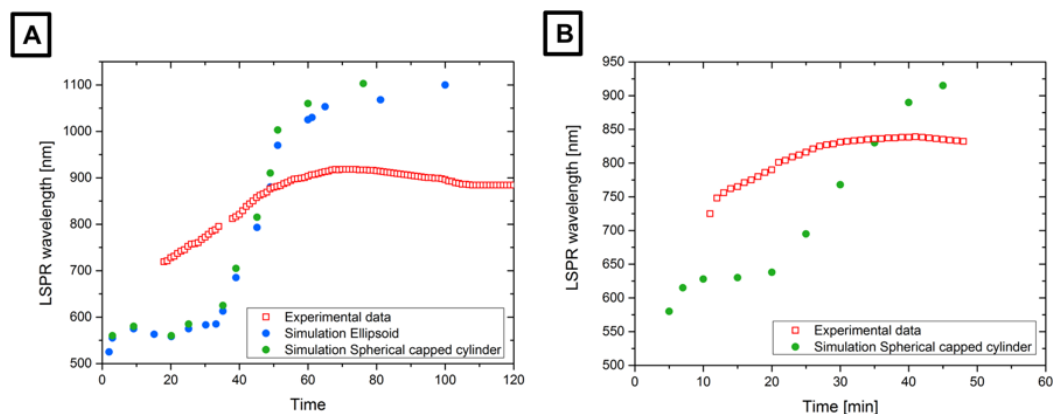


Figure 3.14: Comparison of the experimentally measured LSPR evolution over time with COMSOL simulated LSPR from length and width from the SAXS experiments. Simulations were performed for ellipsoids as well as spherical capped cylinders for synthesis AuNR-S1 (A) and AuNR-S2 (B).

Detailed information about the COMSOL Simulations including the used model and description of the procedure are shown in the Supporting Information.

The fitting model for the small angle X-ray scattering curves showed good results for spheres, ellipsoids and cylinders, although it had to be adjusted slightly to fit the obtained data. This is attributed to the presence of the compact CTAB bilayer present around the gold rods. When the scattering from this layer is included, the thickness of the CTAB layer can be used as a fitting parameter. Hence the CTAB layer can be investigated at each point in time and the fits are shown for all measured syntheses in Figure 3.15. Regardless of synthetic conditions, all rods can be fit assuming the CTAB layer is 3.14 ± 0.1 nm thick.

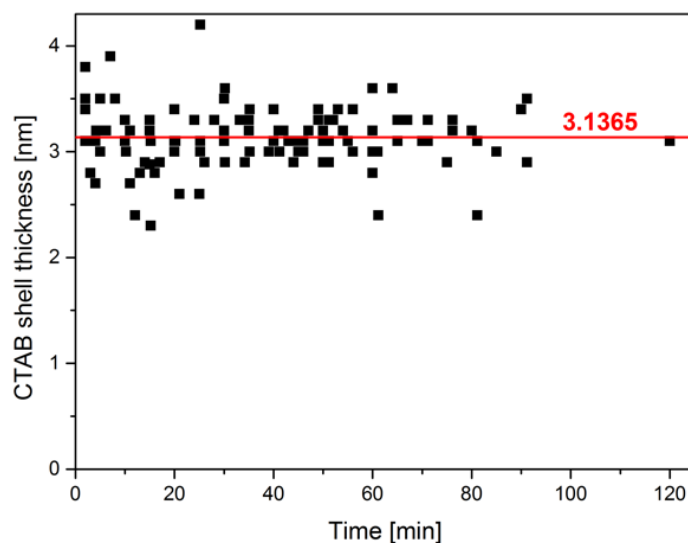


Figure 3.15: CTAB layer thickness from SAXS core-shell fit for different shapes for all investigated syntheses over time, and a linear fit giving an average thickness of 3.1365 nm.

The different CTAB shells, calculated from the SAXS fit with the adjusted core-shell model, show a wide spread in thickness between 2.3 nm and 4.2 nm. This is especially noticeable in the beginning of the synthesis, when the changeover in symmetry from sphere to ellipsoid over to cylinder occurs. However, later in the reaction, the distribution of the CTAB layer thickness gets more narrow. Averaging these values, a mean CTAB shell thickness of 3.1365 nm was found. This is in good agreement with the published work from Spalla et al.^[23], who found an average CTAB shell of 3.2 nm around the standard synthesised gold nanorods, using small angle X-ray scattering in combination with small angle neutron scattering for their investigations of the core-shell behaviour.

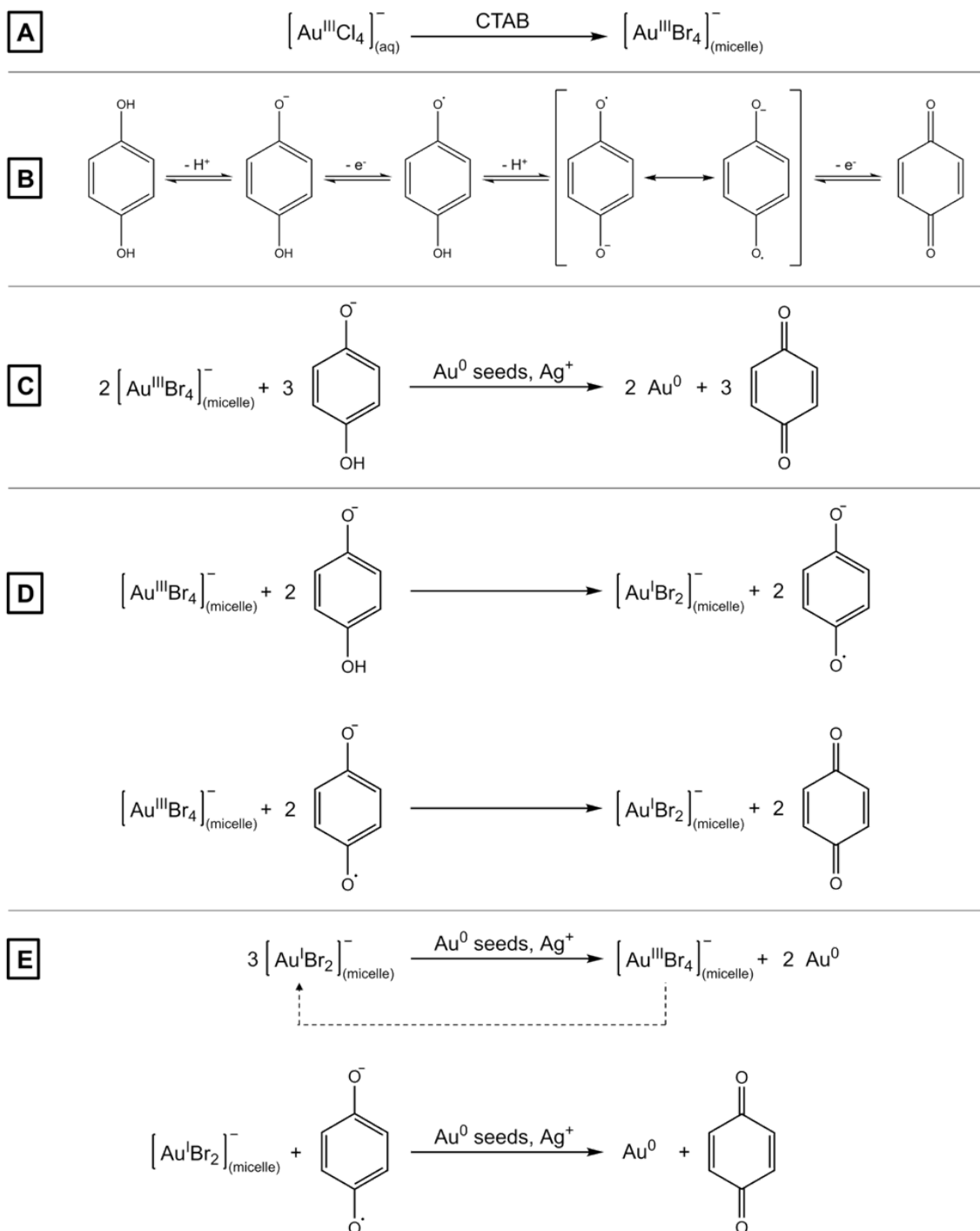
Reaction mechanism

From the SAXS and UV-Vis measurements shown in Figure 3.10 and 3.12, a first impression about the growth kinetics of the hydroquinone based gold nanorod synthesis can be gained. In particular, the variation of synthesis parameters on the reaction time and size of the resulting nanorods could be investigated. However, a surprising double sigmoidal growth behaviour was observed for the first time. To explain this behaviour, a closer look to the actual growth mechanism and the role of each reactant must be taken.

The assumed redox mechanism for the reaction of gold and hydroquinone for each

step is shown in Scheme 3.1. The reaction in Scheme 3.1A shows the formation of $[\text{AuBr}_4]^-$ micelles by adding CTAB to the aqueous $[\text{AuCl}_4]^-$ solution, replacing the chloride ion with bromide as a counter ion.^[24] The two-electron oxidation of hydroquinone is displayed in detail in Scheme 3.1B. Dissolving the hydroquinone in water leads to the negatively charged phenoxide ion, which can be oxidated to the phenoxy radical. This leads to the dominant secondary reducing species in solution, the semiquinone radical anion, which is the strongest reductant in this synthesis. Finally, the second one-electron oxidation leads to the p-benzoquinone form. The net redox reaction for the reduction of Au^{III} to Au^0 in this hydroquinone based gold nanorod synthesis is displayed in Scheme 3.1C. Analogous to the reaction using L-ascorbic acid as a reducing agent^[13], the reduction of Au^{III} using hydroquinone occurs in two steps. Firstly, gold(III) is reduced to gold(I) by the addition of hydroquinone to the growth solution, containing CTAB, gold acid and silver nitrate, shown in Scheme 3.1D. Because the phenoxide ion is the limiting reagent, the semiquinone radical anion produced by reducing Au^{III} to Au^I participates in the reduction of gold as well. This is shown in the second reaction of Scheme 3.1D, forming p-benzoquinone during reaction with the gold(III) bromide micelles. Secondly, the reduction from Au^I to Au^0 takes place by adding the seeds, due to the phenoxide ion being unable to reduce gold(I) in the absence of gold nuclei.^[25] This reaction is displayed in the two mechanisms in Scheme 3.1E, which form a spherical capped gold cylinder in the end, due to the presence of silver ions.^[11,12] The first mechanism is the direct disproportionation of Au^I to Au^0 , with gold(I) being regenerated via Scheme 3.1D. The second reaction is the direct reduction of Au^I by the radical anionic form of hydroquinone leading to the formation of more p-benzoquinone. The production of metallic gold as a function of time shows a sigmoidal shape due to an autocatalytic reaction.^[13,24] However, the double sigmoidal shape of the growth kinetics during the nanorod synthesis cannot be fully explained by this mechanism, as it is not possible to separate the disproportionation reaction and the electrochemical reduction of Au^I to Au^0 .

Scheme 3.1: Reaction mechanisms involved in the reduction of Au^{III} to Au^0 during the gold nanorod growth in the synthesis.



To support the stated mechanism in Scheme 3.1, cyclic voltammetry (CV) measurements were performed during the synthesis. These are shown for various synthesis parameter as well as in comparison with Figure 3.16. For a better understanding and verification of the apparent peaks, reference CV measurements of each reactant and

their combinations with surfactants and reduction by hydroquinone were taken and are shown in the Supporting Information.

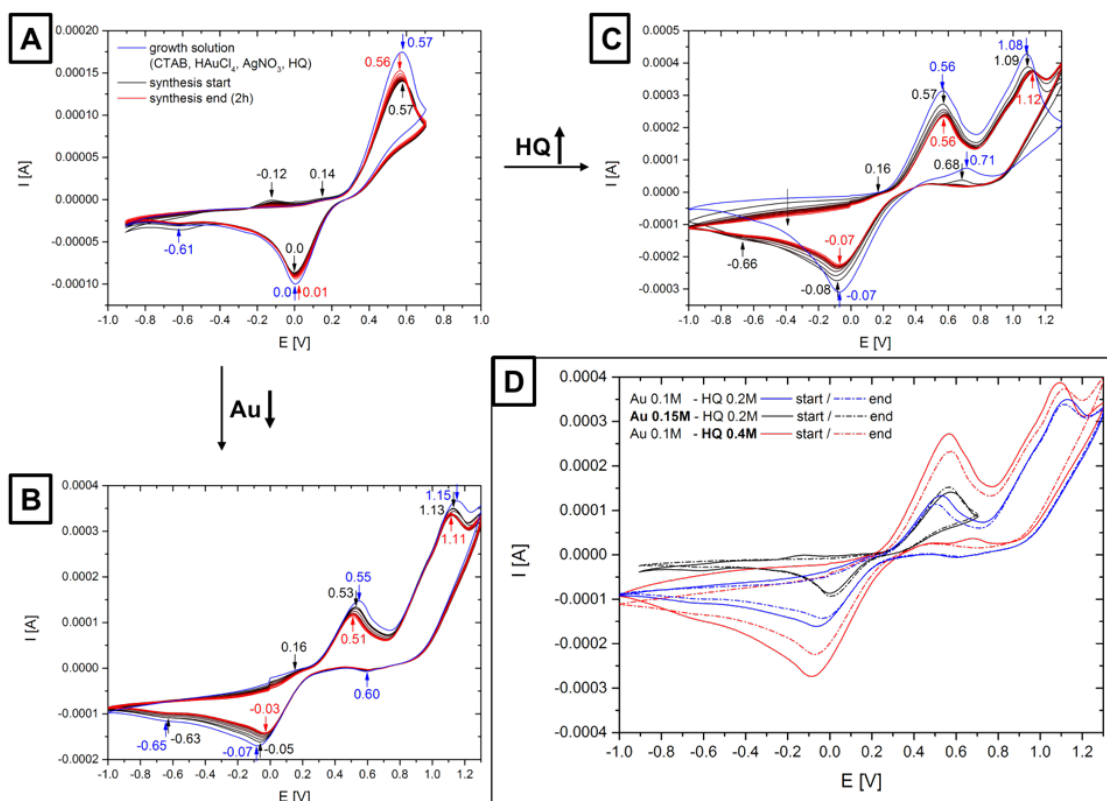


Figure 3.16: Cyclic Voltammetry (CV) curves of different syntheses and their comparison (D) while varying synthesis parameter. The blue curves in (A) to (C) shows the growth solution before addition of seeds. (A) CV curve during 130 minutes of AuNR-S4 synthesis. (B) CV curve during 120 minutes of AuNR-S1 synthesis. (C) CV curve during 90 minutes of AuNR-S5 synthesis.

The first step is the identification of the reactions behind the different oxidation and reduction peaks, using the reference spectra available in the Supporting Information. Equation 3.1 and 3.2, basic relations for potential and current^[26] versus concentration, assist with evaluations about the change of those values during the synthesis. The potential energy is described by the Nernst equation for a reversible system:

$$E = E^0 + \frac{0.059}{n} \log \frac{[Ox]}{[Red]} \quad (3.1)$$

where E^0 is the formal reduction potential of the couple, n the number of electrons transferred in the electrode reaction and the ratio of chemical activities of the oxidised form $[Ox]$ and reduced form $[Red]$. However, E^0 and n are given values for each system, which leads to a direct proportionality of the potential E and the rate of

the oxidised and reduced forms of the reversible couple $E \propto \log \frac{[Ox]}{[Red]}$.

The peak current for a reversible system can be understood by the Randles-Sevcik equation for the forward sweep

$$i_p = (2.69 \cdot 10^5) \cdot n^{\frac{2}{3}} \cdot A \cdot D^{\frac{1}{2}} \cdot C \cdot \nu^{\frac{1}{2}} \quad (3.2)$$

where i_p is the peak current in [A], n the electron stoichiometry, A the electrode area in [cm^2], D the diffusion coefficient in [cm^2/s], C the concentration in [mol/cm^3] and ν is the scan rate in [V/s]. As the electron stoichiometry n , the electrode area A and the diffusion coefficient D are constant and the scan rate ν is set in the experimental conditions, the peak current is directly proportional to the concentration C of the regarded species $i_p \propto C$.

The cyclic voltammograms for the different synthesis in Figure 3.11A-C show three main peaks on the oxidation side (positive current direction) and three peaks on the reduction side (negative current direction). By comparing the synthesis measurements with the references, shown in the Supporting Information, it can clearly be seen that the oxidation peak at 0.56 V is mainly caused by the oxidation of hydroquinone to p-benzoquinone but could involve more than one reaction. Due to the higher amount of hydroquinone present under synthesis conditions, the oxidation peaks of Au^I to Au^{III} and Au^0 to Au^I , if present, are obscured by the HQ oxidation. The corresponding reduction peak of p-benzoquinone to hydroquinone can be found at 0.0 V to -0.07 V. Both reduction and oxidation is slightly displaced comparing the standard values against electrolyte solution, due to the presence of the gold bromide micelles with CTA^+ as surfactant. During the synthesis of gold nanorods, both peaks shift closer to 0 V, which indicates, using equation 3.1 and the linear correlation between potential and chemical activity, a predominating reaction equilibrium on the oxidised form p-benzoquinone. Hence, hydroquinone is getting more and more consumed during the reaction referring to an ongoing reduction of gold ions, producing an excess of p-benzoquinone. The shift in current however shows that this reaction is getting less likely over time, due to the lower amount of hydroquinone as reducing agent in the synthesis solution.

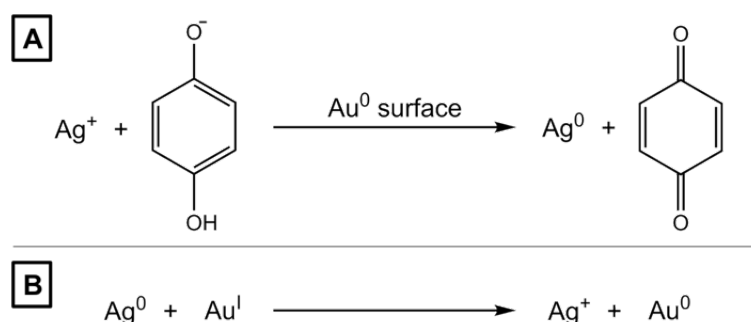
The oxidation peak at 1.1 V – 1.15 V must come from a reaction involving the bromide counter ion, as it can only be seen in measurements with CTAB as surfactant or KBr as electrolyte solution. The actual peak in the synthesis measurement can be a combination of the oxidation of bromide Br^- , present as counter ion, to bromine gas Br_2

and the generation of gold bromide micelles, which indicates the disproportionation reaction from gold(I) to gold(III) and gold(0), shown in Scheme 3.1E.

The main reaction during the growth of gold nanorods is the reduction of gold. After the addition of HQ, only Au^I should be found in the solution in form of [Au^IBr₂]⁻ micelles, which is reduced to Au⁰ to grow on the gold surface of the seeds to rod-shaped nanocrystals. In CV measurements, the reduction peak of this reaction appears at -0.65 V, shown in the reference spectra in Figure A.9 for the gold seed solution and the growth solution. This characteristic peak can also be found in the measured CV curves during the nanorod syntheses. Furthermore, it disappears over the course of the nanorod growth, indicated by a drop of the current, which points out the uptake of mainly gold(I) in the reaction. This development also leads to the conclusion that the reaction is getting more unlikely over time, which agrees with the lower amount of free gold ions in solution to deposit on the gold surface. However, the exact status Au^{III} or Au^I can't be differentiated, which becomes apparent in Figure A.9.

Finally, the oxidation peak at 0.16 V and the reduction peak at 0.60 V can be attributed to the Ag⁺ from dissolved silver nitrate in solution. However, an effect in combination with chloride from the dissolved gold acid is visible, as the oxidation peak is only detected in the reference spectra with CTAC providing Cl⁻ as counter ion in the solution, shown in Figure A.7. The reduction peak on the other side can be seen slightly shifted for both surfactant systems, CTAB and CTAC. In general, a strong reaction of silver nitrate with hydroquinone in either CTAB or CTAC solution can be seen in Figure A.7, which would lead to the assumption that a reduction of Ag⁺ to Ag⁰ takes place in the gold nanorod synthesis solution and silver nanoparticles are produced as a side product during the rod growth. However, no Ag⁰ particles can be detected at any time during the synthesis or in the final solution. The CV measurements of the different gold nanorod syntheses in Figure 3.16 show a slight decrease of both the oxidation peak (0.16 V) and reduction peak (0.60 V) in the beginning of the reaction to a certain value, at which both stay until the end of the rod growth. This suggested mechanism of this reaction between the silver and hydroquinone present in solution is shown in Scheme 3.2.

Scheme 3.2: Reaction mechanism involving the reduction of Ag^I to Ag^0 on the gold surface to induce the symmetry break and gold nanorod growth by reducing Au^I to Au^0 .



The mechanism in Scheme 3.2A shows the reduction of Ag^+ to Ag^0 by hydroquinone on the gold surface. Firstly, the formed Ag^0 passivates the pre-existing $\{111\}$ and $\{001\}$ facets and leads to the formation of a new $\{011\}$ type surface by underpotential deposition (UPD).^[12] Thus, Ag^0 deposits on the $\{011\}$ facet, as it is reduced by HQ, which then is replaced by Au^0 , whilst Ag^0 is getting oxidised back to Ag^+ and redissolved in solution. The corresponding mechanism is displayed in Scheme 3.2B.

Growth kinetics

The actual double sigmoidal growth process of nanoparticles can be described in detail by looking at the reaction rates of the single facet growth from the cuboctahedral particle to the final nanorod. The CTAB stabilised seed synthesis leads to around 4 nm sized single-crystalline gold particles with cuboctahedral shape. Thereby the size at which an anisotropic growth along one facet can occur is limited to a certain seed size and the absolute final size of the nanorod is defined by the $[\text{HAuCl}_4]:[\text{AgNO}_3]$ ratio in the growth solution.^[11] Hence, the seed quality is a crucial factor to make a first growth of the $\{111\}$ facet of the cuboctahedral particle by gold atom deposition possible. This growth can be seen in the first sigmoidal growth step with a fast reaction rate in the temporal evolution of particle size. It also leads to the appearance as an ellipsoidal shape of the particle, as the $\{111\}$ facet is than the other directions.

The growth of the $\{111\}$ facet however changes the free energy of adsorption at each facet. Due to the effect of atomic bonding at corner, edge and central face atomic sites and Ag UDP, the $\{011\}$ growth, however with a much slower reaction rate, leading to a more spherical capped cylindrical shape and the plateau region after the first double sigmoidal growth rate in the particle size evolution. These two growth processes occur in dependency of the Au^{III} ratio in the growth solution, as a high amount of Au^{III}

favours $\{111\}$ and $\{011\}$ facets to grow.^[12]

Once the Au^{III} ratio in the synthesis solution drops to a certain level, the $\{011\}$ becomes more favourable for growth. As the reaction rate of this facet is much greater than the $\{010\}$ and $\{100\}$ facets, the rod starts to grow in a so-called “popcorn”-mechanism in $\langle 100 \rangle$ direction.^[24] This can be identified in the temporal size evolution of the particle in form of the second fast double sigmoidal growth during the reaction. The following plateau in these graphs is due to final small changes in mostly the width of the rod, resulting in the high yield of the synthesis.

To prove the dependency of the aspect ratio of the growing gold nanorods from the free gold in solution, the longitudinal and transversal SPR was investigated during gold overgrowth experiments, as shown in Figure 3.17. The detailed experimental and sample details can be found in the SI.

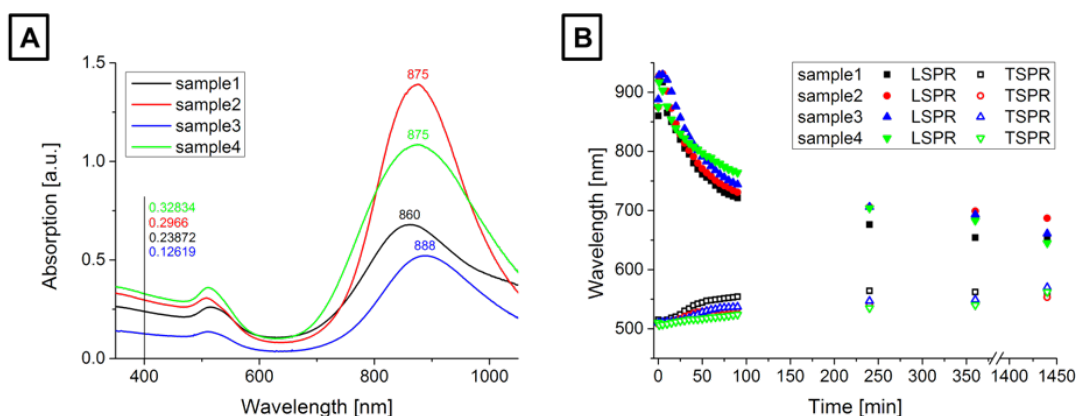


Figure 3.17: (A) Absorption spectra of the gold nanorod samples 1 to 4 used as seeds for the gold overgrowth experiments. The LSPR of all samples is at a similar wavelength although the sizes are different. The concentration of gold in the solution is set to different values to investigate the influence of $\text{Au}^0 / \text{Au}^{III} / \text{Au}^{II}$ ratio in the overgrowth experiment. (B) Temporal evolution of longitudinal and transverse SPR during the overgrowth reaction for all four samples. A clear blueshift of the LSPR and redshift of the TSPR can be seen.

For the gold overgrowth experiment, purified gold nanorods were used as seed solution in the same manner as for the initial gold nanorod growth and added to a growth solution, consisting of CTAB (0.1 M), HAuCl_4 (0.45 mM), AgNO_3 (0.45 mM) and hydroquinone (18.18 mM). The absorption spectra of the samples used as crystalline seed are shown in Figure 3.17A. The LSPR was thereby chosen fairly similar in all samples, although all of them are different in size. Additionally, the gold concentration measured from the absorption at a wavelength of 400 nm was set differently to get a different Au^0 to Au^{III}

/ Au^{II} ratio for all samples. The temporal evolution of TSPR and LSPR was monitored and can be seen in Figure 3.17B. The transverse mode shows a slight redshift over time for all four samples, which mainly can be explained by growth in width of the added nanorods. The longitudinal mode on the other side shows a clear blueshift, coming from the significant change in aspect ratio during the deposition of gold atoms on the nanocrystals. The LSPR redshift in the very early reaction times can be a result of reshaping conditions by adding purified particles in a growth solution with high [Au] and reactive hydroquinone present.

This dependency of the aspect ratio from the free gold in solution leads to the conclusion that the shape of the formed particle depends highly on the amount of Au^{III} / Au^{II} in solution. In the initial gold nanorod synthesis the cuboctahedral particle start to grow as a rod once the Au^{III} decreases. However, if this concentration increased again, the nanocrystal tends to form a different shape by decreasing the aspect ratio, monitored by a significant blueshift of the LSPR in the absorption spectra. This supports the above described growth process of Au^{III} / Au^{II} ratio dependent facet growth from cuboctahedral seed to ellipsoid to spherical capped cylinder.

The double sigmoidal growth of anisotropic forms has been studied in many contexts. The double logistic method thereby showed the best results in case of fitting the measurements, and can be described by the following equation.^[22]

$$y_i = \frac{a_1}{1 + e^{k_1(b_1 - x_i)}} + \frac{a_2 - a_1}{1 + e^{k_2(b_2 - x_i)}} + \epsilon_i \quad (3.3)$$

where y_i is the length / width of the particle in each measurement, x_i the time at each measurement, a_1 the dimension in length / width at the first plateau, a_2 the final dimension in length / width where it reaches the final plateau, k_1 and k_2 are the growth rates for the synthesis, which means the bigger these values are, the faster is the reaction, b_1 and b_2 are the abscissa of the inflection point, which defines the point where the growth rate reaches the maximum, and ϵ_i is a random error associated with the model, assuming it is independently and identically distributed.

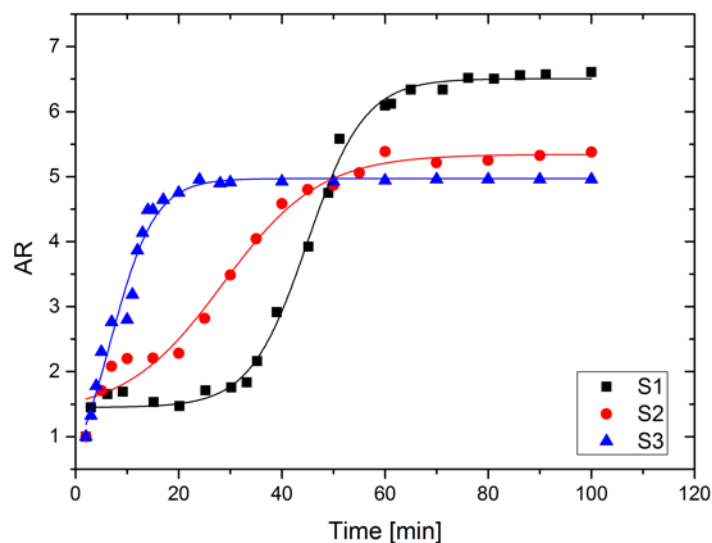


Figure 3.18: Temporal evolution of the aspect ratio for the three synthesis AuNR-S1 (black squares), -S2 (red circles) and -S3 (blue triangles) with double sigmoidal fit after equation 3.3, plotted as lines in the corresponding colours in the graph.

Figure 3.18 shows the double sigmoidal fit after equation 3.3 for the aspect ratios of the three synthesis AuNR-S1, -S2 and -S3 with increasing [HQ] over time. The double sigmoidal fitfunction for all samples can be found in the Supporting Information. From the fitfunction of each synthesis, the growth rates k_1 and k_2 can be determined. These are, together with the according *chi square* and *adj. R square* values listed in Table 3.3. An average growth rate of 0.1 min^{-1} was found for all synthesis. Furthermore, the growth rate for both steps in the double sigmoidal growth is the same.

Table 3.3: Evaluated length and width over time from the SAXS fits and the according LSPR from *in-situ* absorption measurements with the respective shape from the fit model (S = sphere, E = ellipsoid, C = spherical capped cylinder) for sample AuNR-S1.

Sample	k_1 [1/min]	k_2 [1/min]	Chi Sqr.	Adj. R Sqr.
AuNR-S1	0.018014	0.018015	0.03499	0.99324
AuNR-S2	0.10634	0.106511	0.06952	0.97001
AuNR-S3	0.22032	0.23021	0.05544	0.96778
AuNR-S4	0.08597	0.08735	0.22111	0.94517
AuNR-S5	0.05145	0.05146	0.02759	0.99019
AuNR-S6	0.12244	0.08277	0.04005	0.96799
AuNR-S7	0.02680	0.02635	0.07081	0.96586
AuNR-S8	0.03850	0.03851	0.04087	0.98014
AuNR-S9	0.08072	0.15726	0.07427	0.97881
Average	0.10141	0.10673		

3.5. Conclusion

We have presented a novel mechanism for the reduction and oxidation of gold by hydroquinone in the presence of silver leading to the controlled growth of gold nanorods. For the first time, direct insights in the hydroquinone based synthesis of single-crystalline gold nanorods was possible. Hence, we were able to discover a surprising double sigmoidal growth behaviour, following the extension in length and width *in-situ* by absorption spectroscopy and small angle X-ray scattering. The influence of varying synthesis parameters, such as the initial concentration of gold acid and hydroquinone, on the final size and aspect ratio, as well as the reaction kinetics was studied. Furthermore, a model for the growth kinetics, following the shape transition from spheres over ellipsoids to spherical capped cylinders could be developed. Using a core-shell model for the SAXS data analysis of the growing nanorods, a CTAB shell thickness of 3.16 nm could be confirmed. These types of experiments showed the potential to explain and optimise well-known particle synthesis with multi-component solutions. Future investigations might focus more in detail on the influence of silver nitrate concentration on the growth kinetics and, especially, on the symmetry breaking point.

References

- [1] Kinnear, C.; Moore, T. L.; Rodriguez-Lorenzo, L.; Rothen-Rutishauser, B.; Petri-Fink, A. *Chemical Reviews* **2017**, *117*, 11476–11521.
- [2] Knight, M. W.; Sobhani, H.; Nordlander, P.; Halas, N. J. *Science* **2011**, *332*, 702–704.
- [3] Vigderman, L.; Khanal, B. P.; Zubarev, E. R. *Advanced Materials* **2012**, *24*, 4811–4841.
- [4] Turkevich, J.; Stevenson, G. G. P. C. *Journal of Colloid Science* **1954**, *9*, 26–35.
- [5] Sardar, R.; Funston, A. M.; Mulvaney, P.; Murray, R. W. *Langmuir* **2009**, *25*, 13840–13851.
- [6] Jana, N. R.; Gearheart, L.; Murphy, C. J. *Journal of Physical Chemistry B* **2001**, *105*, 4065–4067.
- [7] Nikoobakht, B.; El-Sayed, M. *Chemistry of Materials* **2003**, *15*, 1957–1962.
- [8] Ye, X.; Jin, L.; Caglayan, H.; Chen, J.; Xing, G.; Zheng, C.; Doan-Nguyen, V.; Kang, Y.; Engheta, N.; Kagan, C. R.; Murray, C. B. *ACS Nano* **2012**, *6*, 2804–2817.
- [9] Vigderman, L.; Zubarev, E. R. *Chemistry of Materials* **2013**, *25*, 1450–1457.
- [10] Tebbe, M.; Kuttner, C.; Mayer, M.; Maennel, M.; Pazos-Perez, N.; Koenig, T. A. F.; Fery, A. *Journal of Physical Chemistry C* **2015**, *119*, 9513–9523.
- [11] Tong, W.; Walsh, M. J.; Mulvaney, P.; Etheridge, J.; Funston, A. M. *Journal of Physical Chemistry C* **2017**, *121*, 3549–3359.
- [12] Walsh, M. J.; Tong, W.; Katz-Boon, H.; Mulvaney, P.; Etheridge, J.; Funston, A. M. *Accounts of Chemical Research* **2017**, *50*, 2925–2935.
- [13] Burrows, N. D.; Harvey, S.; Idesis, F. A.; Murphy, C. J. *Langmuir* **2017**, *33*, 1891–1907.
- [14] Sau, T. K.; Murphy, C. J. *Langmuir* **2004**, *20*, 6414–6420.
- [15] Henkel, A.; Schubert, O.; Plech, A.; Soennichsen, C. *Journal of Physical Chemistry C* **2009**, *113*, 10390–10394.
- [16] Morita, T.; Tanaka, E.; Inagaki, Y.; Hotta, H.; Shingai, R.; Hatakeyama, Y.; Nishikawa, K.; Murai, H.; Nakano, H.; Hino, K. *Journal of Physical Chemistry C* **2010**, *114*, 3804–3810.

References

- [17] Hubert, F.; Testard, F.; Thill, A.; Kong, Q.; Tache, O.; Spalla, O. *Crystal Growth & Design* **2012**, *12*, 1548–1555.
- [18] Plech, A.; Kotaidis, V.; Siems, A.; Sztucki, M. *Physical Chemistry Chemical Physics* **2008**, *10*, 3888–3894.
- [19] Chen, X.; Schroeder, J.; Hauschild, S.; Rosenfeldt, S.; Dulle, M.; Foerster, S. *Langmuir* **2015**, *31*, 11678–11691.
- [20] Link, S.; Mohamed, M. B.; El-Sayed, M. A. *The Journal of Physical Chemistry B* **1999**, *103*, 3073–3077.
- [21] Link, S.; El-Sayed, M. A. *The Journal of Physical Chemistry B* **1999**, *103*, 5410–8426.
- [22] Fernandes, T. J.; Pereira, A. A.; Muniz, J. A. *Ciencia Rural* **2017**, *47*.
- [23] Gomez-Grana, S.; Hubert, F.; Testard, F.; Guerrero-Martinez, A.; Grillo, I.; Liz-Marzan, L.; Spalla, O. *Langmuir* **2012**, *28*, 1453–1459.
- [24] Edgar, J. A.; McDonagh, A. M.; Cortie, M. B. *ACS Nano* **2012**, *6*, 1116–1125.
- [25] Perrault, S. D.; Chan, W. C. W. *Journal of the American Chemical Society* **2009**, *131*, 17042–17043.
- [26] Kissinger, P. T.; Heineman, W. R. *Journal of Chemical Education* **1983**, *60*, 702–706.

Chapter 4

4. Publication II

Parallel and perpendicular alignment of anisotropic particles in free liquid micro-jets and emerging micro-droplets.

Mathias Schlenk,^a Eddie Hofmann,^a Susanne Seibt,^a Sabine Rosenfeldt,^{a,d} Lukas Schrack,^b Markus Drechsler,^{a,d} Andre Rothkirch,^e Wiebke Ohm,^e Josef Breu,^{c,d} Stephan Gekle,^b Stephan Förster^{a,*}

^a*Physical Chemistry I, University of Bayreuth, 95440 Bayreuth, Germany.*

^b*Biofluid Simulation and Modeling, University of Bayreuth, 95440 Bayreuth, Germany.*

^c*Inorganic Chemistry I, University of Bayreuth, 95440 Bayreuth, Germany.*

^d*Bavarian Polymer Institute, University of Bayreuth, 95440 Bayreuth, Germany.*

^e*HASYLAB/DESY, 22607 Hamburg, Germany.*

The results presented in this chapter were published in *Langmuir*, **2018**, *34*, 4843-4851.

Individual contribution of involved authors

I provided parts of the samples and helped with the performed experiments and analysis of the data together with Mathias Schlenk and Eddie Hofmann. I wrote parts of the manuscript, Mathias Schlenk wrote the main part together with Prof. Stephan Förster. Sabine Rosenfeldt, Andre Rothkirch and Wiebke Ohm helped with the SAXS data. Lukas Schrack and Stephan Gekle helped with the simulations and scientific discussions. Markus Drechsler helped with the TEM measurements. Joseph Breu helped with scientific discussions.

4.1. Abstract

Liquid micro-jets play a key role in fiber spinning, inkjet printing and coating processes. In all these applications, the liquid jets carry dispersed particles whose spatial and orientational distributions within the jet critically influence the properties of the fabricated structures. Despite its importance, there is currently no knowledge about the orientational distribution of particles within micro-jets and droplets. Here we demonstrate a microfluidic device that allows to determine the local particle distribution and orientation by X-ray scattering. Using this methodology, we discovered unexpected changes in the particle orientation upon exiting the nozzle to form a free jet, and upon jet break-up into droplets, causing an unusual biaxial particle orientation. We show how flow and aspect ratio determine the flow-orientation of anisotropic particles. Furthermore, we demonstrate that the observed phenomena are a general characteristic of anisotropic particles. Our findings greatly enhance our understanding of particle orientation in free jets and droplets and provide a rationale for controlling particle alignment in liquid jet-based fabrication methodologies.

4.2. Introduction

Advanced materials fabrication technologies such as fiber spinning,^[1,2] inkjet-printing,^[3] liquid-based coatings and microparticle fabrication,^[4-7] as well as vacuum liquid sample delivery for free electron lasers^[8] all involve the intermediate generation of liquid micro-jets. These liquid jets contain dispersed particles and microstructures such as polymers, fibers, pigments, microcrystals or proteins whose spatial and orientational distribution within the jets critically determine the properties of the resulting fibers, coatings, or surface patterns. It is thus essential to determine and control the particle distribution and orientation within liquid micro-jets. However, there is hardly any knowledge about the orientational distribution of particles within free liquid jets because this requires to develop challenging in-situ microstructure analysis methodology that so far has not been available.

Early pioneering experiments used synchrotron X-ray scattering to investigate fiber crystallization during fiber spinning.^[9,10] Although averaging over the whole fiber cross-section, it enabled to follow details of the crystallization process starting from the melt exiting the nozzle downstream to the final solidified fiber. With microfocus X-ray beams at third-generation synchrotrons it has become possible to monitor silk fiber production^[11] and even spray coating processes on micrometer length scales.^[4,12] However, a detailed study of particle orientations within a free microjet including its break-up into

single droplets has so far not been possible.

Here we demonstrate that microfocus X-ray scattering combined with a microfluidic setup that continuously generates stable liquid microjets enables determining the spatial and orientational distribution of anisotropic particles within the jets all the way from inside the nozzle to the free microjet and eventually to the emerging droplets. We investigate wormlike micelles and nanoplatelets as examples of one- and two-dimensional anisotropic particles with large axial ratios, as well as gold nanorods as anisotropic particles with small axial ratios to provide general insights into the flow-induced orientation of anisotropic particles within free microjets and microdroplets. For all anisotropic particles we found characteristic changes in their uni-axial order when exiting the nozzle and within the microjets and, surprisingly, a biaxial orientational order in the droplets emerging from the liquid jet. Furthermore, we show how flow and aspect ratio determine the flow-orientation of anisotropic particles. The obtained results provide a first fundamental understanding of particle alignment in free liquid micro-jets and micro-droplets and have important implications for liquid jet-based fiber, particle and coatings fabrication techniques.

4.3. Experimental Section

Synthesis of layered silicates nanoplatelets

Na_{0.5}-fluorohectorite with a nominal composition of [Na_{0.5}]^{inter}[Mg_{2.5}Li_{0.5}]^{oct}[Si₄]^{tet}O₁₀F₂ (Na_{0.5}-Hec) was synthesized by melt synthesis in a gastight molybdenum crucible according to a procedure described in detail by Breu et al.^[13] The material was annealed for 6 weeks at 1045°C to improve intracrystalline reactivity, charge homogeneity and phase purity as described elsewhere.^[14] Afterwards Na_{0.5}-hectorite in its one water layer hydrated form was generated by storing at 43% relative humidity in a desiccator for at least 3 days.

Synthesis of block copolymer wormlike micelles

Polyisoprene₁₁₀-b-ethylene oxide₁₉₈ (PI₁₁₀-b-PEO₁₉₈) with a weight-averaged molecular weight of $M_w = 16,000$ g/mol is synthesized by sequential living anionic polymerization, yielding an amphiphilic block copolymer with narrow polydispersity ($M_w/M_n = 1.02$). The detailed synthesis and characterization of PI₁₁₀-b-PEO₁₉₈ is described elsewhere.^[15] The dry polymer is dissolved in Millipore-quality water with a resistivity of 17.9 MΩ/cm to a concentration of 20% w/w. By using an UltraTurrax T8 (IKA Werke GmbH) the solution

was homogenized.

Synthesis of gold nanorods single crystals

Monodisperse gold nanorods were synthesized following a seeded growth method. For producing cetyltrimethylammonium bromide-capped (CTAB-capped) Au seeds an equal amount of chloroauric acid (HAuCl_4 , 0.5×10^{-3} M) and aqueous CTAB-solution (0.2×10^{-3} M) were mixed and stirred for 10 min at room temperature. Next, a freshly prepared sodium borohydride solution (NaBH_4 , $600 \mu\text{L}$, 0.01×10^{-3} M) was added quickly under vigorous stirring. After 2 min, the stirring was stopped and the seeds were aged 1 h at room temperature. To finally produce the single crystal gold nanorods (AuNRs), an aqueous CTAB-solution (10 mL, 0.1×10^{-3} M) was mixed with HAuCl_4 -solution ($50 \mu\text{L}$, 0.25×10^{-3} M) and silver nitrate (AgNO_3 , 0.1×10^{-3} M) solution until all components are homogeneously dissolved. To reduce the gold acid, hydroquinone was added and the growth solution gently mixed until complete decoloration. Finally, the aged CTAB-capped Au seeds ($400 \mu\text{L}$) was added and mixed thoroughly. The Au nanorods were grown for 24 h at room temperature. The solution was purified by centrifugation (10 min, 14000 rcf) before washing with water two times and redispersed in water (2 mL) to obtain a solution at a concentration of 4.0 mM Au, which for the nanorods corresponds to $\sim 10^{12}$ nanorods/ml.

Sample preparation

The sodium hectorite solution with a concentration of 3% w/w was prepared in a closed vessel by addition of deionized water with Millipore-quality to solid $\text{Na}_{0.5}$ -hectorite for osmotic swelling, and afterwards stored at ambient temperature. The 20% w/w stock solution of wormlike micelles was dissolved down to 10% w/w and filtered through a polytetrafluorethylene filter with pore size of $5 \mu\text{m}$ before the microfluidic experiments could be carried out. Cryo-transmission electron microscopy (cryo-TEM) and transmission electron microscopy (TEM) images of the used concentrations of each sample are shown in electronic supplementary information (ESI Fig. B.3).

Free liquid microjet

The free liquid microjet was generated using a micro glass capillary with an inner diameter of $D = 600 \mu\text{m}$ (wall thickness $50 \mu\text{m}$) fixed in a home-built 3D-printed sample holder. By using a micro gear pump (mzr-7205G) a microfluidic recycling setup was constructed to continuously deliver liquid at high flow rates to generate the microjet.

The whole setup is displayed in detail in electronic supplementary information (ESI Fig. B.1).

Small-angle X-ray scattering

The microfocus small-angle X-ray scattering (SAXS) experiments were performed at the synchrotron beamline P03 at PETRAIII/DESY.^[16] After collecting necessary background data of the pure solvent jet at different positions along the microjet (electronic supplementary information, ESI Fig. B.8), the actual experiments with different type of anisotropic particles were carried out. Measurements across and along the glass capillary as well as the free jet and the droplet area are performed with a microfocused X-ray beam at wavelength of $\lambda = 0.1381$ nm. The beam size was $20 \times 20 \mu\text{m}^2$ for fluorohectorite nanoplatelets as well as wormlike micelles and $105 \times 63 \mu\text{m}^2$ for the gold nanorods. The X-ray scattering patterns were recorded with step sizes of $25 \mu\text{m}$, respectively $100 \mu\text{m}$ behind the microjet using a Pilatus 300K, respectively 1M (Dectris Ltd.) whereby both detectors have a pixel size of $172 \times 172 \mu\text{m}^2$. The sample-detector distance was 5.1 m for the sodium hectorite nanoplatelets with an integration time of 10 s. The wormlike micelles were measured with the same detector distance but with an integration time of 20 s. The detector distance for the gold nanorods was shorter with 2.4 m and the integration time was 60 s.

Microparticle image velocimetry

Micro particle image velocimetry (μPIV) was performed with a high-speed camera, a highly intense, focused light source and the open-source software package JPIV for flow profile analysis.^[17] In combination with a long-distance microscope and a 10x magnification objective the setup allows exposure down to $1.5 \mu\text{s}$ and frame rates up to $210,000 \text{ s}^{-1}$ for the microfluidic experiments. These experiments allowed to determine the flow velocity profile within the glass capillary and free jet as well as the droplet area to observe changes between these different microjet regions. For more details, we refer to the electronic supplementary information.

Lattice-Boltzmann simulations for platelet reorientation during jet ejection

We conducted three-dimensional lattice-Boltzmann simulations using the open source software package ESPResSo.^[18-21] The grid size was $24 \times 24 \times 210$ with a capillary/jet radius of 10 grid cells. Here, we were interested in modeling the re-orientation of platelets right after the exit of the capillary where the jet shape is to a very good approximation cylindrical with the same radius as the capillary. We therefore considered in our

simulations a long undeformable cylinder whose left half models the capillary (no-slip boundary conditions are applied at the cylinder wall) while the right half models the free jet by imposing free-slip boundary conditions, see Fig. 4.2a. Thermal fluctuations were included into the Lattice-Boltzmann fluid.

Platelets were modeled by a grid of five vertices, each of which was frictionally coupled to the fluid.^[22] The shape of the platelets was fixed by stiff springs to enforce (almost) constant vertex distances and angles to maintain a flat shape. In order to avoid artifacts from periodic boundary conditions, platelets were fed into the channel on the left and removed on the right end. Here, the platelet configuration at the inlet was not purely random. Instead, before the actual microjet simulation was run, we first conducted a simulation in a fully no-slip channel at the same flow rate and platelet concentration, but with periodic boundary conditions. Platelets taken from this „feeding simulation“ firstly received the orientation parameter S They were then properly aligned and obeyed the correct radial distribution when they were fed into the microjet simulation. This platelet orientation was then quantified by the orientation parameter

$$S = \left\langle \frac{3 \cos^2 \varphi - 1}{2} \right\rangle \quad (4.1)$$

where φ is the angle between the normal vector of the platelet surface and the flow direction. In this definition, $S = 1$ signals complete alignment in flow direction, $S = 0$ corresponds to random isotropic orientation, and $S = -0.5$ to complete alignment perpendicular to the flow direction. The calculated orientation parameters S of the ensuing microjet simulations are shown in the electronic supplementary information (ESI Fig. B.9-B.11) for all three particle systems.

Potential-flow boundary-integral simulations

In order to predict the shape evolution and flow field within the microjet, we required a method which is able to track the time-dependent free surface shape of the jet. We thus conducted boundary-integral simulations (Fig 4.2) based on potential flow assuming a purely inviscid fluid. Details are given in literature.^[22-26] The goal of these simulations was to obtain an understanding of the flow field in the jet at droplet breakup which is why the presence of the anisotropic particles was excluded.

4.4. Results and Discussion

In order to continuously produce stable liquid micro-jets that can be investigated by microfocus synchrotron X-ray scattering we developed a setup consisting of a glass

capillary to generate the micro-jets and a micro-gear pump to recycle the liquid back to the glass capillary. We used vertically aligned capillaries with 300 μm inner radius and 300 μm orifice radius to generate liquid jets at a flow rate of $Q = 750 \text{ mL/h}$, resulting in a jet velocity of $\nu \sim 1 \text{ m/s}$. The micro-jet is stable over a length of 15 mm, until it breaks up into micro-droplets due to Rayleigh instability. The local orientational distribution of the dispersed particles within the micro-jet and the micro-droplets is determined by scanning with a $20 \times 20 \mu\text{m}$ X-ray beam across a raster of 7-20 horizontal and 5 vertical positions from the capillary downstream the nozzle, free jet and the droplets.

Nanoplatelets

We first investigated solutions of hectorite nanoplatelets as models of two-dimensional anisotropic particles at a concentration of 3 wt%, which is sufficiently high to have a good signal-to-noise ratio, but still having low enough viscosity to continuously pump the solutions through the microfluidic device. The hectorite platelets are fully exfoliated, have a thickness of 1.0 nm and a lateral dimension of 20 μm , and thus have very large axial ratios of $2 \cdot 10^4$.^[27-29] Details of the synthesis, structure, and sample preparation are provided in the electronic supplementary information. For the large axial ratio hectorite nanoplatelets, we expected pronounced orientation effects upon formation of the micro-jets and micro-droplets.

To determine changes in the platelet orientation upon transition from the capillary into the free micro-jet, and upon the subsequent transition from the free micro-jet into the micro-droplets, we performed horizontal scans at five downstream vertical positions (Fig. 4.1a): far within the capillary (I), 100 μm upstream and downstream the orifice (II, III), in the fully developed micro-jet (IV), and in the micro-droplet region (V).

Fig. 4.1b displays the small-angle X-ray scattering (SAXS) patterns for the hectorite nanoplatelets measured at different scan positions from the capillary into the free micro-jet and further downstream into the micro-droplet region. Reference scans outside the liquid and at the air/liquid-interface are provided in the electronic supplementary information (ESI Fig. B.9-B.11). All scattering patterns in Fig 4.1b show a strong anisotropy indicating pronounced shear-alignment of the nanoplatelets.

We first inspect the upper row of the scattering patterns shown in Fig. 4.1b, which was measured in the liquid stream within the glass capillary (position I). The first scattering pattern (I.1) was measured close to the left capillary inner wall. The scattering pattern

is characterized by a sharp equatorial ∞ -shaped high intensity region, indicated in red. The next two scattering patterns (I.2, I.3) were measured towards the center of the capillary. They also show a ∞ -shaped high-intensity region, which is, however, inclined by an angle of $+6^\circ$ with respect to the horizontal axis. In the center of the capillary (I.4) the ∞ -shaped high intensity region has a perfect horizontal alignment with 0° inclination angle. The scattering patterns measured at subsequent scan positions at the right-hand side of the capillary are found to be mirror images of the left-hand side scattering patterns. This is the case for all subsequent downstream scans. In the following discussion, we thus focus only on the scattering patterns measured on the left-hand side of the capillary, micro-jet, and micro-droplets.

The observed characteristic ∞ -shaped high intensity regions result from the form-factor of the nanoplatelets which are strongly aligned in flow-direction, co-planar to the capillary wall. To quantitatively determine the orientational distribution of the nanoplatelets we calculated scattering patterns using different types of orientational distribution functions. We modelled the hectorite nanoplatelets as disks with an average thickness of 1.0 nm and an average radius of $10 \mu\text{m}$ to analytically calculate their formfactor. We obtained best agreement between calculated and measured scattering patterns when using a Gaussian orientational distribution function, for which the orientational order parameter was calculated. Details of the calculations are given in the electronic supplementary information and further in literature.^[30,31] In Fig 4.1c, the lowest row of scattering patterns shows measured (left-half) and calculated (right-half) scattering patterns for selected characteristic scan-positions together with the orientational order parameter which is defined in Equation B.16 of electronic supplementary information and gave the best agreement. We observe very good agreement between measured and calculated scattering patterns. Here, the orientation parameters are determined in the capillary and all have values of $S = -0.46 - -0.48$, with slightly less negative values towards the center of the capillary. In this context, a value of $S = -0.5$ would declare a complete alignment in flow direction, whereas $S = 0$ corresponds to a random isotropic orientation. Thus, the result indicates an alignment of the nanoplatelets in flow-direction, with their basal plane normal vector being perpendicular to the flow direction.

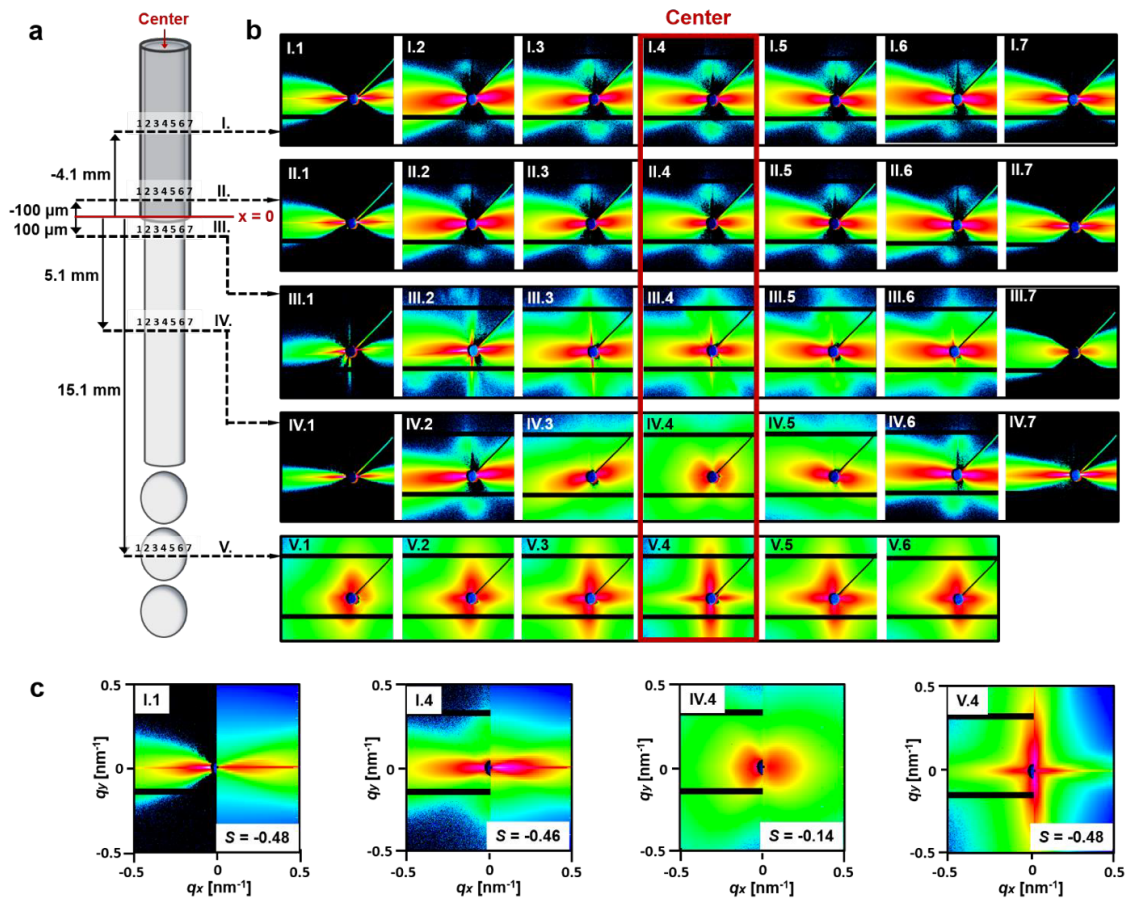


Figure 4.1: Scheme of the microjet and the emerging microdroplets with dispersed nanoplatelets together with the 2D-SAXS patterns measured within the jet and the droplets. (a) Scheme of the capillary, the liquid micro-jet and the micro-droplet region with the scan lines I-V where the 2D-SAXS-patterns were measured. (b) Set of scattering patterns measured for the hectorite nanoplatelets at the specified scan positions. We observe a strong anisotropy resulting from the flow-alignment of the nanoplatelets, with an unexpected biaxial orientation of the nanoplatelets in the microdroplet region (c) Comparison of experimental and calculated scattering patterns to determine the orientational order parameter of the nanoplatelets. The q -range is $-0.5 - 0.5 \text{ nm}^{-1}$.

The slight inclination of the scattering patterns observed towards the center of the capillary (positions I.2, I.3) indicates a small tilt of the flowing nanoplatelets towards the center of the capillary. The value of the inclination angle is a result of the competing effects of flow-orientation preferring the nanoplatelets to orient parallel to the streamlines, corresponding to a 0° inclination angle, and rotational diffusion allowing the particles to explore a larger angular range, resulting in larger inclination angles. For the hectorite nanoplatelets we observe rather small inclination angles indicating that shear orientation dominates over rotational diffusion. This implies that the ratio of shear rates to the rotational diffusion coefficients is much larger than unity, i.e. $\dot{\gamma}/D_{rot} \gg 1$. The value of this ratio can be estimated from the experimental flow

rate and the capillary diameter, from which the wall shear rate $\dot{\gamma} = 4Q/(\pi R^3)$ can be estimated to be $\dot{\gamma} \sim 10^4 \text{ s}^{-1}$, and from the platelet radius R_D , from which a rotational diffusion coefficient^[32] $D_{rot} = 3kT/(32\pi R_D^3) \sim 10^{-4}$ can be estimated. Thus, the condition $\dot{\gamma}/D_{rot} \sim 10^7 \gg 1$ is well fulfilled. The effects due to rotational diffusion, possibly enhanced by interplatelet collisions, are slightly more pronounced towards the center of the capillary, where the shear rates are smaller, leading to slightly larger inclination angles and slightly reduced orientational order.

As shown by the scattering patterns in the second row in Fig 4.1b (II.1 – II.5), which were measured in the capillary 100 μm upstream the orifice, the observed local orientational distribution of the nanoplatelets is stable and stationary across the capillary, even until just before the capillary exit.

The third row of scattering patterns (III.1 – III.5) was measured in the free micro-jet just 100 μm downstream after exiting the capillary orifice. As the micro-jet has a slightly smaller diameter than the orifice, the X-ray beam at the first scan position (III.1) just touches the surface of the liquid jet. This results in a thin horizontal streak with a slight inclination due to the surface orientation of the narrowing jet, together with a weak ∞ -shaped scattering pattern from the oriented nanoplatelets. The sharp vertical streak is caused by the micro-X-ray beam which slightly touches the end of the capillary. At all scan positions across the free micro-jet we observe scattering patterns with nearly zero inclination angle indicating nearly vertical orientation of the nanoplatelets in flow direction. A slight broadening of the ∞ -shaped high-intensity region in the center of the micro-jet indicates a minor loss of orientational order.

A slightly decreasing inclination angle and a minor loss of orientational order are the two characteristic features that we observe when the liquid stream exits the orifice and forms a free liquid micro-jet. They accompany a fundamental change of the flow velocity field when the boundary condition at the liquid surface changes from no-slip condition at the glass wall of the capillary to free-slip condition at the liquid/air-interface of the free jet. To obtain insights into how this transition relates to the observed changes in the nanoplatelet orientation, we performed lattice-Boltzmann simulations. In the simulations the transition from the capillary into the free micro-jet is modeled by a Newtonian liquid stream flowing through a cylindrical channel, where halfway down the channel the boundary conditions change from no-slip to free-slip (Fig. 4.2a). The liquid contains dispersed platelets whose orientational distribution can be followed and analyzed along the channel. Details of the simulations are described in the Methods

Section.

Fig. 4.2b shows the evolution of the orientational order parameter downstream the channel. Within the capillary the platelets are well oriented in flow direction with a calculated orientational order parameter $S = -0.48$ in good agreement with the experiments. We observe in the simulations that directly after the exit, when changing from no-slip to free-slip conditions, the order parameter slightly drops to a value of $S = -0.41$ until the nanoplatelets realign to reach a value of $S = -0.43$. The degree of order in the simulations is higher compared to the experimentally determined values, which is due to the internal flexibility of the hectorite nanoplatelets. Yet, the simulations reveal that the underlying reason for the characteristic change of the orientational distribution is the change of the velocity field, which varies from a parabolic profile characteristic for Poiseuille flow in the capillary to a homogeneous plug flow profile in the free microjet.^[33] This change in the flow velocity profile, illustrated in Fig. 4.2c, involves an acceleration of fluid volume elements in the outer jet region and a deceleration in the center of the micro-jet. To satisfy mass conservation fluid needs to flow radially from the inner to the outer region of the microjet in a transition zone immediately after the capillary exit which carries along platelets and leads to the observed loss of orientational order. The reestablishment of a purely axial flow after the transition zone then partly reorients the platelets parallel to the streamlines thereby leading to near zero inclination angles. The observed characteristic changes of the nanoplatelet orientation in the zone directly after the capillary exit can thus be well rationalized in terms of the changing surface boundary conditions and changing velocity profiles.

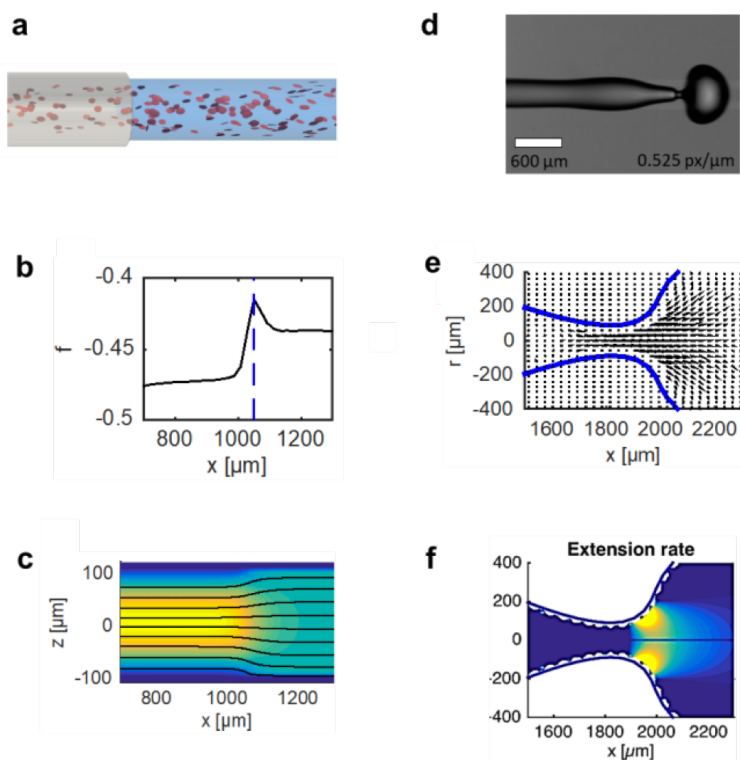


Figure 4.2: Simulation of the platelet orientation upon micro-jet formation and break-up into microdroplets. (a) Snapshot of a Lattice-Boltzmann simulation to determine changes of the platelet reorientation from the nozzle exit into the free jet. (b) Simulated development of the orientational order parameter from the capillary through the nozzle into the free jet with a slight loss of orientational order at the exit, marked by the dashed blue line. (c) Simulated velocity profile where the colors indicate the axial velocity and black lines represent stream lines. (d) Shape of the micro-jet just before droplet breakup imaged with a high-speed camera and (e) simulated with the potential-flow boundary-integral code. The velocity field in the frame of reference moving with the jet features an outward radial flow right after the narrow constriction before entering the droplet. This extensional flow with a high extension rate (f) causes reorientation of the platelets upon entering the droplet and leads to the biaxial orientation observed in the X-ray scattering patterns (Fig. 4.1b, row V).

The fourth horizontal scan (IV) transects the free fully developed micro-jet at $x = 5.1$ mm downstream the capillary exit. At the first scan position inside the free jet (IV.2) we observe a narrow ∞ -shaped high intensity region indicating still high orientational order with only a slight inclination of $+5^\circ$ indicating the onset of rotational diffusion and inter-platelet collision due to the reduced surface shear rates. Both, the loss of orientational order and the increase of the inclination angle, become more significant towards the center of the free jet. The shape of the high intensity region changes from a ∞ -shape to a broad “butterfly”-shape in the center (IV.4), corresponding to a reduction of the orientation order parameter from $S = -0.46$ to $S = -0.14$. Due

to symmetry the inclination angle in the center is zero. Off-center inclination angles, e.g. at position (IV.3), have values of 15° , i.e. significantly higher compared to the liquid stream in the capillary. The loss of orientational order and the increase of the inclination angle indicate that shear rates within the liquid jet, particularly in the center, have strongly decreased. Ideally, for the free micro-jet a homogeneous plug-flow profile with vanishing shear rates would be expected such that orientational order is significantly reduced by rotational diffusion.

To verify the development of a plug-flow profile we carried out microparticle image velocimetry (μ PIV) in the free micro-jet as shown in detail in the electronic supplementary information. It is experimentally impossible to determine the flow velocity profile at the outer edge of the free jet because the jet acts as a cylindrical lens that refracts light such that the outer edge is completely dark. Yet it is possible to determine the flow profile within the micro-jet, where within experimental error we indeed observe a plug-flow profile, leading to a consistent description of the flow velocity profile and the experimentally observed changes in the nanoplatelet orientation.

The last row of scattering patterns (V) was measured at position $x = 15.1$ mm, which is in the region where the free micro-jet has broken-up into a train of micro-droplets due to Rayleigh instability.^[34,35] The micro-droplets have larger diameters than the free jet such that already at position V.1 we probe the orientational distribution of nanoplatelets within the droplet. Fig. 4.2d shows a snapshot taken with a high-speed camera at 50.000 frames s^{-1} to illustrate the development of the micro-droplet from the micro-jet. The droplet breakup occurs in a narrow region at $11 < x < 13$ mm, such that at position V we already probe the microdroplet region.

At all V scan positions the scattering patterns have an unusual appearance characterized by a cross-shaped high intensity region. It originates from two mutually perpendicular ∞ -shaped high intensity regions, one along the horizontal axis, the other along the vertical axis. This indicates an unexpected biaxial orientational distribution of the nanoplatelets, which our scanning experiments reveal for the first time. From the scattering intensities integrated over the meridian and the equation we deduce that approximately 20% of the platelets are oriented parallel to the flow direction, with the platelet normal in the equatorial plane, and 80% *perpendicular* to the flow direction with the platelet normal parallel to the flow direction. In the center of the droplet the fraction of unexpectedly perpendicularly oriented nanoplatelets is significantly larger compared to the parallel oriented nanoplatelets. Compared to the upstream position

in the free micro-jet, the high-intensity regions are sharper, promoting increased orientational order along each of the two platelet orientation axes.

To understand the evolution of the biaxial orientation we simulated the flow profile in the liquid jet during droplet breakup. Since this requires to explicitly consider the dynamics of the free micro-jet surface, including the thinning of the neck and the final droplet pinch-off, we employed boundary-integral simulations as described in the Methods Section. As shown in Fig. 4.2d/e the simulations of the droplet break-up are in good agreement with the experimentally determined break-up. The experiments and simulations were performed for the same conditions, i.e. a micro-jet radius of $300\ \mu\text{m}$ and a flow rate of $Q = 750\ \text{mL/h}$. While these simulations do not include platelet dynamics they nevertheless allow us to get a detailed insight into the local flow fields as shown in Fig. 4.2e. After passing the thin neck and entering into the droplet, the fluid enters an expansion zone with high extension rates (Fig 4.2f) and significant radial outward flow. Within the high extensional rate zone, the platelets are oriented perpendicular to the flow direction. After formation of the final droplet shape the extensional rates become zero and the platelets remain in their biaxial orientation. This is analogous to the recently observed perpendicular orientation of wormlike micelles in the extensional section of tapered microchannels which was similarly caused by high extensional rates perpendicular to the flow direction.^[36]

Thus, our scanning synchrotron X-ray experiments on free liquid micro-jets provide first insights into the orientation of dispersed platelet-shaped particles upon transition from a capillary into a free jet, and upon the subsequent transition into micro-droplets. The changing velocity fields cause characteristic reorientation effects leading to significant and unexpected changes in the platelet orientation, such as the biaxial orientation observed in the micro-droplets.

Wormlike micelles

It is interesting whether the orientational changes observed for nanoplatelets, which are examples of two-dimensional anisotropic objects, are a general characteristic for all anisotropic particles. We therefore also investigated the flow orientation of wormlike micelles, which are examples of one-dimensional anisotropic objects. We used wormlike micelles formed by the self-assembly of poly(isoprene-*b*-ethylene oxide) (PI-*b*-PEO) block copolymers in water. The micelles have a diameter of 20 nm and contour lengths of several micrometers as shown by the cryo-TEM images in the electronic

supplementary information (ESI Fig. B.3b). We used a concentration of $c = 10\%$ w/w in water where the scattering intensity is sufficiently high to quantitatively determine the orientational distribution from the measured scattering patterns. The capillary, flow rates and scanning positions were the same as for the hectorite nanoplatelets.

The first row of scattering patterns (Fig. 4.3, I) was measured across the capillary. The scattering patterns are characterized by two pronounced first order and weak second order Bragg peaks located on the equator. This indicates that the wormlike micelles are oriented in flow-direction with strong positional and orientational correlations. From the position of the Bragg-peaks one can calculate an average distance between adjacent micelles of $d = 42$ nm.

The first scattering pattern (Fig. 4.3, I.1) results from wormlike micelles that are located directly next to the capillary wall. We observe two sickle-shaped high-intensity regions with an inclination angle of 12° with respect to the equator. At subsequent scan positions towards the center of the capillary (I.2-I.4), the Bragg-peaks have lower intensity, a more circular shape, a smaller inclination angle, and are located on a weak Debye-Scherrer ring. This indicates that at all scan positions in the capillary the wormlike micelles are oriented in flow direction, with a significant inclination only next to the capillary wall. The weak Debye-Scherrer ring indicates the presence of a small fraction of isotropically oriented wormlike micelles. At the capillary wall, the characteristic sickle-shaped Bragg-peaks, the higher scattering intensity and the absence of a Debye-Scherrer ring are indications of a dense, nematic phase forming a lubrication layer at the capillary wall as a result of shear-banding.^[37] The small inclination angles in the center of the liquid stream indicate that rotational diffusion is very slow due to the retarded cooperative motion of the wormlike micelles.^[38]

The scattering patterns shown in the second row (II) are measured directly ($100 \mu\text{m}$) upstream the capillary exit and are very similar to the upstream position, indicating stable stationary flow conditions in the capillary. With the exception of the occurrence of the nematic phase close to the capillary wall, the observed orientational distribution for the wormlike micelles in the capillary is very similar to the one observed for the nanoplatelets.

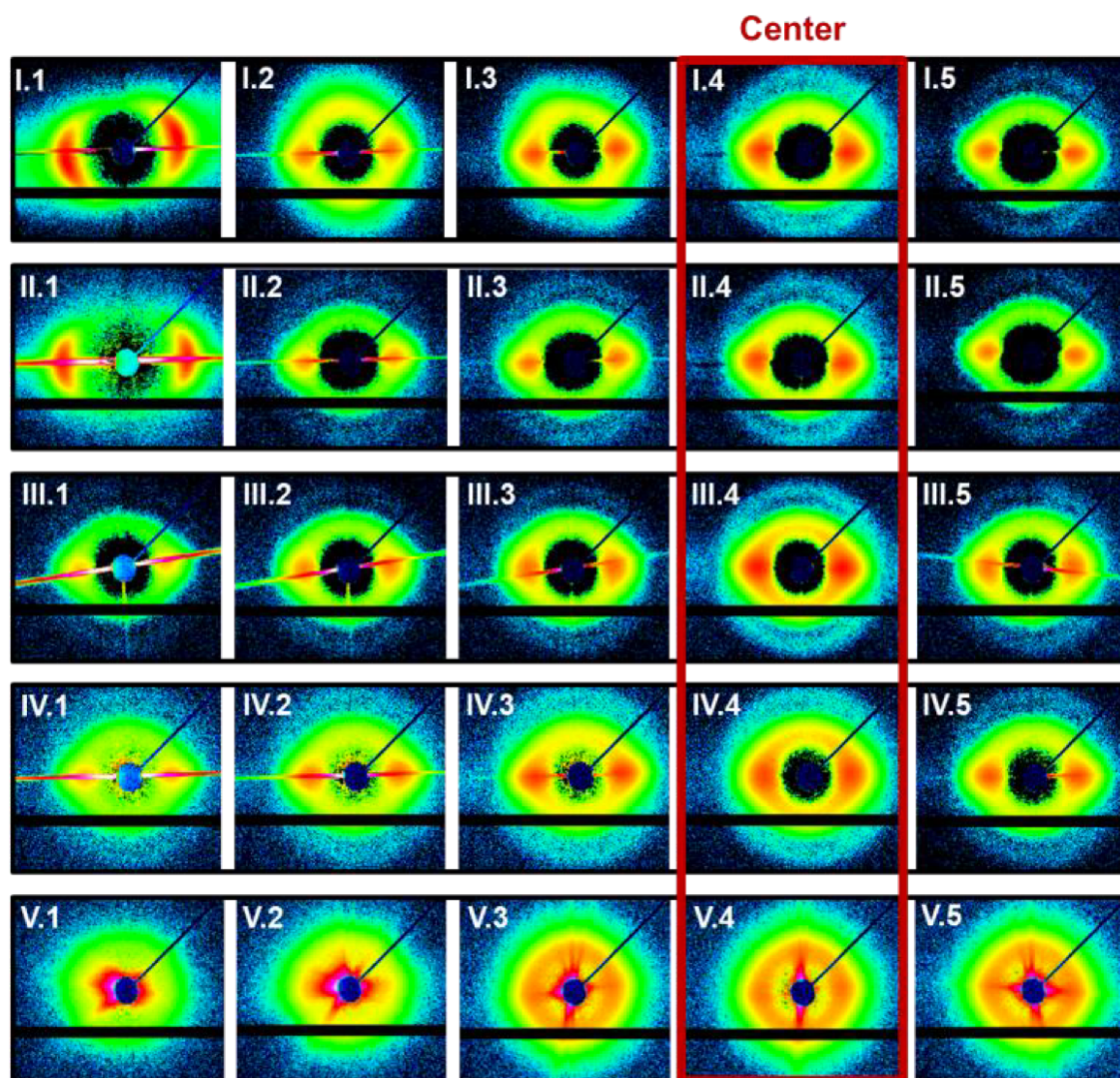


Figure 4.3: Set of 2D-SAXS-patterns measured within the microjet and the emerging microdroplets containing dispersed wormlike micelles. Also for the wormlike micelles we observe pronounced flow-alignment with equatorial Bragg-peaks indicating strong intermicellar correlations. The biaxial orientation of the micelles in the microdroplet region can be observed as slight intensity modulations on the Debye-Scherrer rings (V). The q -range is $-0.5 - 0.5 \text{ nm}^{-1}$.

The third row of scattering patterns (III) was measured just $100 \mu\text{m}$ downstream the capillary exit in the zone of the developing free micro-jet. At the first scan position (III.1) the X-ray beam just touches the micro-jet resulting in a thin streak, yet the Bragg-peaks from the oriented cylindrical micelles are already apparent. At the subsequent scan positions (III.2–III.5) we observe Bragg peaks with increased azimuthal widths indicating some loss of orientational order, particularly towards the center of the free microjet. The inclination angles are very small, indicating a near vertical alignment of the cylindrical micelles in flow direction. The two effects, (1) the loss of orientational

order towards the center of the micro-jet, and (2) the near-zero inclination angles are the same as observed for the nanoplatelets. This indicates that the transition from no-slip to free-slip boundary conditions and the related change of the flow-profile towards plug flow are characteristic for both the nanoplatelets and the wormlike micelles.

The subsequent scans shown in the fourth row (IV) were measured in the fully developed micro-jet 5.1 mm after exiting the capillary. Compared to the previous scan (III) taken directly after exiting the capillary, we observe only a very minor reduction of the orientational order and still near perfect orientation in the flow direction. We conclude that effects of rotational diffusion are negligibly small for the wormlike micelles such that even at strongly reduced shear rates in the center of the free micro-jet the alignment in flow direction well persists. Compared to the nanoplatelets, which were measured in more dilute solutions and where effects of rotational diffusion are more noticeable, the wormlike micelles were measured at higher concentrations where positional and orientational correlations, as apparent from the Bragg peaks, reduce local rotational mobility.

The last row shows the scattering patterns measured in the droplet region (V). The signature of the particle orientation in the scattering patterns is more difficult to recognize due to streaks originating from X-ray reflections from the droplet surface. Yet, from the scan position in the droplet center (V.4) we observe scattering patterns with higher intensity regions on the equator and on the meridian, located on top of a pronounced Debye-Scherrer ring. This indicates a significant loss of orientational order, but with a signature of a biaxial distribution that was also observed for the nanoplatelets.

We thus observe the same characteristic changes of the orientational distribution during transitions from the capillary to the free micro-jet and subsequently from the micro-jet to the micro-droplets for both the nanoplatelets and the wormlike micelles. Observed differences such as the formation of the nematic lubrication layer and the persistence of a high orientational order in the free micro-jet are related to the stronger positional and orientational correlations of the higher concentrated wormlike micelles.

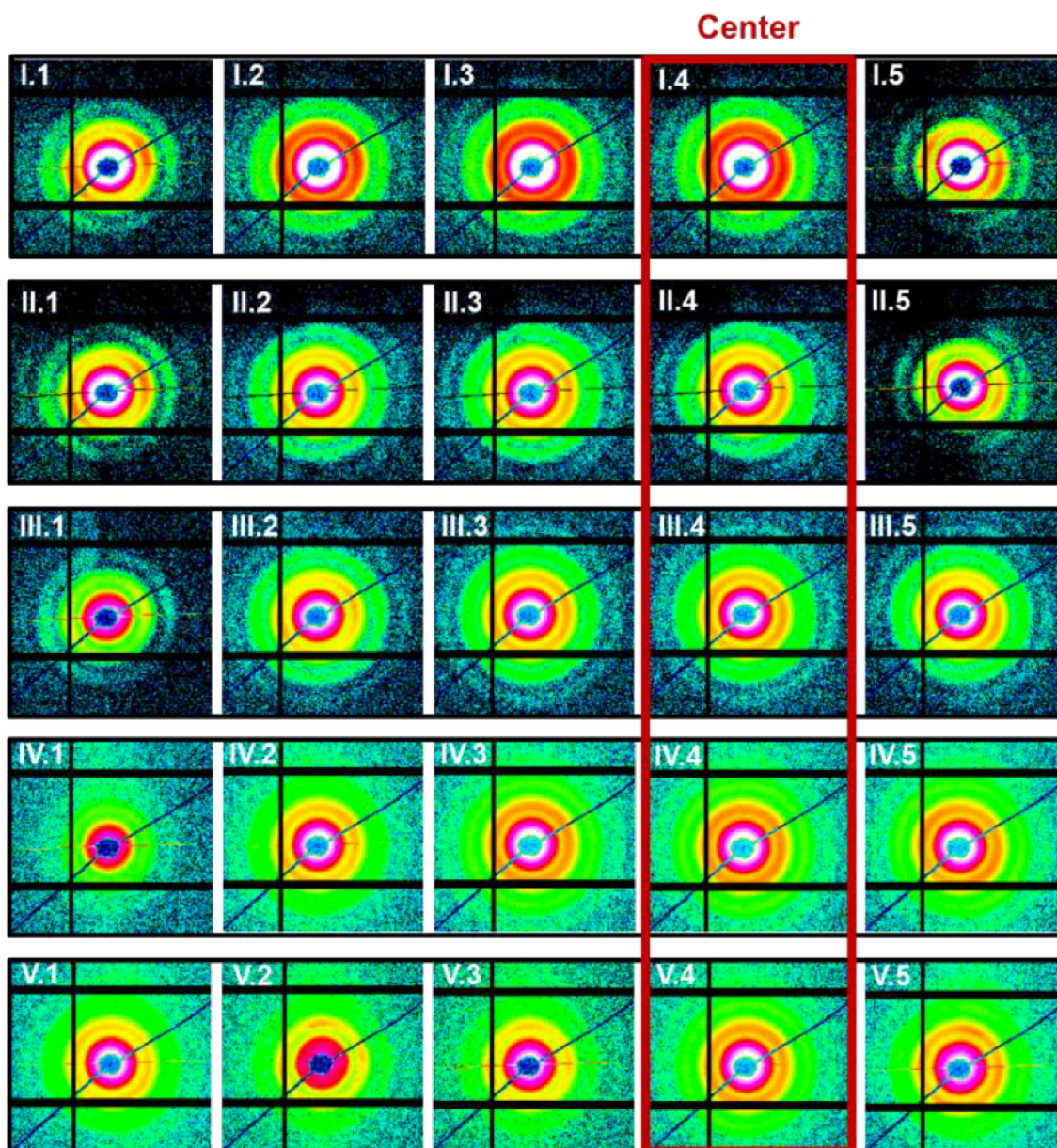


Figure 4.4: Set of 2D-SAXS-patterns measured within the microjet and the emerging microdroplets containing narrow disperse gold nanorods. The scattering patterns feature concentric rings due to the cross-sectional formfactor. Due to the small axial ratio the nanorods are flow-aligned only close to the capillary walls, but even for the short nanorods the biaxial alignment in the micro-droplet region is clearly visible indication strong extensional forces during droplet-breakup. The q -range is $-1 - 1 \text{ nm}^{-1}$.

Gold nanorods

It is finally interesting, whether the observed reorientation behavior generally applies not only to anisotropic particles with large axial ratios, such as hectorite nanoplatelets and wormlike micelles, but also to anisotropic particles with much smaller axial ra-

tios. For the latter case we expected rotational diffusion to significantly reduce shear-orientation effects, but hoped that some of the observed characteristic re-orientation effects might still be observable.

Thus, we also investigated the shear-orientation of gold nanorods. We synthesized monodisperse gold nanorods with an average diameter of $D = 26\text{nm}$ and an average length of $L = 71\text{nm}$, resulting in an axial ratio of only ~ 3 . The synthesis and the corresponding TEM-images are provided in the electronic supplementary information (ESI Fig. B.3c). The set of scattering patterns were measured at the same positions as for the nanoplatelets and the wormlike micelles and are shown in Fig. 4.4.

For the gold nanorods the measured scattering patterns at all scan positions are characterized by concentric rings resulting from cross-sectional form factor oscillations. High-intensity regions along the azimuth of the rings would indicate a preferred orientation. Row (I) shows the scattering patterns measured within the capillary. The first scattering pattern (I.1) was obtained directly next to the inner capillary wall. We indeed observe two increased scattering intensity regions on the formfactor rings, located on a line with an inclination angle of 25° . This indicates an alignment of the nanorods in flow direction with a quite large mean inclination angle of 25° . At all other scan positions, we observe isotropic scattering patterns indicating a completely isotropic orientational distribution resulting from the fast rotational diffusion of the gold nanorods. The rotational diffusion coefficient for the nanorods can be estimated to be^[18] $D_{rot} = 3kT(\ln(2L/d) - \gamma)/\pi\eta L^3 \sim 10^5\text{ s}^{-1}$. It is thus larger than the shear rates, except at the capillary wall where the shear rate is at least of comparable magnitude, leading to the observed shear alignment with a quite large inclination angle.

When inspecting the set of scattering patterns measured at position (II), close to the capillary exit, the slightly preferred orientation in flow-direction with a large inclination angle can be better recognized, not only at position II.1, but also at position II.2. As expected, the degree of orientational order of the short nanorods is generally much lower compared to the extended nanoplatelets and wormlike micelles, and nearly isotropic in the center of the capillary.

The first scan across the free microjet (III.1-III.5) just $100\ \mu\text{m}$ downstream the capillary exit shows only slight changes of the orientational order. At the jet edge (III.1) the flow-orientation is still well observable, whereas at the center the orientational distribution is nearly isotropic. Further downstream in the fully developed microjet (IV) the orien-

tational order is completely lost across the micro-jet as indicated by the fully isotropic concentric formfactor oscillations and scattering patterns.

The last row (V) shows the scattering patterns measured after the droplet breakup region. The off-center scattering patterns clearly show the biaxial distribution with high-intensity regions on the equator and meridian of the concentric form-factor oscillations. It is only in the center of the micro-jet that the scattering pattern is still isotropic. This shows that the extensional rates during droplet pinch-off are very large, leading to a reorientation even of the short nanorods.

Our experiments for the nanoplatelets, wormlike micelles and gold nanorods thus show that the observed reorientation effects, particularly the unusual biaxial distribution in the micro-droplets after droplet break-up, are generally occurring for anisotropic particles. The understanding of the flow-alignment of anisotropic particles is crucial for the controlled fabrication of fiber materials as demonstrated by recent in-situ SAXS experiments on the flow-alignment of biological nano-fibers^[39,40]. Our experiments, which demonstrate the importance of perpendicular extensional forces in affecting particle orientation, underline the necessity to generate extensional forces in flow direction to achieve desired parallel fiber orientation needed for high performance fibers^[39]. Thus experiments at higher particle concentrations to generate fibers is an important next step for further experiments.

4.5. Conclusion

We have demonstrated a microfluidic setup that enabled us to investigate the flow-orientation of anisotropic particles in free liquid jets for the first time, using scanning microfocus X-ray scattering. Our study reveals remarkable and unexpected changes in particle flow-alignment upon exiting the nozzle to form a free jet, within the free jet, and upon jet break-up into droplets, where we observed an unusual biaxial particle orientation. We show how flow and aspect ratio determine the flow-orientation of anisotropic particles. We have furthermore demonstrated that the observed flow-alignment phenomena are a general characteristic of anisotropic particles, comprising one- and two-dimensional particle geometries. Finally, using fluid dynamics simulations we could directly relate the observed particle flow-alignment to the changing flow velocity fields within the micro-jets and micro-droplets.

The developed microfluidic setup is broadly applicable for the investigation of micro-

jets and micro-droplets with dissolved particles, taking advantage of the ever smaller, even sub- μm X-ray beam diameters that become available at dedicated synchrotron beamlines. Our findings greatly enhance our understanding of particle orientation in free jets and droplets and provide the basis for a control of particle alignment in liquid jet-based fabrication, coating and printing techniques.

References

- [1] Cuculo, J. A.; Hotter, J. F.; Zhou, Q. *Structure Formation in Polymeric Fibers.*; Hanser Gardner Publications, 2001.
- [2] Agarwal, S.; Burgard, M.; Greiner, A.; Wendorff, J. H. *Electrospinning: A Practical Guide to Nanofibers.*; Walter de Gruyter GmbH, 2016.
- [3] Le, H. P. *Journal of Imaging and Technology* **1998**, *42*, 49–62.
- [4] Roth, S. A. *Journal of physics / Condensed Matter* **2016**, *28*, 403003.
- [5] Ashgriz, N.; Yarin, A. L. *Capillary instability of free liquid jets.*; Springer US, 2011.
- [6] Ganan-Calvo, A. M. *Physical Review Letters* **1998**, *80*, 285–288.
- [7] Lin, S. P.; Reitz, R. D. *Annual Review of Fluid Mechanics* **1998**, *30*, 85–105.
- [8] Weierstall, U. *Philosophical Transactions of the Royal Society B: Biological Sciences* **2014**, *369*, 20130337.
- [9] Samon, J. M.; Schultz, J. M.; Hsiao, B. S.; Seifert, S.; Stribeck, N.; Gurke, I.; Saw, C. *Macromolecules* **1999**, *32*, 8121–8132.
- [10] White, J. L.; Cakmak, M. *Advances in Polymer Technology* **1986**, *6*, 295–338.
- [11] Riekkel, C.; Madsen, B.; Knight, D.; Vollrath, F. *Biomacromolecules* **2000**, *1*, 622–626.
- [12] Qazi, S. J. S.; Rennie, A. R.; Cockcroft, J. K. *Langmuir* **2012**, *28*, 3704–3713.
- [13] Breu, J.; Seidl, W.; Stoll, A. J.; Lange, K. G.; Probst, T. U. *Chemistry of Materials* **2001**, *13*, 4213–4220.
- [14] Stöter, M.; Kunz, D. A.; Schmidt, M.; Hirsemann, D.; Kalo, H.; Putz, B.; Senker, J.; Breu, J. *Langmuir* **2013**, *29*, 1280–1285.
- [15] Förster, S.; Krämer, E. *Macromolecules* **1999**, *32*, 2783–2785.
- [16] Buffet, A.; Rothkirch, A.; Doehrmann, R.; Körstgens, V.; Hashem, M. M. A.; Perlich, J.; Schwartzkop, M.; Herzog, G.; Gehrke, R.; Müller-Buschbaum, P.; Roth, S. V. *Journal of synchrotron radiation* **2012**, *19*, 647.
- [17] JPIV, v16.08.03: *Open source software package for particle image velocimetry.* Available at www.jpiv.vennemann-online.de. Accessed August 29, 2016).

- [18] Bächer, C.; Schrack, L.; Gekle, S. *Physical Review Fluids* **2017**, *2*, 013102.
- [19] Arnold, A.; Lenz, O.; Kesselheim, S.; Weeber, R.; Fahrenberger, F.; Roehm, D.; Kosovan, P.; Holm, C. *ESPREsSo 3.1: Molecular Dynamics Software for Coarse-Grained Models.*; Springer, 2013.
- [20] Roehm, D.; Arnold, A. *The European Physical Journal Special Topics* **2012**, *210*, 89–100.
- [21] Limbach, H. J.; Arnold, A.; Mann, B. A.; Holm, C. *Computer Physics Communications* **2006**, *174*, 704–727.
- [22] Dünweg, B.; Ladd, A. J. C. *Lattice Boltzmann Simulations of Soft Matter Systems.*; Springer, 2009.
- [23] Hoeve, W. V.; Gekle, S.; Snoeijer, J. H.; Versluis, M.; Brenner, M. P.; Lohse, D. *Physics of Fluids* **2010**, *22*, 122003.
- [24] Gekle, S.; Gordillo, J. M.; van der Meer, D.; Lohse, D. *Physical Review Letters* **2009**, *102*, 034502.
- [25] Gekle, S.; Gordillo, J. M. *International Journal for Numerical Methods in Fluids* **2010**, *67*, 1456–1469.
- [26] Enriquez, O. R.; Peters, I. R.; Gekle, S.; Schmidt, L. E.; Lohse, D.; van der Meer, D. *Journal of Fluid Mechanics* **2012**, *701*, 40–58.
- [27] Rosenfeldt, S.; Stöter, M.; Schlenk, M.; Martin, T.; Albuquerque, R. Q.; Förster, S.; Breu, J. *Langmuir* **2016**, *32*, 10582–10588.
- [28] Stöter, M.; Gödrich, S.; Feicht, P.; Rosenfeldt, S.; Thurn, H.; Neubauer, J.; Seuss, M.; Lindner, P.; Kalo, H.; Möller, M.; Fery, A.; Förster, S.; Papastavrou, G.; Breu, J. *Angewandte Chemie International Edition* **2016**, *55*, 7398–7402.
- [29] Stöter, M.; Rosenfeldt, S.; Breu, J. *Annual Review of Materials Research* **2015**, *45*, 129–151.
- [30] Foerster, S.; Apostol, L.; Bras, W. *Journal of Applied Crystallography* **2010**, *43*, 639–646.
- [31] Foerster, S.; Zielske, K.; Schellbach, C.; Sztucki, M.; Lindner, P.; Perlich, J. *Advances in Colloid and Interface Science* **2011**, *163*, 53–83.
- [32] Ortega, A.; de la Torre, J. G. *The Journal of Chemical Physics* **2003**, *119*, 9914–9919.

- [33] Eggers, J.; Villermaux, E. *Reports on Progress in Physics* **2008**, *71*, 036601.
- [34] Rayleigh, L. *Proceedings of the Royal Society of London* **1879**, *29*, 71–97.
- [35] Goldin, M.; Yerushalmi, J.; Pfeffer, R.; Shinnar, R. *Journal of Fluid Mechanics* **2006**, *38*, 689–711.
- [36] Trebbin, M.; Steinhäuser, D.; Perlich, J.; Buffet, A.; Roth, S. V.; Zimmermann, W.; Thiele, J.; Foerster, S. *Proceedings of the National Academy of Sciences* **2013**, *110*, 6706–6711.
- [37] Olmsted, P. D. *Rheologica Acta* **2008**, *47*, 283–300.
- [38] Förster, S.; Konrad, M.; Lindner, P. *Physical Review Letters* **2005**, *94*, 017803.
- [39] Hakansson, K. M. O.; Fall, A. B.; Lundell, F.; Yu, S.; Krywka, C.; Roth, S. V.; Santoro, G.; Kvik, M.; Pahl-Wittberg, L.; Wagberg, L.; Söderberg, L. D. *Nature Communications* **2014**, *5*, 4018.
- [40] Hakansson, K. M.; Lundell, F.; Pahl-Wittberg, L.; Söderberg, L. D. *The Journal of Physical Chemistry B* **2016**, *120*, 6674–6678.

Chapter 5

5. Publication III

Hydrogelation kinetics measured in a microfluidic device with in-situ X-ray and fluorescence detection.

Susanne Seibt^{a,c}, Sebastian With^a, Andreas Bernet^b, Hans-Werner Schmidt^{b,d},
Stephan Förster^{*,a,c,d}

^aPhysical Chemistry I, University of Bayreuth, Universitätsstraße 30, 95440 Bayreuth, Germany.

^bMacromolecular Chemistry I, University of Bayreuth, Universitätsstraße 30, 95440 Bayreuth,
Germany.

^cJCNS-1/ICS-1, Forschungszentrum Jülich, 52425 Jülich, Germany.

^dBavarian Polymer Institute, University of Bayreuth, 95440 Bayreuth, Germany.

The results presented in this chapter were published in *Langmuir*, **2018**, *34*, 5535-5544.

Individual contribution of involved authors

I performed all experiments and analysed the data. Together with Prof. Stephan Förster I wrote the manuscript. Dr. Sebastian With performed fundamental research on the system and helped with the microfluidic experiments. Dr. Andreas Bernet synthesised and provided the trisamide-based hydrogelator and helped, as well as Prof. Hans-Werner Schmidt with scientific discussions.

5.1. Abstract

Efficient hydrogelators will gel water fast and at low concentrations. Small molecule gelling agents that assemble into fibers and fiber networks are particularly effective hydrogelators. Whereas it is straightforward to determine their critical concentration for hydrogelation, the kinetics of hydrogelation is more difficult to study because it is often very fast, occurring on the subsecond time scale. We used a 3D focusing microfluidic device combined with fluorescence microscopy and *in situ* small-angle X-ray scattering (SAXS) to study the fast pH-induced gelation of a model small molecule gelling agent at the millisecond time scale. The gelator is a 1,3,5-benzene tricarboxamide which upon acidification assembles into nanofibrils and fibril networks that show a characteristic photoluminescence. By adjusting the flow rates the regime of early nanofibril formation and gelation could be followed along the microfluidic reaction channel. The measured fluorescence intensity profiles were analyzed in terms of a diffusion-advection-reaction model to determine the association rate constant, which is in a typical range for small molecule self-assembly. Using *in situ* small-angle X-ray scattering we could determine the dimensions of the fibers that were formed during the early self-assembly process. The detailed structure of the fibers was subsequently determined by cryotransmission electron microscopy. The study demonstrates that 3D focusing microfluidic devices are a powerful means to study the self-assembly on the millisecond time scale, which is applied to reveal early state of hydrogelation kinetics. In combination with *in situ* fluorescence and X-ray scattering these experiments provide detailed insights into the first self-assembly steps and their reaction rates.

5.2. Introduction

Hydrogels are capable of holding large amounts of water in three-dimensional networks. They currently attract considerable attention in biomedical research with specific applications in biofabrication, tissue regeneration, and sustained drug release.^[1] Generally, hydrogels are formed either by cross-linking polymers into networks or by assembly of small molecules into supramolecular networks.^[2] For practical applications the critical gelation concentration, the mechanical properties, and the gelation kinetics are of critical importance. Whereas it is straightforward to determine the critical gelation concentration and the mechanical properties of the resulting hydrogels, the hydrogelation kinetics is more difficult to determine because it often occurs fast and involves addition of components to induce hydrogelation by adjustment of pH, salinity or solvent composition.

Established methods to follow the gelation kinetics are oscillatory rheometry,^[3,4] multiple particle tracking microrheology,^[5,6] and in case of peptide hydrogelators circular dichroism.^[3] These methods allow one to follow hydrogelation kinetics on the time scales of seconds to minutes and hours. Gelation processes on faster time scales are more difficult to study because the components have to be mixed, and the subsequent hydrogelator assembly and hydrogel formation to be followed very fast. The early stages of hydrogel formation involve the decisive step of the formation of supramolecular structures such as nanofibrils that form water-swollen networks that mechanically support the hydrogel. These early hydrogelation steps could, to our knowledge, not yet be investigated on time scales of milliseconds. On time scales of minutes this has been successfully done for the pH-induced hydrogelation of an alanylvaline dipeptide, where also fluorescence, X-ray scattering and transmission electron microscopy (TEM) were used to show fiber formation,^[7] and for a diphenylalanine dipeptide, SANS and cryo-TEM were used.^[8]

For fast kinetic investigations, hydrodynamic flow-focusing in microfluidic devices has been demonstrated to achieve fast, even sub-millisecond time resolution.^[9-12] It is a complementary method to stopped-flow experiments, where hydrogelation is difficult to study as it can lead to channel clogging in the turbulent mixing section. Wall adhesion of hydrogels and microchannel blocking can also be a problem in hydrodynamic flow-focusing. Therefore 3D flow focusing schemes^[13-16] together with the use of buffer layers^[17] have been introduced to avoid wall contact during mixing and reaction of components in the microfluidic channels. Two further advantages of the 3D buffer layer design are a well-defined point of first contact of the reacting streams, and a nearly homogeneous flow velocity profile in the center of the channel. Under well-defined laminar flow conditions it is possible to extract rate constants for reactions occurring by interdiffusion in microchannel streams.^[18]

Here, we use microfluidic chips with a 3D buffer layer design together with fluorescence microscopy, small-angle X-ray scattering (SAXS) and cryo-TEM to investigate the rapid pH-induced self-assembly of a model small molecule hydrogelator into fibrils with the subsequent formation of a hydrogel. The use of fluorescence microscopy^[19] and SAXS^[20-22] to follow self-assembly in microfluidic channels has previously been shown to be very versatile methods. We demonstrate that using this methodology, it is possible to follow the early assembly process into fibers occurring on time scales of milliseconds. We for the first time determined the association rate constant and the radii of the first nanofibers that are formed upon hydrogelation.

5.3. Experimental Section

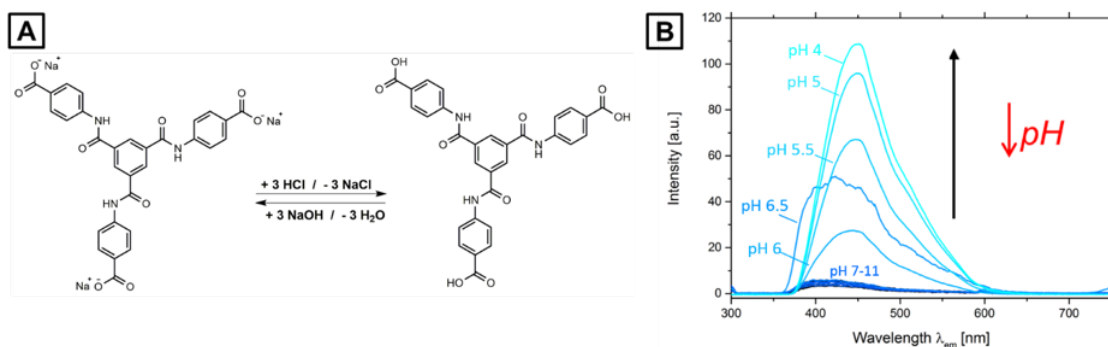


Figure 5.1: (A) Chemical structure of the hydrogelator (BTA) in its charged sodium salt form and its uncharged protonated form. (B) Characteristic fluorescence spectra showing the increase of the fluorescence intensity of aqueous BTA solutions with decreasing pH-value due to the self-assembly into fibers.

Hydrogelator

The synthesis and characterization of the hydrogelator, N,N',N'' -tris(4-carboxyphenylene)-1,3,5-benzene tricarboxamide (BTA), and the respective sodium salt are described in refs. [23,24]. The chemical structures in the deprotonated and protonated form are shown in Figure 5.1A. The BTA sodium salt is well soluble in water due to the repulsive electrostatic intermolecular interactions and the hydration mediated by the three carboxylate groups. Upon acidification the carboxylate groups are protonated. Beyond a certain protonation state this induces aggregation into fibrillar assemblies due to attractive intermolecular π - π - and hydrogen bonding interactions. The pH-induced self-assembly of the BTA hydrogelator can be achieved by different methods such as mixing with aqueous acid, contact with acidic fumes, or the slow and homogeneous hydrolysis of glucono- δ -lactone that is accompanied by the release of protons from the resulting gluconic acid. [25] Depending on the preparation method, stable gels can be obtained at low BTA concentrations, typically in the range of 2 -10 g/L (\triangleq 0.2-1.0 wt. %) which is the range where the kinetic experiments are performed. BTA was chosen as a model system, because the assembly is accompanied by an aggregation-induced emission enhancement [26,27] with the emergence of a blue photoluminescence with a characteristic emission at $\lambda = 450$ nm (Figure 5.1B). Thus, the self-assembly is signaled by a characteristic fluorescence whose time evolution can be monitored *in situ* in microfluidic channel flows.

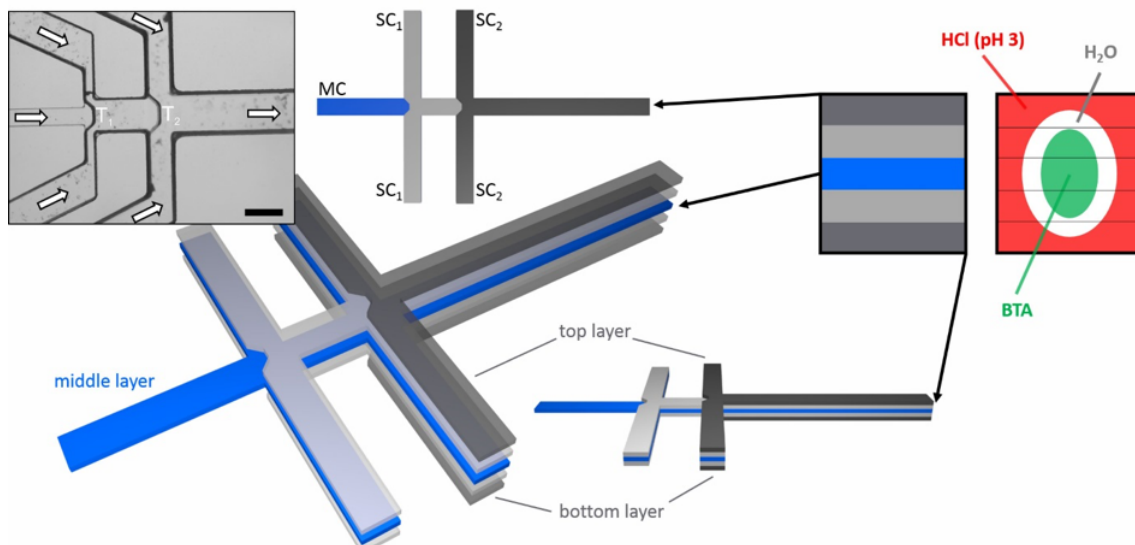


Figure 5.2: Scheme of channel geometry and flow profile in the outlet channel cross section (right) with an optical microscopy image of the channel double-cross (top left). Scale bar is $250\ \mu\text{m}$. Indicated are the different layers resulting from the multilayer device fabrication process, and the inlet channel, main channel (MC), first side channels (SC1), and second side channels (SC2). The two triangular ceiling and floor elements (T_1 , T_2) serve to vertically confine the central streams to prevent contact with the ceiling and the floor in the focusing section.

Fabrication of the microfluidic device

The microfluidic devices were fabricated with poly(dimethylsiloxane) (PDMS), similar to a procedure previously described.^[16,28,29] A silicon master was prepared via photolithographic techniques and then replicated in a soft lithographic step with PDMS (Sylgard 184®). To achieve three-dimensional hydrodynamic focusing, a three-layer channel design was used (shown in Figure 5.2) by aligning and bonding two structured PDMS stamps.

The outlet channel has a width of $230\ \mu\text{m}$ and a height of $250\ \mu\text{m}$. The heights of the individual layers resulting from the photolithographic procedure are $50\ \mu\text{m}$ for the bottom layer, $50\ \mu\text{m}$ for the middle layers, and $50\ \mu\text{m}$ for the top layers. The distance between the two cross junctions is $300\ \mu\text{m}$ (see Figure C.2 in Supporting Information for detailed dimensions). Triangular ceiling and floor elements, denoted as T_1 and T_2 in Fig. 5.2, were implemented to vertically confine the central streams to prevent contact with the ceiling and the flow in the focusing section. The alignment was supported by integrated micron-sized guiding and fitting structures on the PDMS surfaces. After plasma treatment, a drop of water was placed between both PDMS stamps to enable

alignment with micrometer precision before bonding. The devices were dried overnight at 35 °C. They were then connected with a microfluidic syringe pump system (NEMESYS, cetoni GmbH, Germany) via PE tubing.

Microfluidic experiment

For the microfluidic experiments the BTA-sodium salt was dissolved in deionized water at concentrations of 0.1-1 wt %. The BTA solution was introduced into the MC, deionized water (pH = 7) was introduced into SC1, and hydrochloric acid (pH = 3) was introduced into SC2. The flow velocities at all inlet channels are shown in Table 5.1. The flow ratios of the inlets were kept constant at $U_{SC2} = 2U_{SC1} = 4U_{MC}$.

The mean volumetric flow velocity in the central channel is the sum of the volumetric flow velocities of the main channel and the side channels, that is, $U = U_{MC} + 2U_{SC1} + 2U_{SC2}$. The flow velocity in the outlet channel is then given by $v = U/(h \cdot w)$ where h and w are the height and width of the exit channel, respectively.

To achieve ultimate time resolution, the flow speeds should be as high as possible. The flow speeds in our microfluidic device are limited by the stability of the device against delamination and the stability of the tubing connections as very fast flows necessitate large pressures. The devices used in our experiments proved to be stable at overall volume flows of more than 130 000 $\mu\text{l/h}$. For channel geometries with a typical height $h = 250 \mu\text{m}$ and a width $w = 230 \mu\text{m}$ this volume flow equals a flow velocity of $v_{max} = u_{max}/(h \cdot w) \approx 578 \text{ mm/s}$. For detection methods with a spatial resolution in the range of $\Delta x = 1 \mu\text{m}$, such as optical microscopy, a time resolution of below 2 μs is therefore feasible.

Table 5.1: Flow velocities of all inlets for different experiments.

inlet \ experiment	Flow velocity [$\mu\text{l/h}$]				
	(A)	(B)	(C)	(D)	(E)
Main channel (BTA)	30	62	125	250	500
Side channel 1 (H_2O)	62	125	250	500	1000
Side channel 2 (HCl)	125	250	500	1000	2000
Overall volumetric flow in outlet channel	404	812	1625	3250	6500
Overall flow velocity in outlet channel	1.95mm/s	3.92mm/s	7.85mm/s	15.70mm/s	31.40mm/s

Prior to the experiments the microfluidic device was flushed with NaOH-solution (pH = 12) to prevent the gel from assembling in the channels before a stable fluid flow

could be established. For the same reason the tube connecting the devices and the reservoir containing the BTA was filled with ca. 200 μl NaOH-solution. Before starting the experiment, the entire device and the tubing was primed with the liquid.

Fluorescence and confocal laser scanning microscopy

The fluorescence microscopy experiments were performed using an inverted Olympus IX73 microscope. It was equipped with a mercury lamp and an UV-filter with wavelengths for excitation and emission of 340-390 nm and 410 nm, respectively. For confocal laser scanning microscopy, a Leica TCS SP8 with a Leica DMI6000B inverted microscopy stage was used. The procedure was similar to the fluorescence microscopy experiment. Additionally, a solution of fluorescein was introduced into the main channel, water was introduced into the first side channels and a solution of eosin Y was introduced into the second side channels. A laser with a wavelength of $\lambda_{max} = 488$ nm and a detector range of 505 - 550 nm and a laser with a wavelength of $\lambda_{max} = 552$ nm and a detector range of 660 - 800 nm were used for the fluorescein solution and the eosin Y solution, respectively. The ratios of the flow rates were identical to that of the BTA experiments.

Calcium-Green-5NTM model experiment

For the Calcium-Green-5NTM (CG5N) model experiment, a 0.01 mM CG5N in buffer solution (KCl, EGTA, MOPS) and a 0.01 M CaCl_2 solution, with and without 0.005 mM Cascade Blue, were prepared as described by Park *et al.*^[17] The CG5N solution was introduced in the MC instead of the BTA solution, the CaCl_2 was pumped through the SC2 instead of HCl. As a buffer solution for SC1, the actual buffer in which the CG5N was dissolved was used. Details of the experiment are described in the Supporting Information.

Small-angle X-ray scattering (SAXS)

The SAXS-experiments were conducted using a lab-based setup consisting of a Cu rotating microfocus anode (MicroMax 007 HF, Rigaku), a microfluidic sample stage, and an evacuated pinhole camera system (Ganesha SAXS system, SAXSLab) equipped with a 2D-detector (Pilatus 300k, Dectris). This setup is described in more detail in ref.^[30]. The outlet capillary of the microfluidic setup was scanned with the X-ray beam downstream in 200 μm intervals.

5.4. Results and Discussion

Microfluidic device design

For the experiments we fabricated a microfluidic device that allowed 3D hydrodynamic focusing of the BTA hydrogelator main stream (MC) into the center of the reaction channel by using a buffer stream (SC1) and subsequently a stream of dilute acid (SC2) to induce self-assembly. The buffer stream (water) surrounds the stream of assembling BTA molecules until they reach the reaction channel. This prevents premature contact of the molecules with the acid stream at the walls of the channel crosses. We further used 3D flow focusing to keep the stream of assembling molecules exactly in the middle of the buffer stream and the reaction channel.

The use of a 3D channel design and a buffer layer were critical for the success of the experiments. We thereby avoided any wall contact during self-assembly and fiber formation. Hydrogel wall adhesion alters the local velocity profile and potentially leads to channel clogging. The buffer layer (SC1) vanishes by interdiffusion with the main stream (MC) and the acid stream (SC2) and thus provides a well-defined first contact point of the BTA molecules with the acid in the reaction channel. By focusing the BTA molecules into the channel center, there is a nearly homogeneous velocity profile during the self-assembly process.

The exact channel design shown in Fig. 5.2 was optimized by numerical FE-simulations (COMSOL) and test experiments. For the fabrication of the microfluidic chips, we used a multilayer approach which is described in the Supporting Information.

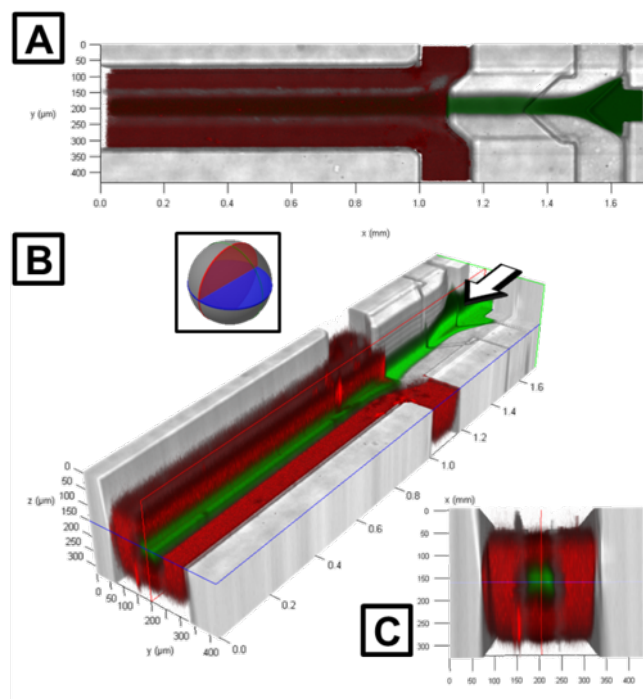


Figure 5.3: CLSM images of the fluid flows in the 3D double focusing microfluidic channel system. The flow directions in the MC and focusing side channels (SC1 and SC2) are marked by arrows. The flows are labeled with fluorescein (MC, green), water (SC1, gray), and eosin Y (SC2, red). The overall volume flow was $U = 6500 \mu\text{l/h}$. (A) Top view of the channel system showing the separation of the central stream (green) and the outer stream (red) by the buffer stream (gray) and (B) perspective 3D view of the channel system. For better visualization, the channel is cut (see sphere) for viewing the channel center. (C) View of the flow profile ca. $1200 \mu\text{m}$ after the beginning of the second channel cross. The images show the circular profile of the central stream, evenly surrounded by the buffer layer.

Flow profile validation. To visualize and validate the stream profiles in the 3D flow focusing devices, we added fluorescent molecules to the main stream and the second side stream. Figure 5.3A shows confocal microscopy images of the fluid stream in the MC, fluorescently marked with fluorescein (green), the first focusing buffer streams in the SC1 (nonmarked, colourless), and the second focusing streams in the SC2, fluorescently marked with eosin Y (red). The microfluidic setup was identical for all experiments. We will observe the subsequent two-fold 3D focusing of the main channel stream by the two side streams. Figure 5.3B shows a 3D reconstruction from a set of confocal microscopy images of the fluid flows to demonstrate 3D flow focusing with a buffer layer that completely and uniformly surrounds the central stream. The almost perfect circular flow profile, as shown in Figure 5.3C, had finally been achieved by implementing the triangular “ceiling” and “floor” elements (see T_1 and T_2 in Figure 5.2), which avoid vertical divergence of the central streams in the flow-focusing sections,

which would otherwise result in an ellipsoidal deformation of the central stream towards the upper and lower channel walls. Along the downstream reaction channel the buffer layer disappears by interdiffusion with the central and outer fluid streams. This marks the position of first contact of both streams, which defines the channel position of first contact, x_0 corresponding to $t = 0$. This position can be shifted along the downstream channel by adjusting the flow velocity of the buffer stream (SC1) relative to the other two streams (MC1 and SC2) as well as by adjusting the overall flow speed.

Fluorescence microscopy experiments to study fiber formation

For the self-assembly experiments we used the same device that was described for the fluorescein/eosin tests. The BTA solution (pH 11) in the MC was first focused with a buffer stream of water (pH 7) at the first intersection (SC1), and subsequently focused with hydrochloric acid (pH 3) at the second intersection (SC2). The fibers formed by the self-assembly process have a characteristic fluorescence emission at $\lambda = 450$ nm which allows to follow their formation downstream the main channel.

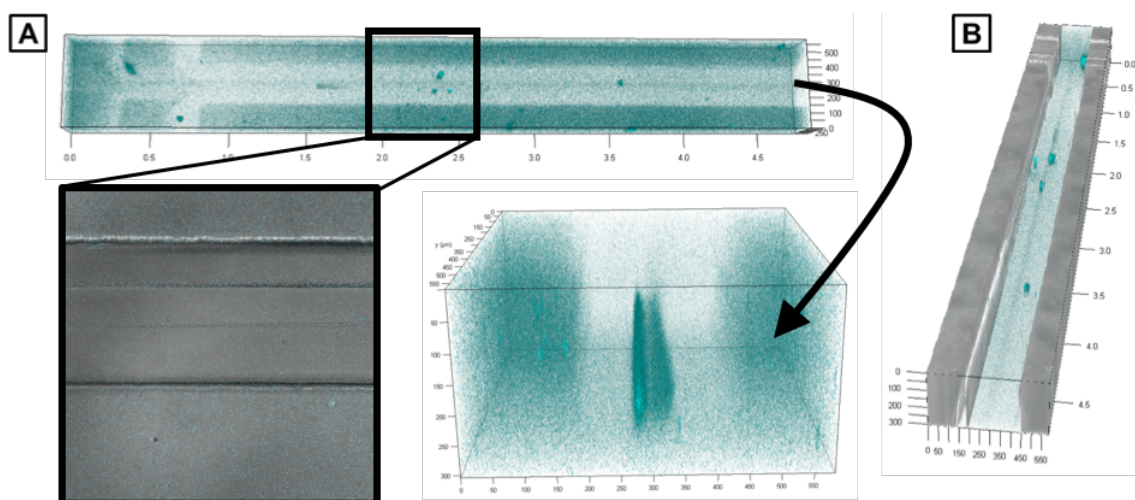


Figure 5.4: Confocal laser microscopy image of the BTA flow-focusing experiment. The top image shows a combined set of single 3D images to display the occurring reaction along the outlet channel, with a cut channel view on the right side to show the surrounding channel dimensions. The black rectangle shows a 2D image of the center of the channel, where the fluorescent BTA stream can be detected. The arrow indicates the front view of the channel in a three-dimensional image, in which the fluorescent circular focused BTA stream is located in the centre of the outlet channel.

We used CLSM to validate the concentric buffer stream profile also for the BTA self-assembly. Fiber formation could, in principle, change the velocity profile which could alter the concentric stream profile. As shown in Figure 5.4, the circular focused BTA fluorescent assemblies are located in the centre of the outlet channel, with an increasing fluorescence along the flow direction. The PDMS autofluorescence at 405 nm laser for excitation allows one to also image the surrounding channel, thus confirming the BTA stream focusing in the centre of the channel.

Whereas excitation at a wavelength of 405 nm allows to validate the stream profile using CSLM, the signal-to-noise-ratio is too weak to be useful for a quantitative analysis. We therefore used fluorescence microscopy using a mercury lamp to obtain a higher fluorescence intensity for quantitative experiments. As seen in Figure 5.5 we well observe the development of the characteristic blue fluorescence in the exit channel at the periphery of the central stream, where the buffer stream has disappeared by interdiffusion with the adjacent streams. This marks the onset of the self-assembly process. The fluorescence intensity steadily increases downstream, indicating the formation of fluorescent fibers. We observe stable flow conditions with no wall contact of the developing hydrogel and no premixing. Videos demonstrating the stability of the flow are available in the Supporting Information.

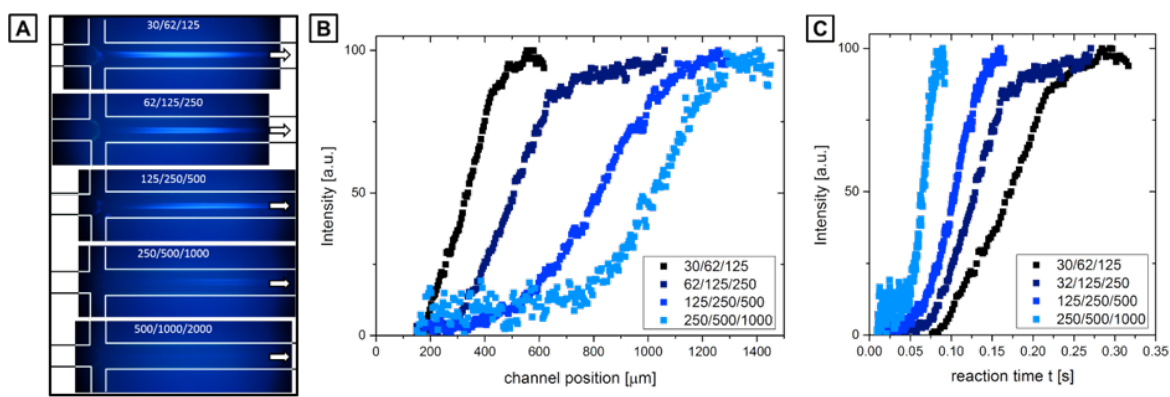


Figure 5.5: (A) Fluorescence microscopy images of the assembly process in the microfluidic exit channel for five different volume flows (left). The arrows indicate the flow direction. The flow rates are indicated in the form $U_{MC}/U_{SC1}/U_{SC2}$ [$\mu\text{l}/\text{h}$] for each single inlet. (B) Normalized averaged intensity distribution along the blue reaction channel. The expected shift of positions with the same relative intensities to larger downstream channel positions with increasing flow rate is well-observed. (C) The same data rescaled against $t = x/\nu$.

For a detailed analysis of the self-assembly process, we analyzed the fluorescence in-

tensity in the microfluidic channels as measured by fluorescence microscopy. In order to image an as large as possible area with high sensitivity along the outlet channel, we used a DSLR camera which was mounted onto the fluorescence microscope. As the area observed with the camera is large and comparable in size to the area illuminated by the mercury lamp, the illumination intensity decreases towards the periphery of the image. To correct for this radially decaying illumination intensity profile and for a slight autofluorescence of the microfluidic chip material, the fluorescence microscopy images of the microfluidic channels containing the flowing trisamide solutions, I_T , of the microfluidic channels containing flowing water, I_W , and of the empty channels, I_E , were measured for the same microfluidic channel, for the same lamp settings and the same flow rates. Then a normalized image, I_N , was calculated according to $I_N = (I_T - I_E)/(I_W - I_E)$ was calculated and used for further analysis as in Figure 5.5B.

Under laminar flow conditions, the elapsed time t after a fluid element has passed channel position x_0 that corresponds to a certain downstream channel position $x_v = x_0 + v \cdot t$. Thus, increasing the flow velocity shifts the positions corresponding to a certain state of the self-assembly process further downstream to larger x values. Keeping the ratios of the flow velocities of the three streams (MC, SC1 and SC2) constant and increasing their absolute value by 1:2:4, the development of the fluorescence intensity in the central channel is systematically shifted further downstream, as expected and observed in Figure 5.5B.

In situ small-angle X-ray scattering and cryo-TEM experiments

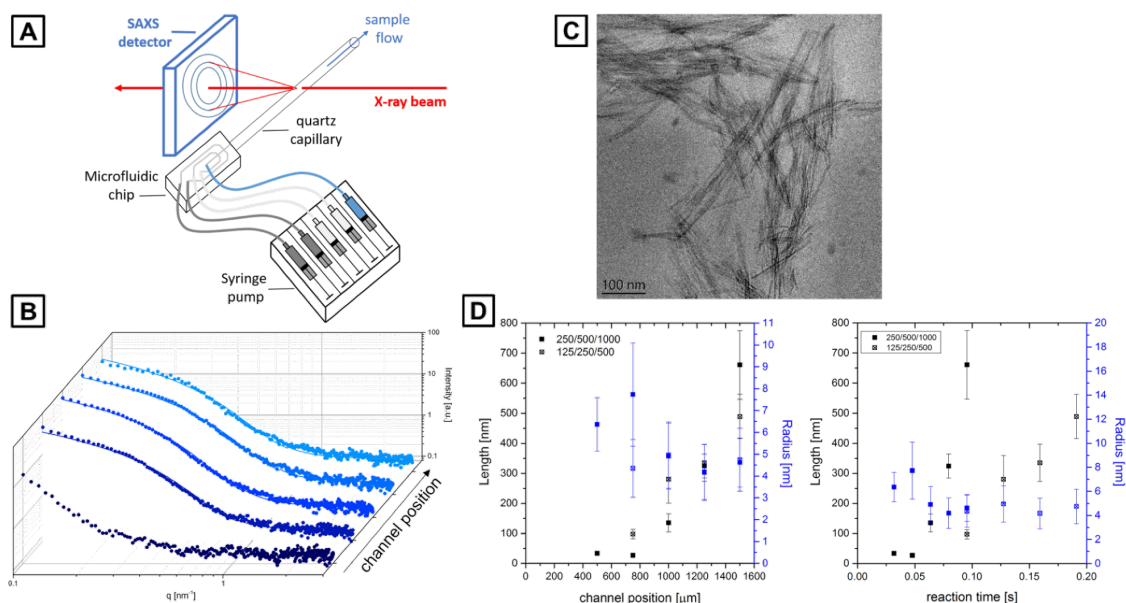


Figure 5.6: (A) Schematic setup of the *in situ* X-ray experiment, using syringe pumps to introduce the reacting solutions into the microfluidic chip. (B) SAXS curves measured at selected positions downstream the outlet capillary with fitted curves for cylindrical structures corresponding to the formation of fibers with a characteristic q^{-1} -scattering. (C) Cryo-TEM image of the nanofibrils collected from the capillary outlet. (D) Evaluated length (black squares) and radii (blue squares) from cylindrical SAXS fits at different channel positions along the outlet channel for the flowrate ratios MC/SC1/SC2 in $\mu\text{L}/\text{h}$ of 250/500/1000 (filled squares) and 125/250/500 (hollow squares) as a function of channel position and reaction time. The error bars represent the polydispersity, calculated by the standard deviation from the cylindrical model fit of the X-ray scattering data.

To investigate the early stages of the BTA self-assembly process we performed *in situ* SAXS experiments. Because the 3D microfluidic chips were fabricated in PDMS, they showed large X-ray absorption which made transmission X-ray scattering experiments difficult. We therefore replaced the exit channel by a thin quartz capillary that was inserted 1 mm behind the second focusing section (SC2). A photograph of the setup can be found in the Supporting Information (see Figure C.4). This hybrid chip consisting of a 3D double focusing design for optimal mixing together with a thin X-ray transparent exit capillary allowed one to obtain scattering patterns with good signal-to-noise ratio under optimal mixing conditions.

To follow the structural evolution during the BTA self-assembly, we recorded SAXS patterns in 250 μm steps downstream the outlet capillary similar to previous experiments.^[30] The scattering patterns were isotropic and were radially averaged to obtain

the corresponding scattering curves as shown in Figure 5.6B. The scattering curves could be well-described by using a model of a solid homogeneous cylinder, where the scattering intensity is given by

$$I(q) = P_{\parallel}(q, L)dP_{\perp}(q, R) \quad (5.1)$$

$$P_{\parallel}(q, L) = \frac{2}{qL} Si(qL) - \left(\frac{\sin\left(\frac{qL}{2}\right)}{\frac{qL}{2}} \right)^2 \quad (5.2)$$

$$P_{\perp}(q, R) = \left(\frac{2J_1(qR)}{qR} \right)^2 \quad (5.3)$$

where q is the modulus of the scattering vector and P_{\parallel} and P_{\perp} are the formfactors parallel and perpendicular to the cylinder axis, $Si(z)$ is the sine integral, and $J_1(z)$ is the Bessel function of the first kind. The formfactors are averaged over a Schulz-Zimm distribution of lengths L and cross-sectional radii R . Details of the calculations and fitting procedure are given in refs.^[31,32]. From fits to the measured scattering curves, the cross-sectional radii and the length of the cylinders could be determined for different positions in the capillary, as shown in Figure 5.6D (see also SI Figure C.5 for SAXS curves at additional flow rates). Beginning from position 2 we observe a characteristic q^{-1} -scattering at low q which is typical for extended cylindrical structures. As shown in Figure 5.6D the cylinders have diameters of approximately 10 nm and grow in length from ca. 50 to more than 200 nm. Because of the position of the beam stop, which limits the smallest accessible scattering angle, lengths larger than 200 nm cannot be determined. The onset of cylinder growth coincides with the increase in fluorescence intensity, shown in Figure 5.5.

To further support the formation of nanofibrils, we performed cryo-TEM of the solutions that exited the outlet capillary. Small portions of the solutions were collected, immediately vitrified and kept under cryogenic conditions for cryo-TEM. Figure 5.6 shows a representative cryo-TEM image where the nanofibrils are observed, showing a tendency to form fiber bundles. The cross-sectional shapes appear to be nonspherical and more ribbon-like such that a range of cross-sectional diameters between 5 and 15 nm is observed, depending on the fiber orientation. These values are consistent with the average value of ca. 10 nm determined by SAXS for a model for fibers with a homogenous spherical cross section. We therefore attempted to fit the measured scattering curves to cylinders with elliptical cross sections but did not obtain better agreement. Alternatively, it is possible that the fibers still have cylindrical cross sections

at the early state of formation, as observed by SAXS, and at a later stage develop a non-spherical cross-section. The observed lengths of >200nm agree well with the fits to the scattering curves (see Supporting Information Figure C.6 for detailed size evaluation and additional Cryo-TEM images). Our experiments therefore demonstrate that at the early self-assembly state nanofibers are formed, concomitant with the observation of a characteristic photoluminescence.

Diffusion-advection-reaction equation

The measured fluorescence intensity along the reaction channel provides a means to determine for the first time an association rate constant for small molecule fiber assembly. The fluorescence intensity is proportional to the concentration of trisamide that has assembled into fibers. The assembly is induced by protonation of negatively charged trisamide upon mixing of the trisamide central stream and the acidic outer stream. The protonation reaction and the subsequent assembly process proceed with a certain rate, which together with mass transport by diffusion and advection determines the distribution of fluorescent trisamides along the reaction channel.

In general, the spatial-temporal evolution of the concentration of educts and products in the interdiffusing streams in the downstream channel is described by the diffusion-advection-reaction equation.^[18,33] Assuming incompressible flow and the diffusion coefficients to be independent of concentration, this equation is given by

$$\frac{\partial c_J}{\partial t} = D_J \nabla^2 c_J - \nu \nabla c_J + R(c_J, c_{J'}) \quad (5.4)$$

where D_J is the diffusion coefficient of component J , ν the local stream velocity, and R the reaction rate of the components. The directions are chosen such that x is parallel to the flow direction, y is the horizontal direction perpendicular to the flow direction, and z is the vertical direction perpendicular to the flow direction.

Under basic conditions, the tricarboxylic acid is in the fully deprotonated state and thus triply negatively charged. The corresponding repulsive Coulomb interactions stabilize the trisamides against aggregation, which is driven by attractive hydrogen bond and π - π -interactions. Upon acidification the trisamides will be protonated which is accompanied by a charge reduction. Eventually, a critical protonation state will be reached where attractive interactions dominate, leading to molecular association and self-assembly into fibers. There are indications that this already occurs at an intermediate protonation state.^[7,34,35]

We can write the corresponding reaction equations for the protonation and self-assembly reactions as



with the deprotonated state T^- , the critical protonation state T^* where association begins, and the first association state T_2 . The corresponding protonation reaction 5.5 occurs with a rate constant k_1 and the subsequent association reaction 5.6 with a rate constant k_2 .

Assuming stationary conditions for the concentration of the intermediate state T^* , we can write the diffusion-advection-reaction equations corresponding to the above reactions as

$$\frac{dc_1}{dt} = D_1 \nabla^2 c_1 - \nu \nabla c_1 - k c_1 c_2 \quad (5.7)$$

$$\frac{dc_2}{dt} = D_2 \nabla^2 c_2 - \nu \nabla c_2 - k c_1 c_2 \quad (5.8)$$

$$\frac{dc_3}{dt} = D_3 \nabla^2 c_3 - \nu \nabla c_3 - k c_1 c_2 \quad (5.9)$$

where $c_1 = [T^-]$, $c_2 = [H^+]$, $c_3 = [T_2]$ and where stationary conditions for the intermediate concentration $[T^*]$ where assumed to write $k_1 = k$ as outlined in the Supporting Information. This set of partial differential equations can be numerically solved for the steady state $\partial c_i / \partial t = 0$ in three dimensions. Details are given in the Supporting Information. As a result, we obtain the concentration profiles $c_j(x, y, z)$ for all three components. As the images taken by fluorescence microscopy are a projection of $c_3(z)$ onto the x,y-plane, we numerically integrated the concentration along the z-direction over the height of the channel to obtain the concentration $c_3(x, y)$, which can be directly compared to the fluorescence images of the experiments.

Table 5.2: Parameters and values used for the numerical calculation of the concentration profiles shown in Figure 5.7B, F. All parameters were set to constant values whereas the rate constant was adjusted to achieve best agreement with the experimental results.

Parameter	Value
Channel length L	1250 μm
Channel width w	230 μm
Channel height h	250 μm
Central stream width w_i	40 μm
Buffer stream width w_b	0 μm
Trisamide T^- diffusion coefficient D_1	$2 \cdot 10^{-9} \text{ m}^2/\text{s}$
Proton H^+ diffusion coefficient D_2	$2 \cdot 10^{-9} \text{ m}^2/\text{s}$
Aggregate T_2 diffusion coefficient D_3	$1 \cdot 10^{-11} \text{ m}^2/\text{s}$
Trisamide BTA concentration c_1^0	0.011 mol/L
Proton concentration c_2^0	0.001 mol/L
Rate constant k	$4 \cdot 10^{-4} \text{ mol/Ls}$
Mean velocity ν	3.92 mm/s

For the model calculations we used the dimensions of the microfluidic reaction channel, the central stream, the buffer stream, the flow velocity and the concentrations of trisamide and protons (pH-values) as used in the experiments. The values are summarized in Table 5.2. The diffusion coefficients that gave best agreement between calculation and experiments are in typical ranges expected for small molecule diffusion ($\approx 10^{-9} \text{ m}^2/\text{s}$) and aggregate diffusion ($\approx 10^{-11} \text{ m}^2/\text{s}$). The procedure for optimizing the agreement between measured and calculated intensity distribution involved iterations of fixing the diffusion coefficients to given values and varying the k -value for best agreement. The calculated intensity profiles sensitively depended on the value of the reaction rate constant k , for which a value of 40000 mol/Ls gave the best agreement. As shown in the Supporting Information, this value would correspond to a reaction half time of 12.5 ms in a simple stirred reactor.

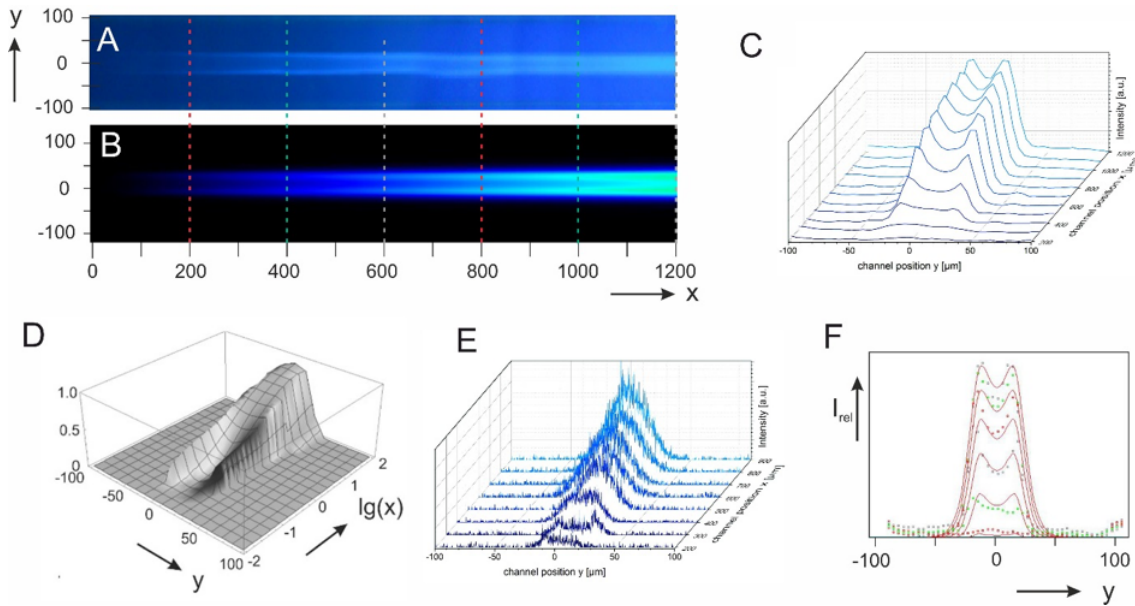


Figure 5.7: Fluorescence microscopy image of the developing fluorescence intensity in the exit channel (A) together with the calculated concentration of BTA assemblies (B). We observe maxima at both peripheries of the central stream due to formation of fluorescent BTA assemblies. The vertical lines indicate positions, where the measured intensity and the calculated concentrations were measured across the channel section and quantitatively compared in (F). (C) Stack plot of the fluorescence intensity measured in (A). (D) 2D concentration profile of BTA assemblies as calculated with the analytical solution in eq. 5.10. The concentration profile qualitatively shows the saturating double peak features that are observed in the experiment. (E) Fluorescence intensity profile of Ca-Green formation, where due to the high diffusivity of the reaction product the central minimum between the peripheral peaks quickly disappears due to fast interdiffusion. (F) Quantitative comparison of the measured fluorescence intensity and the calculated BTA concentration, which allowed the determination of the rate constant of the BTA assembly.

Figure 5.7 shows a comparison of the fluorescence intensity measured experimentally along the outlet channel (Figure 5.7A) together with the calculated concentration profile $c_3(x, y)$ for the aggregates (Figure 5.7B) using the parameters given in Table 5.2. We observe good agreement between the experimentally determined fluorescence intensity and the calculated aggregate concentration. Figure 5.7C shows a stack plot of the normalized fluorescence intensity at $100 \mu\text{m}$ intervals downstream the outlet channel. We observe the formation of a characteristic double peak whose intensity increases and finally saturates in the downstream flow.

Fig. 5.7D shows the calculated concentration profile $c_3(x, y)$ calculated for the midplane in the two-dimensional case. Assuming the laminar flow with mass transport in the flow direction being dominated by advection (Peclet number $Pe_x \gg 1$) and mass transport

in the perpendicular direction being dominated by diffusion ($Pe_y \ll 1$), with an almost constant velocity across the center of the channel, the concentrations can be obtained in the analytical form. The derivation is outlined in the Supporting Information. The calculated profile in Figure 5.7D corresponds to

$$c_3(x, y) = \frac{kx}{\nu} c_1(x, y) c_2(x, y) \quad (5.10)$$

$$c_1(x, y) = c_1^0 \left[1 + \frac{1}{2} \left\{ \operatorname{erf} \left(\frac{y + \frac{w_i}{2}}{\sqrt{\frac{4D_2x}{\nu}}} \right) - \operatorname{erf} \left(\frac{y - \frac{w_i}{2}}{\sqrt{\frac{4D_2x}{\nu}}} \right) \right\} \right] \quad (5.11)$$

$$c_2(x, y) = c_2^0 \left[1 + \frac{1}{2} \left\{ \operatorname{erf} \left(\frac{y - \frac{w_i}{2}}{\sqrt{\frac{4D_2x}{\nu}}} \right) - \operatorname{erf} \left(\frac{y + \frac{w_i}{2}}{\sqrt{\frac{4D_2x}{\nu}}} \right) \right\} \right] \quad (5.12)$$

with the same parameters as in Table 5.2 and where $\operatorname{erf}(x)$ denotes the error function. The derivation is given in the Supporting Information. The calculation shows that the characteristic double peak only emerges and persists if the diffusive transport of the aggregates, that is, the fibers, is much slower compared to the diffusive transport of BTA and the acid. This demonstrates that BTA already at an early stage forms a low diffusivity fiber layer upon self-assembly, which corresponds to a localized hydrogel stream.

If slow diffusive transport of the aggregates causes the characteristic double peak, it should be absent when the reaction product has a comparable diffusivity to the reaction educts. This was investigated with the model reaction of Calcium-Green-5N (CG5N) which upon reaction with Ca^{2+} forms a green fluorescent dye. When using the same flow conditions with CG5N in the main stream (MC) and CaCl_2 in the second focusing stream (SC2), a characteristic green fluorescence emerges in the middle of the outlet channel. Details of the experiment are provided in the Supporting Information. The main result is shown in Figure 5.7E, where only at the earliest stage of the reaction a weak double peak is observed, which then quickly merges to form a single broad peak in the center of the reaction channel; thus supporting the conclusion that a low mobile hydrogel stream is formed upon BTA assembly.

Figure 5.7F shows a measured normalized fluorescence intensity distribution at 200 nm intervals along the reaction channel together with the concentration profile $c_3(x, y)$ of assembled trisamide, calculated from eq. 5.4 without approximations. The calculation well reproduces the double peak with a continuous increase of the fluorescence inten-

sity downstream the reaction channel. Nearly quantitative agreement between calculation and experiment could be obtained with a rate constant of $k = 4 \cdot 10^3 \text{ M}^{-1}\text{s}^{-1}$. This value can be compared to the rate constant for diffusion-limited aggregation $k_f = 8RT/(3\eta)$, which for water with a viscosity of 0.001 Pa·s at 25°C is equal to $k_f = 6.6 \cdot 10^9 \text{ M}^{-1}\text{s}^{-1}$ and thus very much faster. Fast reactions such as the quenching of NATA (N-acetyl-tryptophanamide) fluorescence by N-bromosuccinimide (NBS) have bimolecular rate constants of $k = 7.5 \cdot 10^5 \text{ M}^{-1}\text{s}^{-1}$.^[36] This is in a similar range as fast protonation reactions, where bimolecular rate constants of $k = 2.1 \cdot 10^5 \text{ M}^{-1}\text{s}^{-1}$ have been reported.^[18] For T-jump induced fast amphiphile self-assembly processes such as the sphere-to-rod transition of a CE surfactants, bimolecular reaction rates of $k = 4.4 \cdot 10^6 \text{ M}^{-1}\text{s}^{-1}$ for the shorter chain C_{14}E_8 , and $k = 8.5 \cdot 10^4 \text{ M}^{-1}\text{s}^{-1}$ for longer chain C_{16}E_8 -surfactants were found.^[37] Thus, the investigated BTA assembly occurs at a very similar rate, typical for supramolecular self-assembly of larger molecules.

5.5. Conclusion

We demonstrated that 3D double focusing microfluidic devices provide a powerful means to study the kinetics of fast self-assembly processes. Compared to 2D single focusing devices they avoid wall contact and premixing of the reacting streams, localizing them into the center of the reaction channel. This is essential in order to obtain controlled and well-defined interdiffusion and reaction conditions. The 3D flow profile was validated by CLSM using streams of fluorescein and eosin Y solutions.

The 3D device was used to investigate the pH-induced self-assembly of a model hydrogelator, BTA, into nanofibers. The formation of the fiber assemblies is accompanied by blue photoluminescence, which can be monitored along the reaction channel. This is an important first self-assembly step before the subsequent formation of the hydrogel. The 3D profile was validated by CLSM, and for a quantitative analysis, it was determined by fluorescence microscopy. By solving the advection-reaction-diffusion equation, the association rate constant of a hydrogelator could be determined for the first time. The analysis shows that a localized hydrogel stream is formed early in the self-assembly process. Using a hybrid chip with integrated glass capillary, it was possible to monitor nanofiber formation along the reaction channel by SAXS. 3D 2F-flow focusing thus provides a method to study the reaction rate and structures of fast self-assembly processes by combination with fluorescence microscopy and SAXS and can be successfully applied to reveal for the first time the early self-assembly steps during small molecule hydrogel formation.

References

- [1] Chirani, N.; L'Hocine, Y.; Gritsch, L.; Motta, F. L.; Chirani, S.; Fare, S. *Journal of Biomedical Science* **2015**, *4*, 2–13.
- [2] Du, X.; Zhou, J.; Shi, J.; Xu, B. *Chemical Reviews* **2015**, *115*, 13165–13307.
- [3] Chen, C.; Gu, Y.; Deng, L.; Han, S.; Sun, X.; Chen, Y.; Lu, J. R.; Xu, H. *Applied Material Interfaces* **2014**, *6*, 14360–14368.
- [4] Song, F.; Zhang, L.-M. *Journal of Physical Chemistry B* **2008**, *112*, 13749–13755.
- [5] Larsen, T. H.; Furst, E. M. *Physical Review Letters* **2008**, *100*, 146001.
- [6] Larsen, T. H.; Branco, M. C.; Rajagopal, K.; Schneider, J. P.; Furst, E. M. *Macromolecules* **2009**, *42*, 8443–8450.
- [7] Chen, L.; Morris, K.; Laybourn, A.; Elias, D.; Hicks, M. R.; Rodger, A.; Serpell, L.; Adams, D. J. *Langmuir* **2010**, *26*, 5232–5242.
- [8] Martin, A. D.; Wojciechowski, J. P.; Robinson, A. B.; Heu, C.; Garvey, C. J.; Ratcliffe, J.; Waddington, L. J.; Gardiner, J.; Thordarson, P. *Scientific Reports* **2017**, *7*, 43947.
- [9] Knight, J. B.; Vishwanath, A.; Brody, J. P.; Austin, R. H. *Physical Review Letters* **1998**, *80*, 3863–3866.
- [10] Pollack, L.; Tate, M. W.; Darnton, N. C.; Knight, J. B.; Gruner, S. M.; Eaton, W. A.; Austin, R. H. *Proceedings of the National Academy of Science* **1999**, *96*, 10115–10117.
- [11] Pollack, L. *Biopolymers* **2011**, *95*, 543–549.
- [12] Pabit, S. A.; Hagen, S. J. *Biophysical Journal* **2002**, *83*, 2872–2878.
- [13] Simonnet, C.; Groisman, A. *Applied Physics Letters* **2005**, *87*, 114104.
- [14] Russell, R.; Millett, I. S.; Tate, M. W.; Kwok, L. W.; Nakatani, B.; Gruner, S. M.; Mochrie, S. G. J.; Pande, V.; Doniach, S.; Herschlag, D.; Pollack, L. *Proceedings of the National Academy of Sciences* **2002**, *99*, 4266–4271.
- [15] Kinahan, M. E.; Filippidi, E.; Köster, S.; Hu, X.; Evans, H. M.; Pfohl, T.; Kaplan, D. L.; Wong, J. *Biomacromolecules* **2011**, *12*, 1504–1511.
- [16] Anderson, J. R.; Chiu, D. T.; Jackman, R. J.; Cherniavskaya, O.; McDonald, J. C.; Wu, H.; Whitesides, S. H.; Whitesides, G. M. *Analytical Chemistry* **2000**, *72*, 3158–3164.

- [17] Park, H. Y.; Qiu, X.; Rhoades, E.; Korlach, J.; Kwok, L. W.; Zipfel, W. R.; Webb, W. W.; Pollack, L. *Analytical Chemistry* **2006**, *78*, 4465–4473.
- [18] Salmon, J.-B.; Cubrocq, C.; Tabeling, P.; Charier, S.; Alcor, D.; Jullien, L.; Ferrage, F. *Analytical Chemistry* **2005**, *77*, 3417.
- [19] Schuetze, F.; Stempfle, B.; Jungst, C.; Woll, D.; Zumbusch, A.; Mecking, S. *Chemical Communications* **2012**, *48*, 2104–2106.
- [20] Brennich, M. E.; Nolting, J.-F.; Dammann, C.; Noeding, B.; Bauch, S.; Herrmann, H.; Pfohl, T.; Koester, S. *Lab on a Chip* **2011**, *11*, 708–716.
- [21] Hakansson, K. M. O.; Fall, A. B.; Lundell, F.; Yu, S.; Krywka, C.; Roth, S. V.; Santoro, G.; Kwick, M.; Prael-Wittberg, L.; Wagberg, L.; Söderberg, L. D. *Nature Communications* **2014**, *5*, 4018.
- [22] With, S.; Trebbin, M.; Bartz, C. A.; Neuber, C.; Dulle, M.; Yu, S.; Roth, S. V.; Schmidt, H.-W.; Foerster, S. *Langmuir* **2014**, *30*, 12494–12502.
- [23] Bernet, A.; Albuquerque, R. Q.; Behr, M.; hoffmann, S. T.; Schmidt, H.-W. *Soft Matter* **2012**, *8*, 66–69.
- [24] Howe, R. C. T.; Smalley, A. P.; Guttenplan, A. P. M.; Doggett, M. W. R.; Eddleston, M. D.; Tan, J. C.; Lloyd, G. O. A. *Chemical Communications* **2013**, *49*, 4268–4270.
- [25] Adams, D. J.; Butler, M. F.; Frith, W. J.; Kirkland, M.; Mullen, L.; Sanderson, P. A. *Soft Matter* **2009**, *5*, 1856.
- [26] Hong, Y.; Lam, J. W. Y.; Tang, B. Z. *Chemical Society Reviews* **2011**, *40*, 5361–5388.
- [27] Mei, J.; Hong, Y.; Lam, J. W. Y.; Qin, A.; Tang, Y.; Tang, B. Z. *Advanced Materials* **2014**, *26*, 5429–5479.
- [28] Xia, Y.; Whitesides, G. M. *Annual Review of Materials Research* **1998**, *28*, 153–184.
- [29] Xia, Y.; Whitesides, G. M. *Angewandte Chemie International Edition* **1998**, *37*, 550–575.
- [30] Chen, X.; Schroeder, J.; Hauschild, S.; Rosenfeldt, S.; Dulle, M.; Foerster, S. *Langmuir* **2015**, *31*, 11678–11691.
- [31] Foerster, S.; Apostol, L.; Bras, W. *Journal of Applied Crystallography* **2010**, *43*, 639–646.

- [32] Foerster, S.; Zielske, K.; Schellbach, C.; Sztucki, M.; Lindner, P.; Perlich, J. *Advances in Colloid and Interface Science* **2011**, *163*, 53–83.
- [33] Hundsdorfer, W.; Verwer, J. G. *Springer Series in Computational Mathematics*; 2003; Chapter Numerical solution of time-dependent advection-diffusion-reaction equations., p 33.
- [34] Tang, C.; Smith, A. M.; Collins, R. F.; Ulijn, R. V.; Saiani, A. *Langmuir* **2009**, *25*, 9447–9453.
- [35] Wallace, M.; Iggo, J. A.; Adams, D. J. *Soft Matter* **2017**, *13*, 1716.
- [36] Roder, H.; Maki, K.; Cheng, H.; Shastry, M. C. R. *Methods* **2004**, *34*, 15–27.
- [37] Ilgenfritz, G.; Schneider, R.; Grell, E.; Lewitzki, E.; Ruf, H. *Langmuir* **2004**, *20*, 1620–1630.

Chapter 6

6. Publication IV

Millisecond CdS nanocrystal nucleation and growth studied by microfluidics with in-situ spectroscopy.

Susanne Seibt^{a,b}, Paul Mulvaney^b, Stephan Förster^{c,*}

^a*Physical Chemistry I, University of Bayreuth, Universitätsstraße 30, 95447 Bayreuth, Germany.*

^b*School of Chemistry, The University of Melbourne, VIC-3010 Melbourne, Australia.*

^c*JCNS-1/ICS-1, Forschungszentrum Jülich, 52428 Jülich, Germany.*

The results presented in this chapter were submitted to *Colloids and Surfaces A: Physicochemical and Engineering Aspects*.

Individual contribution of involved authors

I performed all experiments and analysed the data. Together with Prof. Stephan Förster and Prof. Paul Mulvaney I wrote the manuscript.

6.1. Abstract

Microfluidic methods allowing fast mixing allow studying fast chemical reactions on the millisecond time scale. Here the kinetics of nucleation and growth of thioglycerol- and L-cysteine-capped CdS quantum dots is investigated using a continuous-flow microfluidic device in combination with *in-situ* microscopy and spectroscopic techniques. A microfluidic device is developed to three-dimensionally focus a central aqueous Cd²⁺-stream, which is completely enclosed by a water buffer layer, into a stream of aqueous S²⁻. Diffusion-limited nucleation and growth of CdS nanoparticles occurs in the buffer layer downstream the reaction channel which can be followed by *in-situ* confocal laser scanning microscopy and UV-Vis absorption spectroscopy on the time scale of the first 1 - 100 milliseconds, giving direct and unique insights into early colloidal crystal nucleation and growth processes.

6.2. Introduction

Semiconducting nanoparticles, widely known as quantum dots, exhibit remarkable optical properties and are finding applications in diagnostics and electronic devices.^[1,2] Cadmium sulfide (CdS) quantum dots, as II-IV semiconducting nanocrystals, show especially good optical transmittance and a wide band gap of 2.4 eV.^[2-4] Over the last few decades, their unique properties have led to wide spread applications in solar cells, photodetectors, light-emitting diodes or biological labelling, for which the ability to precisely and reproducibly size-tune their optical properties is decisive.^[4] Various synthesis routes to batch processing have been developed to engineer the size, and linked to that, the band gap of CdS nanoparticles.^[2,5-8] However, the fundamental nucleation and growth mechanism behind these syntheses is still unclear, largely as a consequence of their fast reaction kinetics.^[3,9] Previous *in-situ* mechanistic investigations slowed the reaction down by adding stabilising ligands to the initial synthesis solution^[7] or transferring the synthesis to retarding media, like microemulsions^[10] or polymer films.^[11,12] This results in a deceleration of the normally millisecond-second time scale synthesis to one that takes several minutes. However, the addition of stabilizers or the presence of retarding media can significantly alter the nucleation and growth process.

One of the key challenges in macroscopic batch synthesis of nanoparticles is to achieve uniform reactor conditions, such as heat transfer or mixing, as well as to monitor these conditions *in-situ*, which is only possible by taking aliquots out of the reacting solution. Microfluidics has become a powerful tool with great impact in many scientific fields of

modern biology and chemistry for the manipulation of fluids in micrometer-sized channels to finely control these conditions. The fundamental fluid physics change dramatically on microscopic scales when compared to macroscale fluid physical phenomena. It is here that microfluidics is gaining more and more importance for the investigations of nanoparticle synthesis.^[13] Several researchers used microreactors with turbulent^[14,15] or laminar flow,^[13,16] for well-defined synthesis of nanomaterials, finding hydrodynamic focusing to be one of the most efficient techniques. Nanoparticles made from a range of substances, including organic,^[13,14] metallic^[15-17] and semiconductor materials^[18-20] can be synthesized taking advantage of the high reproducibility and real-time process monitoring offered by microfluidics.

Microfluidic investigations of the nucleation and growth mechanisms of CdS nanocrystals range from *in-situ* analysis in droplets,^[21,22] to free-jet setups,^[3] and continuous flow experiments with steady-state reagent streams.^[9] However, these existing technologies face serious challenges due to wall-contact of the emerging CdS nanocrystals at the edges of the microfluidic device, which complicates the spectroscopic analysis of the growing nanoparticles. Furthermore, the interface of droplets a particle aggregates could act as a seed for heterogeneous nucleation.

Three-dimensional microfluidic devices with hydrodynamic focusing, specially designed as reported earlier^[23] would allow to sequentially focus the Cd²⁺ stream in the centre of the channel, separated from the S²⁻ solution through a water buffer layer, to investigate the unperturbed nucleation and growth kinetics for the first time. All-PDMS multilayer devices in combination with laser-cut glass capillaries show complete optical transparency, hence allowing the detection of absorption and emission behaviour *in-situ* using confocal laser scanning microscopy (CLSM) and spectroscopy. Here we investigate the fast nucleation and growth kinetics of thioglycerol- and L-cysteine-stabilised CdS nanocrystal syntheses, using a newly developed microfluidic design to observe undisturbed particle formation for the first time on millisecond time scales. We utilise CLSM to monitor the characteristic fluorescence appearing with growth of the CdS nanoparticles, as well as *in-situ* absorption spectroscopy to detect the shifting absorption edge with position downstream the reaction channel which corresponds to reaction time. This diffusion-limited CdS nanocrystal synthesis in microfluidics provides time-resolution on the millisecond time scale and stable, well-defined conditions to investigate nucleation *ab initio*.

6.3. Experimental Methods

Cadmium chloride, cadmium nitrate, sodium sulfide, thioglycerol and L-cysteine were of analytical grade or of highest purity available and used as received from Sigma Aldrich. Microfluidic synthesis of CdS nanoparticles in aqueous solution was reported by Sounart et al.^[9] who utilized a simple y-shaped channel system creating a supersaturated region at the stream boundary in flow. We used a three-dimensional channel geometry with double hydrodynamic focusing (see Fig. 6.1), resulting in diffusion-limited nucleation and growth of the CdS nanocrystals along the downstream channel.^[23]

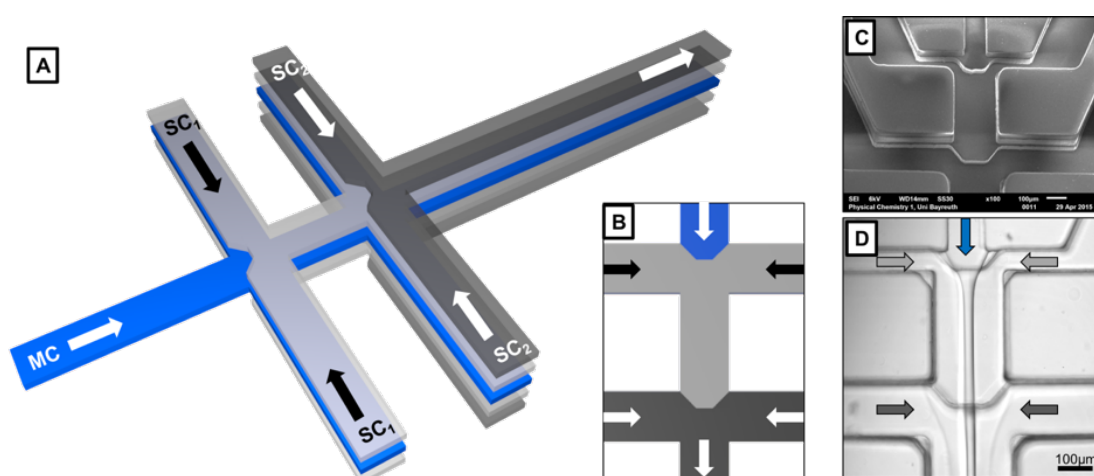


Figure 6.1: (A) Schematic view of the five-layer channel structure for three-dimensional focusing with five inlets. The main channel (MC) as the middle layer shown in blue (height $50\ \mu\text{m}$), the first side channel (SC1) with two more layers in bright grey (height $150\ \mu\text{m}$) and the second side channel (SC2) with another two additional layers in dark grey (height $250\ \mu\text{m}$). (B) Top view scheme of the channel design. The arrows indicate the flow direction of liquids introduced in the channel. (C) Scanning electron microscopy (SEM) image of one of the PDMS replicas showing the layered structure. (D) Optical microscopy image of the channel double cross with the hydrodynamic focused flow profile.

A new synthesis using cadmium chloride and sodium sulfide for the production of thioglycerol-stabilised CdS nanoparticles^[4,5,24] and an established method for the batch preparation of L-cysteine-capped nanocrystals^[25] were adapted to the microfluidic reactor for synthesis in continuous flow.

Thioglycerol-stabilised CdS synthesis

As a Cd^{2+} source, cadmium chloride powder was dissolved in deionised water (50 mM and 100 mM) before the stabilising agent thioglycerol (TG) was added to the solution in

the ratios 1:1, 1:2, 1:10 and 1:20 Cd: TG. The sulfide source (100 mM Na₂S) was dissolved in pure deionised water with no thioglycerol.

L-cysteine-stabilised CdS synthesis

The cadmium source (50 mM Cd(NO₃)₂) and the sodium source (100 mM Na₂S) were dissolved in pure deionised water. As a buffer-layer solution, a 150 mM L-cysteine solution in Millipore water was prepared.

Fabrication of microfluidic devices

The microchannel master of the microfluidic device was prepared using photo lithography.^[26] The microchannel network was designed in AutoCAD 2011 (Autodesk) and printed on a mask foil with UV-absorbent ink. The all-PDMS devices were fabricated based on a procedure described in the literature^[27] using soft lithography with Polydimethylsiloxane Sylgard® 184. To achieve three-dimensional hydrodynamic focusing, a five-layer channel design was used. For this, two structured PDMS stamps were first aligned with each other and then bonded. The resulting outlet channel has a width, w , of 230 μm and a height, h , of 250 μm , consisting of five individual layers of 50 μm each from the photolithographic process. The distance between the two cross junctions is 300 μm . A glass capillary with an outer diameter of 400 μm and 10 μm wall-thickness was inserted in the outlet channel right after the last mixing cross to form a hybrid chip providing scattering transparency. These devices could then be connected to a microfluidic high precision syringe pump system (NEMESYS, cetoni GmbH, Germany) with PE tubings.

Microfluidic experiments

For the synthesis of thioglycerol-stabilised CdS nanoparticles, the aqueous cadmium chloride / TG solution was introduced into the main channel (MC), while deionised water was fed into the first side channels (SC1) to function as a buffer layer, and the aqueous sodium sulfide solution was introduced into the second side channels (SC2). The flow velocities of the pumping units were set to $U_{MC} = 235.3 \mu\text{L/h}$ and $U_{SC1} = U_{SC2} = 941.2 \mu\text{L/h}$, with an overall outlet flow of $U = 4000 \mu\text{L/h}$ and an overall outlet flow speed of 19,32 mm/s. For the use of hybrid devices with inserted glass capillary, the flow velocities needed to be adjusted, resulting in an increased overall flowrate, to shift the beginning of nucleation out of the PDMS device part into the transparent region of the glass capillary. Hence, the pumping units were set to $U_{MC} = 888.9 \mu\text{L/h}$ and $U_{SC1} = U_{SC2} = 1777.8 \mu\text{L/h}$, with an overall outlet flow of $U = 8000 \mu\text{L/h}$ and an

overall outlet flow speed of 38,65 mm/s. For the synthesis of L-cysteine-capped CdS nanocrystals, the aqueous cadmium nitrate solution was introduced into the MC, while the L-cysteine solution was introduced into SC1 and sodium sulfide was introduced into SC2. The pumping units for this microfluidic synthesis were set to $U_{MC} = 61 \mu\text{L/h}$ and $U_{SC1} = U_{SC2} = 610 \mu\text{L/h}$, with an overall outlet flow of $U = 2501 \mu\text{L/h}$ and an overall outlet flow speed of 12,08 mm/s. To prevent reactions in the channel before a stable flow could be established and to clear the tubing and device of air bubbles, the entire microfluidic chip setup was flushed and filled with water prior to the experiment.

Sepctroscopic analysis

The confocal laser scanning microscopy (CLSM) experiments were performed using a Leica TCS SP8 with a Leica DMI6000B microscope. A laser with a wavelength of 405 nm and a detection range of 410 – 650 nm were used to monitor the appearance of the characteristic fluorescence of growing CdS nanoparticles in solution. *In-situ* photoluminescence was investigated by wavelength (λ)-scans between 420 nm and 750 nm with a detection bandwidth of 10 nm and a λ -detection stepsize of 3 nm. For *in-situ* absorption spectroscopy measurements, an OceanOptics UV-Vis setup, composed of a HR2000 detector (detection range 200 – 1100 nm) in combination with a DH-2000-BAL UV-Vis-NIR lightsource (deuterium and halogen lamp, illumination range 215 – 2000 nm) and QP400-2-SR optical fibres (operating range 200 – 1100 nm), was used. The XRD measurements were performed using a Bruker D8 Advance Diffractometer with standard Ni-filtered Cu K_{α} radiation.

6.4. Results and Discussion

The channel design used in this work was optimised and tested as described in a previous publication.^[23] The aim was to use a continuous flow device with three-dimensional hydrodynamic focusing to focus the main channel Cd^{2+} -solution at a sufficient distance from the channel walls in the downstream channel. In addition, a buffer layer was created between reactant-containing central and focusing streams to prevent their pre-mixing. This allows the investigation of CdS nanoparticle nucleation and growth in the buffer layer in steady state conditions of continuous flow, due to the diffusion-limited reaction of Cd^{2+} with S^{2-} , which is occurring downstream the outlet channel.

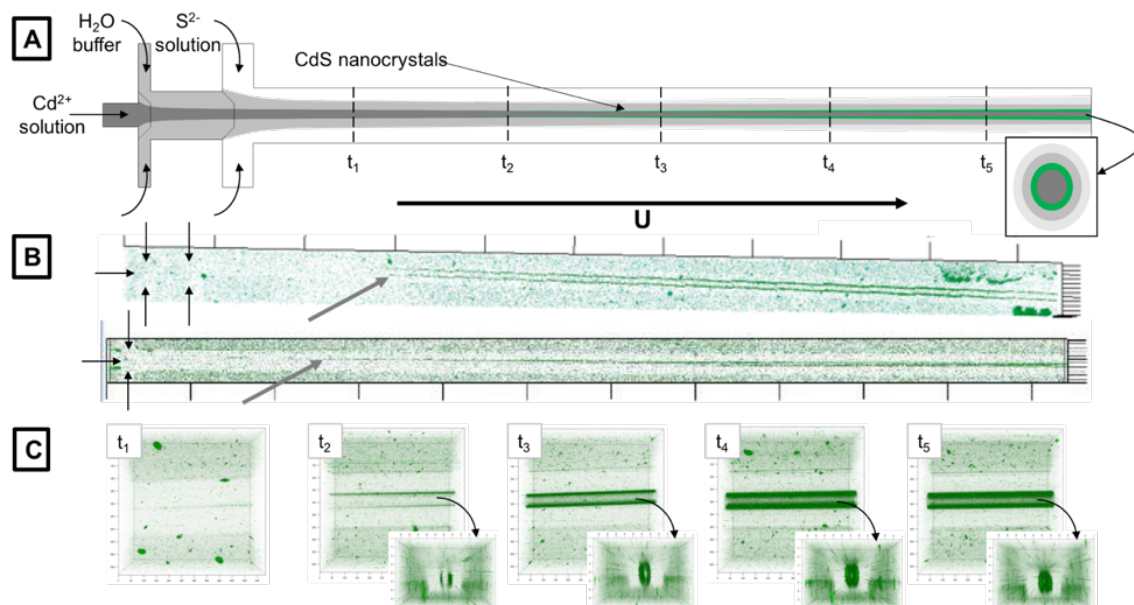


Figure 6.2: (A) Sketch of the microfluidic continuous flow device with hydrodynamic focusing, showing the interdiffusion of the different solutions along the outlet channel. The green colour indicates growing CdS nanocrystals. (B) Confocal microscopy image of the full channel during the CdS nanoparticle synthesis with thioglycerol (top) and L-cysteine (bottom) as stabilising agents. The grey arrow indicates the region of first detection of fluorescence due to nucleation and growth of CdS nanoclusters. (C) Three-dimensional CLSM scans at different times t_1 to t_5 along the outlet channel in top and front view showing the circular flow profile.

Figure 6.2A shows the schematic design of the three-dimensional microfluidic device. The interdiffusion of the different solutions along the channel is shown in grey scale. The green streams indicate the appearing fluorescence due to growing CdS nanocrystals. The cross-sectional view shows the intended circular flow profile, preventing contact between the channel walls and the growing nanoparticles (green). With 3D-reconstructions from a set of confocal microscopy images of the thioglycerol-stabilised CdS synthesis (see Fig. 6.2B, top) and the L-cysteine-stabilised CdS synthesis (see Fig. 6.2B, bottom), we can see for the first time the start of the nucleation and growth of CdS nanocrystals, indicated by their characteristic fluorescence, in the downstream channel during a real-time synthesis on the millisecond timescale. The grey arrow indicates the region of first detection of fluorescence due to the formation of CdS nuclei. Additionally, we are able to shift the onset point of the nucleation process further downstream by increasing the flow velocity or the thickness of the buffer layer. Three-dimensional CLSM scans of single positions at different times (t_1 to t_5) after the first contact of all layers ($t = 0$) at the second mixing cross are shown in Figure 6.2C. The top view shows an augmented presentation of the circularly-focused growing nanoparticles from directly after the second crossing t_1 without nanocrystal emission,

to the beginning of the nucleation and the connected appearance of fluorescence at t_2 , and increasing fluorescence along the downstream channel at $t_3 - t_5$. By rotating the 3D stack 90 degrees, the focusing and channel dimensions are visible. The confocal microscopy scan was taken in the dimensions $w = 500 \mu\text{m}$, $l = 500 \mu\text{m}$ and $h = 300 \mu\text{m}$ to image the whole microfluidic channel ($w = 230 \mu\text{m}$, $h = 250 \mu\text{m}$).

Both thioglycerol-stabilised and L-cysteine-stabilised syntheses generate a stable, yellow-coloured and yellow-green fluorescent CdS nanoparticle solution. Transmission electron microscopic analysis for one example of each sample is shown in the Supporting Information, Figure D.1. Uniform particles with diameter 2.6 nm or 3.2 nm were produced for TG and L-cys stabilisation respectively. The absorption spectra shown in Figure D.1 display the typical absorption edge of quantum dots, shifting to higher wavelength with increasing size of the nanoparticle.^[6] Typical trap emission from the CdS nanocrystals can be seen in the emission spectra, which is broadened by the dispersity of the microfluidic synthesised particles. The characteristic fluorescence peak at 550 nm for a nanoparticle size of 2.6 nm and 570 nm for a particle size of 3.2 nm can be clearly observed.^[4,28]

For measuring the optical properties of nucleation and growth *in-situ* during the reaction along the downstream channel, the system had to be transferred from the all-PDMS device to a hybrid microfluidic chip with an inserted glass capillary (shown in the Supporting Information, Figure D.2A). These devices have the advantage of complete optical and X-ray transparency while the hydrodynamic focusing could be easily adjusted by the design of the mixing crosses in the PDMS part. To prove that the focused flow profile of the different streams remains undisturbed by inserting the capillary, confocal optical microscopy images were taken. Figure D.2B shows the hydrodynamic focused reaction solution streams without interfering turbulences after passing the capillary orifice. Thus, the cadmium sulfide nanoparticle synthesis with either stabiliser could be adapted to the new PDMS-glass hybrid device, shown in Figure D.3. To position the point of onset of nucleation and growth (as detected by fluorescence) in the glass capillary after leaving the PDMS device, we increased the flow rate and adjusted the buffer layer thickness to produce a stable reaction system along the channel. The circularly focused, fluorescent stream of growing CdS nanocrystals along the capillary is shown in Figure D.3. Moreover, as the capillary provides an elongated outlet channel and thereby allows the reaction to be followed for a longer time, the complete interdiffusion of the reacting ions to form a fully photoluminescent central layer can be seen (Fig. D.3B right). The surrounding glass appears in the form of a

fluorescent ring as a result of inelastic scattering of the incoming light (405 nm laser) at the silica glass. This Raman scattering effect leads to a weak intensity but broad emission signal between 450 and 700 nm.

The spectral distribution of the thioglycerin-stabilised CdS nanoparticles in absorption and emission was measured at several positions along the capillary to investigate the influence of various synthetic parameters.

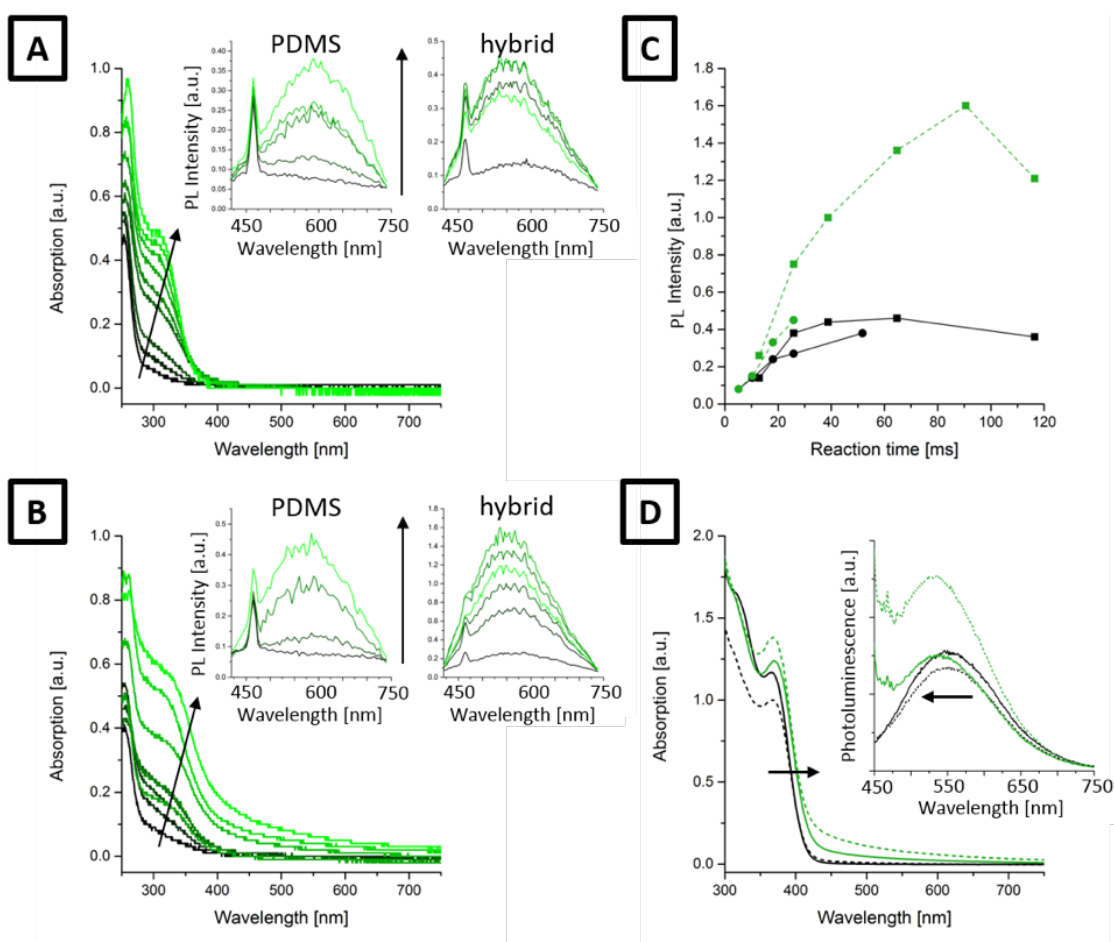


Figure 6.3: Spectroscopic investigations of the nucleation and growth kinetics *in-situ* for a Cd:S ratio of 1:2 (A) and 1:1 (B). The UV-Vis spectra show the characteristic appearance of the absorption edge for CdS nanoparticles, the arrow indicates the shift during the reaction. The emission spectra shown for the synthesis in PDMS (left) and hybrid (right) microfluidic devices shows an increase in fluorescence along the channel. (C) Kinetics of PL intensity for Cd:S ratio 1:1 (black solid line) and 1:2 (green dashed line). Measurements in PDMS (●) and in the hybrid device with glass capillary (■). (D) Absorption and emission spectra of the collected nanoparticle solution for Cd:S 1:2 (black) and 1:1 (green) after synthesis without (solid line) and with (dashed line) inserted capillary. The arrow shows the spectral shift for the different ratios.

For the first time, we are able to follow the structural evolution of CdS nanocrystals by absorption and emission in real time, without influencing the reaction. The *in-situ*

UV-Vis spectra, shown in Figure 6.3A for a Cd:S ratio of 1:2, display the characteristic appearance and shift of the absorption edge, indicated by the arrow, during the nucleation and growth of CdS nanoclusters.^[22] An increasing Cd:S ratio from 1:2 to 1:1 results in bigger CdS nanoparticles. Hence, the absorption edge in the UV-Vis spectra shifts to higher wavelength, which is shown in Figure 6.3B. The *in-situ* photoluminescence shows a general increase in intensity over time with a broadband emission in the visible range, peaking at about 560 nm.^[9] A significant difference in kinetics can be determined when comparing the different flow velocities employed in the hybrid channel to shift the beginning of particle nucleation and growth into the detectable region. The final absorption and emission spectra for both synthesised samples are represented by the plots in Figure 6.3D. The arrows indicate the redshift in absorption and the blueshift in emission by increasing Cd:S ratio. Comparing the solid and dashed lines for both syntheses it is clear that changing the device and flowrates does not influence the final size of the particles and their optical properties. Only the ratio of Cd:S, adjusted by the concentrations of the reactant solutions, determines the final nanoparticle size.

From the height h and width w of the channel, the flow velocity ν , given by $\nu = U/(hw)$, and consequentially the reaction time can be calculated at every position along the outlet stream ($\tau = \text{channel position } t_x/\nu$). Allocating the maximum fluorescence intensity to the according channel position, and thereby reaction time, results in the *in-situ* kinetic plot shown in Figure 6.3C. Increasing the Cd:S ratio from 1:2 (black solid lines) to 1:1 (green dashed lines) leads to slower reaction kinetics due to the higher volume fraction. Furthermore, the remarkable influence of the thickness of the buffer layer can be seen, comparing the measurements in PDMS (●) and in the hybrid device with glass capillary (■). As the ratio of the flow velocities changes from $U_{MC} = 4U_{SC1} = 4U_{SC2}$ for the synthesis in the all-PDMS device to $U_{MC} = 2U_{SC1} = 2U_{SC2}$ in the hybrid device, the buffer layer gets thinner and, as a consequence, the reaction kinetics increase. This leads to a steeper slope in the reaction time - intensity plot, shown in Figure 6.3C by comparing circular and rectangular data points of the same Cd:S ratio. Further variation of synthetic parameters, such as the investigation of the *in-situ* absorption behaviour without stabilising agent (Fig. D.4A and B) and the *in-situ* photoluminescence for different Cd:S and Cd:TG ratios along the outlet channel (Fig. D.4D), as well as a photograph of the fluorescent CdS nanoparticle sample (Fig. D.4C) can be found in the Supporting Information.

The powder diffraction (XRD) measurements of microfluidic synthesised particles with

varying precursor ratio are shown in Figure 6.4. All peaks in the diffraction pattern are indexed according to the JCPDS data (No. 10-454) according to a face centred cubic structure of CdS. The peaks at around 26° , 44° and 52° correspond to the crystal planes (111), (220) and (311) and are in good agreement with reported patterns of CdS nanoparticles.^[4,24] The observed XRD pattern also shows the zinc blend phase of the particle structure. A small shift between the two precursor ratios, especially at the (111) peak, indicates the slight difference in the particle size, which is in conclusion to the previous shown results.

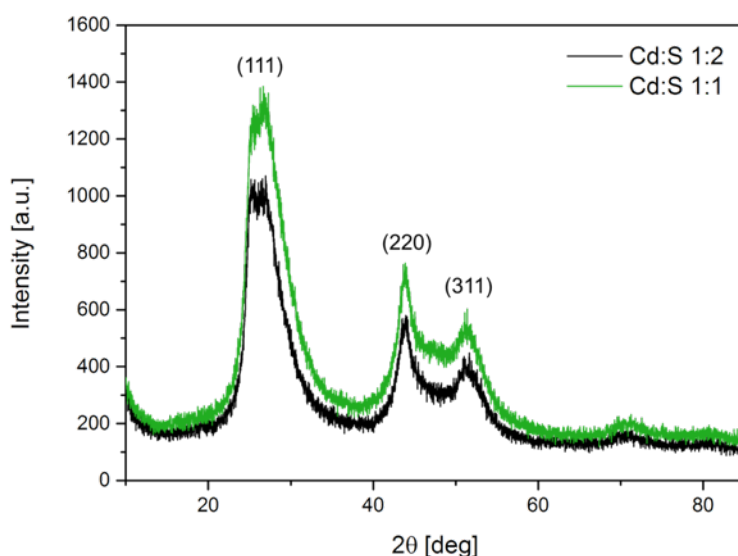


Figure 6.4: X-ray diffraction (XRD) measurements of the dried CdS nanoparticles produced in a microfluidic reaction varying the Cd:S ratio in the precursor solutions.

Early studies from Vossmeier *et al.* found that the pH of the reactant solution can be of crucial importance for the outcome of a CdS nanoparticle synthesis using thioglycerol as stabilising agent.^[5] Even though the initial Cd^{2+} and S^{2-} sources were different, the pH of the cadmium salt solution, containing thioglycerol, was increased by adding NaOH before mixing with the sulfide solution. The different *in-situ* studies for photoluminescence along the outlet channel during the reaction are shown in Figure D.5A in the Supporting Information. These show the increase in reaction kinetics due to NaOH addition to the Cd-precursor solution resulting in a fast evolution of fluorescence with almost no alteration downstream in comparison to the lower pH synthesis. The final absorption and emission spectra of the synthesised CdS nanocrystals can be found in Figure D.5B.

As the investigated synthesis is performed at room temperature, collected CdS quantum dot samples should be stored at low temperatures around 4°C to prevent ongoing

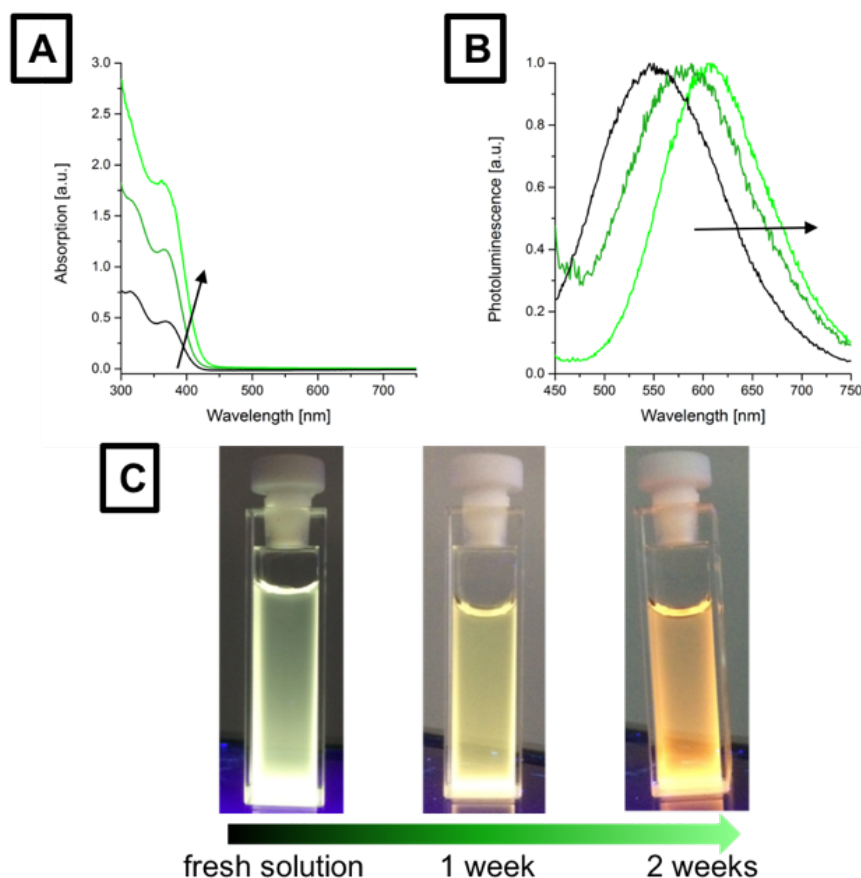


Figure 6.5: Absorption (A) and emission (B) spectra of CdS solutions collected after microfluidic synthesis and stored at room temperature. The black spectrum shows the fresh sample, collected directly out of the microfluidic device. The arrow indicates the progress with measured spectra after one and two weeks. (C) Photographs of the changing fluorescence of the CdS nanoparticle solution from the fresh sample over two weeks.

synthesis and aggregation. The continuing slow progress of the reaction at RT can be seen after the majority of Cd^{2+} and S^{2-} ions have been reacted. The optical properties of a CdS solution collected after synthesised in a microfluidic device and monitored over a period of two weeks are shown in Figure 6.5. The significant redshift of absorption (Fig. 6.5A) and emission (Fig. 6.5B) indicate further particle growth in the aqueous solution. This change in the spectra can also be observed by a visual difference in photoluminescence of the sample, shown in the photograph in Figure 6.5C. The visible fluorescence changes from yellow-green, to bright yellow, to orange over two weeks.

6.5. Conclusion

We have observed the first real-time, undisturbed cadmium sulfide nanoparticle synthesis in a microfluidic channel with three-dimensional hydrodynamic focusing. The mi-

crofluidic device design focuses the main stream channel, containing the Cd^{2+} source, in the centre of the outlet channel, completely surrounded by a water buffer layer to achieve total separation from a surrounding sulfide solution. The diffusion-limited synthesis of CdS nanocrystals was followed for the first time *in-situ* by the appearance and shifting of bandgap emission and band edge absorption along the downstream channel. The influence of various synthetic parameters, such as the Cd:S and the Cd:TG ratio and solution pH, on the reaction kinetics were investigated. Long-term growth kinetics over a period of weeks could also be followed by photoluminescence. The unique reaction conditions of this experiment open up the potential for following quantum dot nucleation and growth kinetics *in-situ* on a millisecond time scale. Thus, early stages of synthesis *ab initio* can then be followed by optical spectroscopy as well as X-ray diffraction and can provide important information for optimisation and control of colloidal chemical reactions.

References

- [1] Peng, X.; Wickham, J.; Alivisatos, A. P. *Journal of the American Chemical Society* **1998**, *120*, 5343–5344.
- [2] Trindade, T.; O'Brien, P.; Pickett, N. L. *Chemistry of Materials* **2001**, *13*, 3843–3858.
- [3] Schiener, A.; Magerl, A.; Krach, A.; Seifert, S.; Steinrueck, H.-G.; Zagorac, J.; Zahn, D.; Weihrich, R. *Nanoscale* **2015**, *7*, 11328–11333.
- [4] Unni, C.; Philip, D.; Gopchandran, K. G. *Spectrochimica Acta Part A* **2008**, *71*, 1402–1407.
- [5] Vossmeier, T.; Katsikas, L.; Giersig, M.; Popovic, I. G.; Diesner, K.; Eychmüller, A. C. A.; Weller, H. *Journal of Physical Chemistry* **1994**, *98*, 7665–7673.
- [6] Yu, W. W.; Qu, L.; Guo, W.; Peng, X. *Chemistry of Materials* **2003**, *15*, 2854–2860.
- [7] Nosaka, Y.; Yamaguchi, K.; Miyama, H.; Hayashi, H. *Chemistry Letters* **1988**, *17*, 605–608.
- [8] Spanhel, L.; Haase, M.; Weller, H.; Henglein, A. *Journal of the American Chemical Society* **1987**, *109*, 5649–5655.
- [9] Sounart, T. L.; Safier, P. A.; Voigt, J. A.; Tallant, D. R.; Matzke, C. M.; Michalske, T. A. *Lab on a Chip* **2007**, *7*, 908–915.
- [10] Gacoin, T.; Lahlil, K.; Boilot, P. L.-P. *Journal of Physical Chemistry B* **2001**, *105*, 10228–10235.
- [11] Luccio, T. D.; Laera, A. M.; Tapfer, L.; Kempter, S.; Kraus, R.; Nickel, B. *Journal of Physical Chemistry B* **2006**, *110*, 12603–12609.
- [12] Nagamura, T.; Inoue, H.; Grieser, F.; Urquart, R.; Sakaguchi, H.; Furlong, D. N. *Colloids and Surfaces A: Physicochemical and Engineering Aspects* **1999**, *146*, 265–272.
- [13] Lu, M.; Ozcelik, A.; Grigsby, C. L.; Zhao, Y.; Guo, F.; Leong, K. W.; Huang, T. J. *Nano Today* **2016**, *11*, 778–792.
- [14] Jiang, L.; Wang, W.; Chau, Y.; Yao, S. *RSC Advances* **2013**, *3*, 17762–17769.
- [15] Lazarus, L. L.; Riche, C. T.; Marin, B. C.; Gupta, M.; Malmstadt, N.; Brutchey, R. L. *Applied Materials & Interfaces* **2012**, *4*, 3077–3083.

- [16] Chen, X.; Schroeder, J.; Hauschild, S.; Rosenfeldt, S.; Dulle, M.; Foerster, S. *Langmuir* **2015**, *31*, 11678–11691.
- [17] Lazarus, L. L.; Yang, A. S.-J.; Chu, S.; Brutchey, R. L.; Malmstadt, N. *Lab on a Chip* **2010**, *10*, 3377–3379.
- [18] Nightingale, A. M.; de Mello, J. C. *Journal of Materials Chemistry* **2010**, *20*, 8454–8463.
- [19] Lignos, I.; Maceiczky, R.; de Mello, A. J. *Accounts of Chemical Research* **2017**, *50*, 1248–1257.
- [20] Rempel, J. Y.; Bawendi, M. G.; Jensen, K. F. *Journal of the American Chemical Society* **2009**, *131*, 4479–4489.
- [21] Hung, L.-H.; Choi, K. M.; Tseng, W.-Y.; Tan, Y.-C.; Shea, K. J.; Lee, A. P. *Lab on a Chip* **2006**, *6*, 174–178.
- [22] Shayeganfar, F.; Javidpour, L.; Taghavinia, N.; Tabar, M. R. R.; Sahimi, M.; Bagheri-Tar, F. *Physical Review E* **2010**, *81*, 026304.
- [23] Seibt, S.; With, S.; Bernet, A.; Schmidt, H.-W.; Foerster, S. *Langmuir* **2018**, *34*, 5535–5544.
- [24] Wang, W.; Liu, Z.; Zheng, C.; Xu, C.; Liu, Y.; Wang, G. *Materials Letters* **2003**, *57*, 2755–2760.
- [25] Mullaugh, K. M.; III, G. W. L. *Journal of Nanoparticle Research* **2011**, *13*, 393–404.
- [26] Nguyen, N.-T.; Wereley, S. T. *Fundamentals and applications of microfluidics*; Artech House, 2002.
- [27] Xia, Y.; Whitesides, G. M. *Annual Review of Materials Research* **1998**, *28*, 153–184.
- [28] Herron, N.; Wang, Y.; Eckert, H. *Journal of the American Chemical Society* **1990**, *112*, 1322–1326.

Chapter 7

7. Publication V

Diffusion-limited self-assembly in microfluidics as a platform for structural analysis of anionic conjugated polyelectrolytes.

Susanne Seibt^{a,b}, Brett Johnson^c, Martina Schmidt^d, Mukundan Thelakkat^d, Paul Mulvaney^b, Stephan Förster^{*,e}

^a*Physical Chemistry I, University of Bayreuth, Universitätsstraße 30, 95447 Bayreuth, Germany.*

^b*Bio21 & School of Chemistry, The University of Melbourne, VIC-3010 Melbourne, Australia.*

^c*School of Physics, The University of Melbourne, VIC-3010 Melbourne, Australia.*

^d*Macromolecular Chemistry I, University of Bayreuth, Universitätsstraße 30, 95447 Bayreuth, Germany.*

^e*JCNS-1/ICS-1, Forschungszentrum Jülich, 52428 Jülich, Germany.*

The results presented in this chapter are prepared as a manuscript in progress.

Individual contribution of involved authors

I performed all experiments and analysed the data. Together with Prof. Stephan Förster and Prof. Paul Mulvaney I wrote the manuscript. Brett Johnson helped with the Raman spectroscopic measurements, Martina Schmidt provided the polymer and helped together with Prof. Mukundan Thelakkat with scientific discussions.

7.1. Abstract

The inherent electrical conductivity of polyelectrolytes, and their interactions with ions in solution, makes them of interest to broad range of scientific fields. However, structural transitions of these polymers through varying conditions such as solvent quality have not yet been studied in great detail. In order to study these transitions, fast solvent exchange induced diffusion-limited self-assembly of poly (tetrabutylammonium 6-(thiophen-3-yl) (PTHS) was studied in-situ using three-dimensional double focusing continuous flow microfluidic devices. The fluorescent PTHS single polymer chain in organic solvent was assembled in a controlled manner by an interdiffusing solvent exchange with water. Fluorescence quenching from the assembly process was then followed by confocal laser scanning microscopy and confocal Raman spectroscopy, demonstrating this microfluidic device design as a choice platform for studying fast structural transitions of conjugated polymers in solution.

7.2. Introduction

Organic optoelectronic polymers for solar cells and OLEDs have garnered great interest over the past decades. This was due to the demand for easily processable conjugated polymers, soluble in water or similar nontoxic polar solvents,^[1] which can be used for sensing, fluorescence imaging, diagnosis and biomedical therapy,^[2] as well as in solar cells and OLEDs. To increase the polymer solubility in solvents like water or alcohols, polar groups were introduced in the molecular structure.^[3-5] Since the first report in 1980,^[6] water-soluble poly (3-hexylthiophene) (P3HT) analogues were widely studied and perfected for well-defined optical and electrochemical properties.^[7,8] However, the self-assembled structure formed by these polymers in solvents of varying quality is unclear. Changes in the structure of self-assembled polyelectrolytes can be induced through alterations in the concentration, temperature, pH, or solvent. These easily controlled parameters have resulted in an increased interest in following the fast kinetics of these processes.^[9-12] Understanding the underlying structure-formation mechanism is necessary for a better control of formulations as well as structure-related properties.^[13]

Microfluidics is a particularly useful experimental technique for the investigation of fast kinetic processes.^[14,15] Progress in microfluidic device design engineering has made investigations of fast mixing processes, even in complex fluids, and the formation of well-defined assembled structures possible.^[16,17] The main breakthrough was the use and optimization of continuous flow devices with hydrodynamic focusing. In those devices, a central stream consisting of slowly diffusing macromolecules is hydrody-

namically focused into the middle of the outlet channel by two, or more, orthogonal side streams with contain fast diffusing molecules, primarily solvents. By diffusion of the latter into the central stream, the self-assembly of macromolecules to superstructures is initiated and can be followed by several techniques *in-situ*.^[13,18] This is possible due to the laminar flow conditions in microfluidic devices, where mixing occurs exclusively by interdiffusion, even at high flowrates. This enables concentration gradients to form along and across the channel, leading to a time-distance relationship between the reaction time and the channel position. Hence, the temporal resolution which can be achieved is mainly limited by the spatial resolution of the detection technique.^[13,17]

Various detection techniques have been used in combination with microfluidics to study the fast reaction kinetics of nanoparticle nucleation and growth, as well as polymer self-assembly. One of the most commonly used methods is confocal laser scanning microscopy (CLSM). Due to the wide uptake of this technique in biological studies of cells and organisms,^[19-21] great technological leaps have been made and devices can now be used to investigate the mixing abilities of a microchannel^[22] and even goes as far as observing^[23] colloids flowing through a micronized channel. The latter is known as micro particle imaging velocimetry (μ -PIV) and can be useful for device testing as well as investigations on particle flow behavior.^[24] Another very powerful method for the rapid detection of chemical reactions is Raman spectroscopy. As a label-free method, it enables the measurement of velocity profiles *in vitro* as well as *in-situ* in non-biological reactions.^[25-27] Raman spectroscopy, just as infrared spectroscopy, provides characteristic information on molecular vibrations and can therefore be used in microfluidic experiments to gain insights in reaction processes on a molecular level.

Here we used the fluorescent P3HT derivate poly (tetraethylammonium 6-(thiophen-3-yl) hexane 1-sulfonate) (PTHS) to study the structural change from a free random walk polymer chain to micellar superstructures upon fast solvent exchange. Confocal laser scanning microscopy was used to investigate the transition from a fluorescent single molecule in a polar organic solvent, such as dimethylsulfoxide (DMSO) or dimethylformamide (DMF), to the non-fluorescent self-assembled structure by exchanging the solvent with water. In addition, the assembly process was studied by *in-situ* confocal Raman spectroscopy. In concert with COMSOL simulations, the precise solvent composition and PTHS concentration across the outlet channel could be determined, enabling mapping of the assembly process, via fluorescence, against time. To reduce the background scattering of PDMS, a combination of pure three-dimensional double focusing PDMS and previously optimized PDMS-glass hybrid microfluidic chips were used for the

experiments. This provides a powerful platform for future detailed structure analysis studies.

7.3. Experimental Methods

DMSO and DMF were of analytical grade and used as received from Sigma Aldrich. Water was purified using a MilliQ-system (Millipore), leading to a final resistivity of >18 M Ω cm. For the 1:1 mixtures, an equal volume of organic solvent (DMSO or DMF) and water was mixed in a glass vial. The polymer PTHS was synthesized by M. Schmidt (Macromolecular Chemistry I, University of Bayreuth) and used as received in the dried state. For the microfluidic experiments, a solution of the polymer in DMSO and DMF with the concentration of 20 mg/L was produced.

For the microfluidic reactor device, a three-dimensional channel geometry with double hydrodynamic focusing was used.^[28] This guaranteed solvent exchange was limited by diffusion only. For confocal laser scanning microscopy, all-PDMS devices were used, whereas the Raman spectroscopy was performed in PDMS-glass hybrid devices to prevent scanning through thick layers of PDMS.

Microfluidic experiment

For the microfluidic controlled polymer self-assembly, the PTHS solution consisting either DMSO or DMF was introduced in the main channel (MC). A 1:1 volume ratio mixture of organic solvent and water was fed into the first side channels (SC1) to mildly start the solvent exchange, and the pure water was introduced in the second side channel (SC2). The flow velocities of the pumping units for the CLSM experiments are shown in Table 7.1.

Table 7.1: Flow velocities of all inlets for different experiments.

inlet \ experiment	Flow velocity [μ l/h]		
	(A)	(B)	(C)
Main channel (BTA)	62	125	250
Side channel 1 (H ₂ O)	125	250	500
Side channel 2 (HCl)	250	500	1000
Overall volumetric flow in outlet channel	812	1625	3250
Overall flow velocity in outlet channel	3.92mm/s	7.85mm/s	15.70mm/s

Table 7.2 shows the flow velocities of the syringe pump units for the Raman experiments in PDMS-glass hybrid chips.

Table 7.2: Flow velocities of all inlets for different experiments.

inlet \ experiment	Flow velocity [$\mu\text{l/h}$]		
	(A)	(B)	(C)
Main channel (BTA)	62	125	125
Side channel 1 (H_2O)	125	250	250
Side channel 2 (HCl)	250	500	1000
Overall volumetric flow in outlet channel	812	1625	2625
Overall flow velocity in outlet channel	3.92mm/s	7.85mm/s	12.68mm/s

In these experiments, temporal resolutions of milliseconds can be achieved, at 1 mm post mixing, and at an overall flowrate of 2625 $\mu\text{L/h}$, the reaction has progressed by approximately 0.1 seconds.

Confocal laser scanning microscopy

The confocal laser scanning microscopy experiments were performed using a Leica TCS SP8 with a Leica DMI6000B inverted microscopy stage. A laser with a wavelength of $\lambda_{max} = 488 \text{ nm}$ and a detector range of 550 – 625 nm and 560 – 600 nm were used for DMSO and DMF, respectively.

Confocal Raman spectroscopy

For the Raman spectroscopy experiments, a Renishaw inVia Raman microscope in combination with a Nikon 50 / 0.45 L plan objective was used. For excitation, a 532 nm laser was used. The spectra were collected from 100 to 4000 cm^{-1} with a 10 s integration time for each spectrum. To scan across the channel, 10 μm steps through the middle of the capillary were set giving the spatial resolution.

7.4. Results and Discussion

Figure 7.1 shows the chemical structure and optical properties of the used PTHS in DMSO and DMF solution.

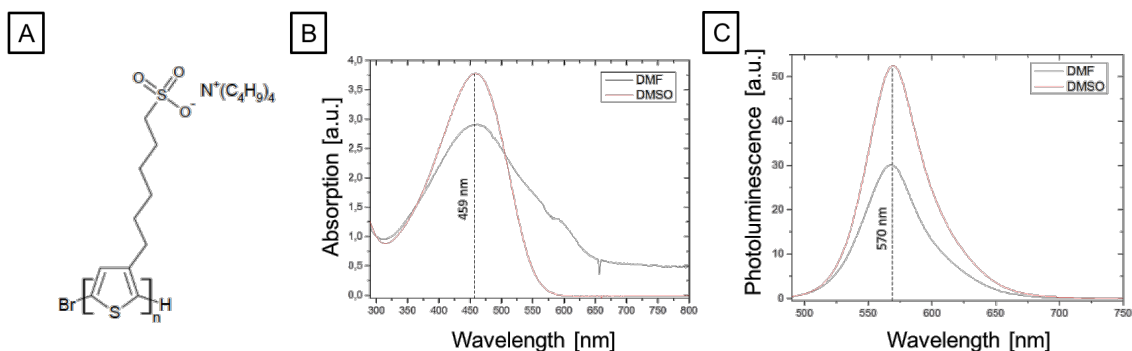


Figure 7.1: (A) Chemical structure of the poly (tetrabutylammonium 6-(thiophen-3-yl) hexane 1-sulfonate) used in this study. (B) Absorption spectra of a 20 mg/L concentrated solution of PTHS in DMSO (black) and DMF (red). (C) Emission spectra of a 20 mg/L concentrated solution in DMSO (black) and DMF (red) at an excitation wavelength of 460 nm.

The absorption maximum is located at 459 nm for both PTHS solutions in DMSO and DMF. This is in agreement with the published optical properties about the synthesized molecule^[7], therefore it was assumed that a solvent exchange in microfluidic systems should lead to a conforming fluorescence behaviour due to polymer self-assembly processes. The emission of the fluorescent polymer can be found at 570 nm, which was needed for the confocal scanning microscopy measurements.

The microfluidic channel design used, along with its method of operation, has been described in a previous publication.^[28] The reason for using a three-dimensional hydrodynamic focusing design was to provide enough solvent for a complete solvent exchange leading to the disappearance of the polymer fluorescence through a self-assembly process, while avoiding artefacts due to contact of the polymer with the channel walls.

Solvent stability experiments

Before starting the investigation on the PTHS self-assembly in a microfluidic environment, it is important to study the compatibility of the different solvents with the PDMS-microfluidic device. The three different solvents H_2O , DMSO, and DMF, as well as the mixtures of $\text{H}_2\text{O}/\text{DMSO}$ and $\text{H}_2\text{O}/\text{DMF}$ as individual solutions, have a high compatibility with PDMS without any swelling effects while flowing through microfluidic channel systems. However, during the self-assembly experiments the solvents are not premixed and come into contact by hydrodynamic focussing at the mixing-cross section of the chip. The influence of this is shown in Figure 7.2. In these experiments, pure DMSO

or DMF was introduced in the main channel (MC), whereas pure water was pumped in from all side channels. During the observation time of 30 min, pictures were taken every 10 min.

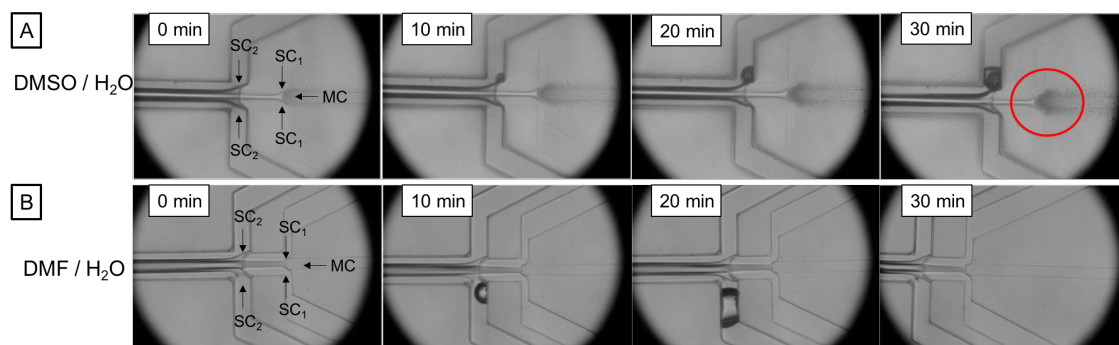


Figure 7.2: (A) Optical microscopy images of the DMSO / H₂O solvent mixing experiment in the microfluidic device. The mixture of DMSO (MC) and H₂O (SC₁ and SC₂) shows an exothermic reaction, leading to heat generation which deforms the channel geometry (red circle). This effect increases over time (left to right). (B) Optical microscopy images of the DMF / H₂O solvent mixing experiment. No damage on the PDMS chip can be detected.

Due to the exothermic reaction of DMSO with water, heat is generated during the mixing process. This leads to a deformation of the channel geometry, shown in Figure 7.2A (red circle), that progresses over the duration of the reaction time. Despite the damaged channel geometry of the PDMS device, the focusing in the outlet channel remains. In contrast to the mixture of DMSO and water, DMF as organic solvent does not induce any damage to the microfluidic chip or channels (see Figure 7.2B).

To minimise the effect of heat-induced deformation through the solvents reacting, a 50/50 vol. mixture solution of water and DMSO was introduced in the first side channels. Furthermore, this solvent mixture has the advantage of a higher amount of water in the outlet channel in the self-assembly experiments. This leads to a higher rate of assembled polymer than using pure water as a intermediate layer between the stream of the main channel and the second side channel.

Confocal laser scanning microscopy investigations

As published by Brendel et al.^[7] the PTHS polymer shows a significant decrease in fluorescence intensity as the ratio of H₂O to DMSO or DMF increases in the solvent due to polymer self-assembly. Therefore, this quenching of the fluorescence can be followed *in-situ* via confocal laser scanning microscopy. The flow velocities of each inlet

were varied according to Table 7.1 to investigate the influence on the position at which the decrease in fluorescence at the outlet channel occurs.

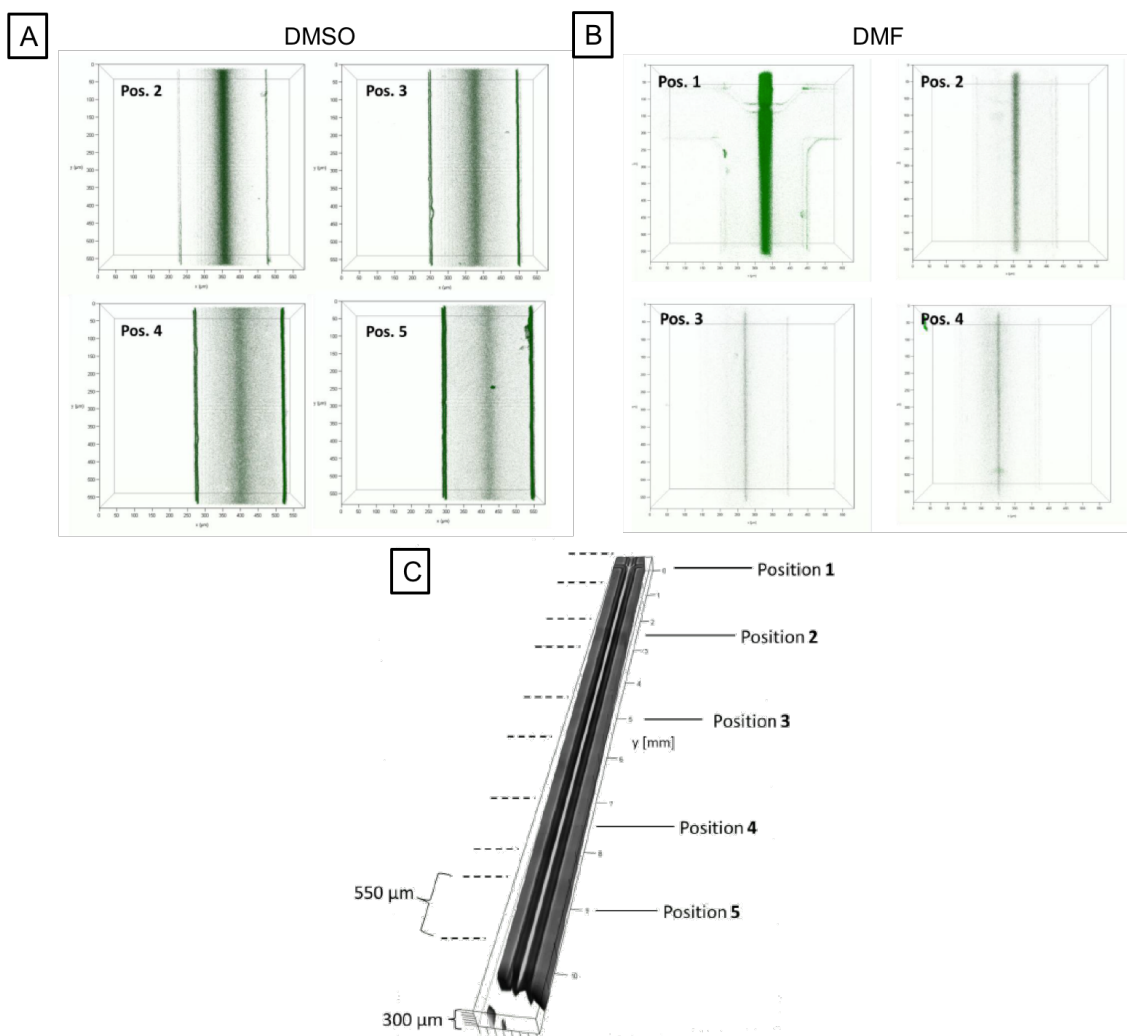


Figure 7.3: (A) Three-dimensional CLSM scans at different positions along the outlet channel for the self-assembly experiment of PTHS in DMSO by solvent exchange with H₂O with the flow velocities A (see Table 7.1). A clear decrease in fluorescence intensity can be seen with increasing water amount in the solvent mixture. (B) Three-dimensional CLSM scans at different positions along the outlet channel for the self-assembly experiment of PTHS in DMF by solvent exchange with H₂O with the flow velocities A (see Table 7.1). Similar to the DMSO experiments, a decrease in fluorescence intensity can be seen along the channel. However, a much higher rate of fluorescence quenching was found for DMF as solvent. (C) Explanation of the scan positions one to five shown in (A) and (B) along the outlet channel. The distance between each position is 2.5 mm. The spacer for 555 μm and 300 μm show the dimensions of the single CLSM measurement, which were combined to the scan along the whole outlet channel.

The three-dimensional CLSM scans of the DMSO / H₂O experiment with the flow velocities A $U_{MC} = 62 \mu\text{L/h}$, $U_{SC1} = 125 \mu\text{L/h}$ and $U_{SC2} = 250 \mu\text{L/h}$ according to Table 7.1,

displayed in Figure 7.3A, show a major decay in the fluorescence intensity along the outlet channel as a result of diffusion-controlled polymer self-assembly. For the DMF / H₂O experiment the three-dimensional CLSM scans with the same flow velocities are shown in Figure 7.3B. In contrast to the DMSO experiment, a drastic quenching of the fluorescence on a small scale after entering the outlet channel can be seen. After the second position about 2.5 mm after the mixing cross, the decrease of emission levelled out.

To compare the self-assembly induced fluorescence decay for the flow velocities *B* ($U_{MC} = 125 \mu\text{L/h}$, $U_{SC1} = 250 \mu\text{L/h}$, $U_{SC2} = 500 \mu\text{L/h}$) and *C* ($U_{MC} = 250 \mu\text{L/h}$, $U_{SC1} = 500 \mu\text{L/h}$, $U_{SC2} = 1000 \mu\text{L/h}$) from Table 7.1, images from the complete channel were taken. These are shown for the case of both DMSO and DMF in Figure 7.4.

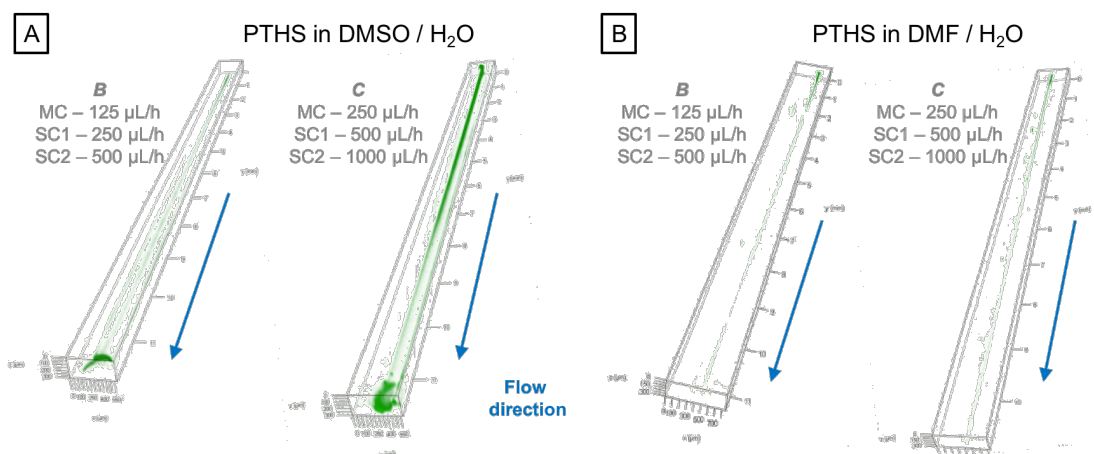


Figure 7.4: Confocal microscopy image of the full channel during the PTHS assembly experiment by solvent exchange from DMSO to water (A) and DMF to water (B) for the flow velocities *B* (left) and *C* (right). The influence of doubling the flowrate can clearly be seen in all four CLSM tiles. The flow direction along the outlet channel is indicated by the blue arrow.

Figure 7.4A shows the images of the full channel for the PTHS self-assembly experiments in DMSO for the flow velocities *B* (Fig. 7.4A left) and *C* (Fig. 7.4A right). In comparison to the position scans in Figure 7.3A, the assembly of PTHS occurred at a later stage along the channel could be investigated. For the velocities *B* ($U_{MC} = 125 \mu\text{L/h}$, $U_{SC1} = 250 \mu\text{L/h}$ and $U_{SC2} = 500 \mu\text{L/h}$) the assembly starts around 3 mm after the mixing cross, whereas for the doubled velocity *C* ($U_{MC} = 250 \mu\text{L/h}$, $U_{SC1} = 500 \mu\text{L/h}$ and $U_{SC2} = 1000 \mu\text{L/h}$) a loss in emission intensity could be seen after 7 mm, confirming the assumed flow velocity dependency of the quenching process.

The same effect was investigated with DMF as the organic solvent, displayed in Figure

7.4B. For the experiment with flow velocity *B* (Fig. 7.4B left), the emission lost intensity after about 2 mm. For the doubled flow velocities in experiment *C* (Fig. 7.4B right) the fluorescence intensity decreases significantly after 4.5 mm, which is in agreement to the previously seen flow velocity dependency. However, the photoluminescence intensity during the experiments in DMF is lower in than the intensity in DMSO. This is consistent with the emission spectra of the stock solutions shown in Figure 7.1. Additionally, the absorption spectra of the stock solution is broader in DMF than DMSO. Partial assembly of PTHS in the DMF solution due to the presence of a small amount of water or a pre-reaction of DMF because of its high electron density could explain this observation. It would also explain the significant difference in reaction times until the assembly commences along the outlet channel between the DMSO and DMF cases.

Confocal Raman spectroscopy measurements

As a reference, background Raman spectra from all solvents were measured. These are displayed in Figure 7.5.

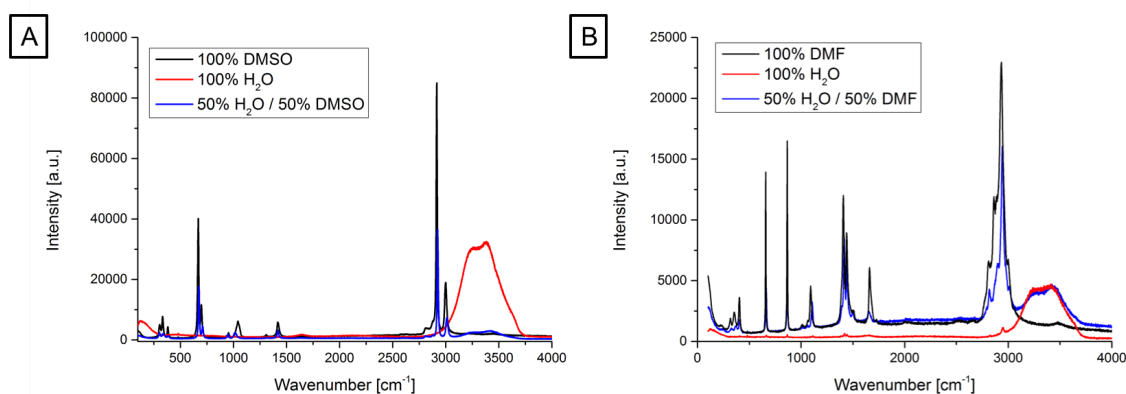


Figure 7.5: Background Raman spectra for (A) 100% DMSO (black line), 100% water (red line) and a 50 vol-% - 50 vol-% mixture of DMSO and water (blue line) and (B) 100% DMF (black line), 100% water (red line) and a 50 vol-% - 50 vol-% mixture of DMF and water (blue line) from 100 cm⁻¹ to 4000 cm⁻¹.

For both organic solvents (Fig. 7.5 black lines), various peaks can be clearly differentiated from the characteristic water peaks (Fig. 7.5 red lines) at wavenumbers of 3200 – 3650 cm⁻¹. Furthermore, in the mixture of both solvents (Fig. 7.5 blue lines), all signals can be assigned to the according structure. However, the spectrum of the water/DMSO mixture shows a quenched signal of water through the exothermic reaction with DMSO. In the case of DMF both signals for water and the pure organic solvent are still visible and are reduced by half the intensity. In the spectra in Figure 7.5 however, the spectra

involving the organic solvent are normalized to the peak maximum at 2900 cm^{-1} .

By using only DMSO, DMF, and water, without the fluorescent PTHS, the focusing of the streams in the outlet channel can be observed. This is shown for DMSO and water in Figure 7.6 for experimental configurations *X* to *Z* as described in Table 7.2. The experimental data for DMF can be found in the Supporting Information. The spectra were measured according to the signals seen in Figure 7.5 in a region where both characteristic peaks from the organic solvent as well as water can be seen at the same time from 2700 cm^{-1} to 3700 cm^{-1} . Data at lower wavenumbers was not measured for brevity.

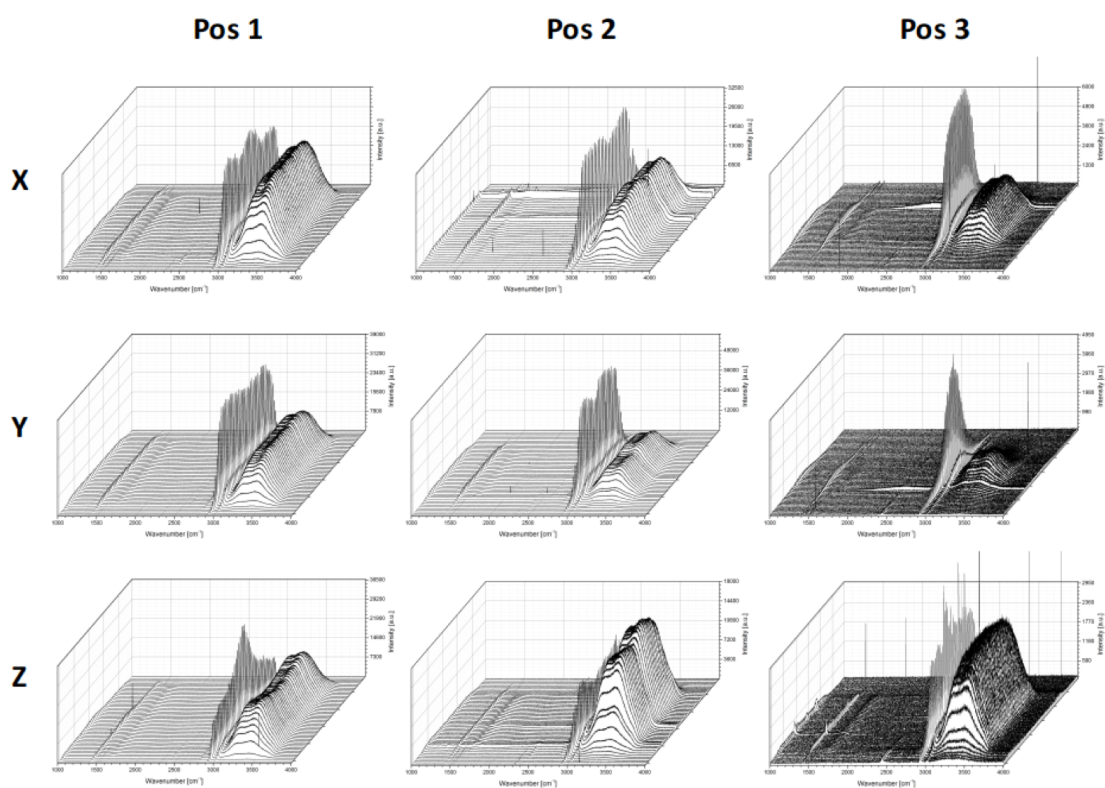


Figure 7.6: Confocal Raman spectroscopy scans in $10\ \mu\text{m}$ steps across the outlet channel (edge to edge) for the flow velocities *X*, *Y* and *Z* for DMSO as organic solvent without PTHS. Three different positions in 4 mm distances were investigated according to the shown positions along the outlet channel at the beginning (Pos. 1 = 1 mm after mixing cross), the middle (Pos. 2 = 5 mm after mixing cross) and the end (Pos. 3 = 9 mm after mixing cross).

By scanning across the outlet channel from edge to edge, the change from predominantly water on the outside to a mixture of both solvents leading to the pure organic solvent in the middle can be seen by the changing intensities at the characteristic wavenumbers for each solvent. However, as the first scan was taken approximately

1 mm after the mixing cross, where the PDMS ends and the glass capillary was inserted, slightly interdiffusing solvents without clear pure solvent regions can be found. Further along the outlet channel at positions 5 mm and 9 mm after the mixing cross, the interdiffusion of the solvents is clearly visible by the change in the ratios of intensities of the characteristic solvent wavenumbers. Furthermore, the influence of the varying flow velocities and flowrate ratios between the main and side channels in the different experiments shows a distinct effect on the interdiffusion rate along the channel. Higher overall flow velocity leads to a slower interdiffusion and a thinner buffer layer from the first side channel though a higher flowrate in the second side channel leads to faster interdiffusion as more water is fed into the outlet channel.

In the next step, the polymer PTHS was added to the DMSO solution in the main channel. Due to its strong emission at 570 nm, no characteristic Raman signal could be seen. However, the focused fluorescence in the main channel in addition to the solvent signal could be investigated. The fluorescence intensity along the channel decreases, conforming with the CLSM measurements. The polymer self-assembly by solvent interdiffusion for the flow velocity experiments *X* and *Z* for all three positions is shown in Figure 7.7.

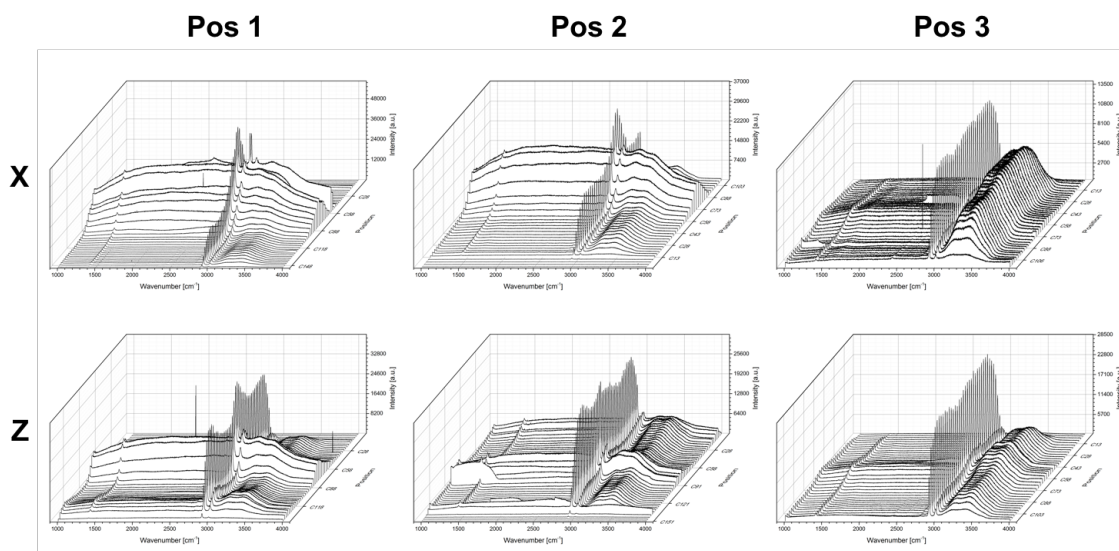


Figure 7.7: Confocal Raman spectroscopy scans in 10 μm steps across the outlet channel for the flow velocities *X* and *Z* for DMSO as organic solvent with PTHS. Three different positions in 4 mm distances were investigated according to the shown positions along the outlet channel at the beginning (Pos. 1 = 1 mm after mixing cross), the middle (Pos. 2 = 5 mm after mixing cross) and the end (Pos. 3 = 9 mm after mixing cross).

As the flow velocities for all inlets from the experiment *X* in the confocal Raman spectroscopy measurements are the same as the flow velocities from *A* in the CLSM ex-

periments, it is only conclusive that the fluorescence shows the same spatial evolution in decreasing fluorescence intensity along the outlet channel. For the flow velocities from experiment Z on the other side, the higher amount of water due to the higher flowrate of the second side channel shows a significant influence in the decay of the fluorescence at the three measured positions. Already at the second positions almost no fluorescence of the polymer can be detected, as the diffusion-induced PTHS assembly starts soon after the mixing cross. The equivalent spectra for DMF as solvent can be found in the Supporting Information.

Finally, the diffusion of PTHS in DMSO from the main channel investigated. Specifically, the polymer solution in DMSO was pumped in the main channel and only DMSO was added in all side channels. By using the same flowrates as in the previously shown experiments in the hybrid microfluidic chip (see Table 7.2), identical focusing conditions in the outlet channel could be guaranteed.

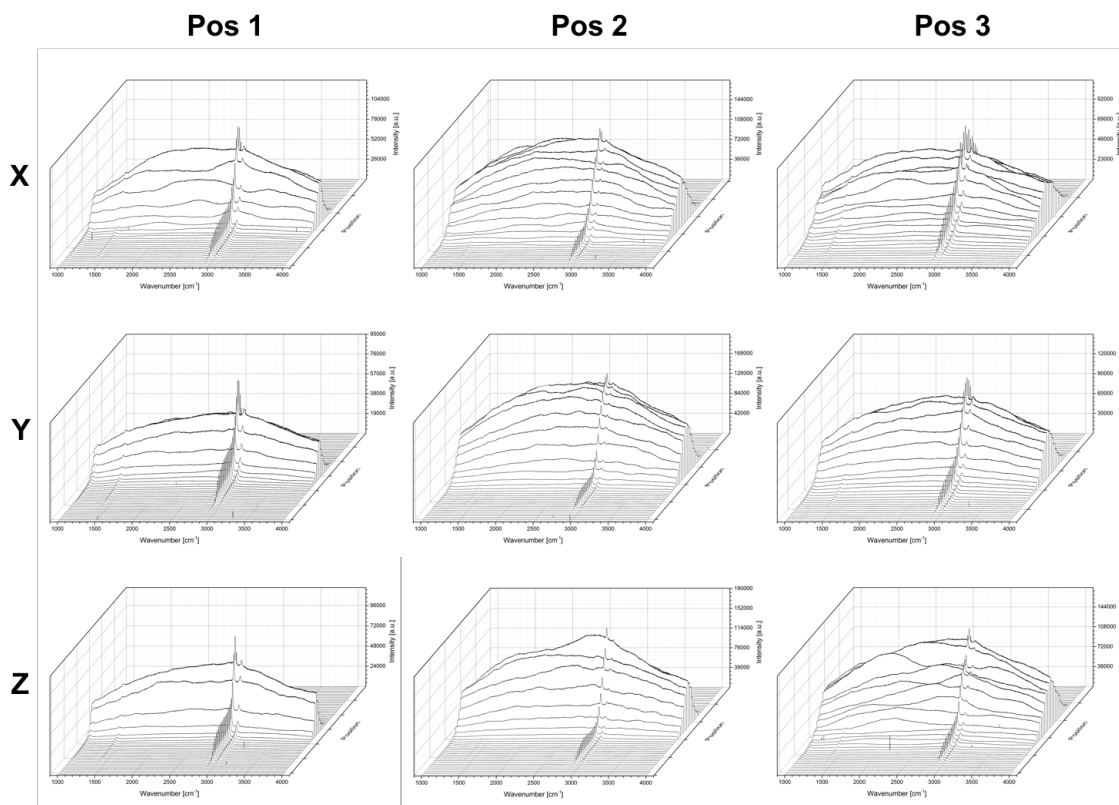


Figure 7.8: Confocal Raman spectroscopy scans in 10 μm steps across the outlet channel for the flow velocities X , Y and Z for the PTHS diffusion in DMSO. PTHS dissolved in DMSO in the main channel, focused by only DMSO in all side channel. Three different positions in 4 mm distances were investigated according to the shown positions along the outlet channel at the beginning (Pos. 1 = 1 mm after mixing cross), the middle (Pos. 2 = 5 mm after mixing cross) and the end (Pos. 3 = 9 mm after mixing cross).

Figure 7.8 shows the same three positions along the channel (Pos. 1 = 1 mm, Pos. 2 = 5 mm, Pos. 3 = 9 mm) with the three different flow velocities X ($U_{MC} = 62 \mu\text{L/h}$, $U_{SC1} = 125 \mu\text{L/h}$ and $U_{SC2} = 250 \mu\text{L/h}$), Y ($U_{MC} = 125 \mu\text{L/h}$, $U_{SC1} = 250 \mu\text{L/h}$ and $U_{SC2} = 500 \mu\text{L/h}$) and Z ($U_{MC} = 125 \mu\text{L/h}$, $U_{SC1} = 250 \mu\text{L/h}$ and $U_{SC2} = 1000 \mu\text{L/h}$) according to Table 7.2, where only DMSO was present in the main channel and side channels. The influence of the different overall flowrates and inlet flowrate ratios can clearly be seen in the diffusion speed of the PTHS molecules towards the edge of the channel. The broadening of the Raman scattering intensity across the channel, shown as the cross-section of the waterfall plots, is wider for slower overall flowrates and much thinner for the higher ratio of SC2 to SC1 in the experiment Z. This is displayed as a function of reaction time in Figure 7.9.

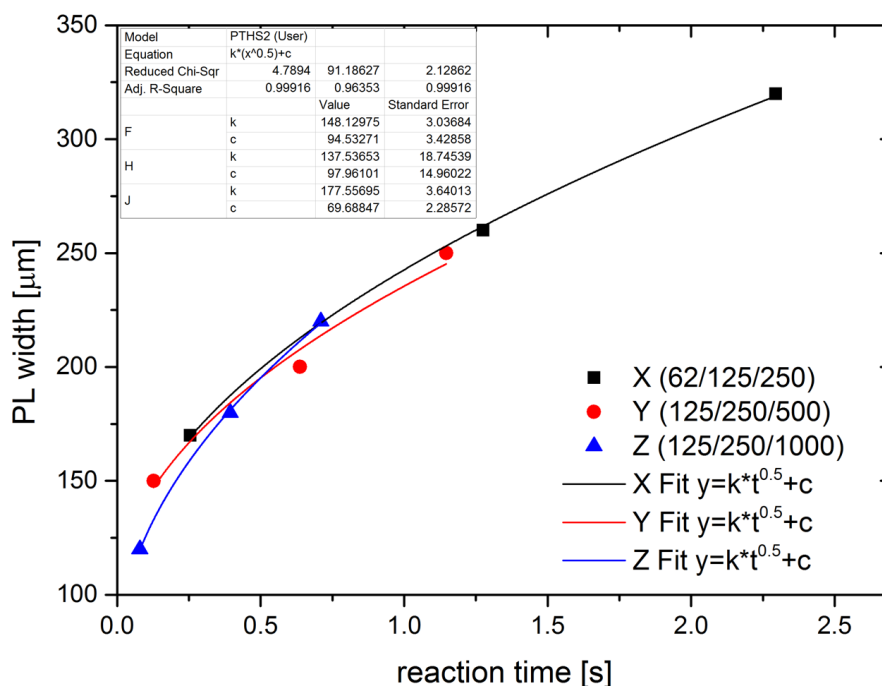


Figure 7.9: Diffusion of the PTHS polymer in DMSO evaluated from the width of the fluorescence in Figure 7.8 against channel position, here recalculated as a function of reaction time from the corresponding flowrate and channel position.

The previously described broadening of the fluorescence in the Raman signal across the channel can be evaluated by the spatial distribution as a function of the position for each experiment. With the corresponding overall flow velocity (see Table 7.2), the position can be recalculated in a reaction time, which results in a comparability of the measured diffusions. Figure 7.9 shows a mostly linear progression of the width of fluorescent signal from the polymer diffusion through DMSO. A second order growth fit following a $t^{0.5}$ -function showed an average diffusion rate of $154.41 \mu\text{m}^2/\text{s}$ of the polymer through the pure solvent.

7.5. COMSOL Simulations

To measure the interdiffusion of the organic solvent with water along the outlet channel to be able to link the volume fraction of DMSO to water to the fluorescence at every point, COMSOL simulations were performed. Figure 7.10 shows the simulations for all three experiments X, Y and Z (see Table 7.2) in the PDMS-glass hybrid chip in a sliced view. A volume fraction of 0 thereby means pure water, 1 equals pure DMSO.

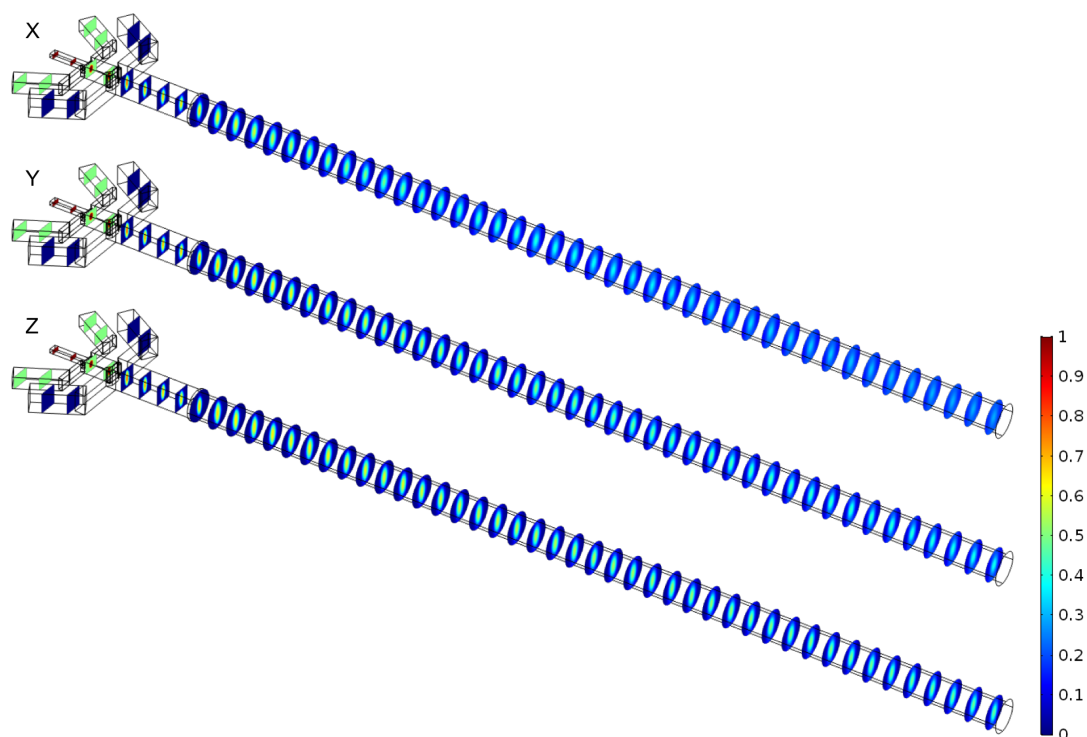


Figure 7.10: COMSOL simulations of the experiments *X* (top), *Y* (middle) and *Z* (bottom) with DMSO as solvent. Sliced view along the channel.

The interdiffusion of the solvents can clearly be seen in the changing volume fraction of DMSO and water in the single frames along the outlet channel. A significant difference can be seen between the different flow velocities (*X*: $U_{MC} = 62 \mu\text{L/h}$, $U_{SC1} = 125 \mu\text{L/h}$, $U_{SC2} = 250 \mu\text{L/h}$; *Y*: $U_{MC} = 125 \mu\text{L/h}$, $U_{SC1} = 250 \mu\text{L/h}$, $U_{SC2} = 500 \mu\text{L/h}$; *Z*: $U_{MC} = 125 \mu\text{L/h}$, $U_{SC1} = 250 \mu\text{L/h}$, $U_{SC2} = 1000 \mu\text{L/h}$). By changing the overall speed from experiment *X* to *Y*, the interdiffusion takes place at a later stage along the channel, which is in good agreement to the fluorescence detection experiment of the PTHS polymer. However, by changing the flowrate ratio and introducing a thicker water layer on the outside through the second side channel, the simulation reveals an opposite effect. Less water is interdiffusing in the main channel, which would lead to a lower rate of self-assembled polymer. To make this effect more visible, the single cross-sections at six positions along the outlet channel are compared in Figure 7.11. The positions are just before the change-over from PDMS in the glass capillary (-0.5 mm), just after entering the glass capillary (0 mm) and from there in equidistant 2.5 mm steps.

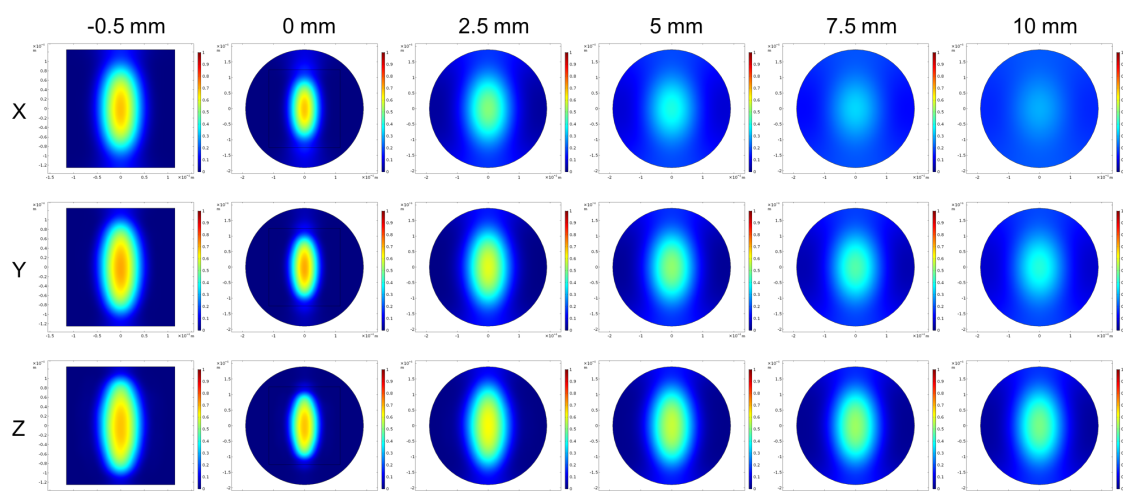


Figure 7.11: Cross sections of COMSOL simulations of the experiments X (top), Y (middle) and Z (bottom) with DMSO as solvent. A significant difference in dependency of the flow velocity can be seen at positions right before (-0.5 mm) and after (0 mm) entering the capillary, and in equidistant 2.5 mm positions along the outlet channel.

Again, the difference in the solvent interdiffusion can clearly be seen, comparing all three experiments. In addition, the ellipsoidal flow profile due to the device geometry are visible. This leads to a broader diffusion range in the vertical direction than the simulation shows in the horizontal direction. As the Raman spectra of the fluorescent PTHS experiments were measured *in-situ* across the horizontal diameter, the volume fraction as a function of distance along this axis for the positions in Figure 7.11 are shown in comparison of all experiments in Figure 7.12.

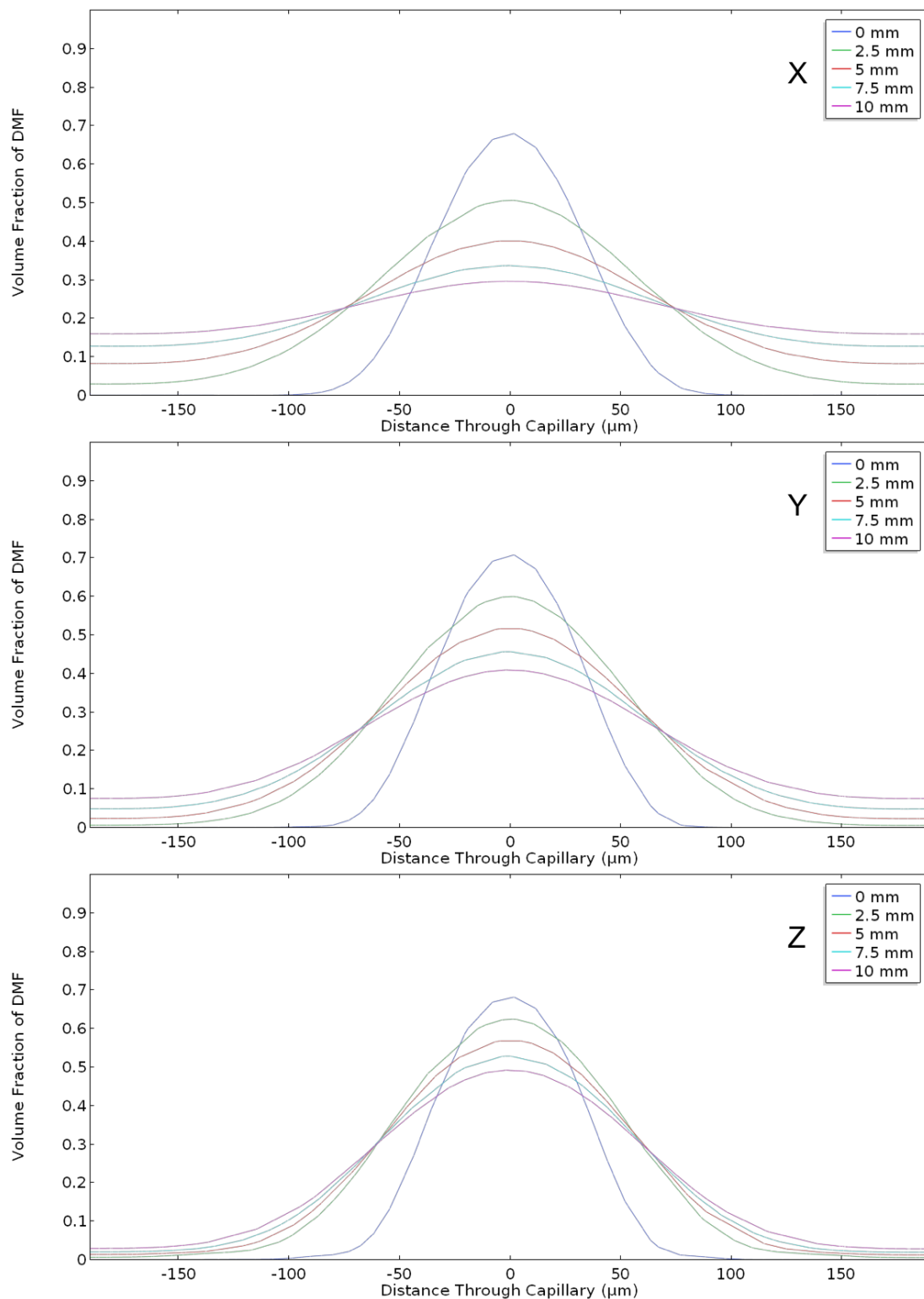


Figure 7.12: Volume fraction as a function of distance vertically through the middle of the outlet channel. The positions are the same as shown in Figure 7.12 from the according COMSOL simulation of the experiments X (top), Y (middle) and Z (bottom) with DMSO as solvent. A higher volume fraction means a lower rate of PTHS self-assembly and therefore higher fluorescence in CLSM and Raman.

A higher volume fraction in this case means more DMSO remaining in the centre of the channel. This also means a lower rate of polymer self-assembly leading to a higher fluorescence intensity in CLSM and Raman measurements. This could now be directly related to the measurements of the PTHS assembly by the background spectra measured from Brendet et al.^[7]

The according simulations for DMF can be found in the Supporting Information.

7.6. Conclusion

We find that the use of microfluidic devices is a very promising technique for investigating fast self-assembly processes of polymers in solution. The temporal structural evolution during the assembly process, in this case indicated by the decrease in fluorescence intensity, can be mapped onto different positions along the outlet microchannel down to millisecond time resolution. By using a highly optimized microfluidic channel geometry, the ratio between organic solvent and water could be precisely adjusted and the polymer self-assembly studied in high spatial resolution across the channel. Thus, this system is promising as a platform for future scattering experiments of various systems with structural rearrangements on the nano- and mesoscale, which are complex in accessibility and structure evaluation.

References

- [1] Sondergaard, R.; Helgesen, M.; Jorgensen, M.; Krebs, F. C. *Advanced Energy Materials* **2011**, *1*, 68–71.
- [2] Zhu, C.; Liu, L.; Yang, Q.; Lv, F.; Wang, S. *Chemical Reviews* **2012**, *112*, 4687–4735.
- [3] Zhong, C.; Duan, C.; Huang, F.; Wu, H.; Cao, Y. *Chemistry of Materials* **2011**, *23*, 326–340.
- [4] Jiang, H.; Taranekar, P.; Reynolds, J. R.; Schanze, K. S. *Angewandte Chemie International Edition* **2009**, *48*, 4300–4316.
- [5] Ghooos, T.; Brassine, J.; Fustin, C.-A.; Gohy, J.-F.; Defour, M.; den Brande, N. V.; Mele, B. V.; Lutsen, L.; Vanderzande, D. J.; Maes, W. *Polymer* **2013**, *54*, 6293–6304.
- [6] Patil, A. O.; Ikenoue, Y.; Wudl, F.; Heeger, A. J. *Journal of the American Chemical Society* **1987**, *109*, 1858–1859.
- [7] Brendel, J. C.; Schmidt, M. M.; Hagen, G.; Moos, R.; Thelakkat, M. *Chemistry of Materials* **2014**, *26*, 1992–1998.
- [8] Schmidt, M. M.; ElMahmoudy, M.; Malliaras, G. G.; Inal, S.; Thelakkat, M. *Macromolecular Chemistry and Physics* **2018**, *219*, 1700374.
- [9] Knight, J. B.; Vishwanath, A.; Brody, J. P.; Austin, R. H. *Physical Review Letters* **1998**, *80*, 3863–3866.
- [10] Toma, A. C.; Pfohl, T. *Supramolecular Chemistry*; John Wiley & Sons, 2012.
- [11] Ihee, H. *Accounts of Chemical Research* **2009**, *42*, 356–366.
- [12] Liu, Y.; Li, M.; Bansil, R.; Steinhardt, M. *Macromolecules* **2007**, *40*, 9482–9490.
- [13] With, S.; Trebbin, M.; Bartz, C. A.; Neuber, C.; Dulle, M.; Yu, S.; Roth, S. V.; Schmidt, H.-W.; Foerster, S. *Langmuir* **2014**, *30*, 12494–12502.
- [14] Squires, T. M.; Quake, S. R. *Reviews of Modern Physics* **2005**, *77*, 977–1026.
- [15] Stone, H. A.; Stroock, A. D.; Ajdari, A. *Annual Reviews in Fluid Mechanics* **2004**, *36*, 381–411.
- [16] Brennich, M. E.; Nolting, J.-F.; Dammann, C.; Noeding, B.; Bauch, S.; Herrmann, H.; Pfohl, T.; Koester, S. *Lab on a Chip* **2011**, *11*, 708–716.

- [17] Lu, M.; Ozcelik, A.; Grigsby, C. L.; Zhao, Y.; Guo, F.; Leong, K. W.; Huang, T. J. *Nano Today* **2016**, *11*, 778–792.
- [18] Chen, X.; Schroeder, J.; Hauschild, S.; Rosenfeldt, S.; Dulle, M.; Foerster, S. *Langmuir* **2015**, *31*, 11678–11691.
- [19] Jang, K.-J.; Suh, K.-Y. *Lab on a Chip* **2009**, *10*, 36–42.
- [20] Numata, M.; Takigami, Y.; Takayama, M. *Chemistry Letters* **2011**, *40*, 102–103.
- [21] Cheng, Y.; Zheng, F.; Lu, J.; Shang, L.; Xie, Z.; Zhao, Y.; Chen, Y.; Gu, Z. *Advanced Materials* **2014**, *26*, 5184–5190.
- [22] Ahn, Y.-C.; Jung, W.; Chen, Z. *Lab on a Chip* **2008**, *8*, 125–133.
- [23] Prasad, V.; Semwogerere, D.; Weeks, E. R. *Journal of Physics: Condensed Matter* **2007**, *19*, 113102.
- [24] Schlter, M.; Hoffmann, M.; Rbiger, N. *Characterization of Microfluidic Devices by Measurements with u-PIV and CLSM.*; Springer, 2007.
- [25] Park, T.; Lee, S.; Seong, G. H.; Choo, J.; Lee, E. K.; Kim, Y. S.; Ji, W. H.; Hwang, S. Y.; Gweon, D.-G.; Lee, S. *Lab on a Chip* **2005**, *5*, 437–442.
- [26] Lima, R.; Wada, S.; Tsubota, K.; Yamaguchi, T. *Measurement Science and Technology* **2006**, *17*, 797–808.
- [27] Dochow, S.; Krafft, C.; Neugebauer, U.; Bocklitz, T.; Henkel, T.; Mayer, G.; J. Albert, J. P. *Lab on a Chip* **2011**, *11*, 1484–1490.
- [28] Seibt, S.; With, S.; Bernet, A.; Schmidt, H.-W.; Foerster, S. *Langmuir* **2018**, *34*, 5535–5544.

Concluding Remarks

Many hypotheses posed by researchers across the world could, in theory, be answered by observing reactions in real time. To do this, one must merge together two major technologies: advanced scattering and spectroscopy methods with optimized microfluidic setups. It has only recently been possible, due to decades of research and development, to combine these fields. Nevertheless, it remains a demanding intersection which has the potential to answer many fundamental questions around nucleation, growth, and self-assembly of nanomaterials.

The general aim of this thesis was to utilize advanced microfluidic systems to gain insights into the reaction mechanisms and kinetics of various nanomaterial syntheses. To this end, a microfluidic flow reactor was designed that could be used to study a broad range of materials.

To answer the first research question, a new hydroquinone-based gold nanorod synthesis route was studied *in-situ* with regard to the reaction rate and growth mechanism, described in Chapter 3. This reaction was chosen instead of the more commonly applied synthesis with L-ascorbic as a reducing agent. It is known that the hydroquinone-based method produces far higher quality nanorods, however the growth kinetics of this system were unknown. It was found that the reaction mechanism follows a novel, and unusual, double-sigmoidal growth, which could be linked to the relative difference in growth rates of different facets as they formed as a function of the amount of free gold salt in solution. Future work is expected to corroborate this mechanism via high resolution transmission electron microscopy (HRTEM) measurements at different stages of the nanorod growth. It was found that the different stages of nanorod growth could be mapped onto shape transitions of the growing seed: a cuboctahedral seed grew into an ellipsoid before finally forming the spherical capped cylinders, as observed in the X-ray scattering patterns. The generality of this observed growth mechanism is evident as when the gold, hydroquinone, and silver concentrations were altered, the same growth stages were observed. However, the remaining synthesis parameters, such as CTAB concentration, temperature, and pH, were kept constant throughout all experiments. It is known that changes in these can have a significant influence on the growth of gold nanorods, and is hence an avenue which could be investigated further. The X-ray scattering experiments required a highly monodisperse sample to get precise structural information about the growing nanoparticles in suspension. Due to the high quality of these nanorods, they were prime candidates to study the sedimentation and diffusion behaviour of anisotropic particles as a function of their aspect ratio. Analyt-

ical ultracentrifugation (AUC) measurements for the determination of a sedimentation coefficient and dynamic light scattering (DLS) experiments for the determination of the diffusion coefficients in transversal and rotational mode as an example could be performed.

While there have been numerous theoretical hydrodynamic models postulated to describe the behavior of anisotropic diffusive particles, there have been far less experimental studies on these systems. Therefore, the high quality gold nanorods were used to address the second research question, as outlined in Chapter 4. The alignment of rods under shear flow was studied using a liquid microjet setup in combination with X-ray scattering. This microjet method was used to provide a stable stream of nanoparticles, thus allowing the probing of nanoparticle alignment before leaving the nozzle, in the free jet, and even in the final stages where the jet breaks up into droplets. Gold nanorods were compared to wormlike micelles and nanoplatelets, with an interesting parallel and perpendicular alignment behaviour with different specificity for each type of nanorod was found.

Previous studies on the alignment of wormlike micelles in microfluidic environments gave similar results where an axial-ratio dependency was found, along with stable alignment in the flow long after the tapering region. Therefore, future work should focus on using nanorod materials, such as gold nanorods, for comparative investigations. This would enable the mapping of a broad range of aspect ratios in combination with varying device parameters (i.e. tapering length, ratio and overall width). One technological challenge to overcome, however, was to find a suitable chip material with low background scattering such as a hybrid PDMS-glass capillary design that was described in the later chapters.

To answer the third question, a new approach to study fast reaction kinetics was carried out, shown in Chapter 5. The fast formation of pH induced hydrogel nanofibres could not be investigated under static conditions due to its rapid onset. Hence, the use of a microfluidic device with hydrodynamic flow focusing was necessary to ensure diffusion limited reaction conditions were present and to spread the reaction time over an addressable spatial dimension. Due to the affinity between the hydrogel and the channel walls, a new design with lateral and vertical focusing at the mixing cross was developed, which enabled the detailed study of the formed benzyltricarboxamide (BTA) nanofibres with various techniques. This system showed an increase in fluorescence with decreasing pH. Using this property to track fibre formation, the reaction kinetics along the microfluidic channel could be investigated via fluorescence microscopy

and confocal laser scanning microscopy (CLSM). The structural development of the growing fibres was monitored by X-ray scattering, where the all-PDMS device was replaced by a more suitable PDMS-glass hybrid device, thus minimizing the scattering background signal. Regarding fibre production, this device design has the potential for the continuous production of a variety of supramolecular self-assembled materials. Indeed, continuous flow synthesis of compounds and materials has not yet been widely adopted, however, it is expected to be the future for a wide array of industries due to the tunability and scalability of the method. One area of interest is fibres produced in flow-focused streams, which could hypothetically be directly spun out of the channel or collected for use in various applications.

In regards to fibre production, this kind of device design has the potential for a continuous production device for all kinds of supramolecular self-assembly to fibers, i.e. made of spider silk for medical applications. These could then be either studied in flow or in an even better approach directly spun out of the channel and measured as a free standing fibre.

What is the fastest possible reaction that could be realistically investigated in situ and in real time using continuous microfluidic flow is the question addressed in Chapter 6. The nucleation and growth of CdS nanoparticles is practically instant, and therefore demands a setup with fast time resolution. This setup was described in Chapter 5, and was given for continuous flow experiments in the newly developed three-dimensional hydrodynamic flow-focusing design. This enabled the investigation of the nucleation and growth of uniform CdS quantum dots which gave a controlled, diffusion-limited growth of nanoparticles. With this device design, the undisturbed reaction could be investigated, for the first time, where the precursor concentrations as well as the stabilising agent was altered. The reaction kinetics were studied via CLSM and absorption spectroscopy in-situ, utilizing the size-dependent optical properties of CdS nanoparticles.

The new microfluidic device design is an ideal platform for future X-ray scattering investigations. In theory, the system could investigate processes occurring at a timescale of milliseconds. Further development of synchrotron beamline capabilities and a highly characterised system as a starting point, this system is a promising start for the investigation of quantum dot syntheses. A major challenge, however, for this tool is how to address high-temperature syntheses which react rapidly. Others have investigated these systems by taking aliquots out of a hot reaction mixture batch with microfluidic channels, however, nobody has yet developed a reliable method for on chip high-temperature synthesis and *in-situ* characterization.

Following the macromolecular self-assembly of BTA molecules to hydrogel fibres, Chapter 7 describes the ability of the previously described device design as an ideal reaction environment to investigate the controlled self-assembly of the water soluble conjugated polymer poly (tetrabutylammonium 6-(thiophen-3-yl) hexane-1-sulfonate) (PTHS) as followed by CLSM and Raman spectroscopy. With this chip design, it was possible to follow the spatially distributed structural rearrangement by monitoring the decreasing fluorescence with ongoing solvent exchange across and along the channel. This provides an easy method to test the influence of various parameters on the self-assembly process of polymers in solution through simply changing the composition of chemicals and solvents within each channel.

Upon answering the main research questions, a new device was designed that showed great promise in studying a wide variety of systems – from organic to inorganic and from crystal growth to self-assembly. Nevertheless, as is often the case, many questions worth further investigation were raised during these studies. In addition, there are several recommendations to further improve this advanced microfluidic platform as well as other systems where it could be used to great effect.

1. Continuous flow production for temporally unstable materials like perovskites with flow focusing?
2. Scaling relations between flow rates, viscosities, diffusion coefficients, and the effective reaction time point vs position in channel?
3. How does extensional shear flow affect the growth of nanocrystals?
4. How could hot reactions be realised in microfluidic devices?
5. Is there an ultimate chip material suitable for every application? And an ultimate chip design? Could we fabricate them conveyor like in a cost saving way?
6. What improvements would be needed to truly see the onset of nucleation? Can we see Ostwald ripening?

Scientific Contributions

Publications

Schulreich, C.; Angermann, C.; Höhn, S.; Neubauer, R.; Seibt, S.; Stehle, R.; Lapp, A.; Richardt, A.; Diekmann, A.; Hellweg, T. Bicontinuous microemulsions with extremely high temperature stability based on skin friendly oil and sugar surfactants. *Colloids and Surfaces A: Physicochemical and Engineering Aspects*, **2013**, *418*, 39-46.

Schlenk, M.; Hofmann, E.; Seibt, S.; Rosenfeldt, S.; Schrack, L.; Drechsler, M.; Rothkirch, A.; Ohm, W.; Breu, J.; Gekle, S.; Förster, S. Parallel and perpendicular alignment of anisotropic particles in free liquid micro-jets and emerging micro-droplets. *Langmuir*, **2018**, *34*, 4843-4851.

Seibt, S.; With, S.; Bernet, A.; Schmidt, H.-W.; Förster, S. Hydrogelation kinetics measured in a microfluidic device with in-situ X-ray and fluorescence detection. *Langmuir*, **2018**, *34*, 5535-5544.

Seibt, S.; Zhang, H.; Mudie, S.; Förster, S.; Mulvaney, P. Growth Kinetics of Gold Nanorods: A SAXS Study. *Manuscript ready for submission*.

Seibt, S.; Mulvaney, P.; Förster, S. Millisecond CdS nanocrystal nucleation and growth studied by microfluidics with in-situ spectroscopy. *submitted to Colloids and Surfaces A*.

Seibt, S.; Johnson, B.; Schmidt, M.; Thelakkat, M.; Mulvaney, P.; Förster, S. Diffusion-limited self-assembly in microfluidics as a platform for structural analysis of anionic conjugated polyelectrolytes. *Manuscript in progress*.

Non-peer-reviewed publications

Schlenk, M.; Seibt, S.; Rosenfeldt, S.; Breu, J.; Förster, S. Reorientation of Anisotropic Particles in Free Liquid Microjets. *International Journal of Chemical and Materials Engineering*, **2017**, *11*.

Presentations

Oral presentations

Seibt, S. *Revealing the role of quantum coherence and ordering effects for energy- and charge transport in multichromophoric systems - GRK 1640 Workshop, Untertiefengrün (Germany), October, 5.-7., 2015.*

Microfluidics for in-situ investigations of reaction kinetics.

Seibt, S. *Recent Advances in Polymer Science - Workshop, Amherst (USA), December, 7.-8., 2015.*

Microfluidics for in-situ investigations of reaction kinetics.

Seibt, S. *Reviewing the energy- and charge transport in multichromophoric systems - GRK 1640 Workshop, Selb (Germany), October, 5.-7., 2016.*

Investigations of in-situ growth and self-assembly kinetics using microfluidics in combination with scattering techniques and spectroscopy.

Seibt, S. *Australian Colloid & Interface Symposium, Coffs Harbour (Australia), January, 29. - February, 2., 2017.*

Synthesis and Controlled Growth of Monodisperse Gold Nanorods.

Seibt, S. *Rheoscattering Workshop, Clayton (Australia), August, 14, 2017.*

How Microfluidics forces Particles to Self-assembly - a Rheo-optical Study.

Seibt, S. *International Conference on Nanoscience and Nanotechnology, Wollongong (Australia), January, 29. - February, 2., 2018.*

In-situ Investigation of Molecular Self-Assembly Using Microfluidics.

Seibt, S. *PhD Completion Seminar, Melbourne (Australia), February, 21., 2018.*

In-situ Investigation of Molecular Self-Assembly Using Microfluidics.

Poster presentations

Fürst, C.; Seibt, S.; With, S.; Förster, S. *International Association of Colloid and Interface Scientists*, Mainz (Germany), May, 24.-29., **2015**.

CLSM and SAXS Life-Monitoring of Fast Amphiphile Self-Assembly.

Chen, X.; Seibt, S.; Michaelis, M.; S. Förster *International Association of Colloid and Interface Scientists*, Mainz (Germany), May, 24.-29., **2015**.

SAXS/WAXS/UV-Vis Life-Monitoring of Nanoparticle Nucleation and Growth.

Seibt, S.; S. With, S.; Förster *Recent Advances in Polymer Science - Workshop*, Amherst (USA), December, 7.-8., **2015**.

SAXS and CLSM Life-Monitoring of Trisamide Self-Assembly and Nanoparticle Nucleation and Growth.

Seibt, S.; Dulle, M.; Mulvaney, P.; Förster, S. *Gordon Research Conference Noble Metal Nanoparticles*, South Hadley (USA), June, 18. - 24., **2016**.

SAXS/WAXS/UV-Vis Life-Monitoring of Nanofiber Self-Assembly and Seeded Gold Nanorod Growth.

Acknowledgements

Throughout my PhD many people have made a significant contribution and without whom surely this thesis would not have been possible.

First and foremost, I would like to thank my supervisors Professor Stephan Förster and Professor Paul Mulvaney, who had the courage to guide me through this hell of a ride called joint degree. I will be forever thankful for the opportunity Stephan gave me to start my PhD in Bayreuth and just as much for being welcomed at Paul's group in Melbourne half way through. I want to thank both of you for your constant support, the guidance and motivation, for all the input in my projects and the freedom to pursue my own ideas.

I would like to specially thank Alexandra Strich and Johanna Monk, who helped me getting settled in Melbourne more than once and without whom I would have just been lost in the jungle of Australian bureaucracy. I would also like to express my gratitude to my panel members within the BayNAT Graduate School, Prof. Mathias Karg and Prof. Hans-Werner Schmidt, as well as the committee panel members in Melbourne, Prof. Jonathan White and Prof. Muthupandian Ashokkumar for their support. Many thanks to Prof. Barbara Rothen-Ruthishauser for kindly mentoring me from Switzerland.

A close friend once told me 'you undertake your PhD for the people you meet on the way' and I cannot agree more. In this regard I would like to thank the two amazing groups I had the honor to spend my time with. Firstly, I would like to send a warm thank you to my fellow PC1'ers in Bayreuth (and now Jülich), past and present. You have made my time here wonderful and working alongside you all has been an inspiration. Special thanks go to my 'Kellerkinder' girls Maria and Miriam, and my everlasting partner in crime Olga. I don't even find words praising high enough how grateful I am that I've had you by my side throughout all the years of studying and PhD. Many of the group members are now amongst my dearest friends: Carolin Fürst, Corinna Stegelmeier, Sascha Ehlert, Kirsten Volk, and Astrid Rauh to name just a few. I would like to thank the whole group for making my PhD journey remembered fondly.

Secondly, I would like to express my thanks to the NSL group for giving me a warm welcome when I first arrived - and every time I came back to Melbourne. Special thanks go to Chris, James, Heyou, Sarah and Pegah for always being a shoulder to lean on and supporting me throughout my time in Australia. Many thanks also to the rest of the NSL to make me feel as a part of the group.

Acknowledgements

I thank all members, past and present, of the JCF Bayreuth for including me as a part of such an inspiring and motivating group of scientists throughout all fields. I would like to especially acknowledge Dagmar and Aniela, who became close friends of mine even beyond this forum.

Also I would like to acknowledge the DAAD for their financial support and the opportunity to build an international network of friends and colleagues.

I am eternally grateful for the constant support of my family, especially my parents and my brother, to whom I dedicate this thesis. Thank you for always believing in me. Finally, I would like to thank Calum, who made my time in Australia simply perfect. I am certain this thesis could not have happened without your support at work and, especially, in private. Thank you for your encouragement, motivation, laughter and love, particularly in the past weeks of writing (even from far away).

Thank you!

Appendix

Supplementary Information

A. SI: Growth Kinetics of Gold Nanorods: A SAXS Study

In-situ investigations of gold nanorod synthesis

Optical evolution during the reaction of all samples, displayed as contour plot to show the clear shift to higher wavelength of the LSPR according to Figure 3.5.

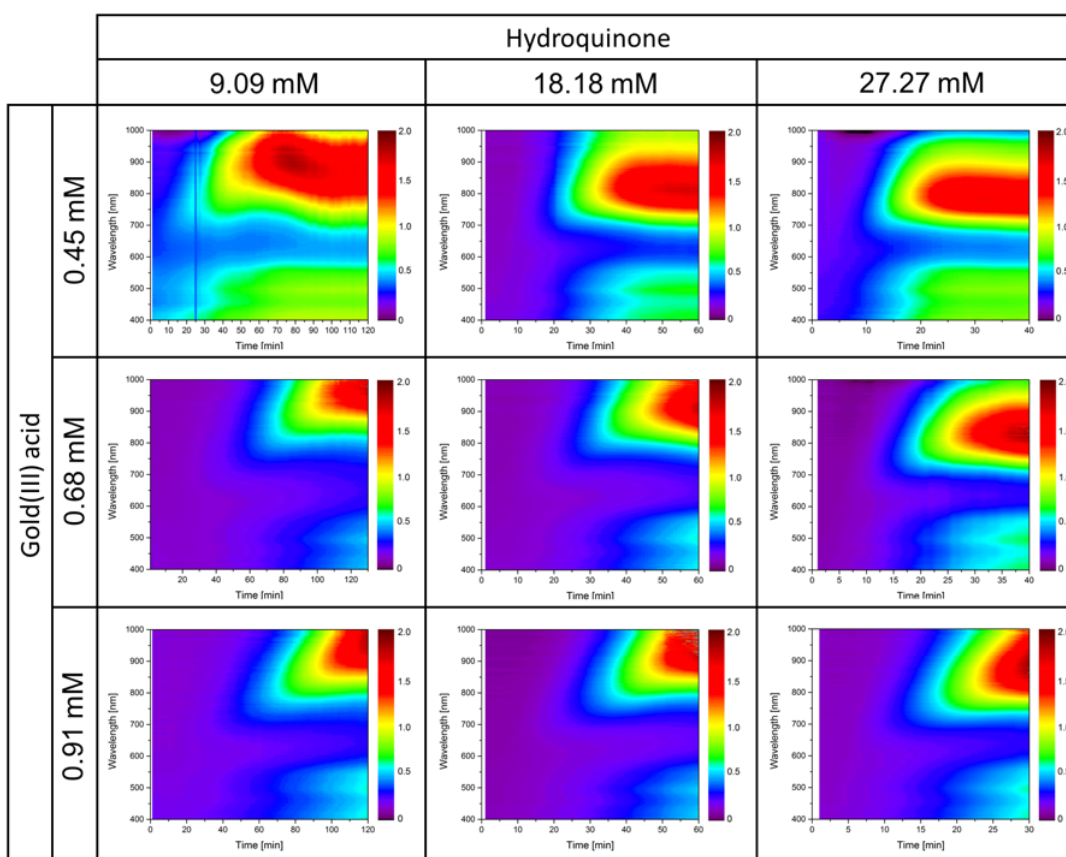


Figure A.1: Contour plots of the absorption behaviour in the same 3x3 matrix, according to Figure 3.5.

To give an impression about the SAXS fitting of the radial averaged SAXS patterns collected over the reaction time, Figure A.2 shows three waterfall plots of examples with fitting curves for spheres, ellipsoids and spherical capped cylinders for varying precursor concentrations.

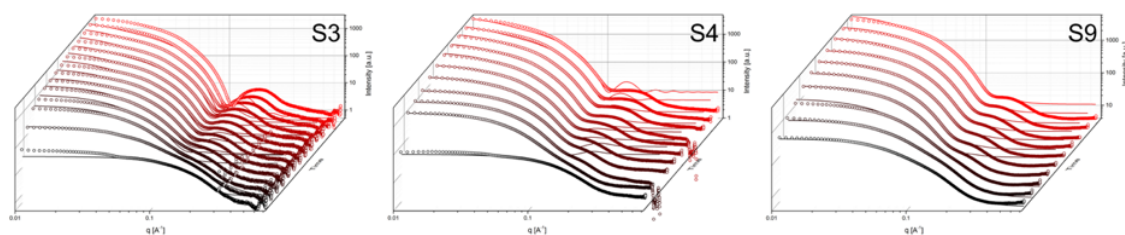


Figure A.2: Waterfall plots of the SAXS data including the fit for spherical, ellipsoidal and cylindrical particles as a function of time for three different synthesis.

During the fitting of the SAXS data, the decision has to be made when the scattering curve is fitted as a sphere, an ellipsoid or a spherical capped cylinder. Therefore, Figure A.3 shows four different scattering curves at different times during the reaction and the attempt to fit them with each shape. It can clearly be seen, that only one shape for each fitting of the scattering data gives a matching result. At the early stages in the reaction, the ellipsoidal fit as well as the spherical fit can be used. However, the ellipsoidal fitting model has an anisotropy factor (equal to the aspect ratio), which is in these cases close to one, so the particle appears as a spherical shape.

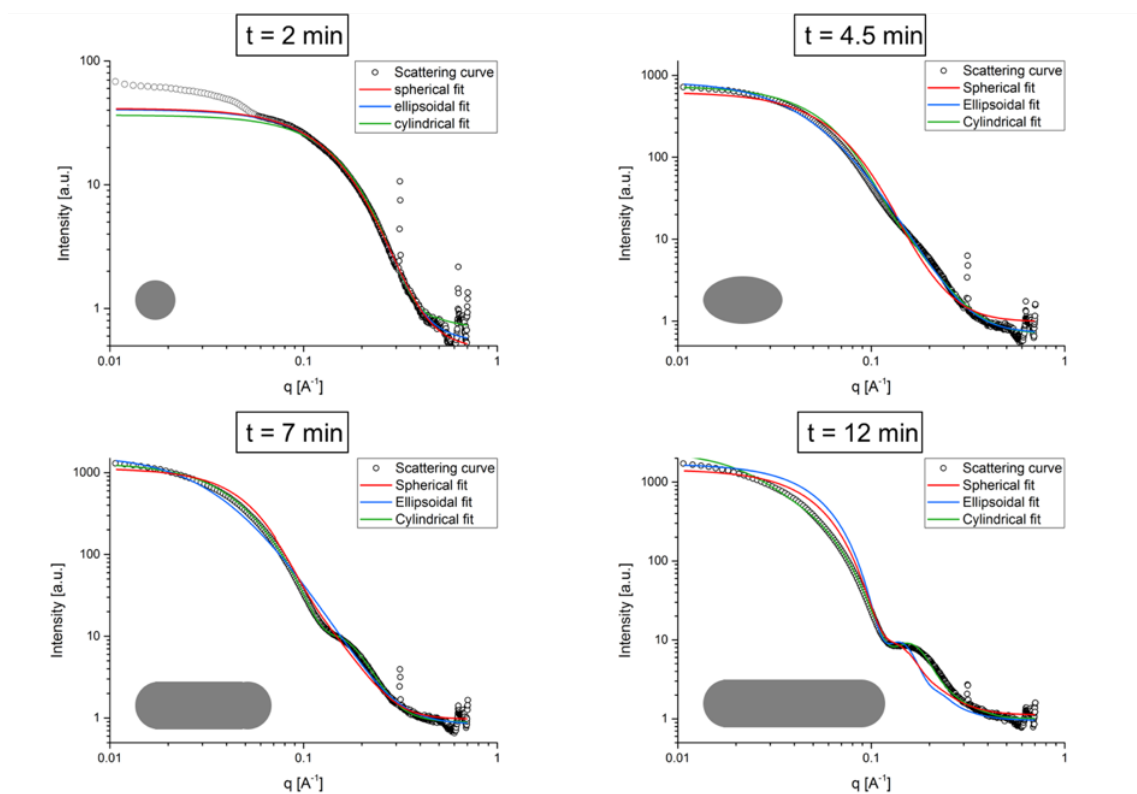


Figure A.3: Fitting of SAXS curves at different times during the reaction of sample AuNR-S3 with spherical, ellipsoidal and cylindrical (spherical capped) fit model to display the selection criteria for the according evaluation method of size parameters.

Modelling and fitting of the scattering curves

The scattering curves could be well described by using a model of core shell-spheres, ellipsoids or cylinders.

For spherical core/shell particles with inner radius R_c and outer radius R , the form-factor $P_S(q)$ is given by

$$P_S(q, R_c, R) = F_{S_{cs}}^2(q, R_c, R) \quad (\text{A.1})$$

with the scattering amplitude

$$F_{S_{cs}}^2(q, R_c, R) = \frac{\left[\frac{(1-\rho)}{3} F_S(q, R_c) + \frac{\rho}{3} p^{-3} F_S(q, R) \right]}{\left[\frac{1-\rho}{3} + \frac{\rho p^{-3}}{3} \right]} \quad (\text{A.2})$$

$$F_S(q, R) = \frac{3}{(qR)^3} (\sin(qR) - qR \cos(qR)) \quad (\text{A.3})$$

where $\rho = \rho_s/\rho_c$ is the ratio of the scattering length densities of shell and core, and $p = R_s/R_c$ is the ratio of the inner and outer particle radii.

The formfactor $P_C(q)$ for core-shell cylinders of inner radius R_c , outer radius R and length L is given by

$$P_C(q, R_c, R, L) = P_{\parallel}(q, L) P_{\perp}(q, R_c, R_m) \quad (\text{A.4})$$

$$P_{\parallel}(q, L) = \frac{2}{qL} Si(qL) - \left(\frac{\sin(qL/2)}{qL/2} \right)^2 \quad (\text{A.5})$$

$$P_{\perp}(q, R_c, R_m) = F_{S_{cs}}^2(q, R_c, R) \quad (\text{A.6})$$

$$F_{S_{cs}}^2(q, R_c, R) = \frac{\left[\frac{1-\rho}{2} F_C(q, R_c) + \frac{\rho}{2} p^{-2} F_C(q, R) \right]}{\left[\frac{1-\rho}{2} + \frac{\rho p^{-2}}{2} \right]} \quad (\text{A.7})$$

$$F_C(q, R) = \frac{2J_1(qR)}{qR} \quad (\text{A.8})$$

where $Si(z)$ is the sine-integral and $J_1(z)$ is the Bessel function of the first kind.

The formfactor $P_E(q)$ for core-shell ellipsoids of revolution with inner radius R_{rc} , outer

radius R_r and the axial ratio $\epsilon = R_z/R_r$ of the outer long-axis R_z in z-direction to the perpendicular short-axis R_r is given by

$$P_E(q, \epsilon, R_C, R) = \int_0^\pi F_{Ecs}^2(q, \epsilon, \theta, R_C, R) \sin \theta d\theta \quad (\text{A.9})$$

with the scattering amplitude

$$F_{Ecs}(q, \epsilon, \theta, R_C, R) = \frac{\left[\frac{1-\rho}{3} F_E(q, \epsilon, \theta, R_C) + \frac{\rho}{3} p^{-3} F_E(q, \epsilon, \theta, R) \right]}{\left[\frac{(1-\rho)}{3} + \frac{\rho p^{-3}}{3} \right]} \quad (\text{A.10})$$

$$F_E(q, \epsilon, \theta, R) = \frac{3}{(qR_{\theta,\epsilon})^3} (\sin(qR_{\theta,\epsilon}) - qR_{\theta,\epsilon} \cos(qR_{\theta,\epsilon})) \quad (\text{A.11})$$

$$R_{\theta,\epsilon} = R_r \sqrt{\sin^2 \theta + \epsilon^2 \cos^2 \theta} \quad (\text{A.12})$$

The formfactors are further averaged over a Schulz-Zimm distribution for the radii and lengths with a relative standard deviation σ_R for the radii and σ_L for the lengths.

Details of the derivations and numerical calculations can be found in [1,2,3]. The fits are performed with the software *Scatter* [4]. The fitted radii and length are given as number averages.

Experimental data from *in-situ* absorption and SAXS measurements

Table A.1 and A.2-A.4 show the experimental data for the temporal evolution of LSPR and length and width for all nine syntheses measured by *in-situ* SAXS and UV-Vis.

Table A.1: LSPR wavelength evolution over time for all nine samples with different synthesis parameters according to Table 3.1.

Time	S1	S2	S3	S4	S5	S6	S7	S8	S9
[min]	[nm]								
1									
2									
3									
4									
5									
6									
7									
8			727			696			
9			742			720			704
10			754			737			722
11		725	767			750			730
12		748	779		702	757			741
13		756	789		718	765			750
14		762	796		727	774			763
15		765	803		735	783			774
16		771	807		742	791			783
17		775	810		747	799			798
18	719	780	810		751	806		748	811
19	721	786	810		766	811		757	820
20	728	790	811		772	814		766	826
21	731	801	812		776	821		775	831
22	737	804	811		785	826		783	838
23	742	809	810		792	830		788	845
24	745	812	809		796	833		792	854
25	752	816	808	736	803	839		803	861
26	757	821	807	737	811	841		807	869
27	758	825	807	742	817	845		813	876
28	760	827	807	745	821	847		816	884
29	767	828	807	751	823	848		819	888
30	772	831	807	758	827	850		825	895
31	778	832		760	830	851	737	828	901
32	785	833		763	836	851	739	834	903
33	788	834		765	843	849	740	838	904
34	795	835		766	851	846	743	845	904

SI: Growth Kinetics of Gold Nanorods: A SAXS Study

35		836		767	856	845	746	853	903
36		836		768	859	845	749	860	902
37		837		770	864	845	751	863	900
38	812	837		774	868	845	753	868	
39	816	838		777	872	845	756	872	
40	821	838		787	876	845	761	879	
41	829	839		790	879	844	763	881	
42	838	838		792	881	843	767	887	
43	844	837		795	883	842	771	893	
44	850	836		797	885	842	773	900	
45	857	835		798	886	841	774	908	
46	862	834		799	889	841	776	914	
47	865	833		800	889	840	778	918	
48	869	832		804	890	840	781	920	
49	876			806	891	839	787	921	
50	879			809	891	839	789	925	
51	881			811	892	839	792	926	
52	883			814	891	839	796	927	
53	887			817	890	838	798	928	
54	890			820	889	838	801		
55	894			823	888	838	804		
56	897			827	887	838	806		
57	898			829	887	838	807		
58	899			830	886	837	809		
59	900			835	885	837	811		
60	903			837	884	837	814		
61	906			839			816		
62	907			843			817		
63	909			845			819		
64	911			850			822		
65	913			852			826		
66	914			853			829		
67	917			855			834		
68	918			858			836		
69	917			861			839		
70	918			864			843		
71	918			873			845		
72	918			876			848		
73	918			879			851		
74	918			884			854		
75	917			887			857		
76	917			891			860		
77	917			894			864		

78	916			897			866		
79	916			902			868		
80	915			903			872		
81	914			903			875		
82	913			904			878		
83	912			905			882		
84	911			909			886		
85	910			914			888		
86	909			917			891		
87	908			920			894		
88	907			923			897		
89	906			925			899		
90	905			926			901		
91	904			930			903		
92	903			932			906		
93	902			933			908		
94	901			934			909		
95	900			935			911		
96	900			936			915		
97	899			937			919		
98	899			937			920		
99	898			937			923		
100	896			937			925		
101	893			936			927		
102	892			937			929		
103	889			937			932		
104	888			936			934		
105	886			937			938		
106	886			936			941		
107	885			936			944		
108	884			936			946		
109	884			936			949		
110	884			936			951		
111	884			936			951		
112	884			936			952		
113	884			936			953		
114	884			936			952		
115	884			936			953		
116	884			936			955		
117	884			936					
118	884			936					
119	884			936					
120	884			936					

Table A.2: Temporal evolution of length and width of the nanorod for sample AuNR-S1, -S2 and -S3, evaluated by fitting the X-ray scattering curves with spherical (red), ellipsoidal (blue) and spherical capped cylindrical (green) core-shell model.

	AuNR-S1		AuNR-S2		AuNR-S3	
Time	Length	Width	Length	Width	Length	Width
[min]	[nm]	[nm]	[nm]	[nm]	[nm]	[nm]
2	3,3	3,3	3,6568	3,6568	3,42	3,42
3	5,22	3,6			5,07	3,84
4					7,69	4,32
5			7,0452	4,12	11,3	4,9
6	7,21	4,36				
7			9,568	4,6	13,7	4,96
9	7,95	4,7				
10			11,1	5,04	14,9	5,32
11					17,4	5,46
12					21,5	5,56
13					23,9	5,78
14					26,3	5,86
15	8,33	5,44	12,6	5,7	27,1	6,04
17					28,5	6,14
20	8,67	5,9	13,7	6	30,9	6,5
24					32,8	6,62
25	10,3	6,02	17,6	6,24		
28					33,4	6,82
30	10,7	6,1	22,3	6,4	33,5	6,82
33	11,4	6,22				
35	13,5	6,24	26,2	6,48		
39	18,3	6,28				
40			29,8	6,5	33,6	6,82
45	24,8	6,32	31,6	6,58		
49	30,2	6,36				
50			32,2	6,62	33,7	6,84
51	35,6	6,38				
55			34,1	6,74		
60	39,6	6,5	36,3	6,74	33,8	6,84
61	39,8	6,5				
65	41,2	6,5				
70			36,8	7,06	33,9	6,84
71	41,2	6,5				
76	42,5	6,52				
80			37,4	7,12		
81	43,2	6,64				

86	43,3	6,6				
90			37,9	7,12		
91	44,7	6,8				
100	45,2	6,84	38,3	7,12		

Table A.3: Temporal evolution of length and width of the nanorod for sample AuNR-S4, -S5 and -S6, evaluated by fitting the X-ray scattering curves with spherical (red), ellipsoidal (blue) and spherical capped cylindrical (green) core-shell model.

	AuNR-S4		AuNR-S5		AuNR-S6	
Time	Length	Width	Length	Width	Length	Width
[min]	[nm]	[nm]	[nm]	[nm]	[nm]	[nm]
2	3,12	3,12	3,22	3,22	3,38	3,38
5			5,33	4,24	5,44	4,16
7			7,56	4,52		
8					9,71	4,42
10	6,99	5	9,5	4,82	11,9	4,6
15	8,83	5,48	11,8	5,16	13,8	4,78
20	11,6	5,62	13,2	5,4	17	5,02
25	12,6	5,74	14,9	5,48	20	5,34
30			18,3	5,8	23,8	5,62
33	14,7	6,04				
35			20,9	6,1	26,2	5,9
37					28,8	6,42
40	17,1	6,12	24,2	6,58	31,2	6,88
45	18,8	6,22				
46					33,2	7,44
48			29,5	6,74		
50	21,3	6,3			33,8	7,6
55	22,7	6,42	35,1	7,1	34,1	7,82
60	26,3	6,78	38,5	7,44	34,3	7,96
65			40,3	7,58	34,5	8,1
66	34,6	7,16				
70	39,5	7,22	41,1	7,64	34,8	8,16
75	48,1	7,38	42,2	7,72		
80	51,3	7,48	42,9	7,76	35,1	8,3
85			43,7	7,8		
90	52,4	7,72			35,3	8,34
91			44,2	7,82		
99			45,4	7,84		
100	52,8	7,88				

105			45,6	7,92		
120	52,8	8,14				

Table A.4: Temporal evolution of length and width of the nanorod for sample AuNR-S7, -S8 and -S9, evaluated by fitting the X-ray scattering curves with spherical (red), ellipsoidal (blue) and spherical capped cylindrical (green) core-shell model.

	AuNR-S7		AuNR-S8		AuNR-S9	
Time	Length	Width	Length	Width	Length	Width
[min]	[nm]	[nm]	[nm]	[nm]	[nm]	[nm]
2	3,32	3,32	3,24	3,24	3,08	3,08
3					4,3296	3,28
4	4,6964	3,98				
5			6,43	4,2	6,258	4,2
10	4,92	4,22	8,4	4,56	10,2	4,9
15	6,11	4,3	10	4,94	11	5,36
20	8,17	4,34	11,7	5,02	12,5	5,5
25	9,14	4,5	12,3	5,32	13	5,68
30	10,7	4,8	14,8	5,44	15,6	5,96
35	11,3	4,7	15,7	5,58	18,9	6,1
40	14,8	4,94	17,6	5,7		
41					24,2	6,14
45	16,3	5,16	19,1	5,82	29,8	6,32
50	18,1	5,66	20,8	6,06	35,3	6,42
55	18,8	5,62	25,2	6,36	40,1	6,5
60	20,2	5,96	30,5	7,24	40,8	6,66
65	23,4	6,58	38,2	8,38		
70	26,5	7,02	43,3	8,94	41,5	7,22
75	34,3	8,18	47,1	9,44		
80	42,8	9,72	50,7	9,58	42,3	7,56
85	54,1	10,84	52,4	9,6		
90	61,4	11,4	53,2	9,86	42,7	7,72
100	61,5	11,4				

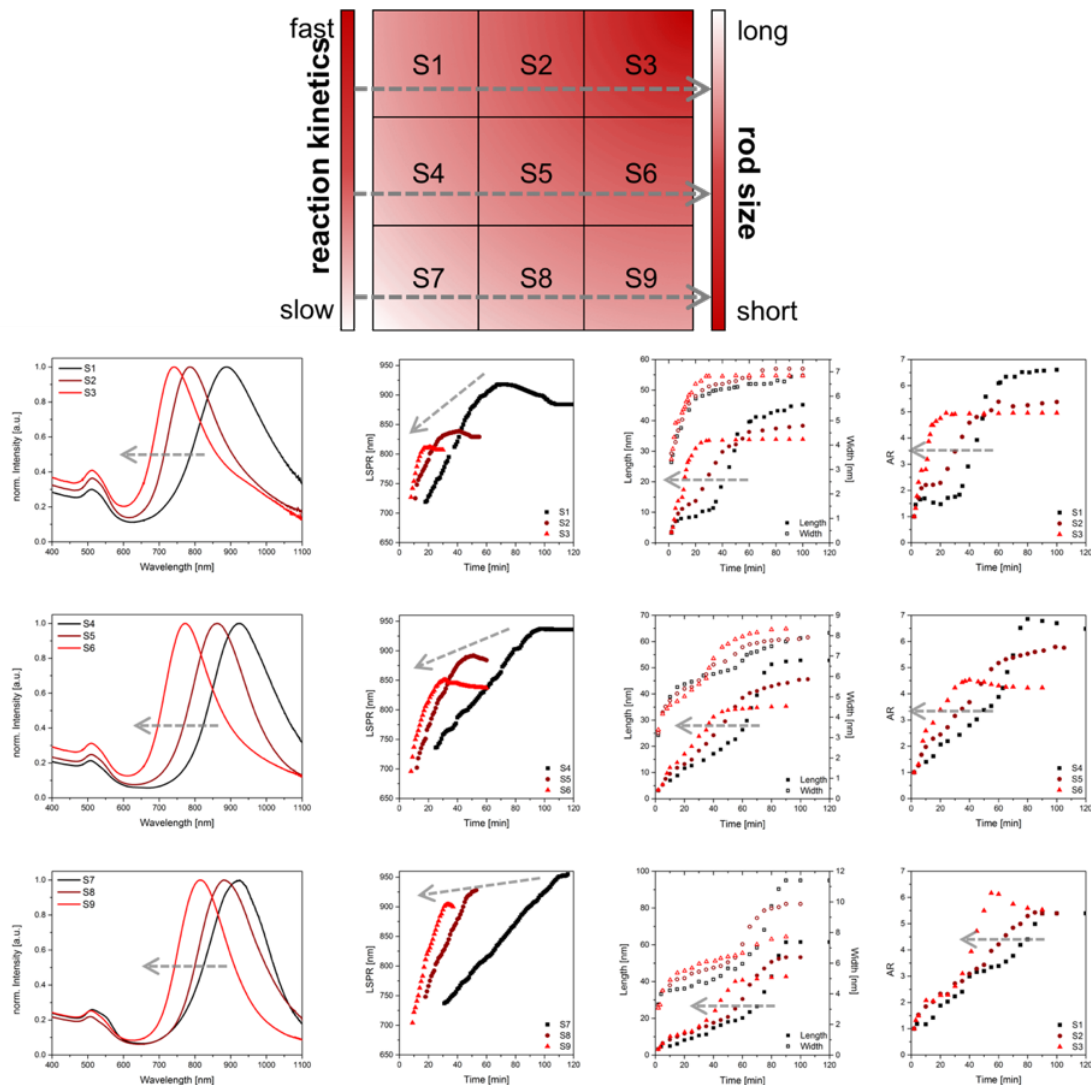


Figure A.4: Comparison of the optical properties and the length and width growth of the synthesis along the rows of Table 3.1, systematically increasing the hydroquinone concentration, shown for three different gold acid concentrations.

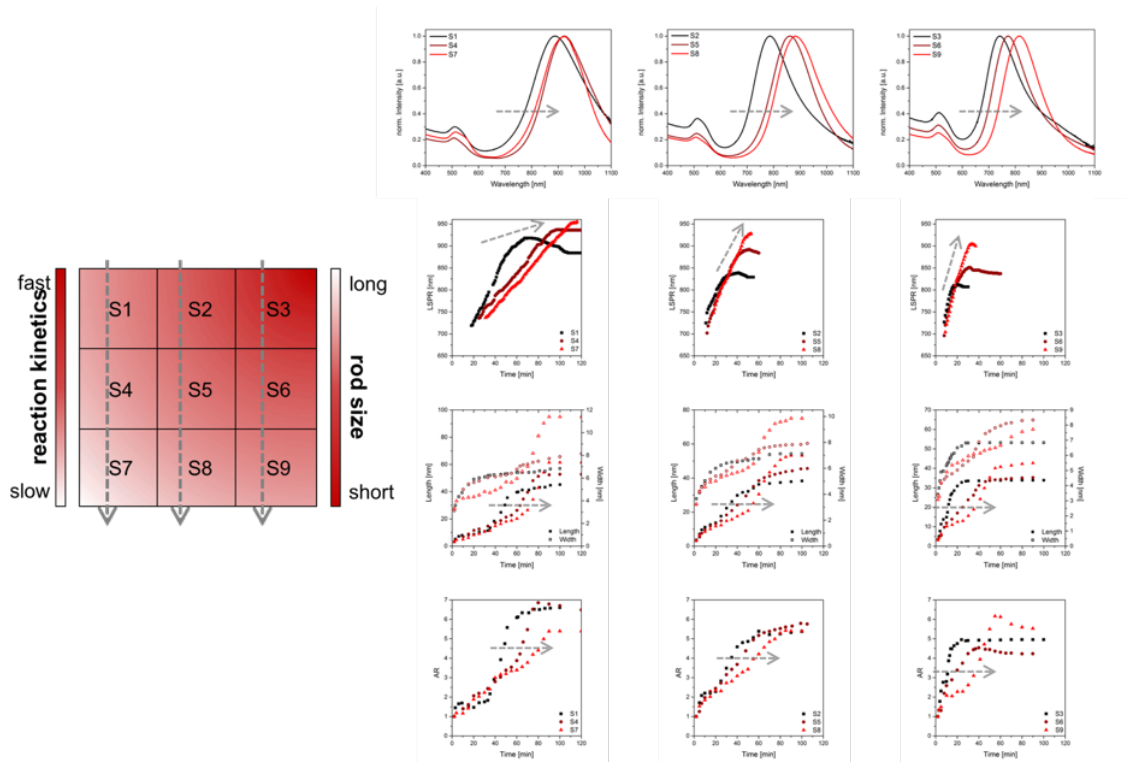


Figure A.5: Comparison of the optical properties and the length and width growth of the synthesis along the columns of Table 3.1, systematically increasing the gold acid concentration, shown for three different hydroquinone concentrations.

COMSOL Simulation

We simulated absorption spectra of single gold nanorods in solution with refractive index ($n = 1.4$) by exploiting a rigorous solution of Maxwell's wave equations (Numerical Solution). The simulation domain (400 nm in length x 400 nm in width x 600 nm in height) consisted of a single spherical capped cylinder (gold nanorod) with a series of dimensions shown in Table A.2-A.5. The gold nanorod was meshed with three-dimensional grids of 1 nm spacing, and the central region (200 nm x 200 nm x 400 nm) was further meshed with three-dimensional grids of 5 nm spacing. The dielectric function of gold was extracted from the data of Johnson and Christy.[5]

Cyclic Voltammetry

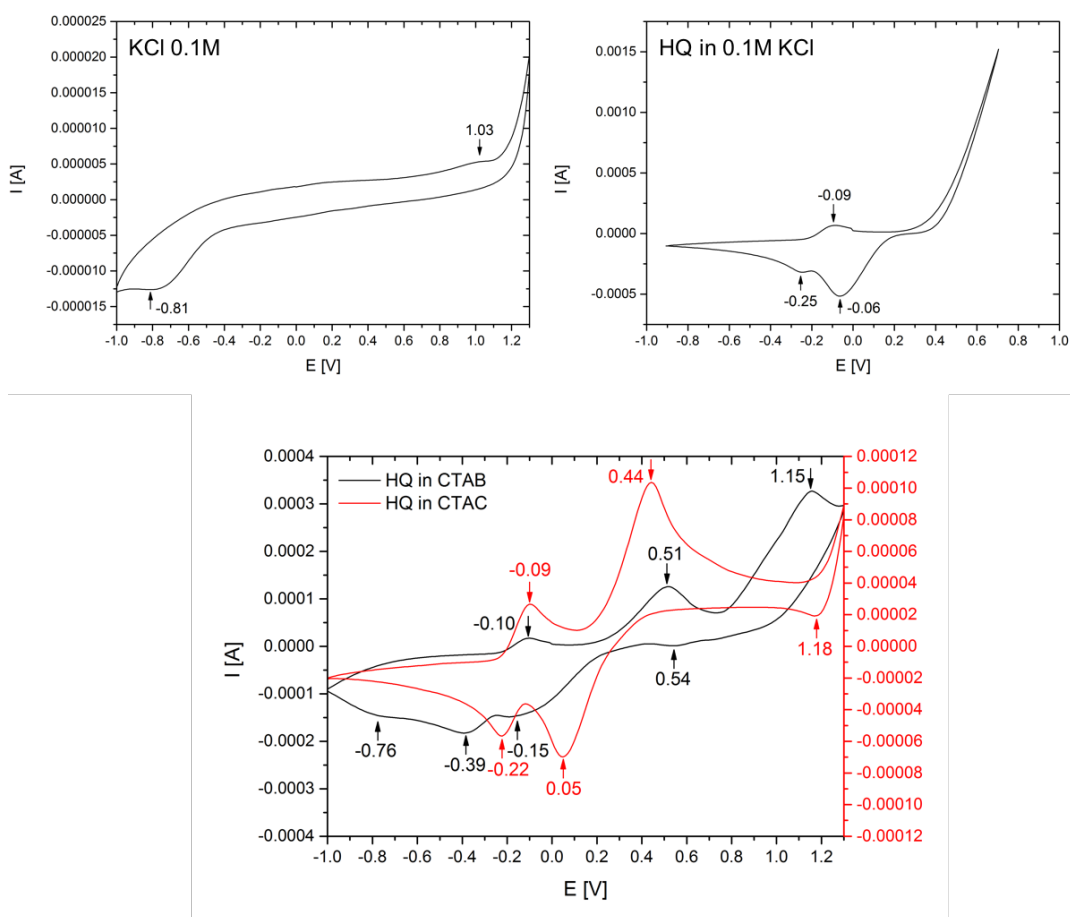


Figure A.6: Reference CV spectra for KCl electrolyte (0.1 M), hydroquinone in an 0.1 M KCl solution and in 0.05 mM CTAB and CTAC solution to see the difference of chlorine and bromide as counter ion.

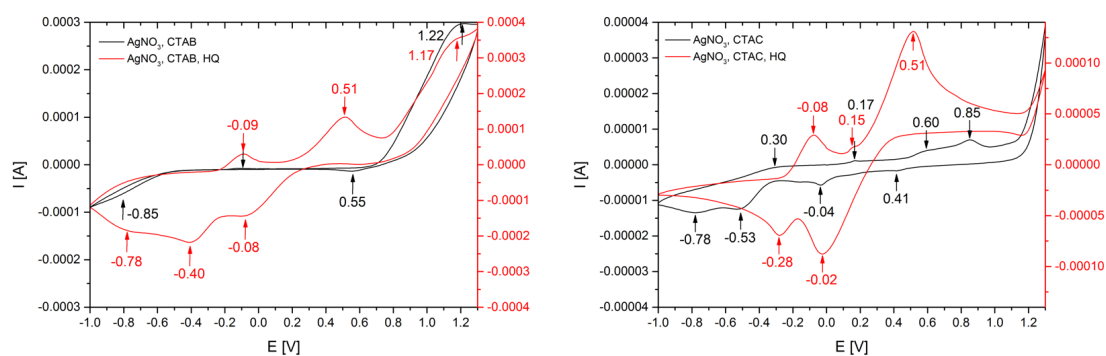


Figure A.7: Reference CV spectra for AgNO_3 in CTAB (left) and CTAC (right), both before (black line) and after (red line) the addition of hydroquinone as a reducing agent.

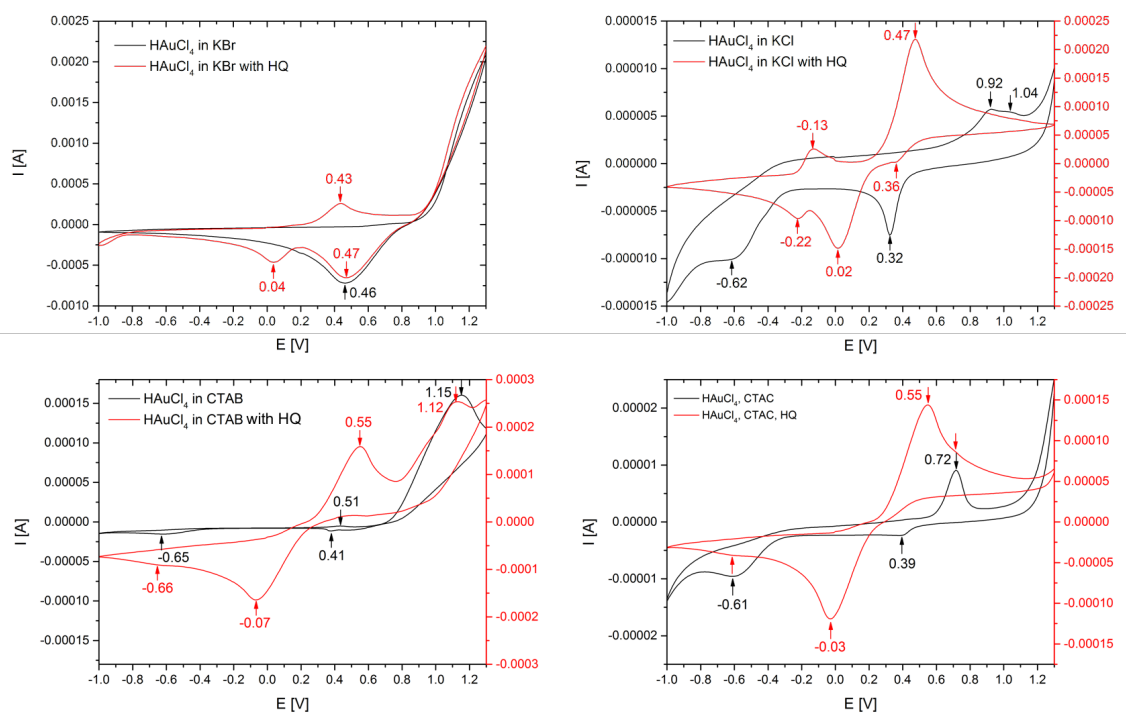


Figure A.8: Reference CV spectra for HAuCl_4 in 0.1 M KBr and 0.1 M KCl solution (top), as well as 0.05 M CTAB and 0.05 M CTAC solution (bottom). Each mixture was measured before (black line) and after (red line) the addition of hydroquinone as a reducing agent.

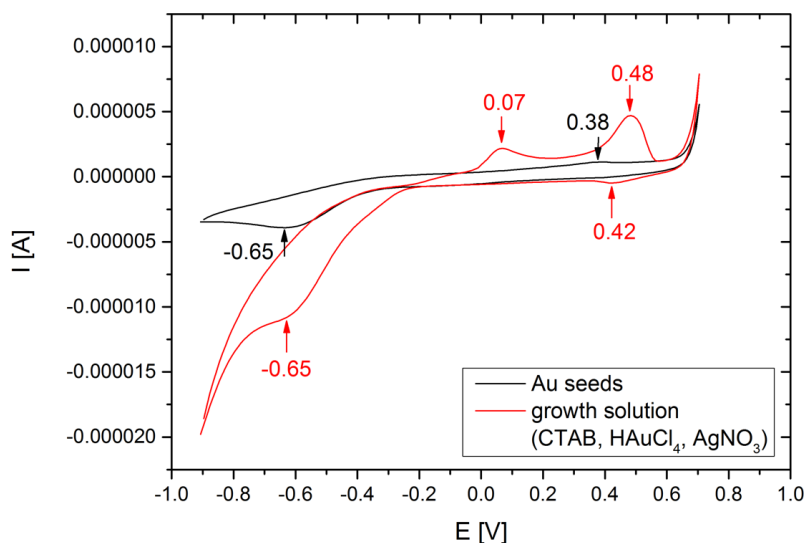


Figure A.9: Reference CV spectra of the produced gold seed solution (black line), used for the final gold nanorod synthesis and the reaction growth solution (red line) containing CTAB, HAuCl₄ and AgNO₃ before the addition of hydroquinone and the seed solution.

Gold overgrowth experiment

To 2.5 mL of a 0.1 M CTAB solution, 12.5 μL of 0.1 M HAuCl₄ solution and 0.1 M AgNO₃ solution was added and mixed until everything was homogeneously dissolved. 125 μL of an aqueous 0.4 M HQ solution was then added and the growth solution gently mixed, leading to complete decolourisation. Finally, 100 μL of the purified and diluted gold nanorods were added as seeds and mixed thoroughly. Experiments were carried out at 22°C. The solutions were undisturbed for the overgrowth for 24 h at room temperature. The solution was purified by centrifugation (10 min, 14000 rcf) before being washed with water and redispersed in 0.5 mL of Millipore water to yield a concentration four times higher than the initial synthesis concentration.

In-situ UV-Vis measurements were performed every 5 minutes, starting from the moment of nanorod seed addition.

For the TEM analysis, 4 μL of the as-prepared solution was dried on a mesh copper grid with carbon foil. For size evaluation, the software ImageJ (version 1.44p, U.S. National Institute of Health) was used.

Figure A.10 shows TEM images of the gold nanorods before and after the gold overgrowth experiment.

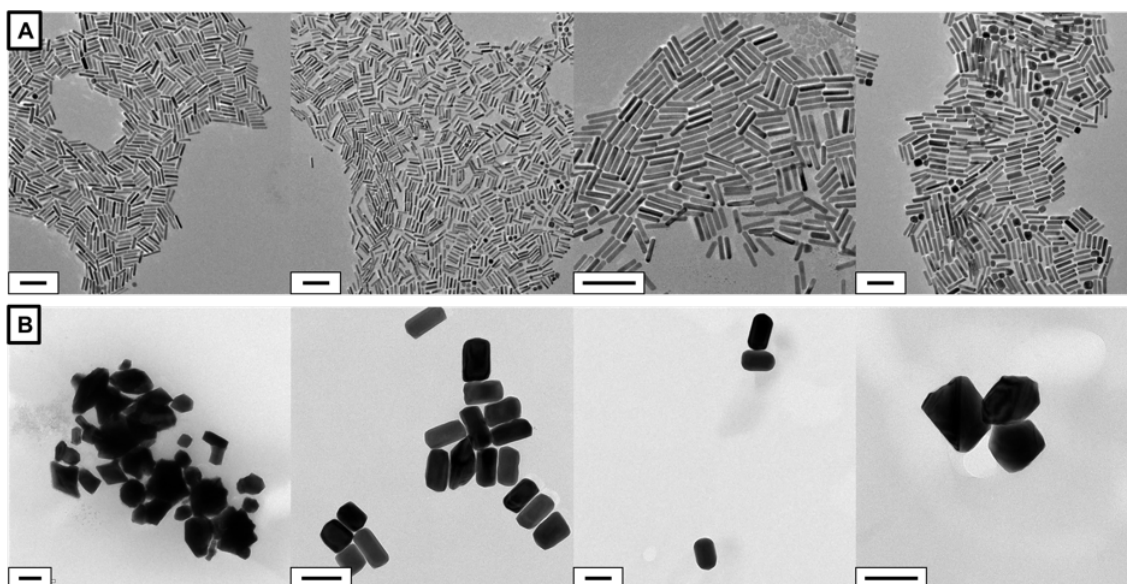


Figure A.10: TEM images of the gold nanorods before (A) and after (B) the gold overgrowth experiments. From left to right showing sample one to four. The scale bar is 100 nm. A clear change of shape and size can be seen for all samples.

Table A.5 shows the size evaluation and the used gold concentration of all four samples used in the gold overgrowth experiment.

Table A.5: Size evaluation and used gold concentration in the dilute aqueous solution for all four samples used in the gold overgrowth experiment.

Sample	Length [nm]	Width [nm]	Aspect Ratio	[Au] [mol/L]
1	51,6	9,1	5,65	9.95e-5
2	42,1	7,5	5,65	1.24e-4
3	50,3	8,6	5,82	5.26e-5
4	65,3	12,2	5,36	1.37e-4

Figure A.11 displays the temporal evolution of the absorption spectra for all four samples as three-dimensional, two-dimensional and contour plot.

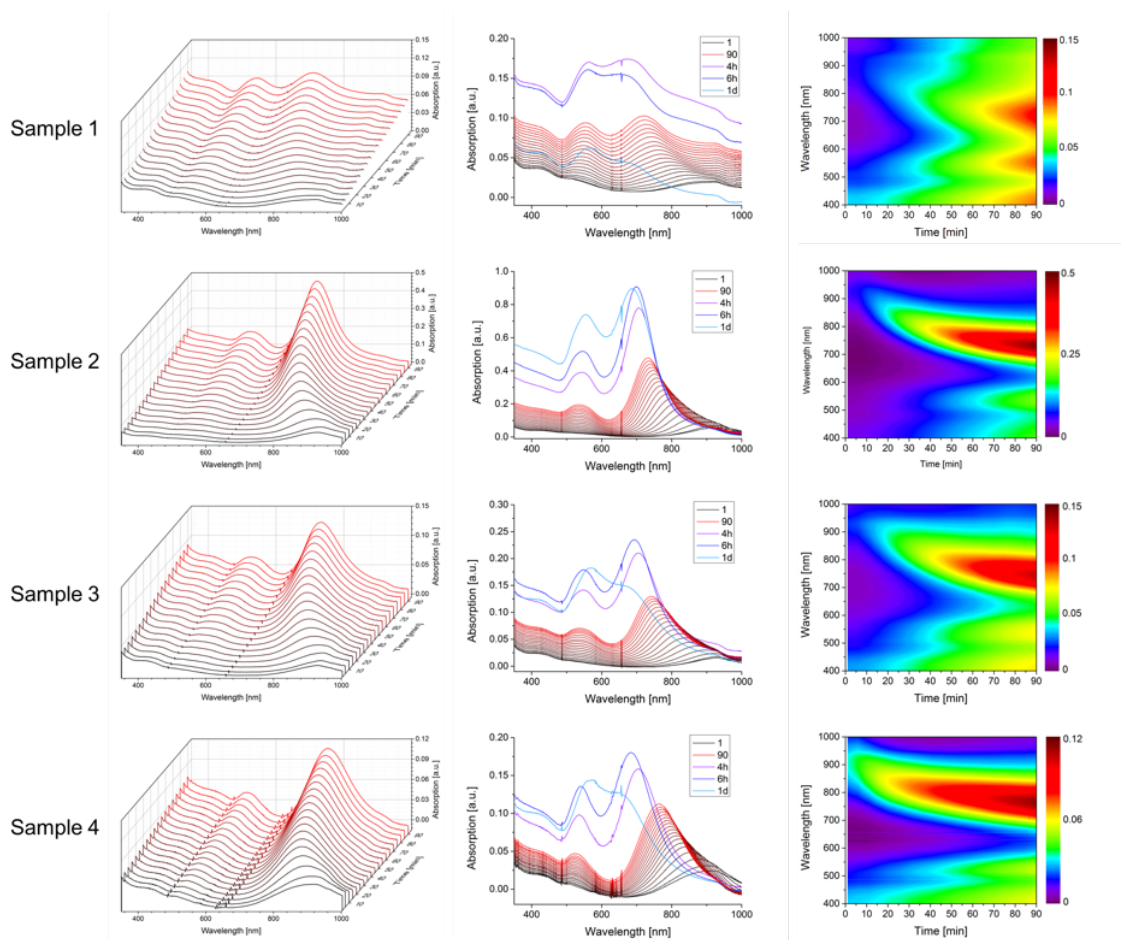


Figure A.11: Temporal evolution displayed as three-dimensional, two-dimensional and contour plot for all four samples during the gold overgrowth reaction. A clear LSPR blueshift and TSPR redshift can be seen.

Figure A.12A shows the temporal evolution of the transverse SPR and Figure A.12B of the longitudinal SPR during the gold overgrowth experiment.

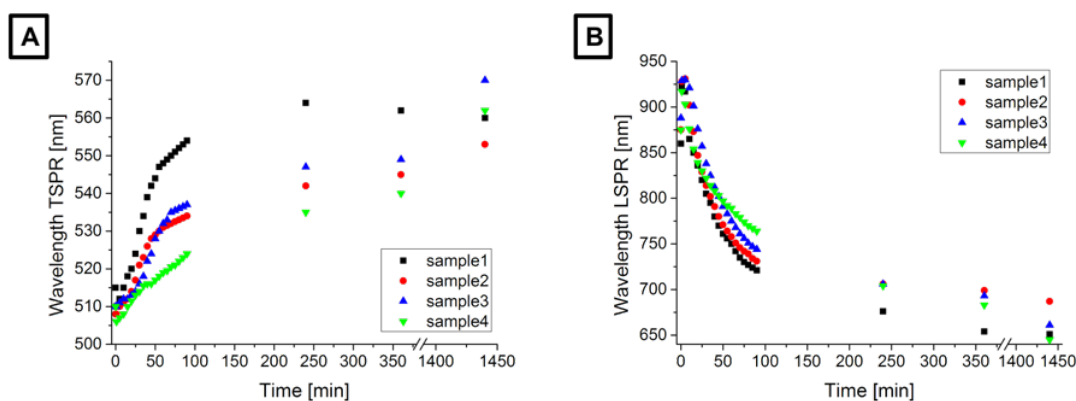


Figure A.12: Temporal evolution of TSPR (A) and LSPR (B) for all four samples during the gold overgrowth experiment according to Figure A.11.

Double sigmoidal fitting of AR against time

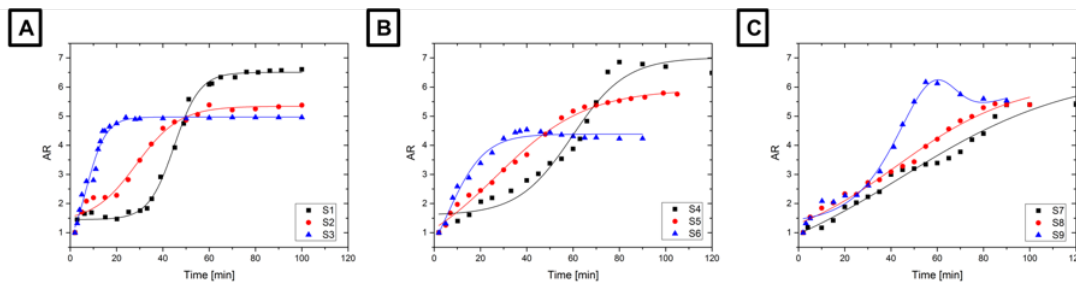


Figure A.13: Temporal evolution of the aspect ratio of the synthesis AuNR-S1 to -S3 (A), AuNR-S4 to -S6 (B) and AuNR-S7 to -S9 (C). The lines are the according fit after equation 3.3.

[1] S. Förster, C. Burger, Scattering functions of polymeric core-shell particles and excluded volume chains, *Macromolecules* **1998**, *31*, 879.

[2] S. Förster, A. Timmann, M. Konrad, C. Schellbach, A. Meyer, S.S. Funari, P. Mulvaney, R. Knott, Scattering curves of ordered mesoscopic materials, *J. Phys. Chem. B.* **2005**, *109*, 1347.

[3] S. Förster, S. Fischer, K. Zielske, C. Schellbach, M. Scztuki, P. Lindner, J. Perlich, Calculation of scattering-patterns of ordered nano- and mesoscale materials, *Adv. Colloid. Interface Sci.*, **2011**, *163*, 55-83.

[4] S. Förster, L. Apostol, W. Bras, Scatter: a software for the analysis of nano- and mesoscale small-angle scattering, *J. Appl. Cryst.* **2010**, *43*, 639-646.

[5] P. B. Johnson, R. W. Christy, Optical Constants of the Noble Metals. *Phys. Rev. B*, **1972**, *6*, 4370-4379

B. SI: Parallel and perpendicular alignment of anisotropic particles in free liquid micro-jets and emerging micro-droplets.

Microfluidic Device

All micro-jet experiments were performed using a newly developed microfluidic setup that allows to cycle small liquid volumes at high flow rates to continuously generate stable micro-jets. The microfluidic setup consists of a micro annular gear pump (mzr-7205G, HNP Mikrosysteme GmbH) with an electrical control terminal box (S-G05) to precisely adjust flow rates as visible in Figure B.1a. The pump is connected with silicone tubes to a specially fabricated 3D-printed sample holder which was designed in AutoCAD 2013 (Autodesk) and printed in polylactide using an Ultimaker 2 (Ultimaker B.V.). The 3D-printed sample holder was fabricated to hold a micro glass capillary (Hilgenberg GmbH) with an inner diameter of 600 μm (wall thickness 50 μm) and is constructed for long-time small angle X-ray scattering (SAXS) measurements at synchrotrons as it is shown in Figure B.1b-d.

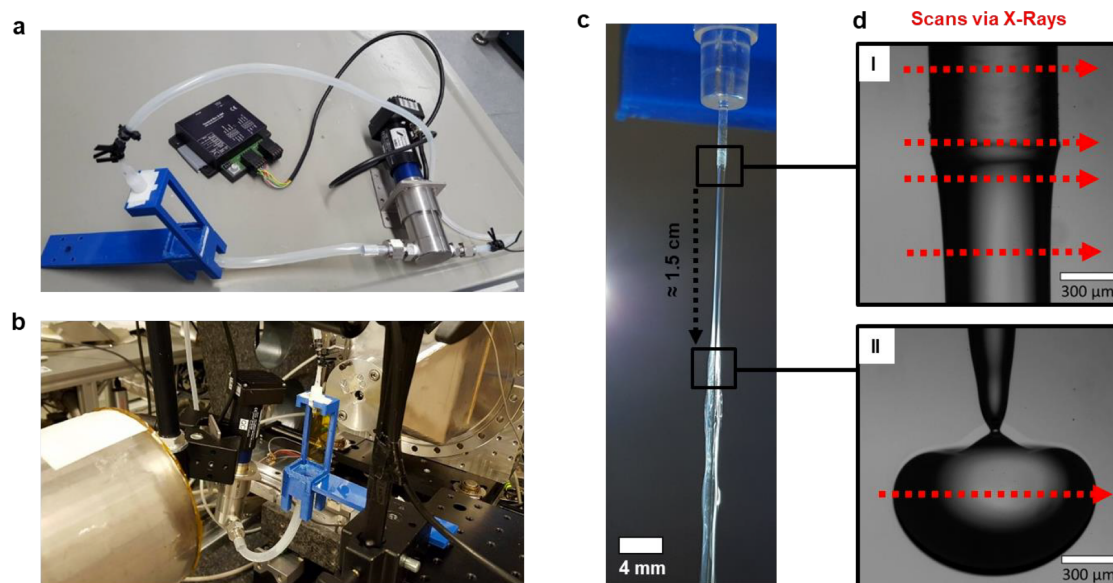


Figure B.1: Overview about the whole microjet setup. (a) 3D-printed sample holder (blue) and micro annular gear pump with control module. (b) Setup generating the microjet with a gear pump (7205G) at the synchrotron DESY, Petra III, beamline P03. (c) Video snapshot of the microjet indicating the nozzle exit as well as the droplet breakup area further downstream. Due to the extreme high flow rates and the high shutter speed of a normal camera, no drop formation is visible. (d) The droplet breakup is just visualized by a high speed camera that can run very short exposure times between each picture, whereby the SAXS positions for scans at the nozzle exit are shown at the top image (I) and at the droplet breakup area 1.5 cm further downstream at the bottom image (II).

Determination of the droplet breakup position

Figure B.2 shows the position for the droplet breakup at $\sim 13\text{mm}$ downstream the glass capillary with diameter of $ID = 600\mu\text{m}$ and a flow rate of $Q = 750\text{mL}/\text{h}$ that is used during the SAXS experiments. Shown in the top row (Figure B.2a) is a series of 20 subsequent 0.7 ms-snapshots of droplet breakups. Here we observe just a slight variation of the position for the droplet breakup between 0.5 – 1 mm at short time scales. The bottom row (Figure B.2b) illustrates the droplet breakup over longer time scales of 1 second intervals. We observed just a small deviation from the droplet position of around 0.5 – 1 mm. All measurement positions were double checked by video microscopy to be sure about being either in the continuous jet or in the droplet regime (15.2 mm).

SI: Parallel and perpendicular alignment of anisotropic particles in free liquid micro-jets and emerging micro-droplets.

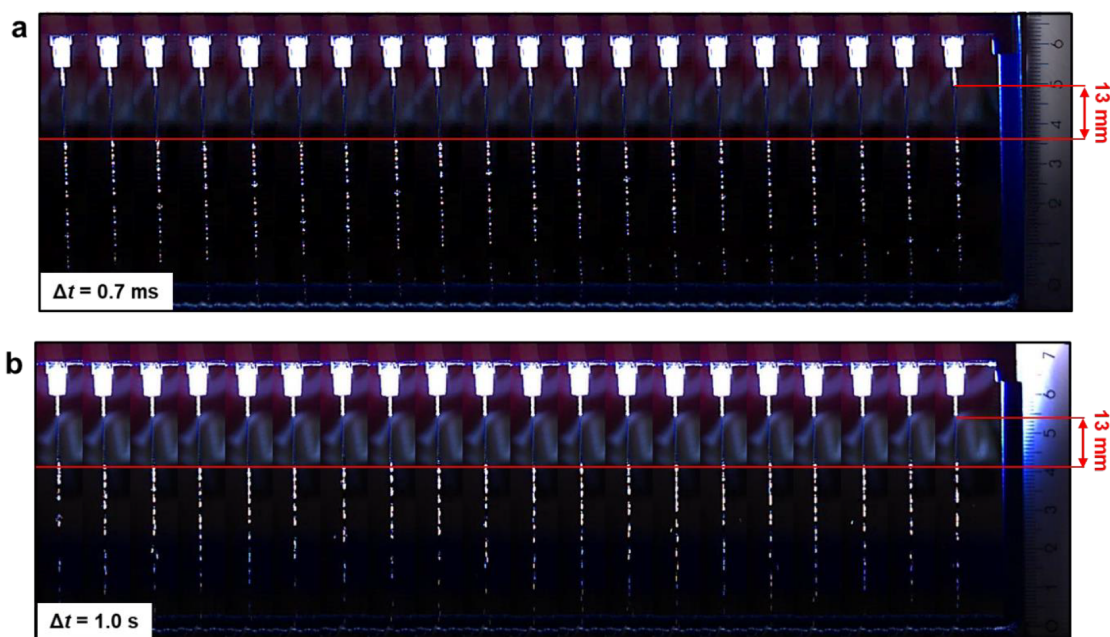


Figure B.2: Determination of the droplet breakup position. (a) Image series of the droplet breakup position for a capillary with diameter of $ID = 600\mu m$ and a flow rate of $Q = 750mL/h$ for short time intervals of $\Delta t = 0.7ms$ and (b) longer time intervals of $\Delta t = 1.0s$.

Characterization of anisotropic particles

The liquid micro-jet setup has been run with three different types of anisotropic particles. Cryo-TEM and TEM-images are shown in Figure S3. The first sample, 1% w/w sodium hectorite nanoplatelets dispersion in water, is visible in Figure B.3a. The 10% w/w of wormlike micelles solution and the dispersed gold nanorods are illustrated in Figure B.3b, c.

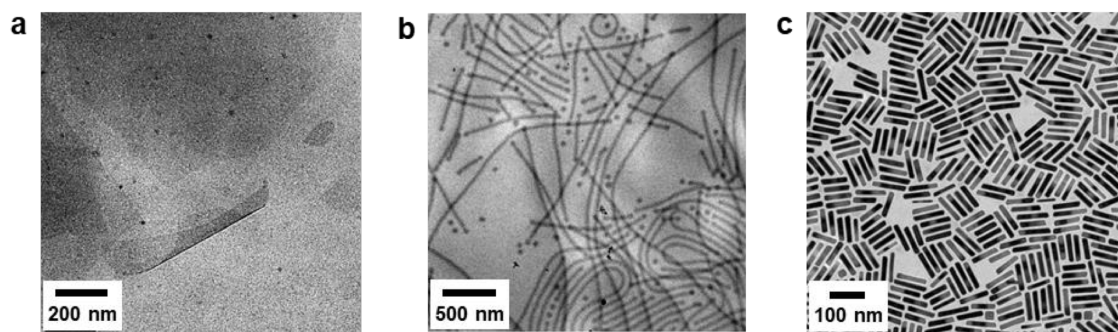


Figure B.3: Characterization of anisotropic particles via transmission electron microscopy. (a) Cryo-transmission electron microscopy (Cryo-TEM) image of Na_{0.5}-hectorite nanoplatelets with a concentration of $c = 1\%$ w/w in water. The sample was milled by ultrasonic treatment to shorten the originally aspect ratio of 20.000. (b) Cryo-TEM image of Pl₁₁₀-PEO₁₉₈ wormlike micelles solution with a concentration of $c = 0.1\%$ w/w in water. (c) Transmission electron microscopy (TEM) image of single crystal gold nanorods (Au-Nanorods).

Microparticle Image Velocimetry

To determine the velocity profile experimentally, we used microparticle image velocimetry (μ PIV). The setup consists of a Phantom v1612 high-speed camera (Vision Research), and a highly intense, focused light source Halolux LED-30 (Streppel Glasfaser-Optik oHG). In combination with a Model K1 CentriMaxTM long distance microscope (Infinity Photo-Optical Company) and a 10x /0.30 P UPlanFL N magnification objective (Olympus Corporation) the setup allows exposure down to 1.5 μ s and frame rates up to 210,000 s^{-1} for the performed experiments. Due to the narrow depth of focus of this kind of setup a precise vertical position control within the microjet is possible. The sample-holder was adjusted in the way that the focus distance was always set to the inner center part of the microjet and just frames of that position are taken by the high-speed camera. In total, always 30 frames are taken from exactly the same position at the center for averaging. For data collection via high-speed camera measurements the Phantom PCC v2.8.761.0 software was used. The obtained high-speed image sequence is autocorrelated and analyzed using the open-source software package JPIV. Measurements were made in pure water that contained 0.1% w/v of 4.89 μ m diameter monodisperse polystyrene tracer particles (Micro Particles GmbH). The results as well as analysis of the water microjet flow profiles based on a 300 μ m diameter glass capillary and the generally used flow rate of 750 ml/h is shown in Figure B.4.

Concerning the μ PIV experiments, analysis problems appear due to light reflexions on

the curved outer free jet but especially at the curved glass capillary. As a consequence, dark areas at the edge of the glass capillary are emerging and no valid evaluation within these black regions is possible by the software since the particles are not visible anymore for tracing. However, flow profile analysis for the freejet area is possible up to a certain point. The black area is just present at the outermost edge of the freejet and thus we can determine most of the flow profile. In Figure B.4a, the freejet position 5 mm after outlet is analyzed via JPIV whereby the red marked jet edges of the dark regions are not considered. The results in Figure S4b are showing a velocity profile which is like plug flow with an average velocity of around $v_{average} = 2.0 m/s$, whereby the zero velocity directly at the edge of the freejet is not available. Additionally, we have simulated the flow profile out of a capillary with a diameter of $D = 30 \mu m$ and a flow rate of $Q = 10 \mu L/h$ at the freejet area which is visible in Figure B.4c. Here, a whole plug flow profile is recognized and matches quite good to the analyzed part of the experimentally found flow profile for the freejet area. Moreover, the flow profile within a capillary has also been simulated for the same parameters and the expected parabolic flow profile was determined, as seen in Figure B.4d. However, a detailed analysis of an experimental flow profile is not possible due to intense light reflexions at the glass capillary. Nevertheless, a changing from a parabolic flow profile within the capillary to a plug flow profile within the freejet is identifiable by simulations and supported by experimental data. Consequently, this drastic change of the flow profile benefits the loss of orientation within and along the free jet.

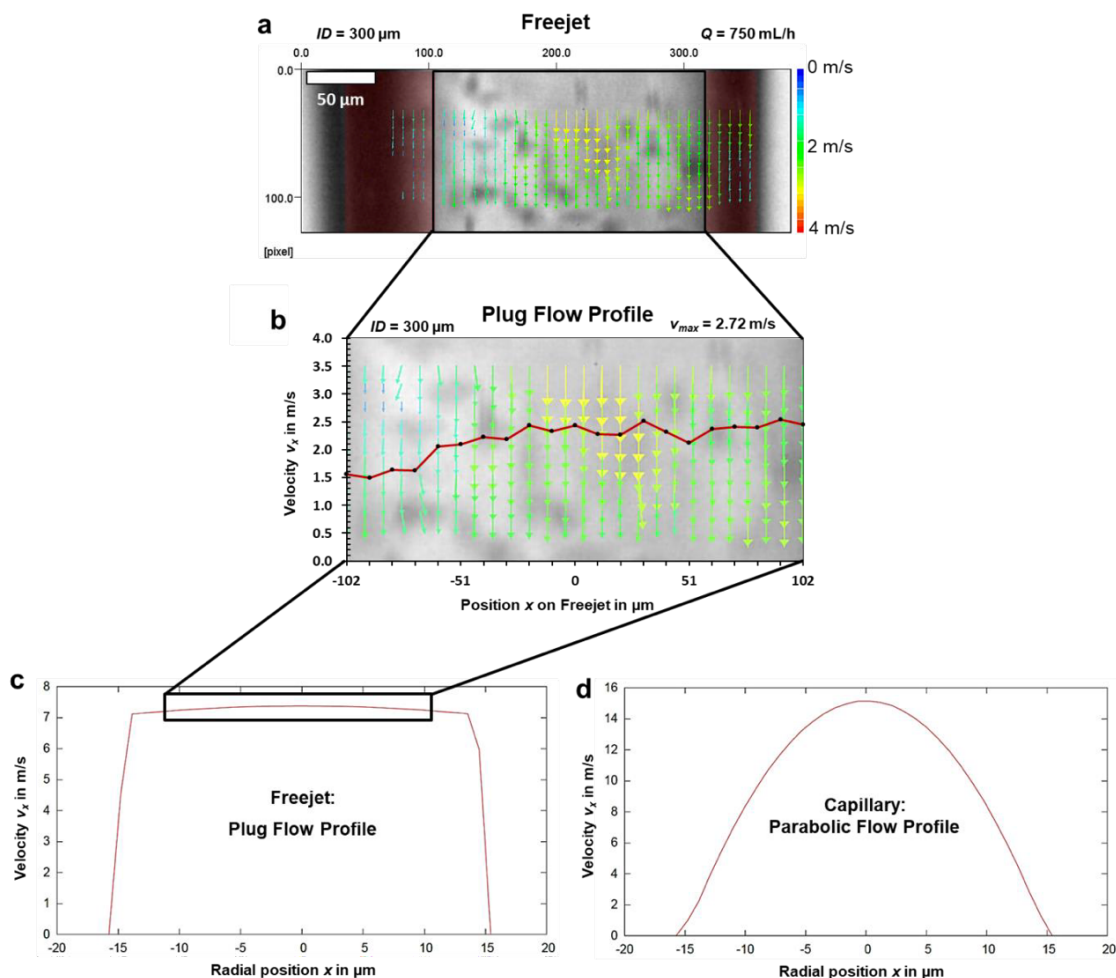


Figure B.4: Microparticle image velocimetry. (a) μ PIV measured flow profile of water including monodisperse polystyrene tracer particles which are jetting out of a glass capillary with an inner diameter of 300 μm and flow rate of $Q = 750$ mL/h. The measurement position is on the freejet 5 mm after outlet. (b) Graph of analyzed plug flow profile with velocity V_x [m/s] versus position x on freejet in [μm]. (c) Simulated plug flow profile of the freejet out of a capillary with diameter of 30 μm and flow rate of 10 $\mu\text{L/h}$. (d) Simulated parabolic flow profile within the capillary and same flow rate.

In the further μ JPIV experiments, we present the flow profile generated by a smaller 200 μm diameter glass capillary to show the influence of the microjet diameter and velocity on the flow profile. In Figure B.5, the flow profile for the experimental flow rate of $\nu = 750\text{mL/h}$ is shown for different positions on the microjet. As discussed before, the vector arrows in the dark areas of the capillary and freejet of Figure B.5 are not allowed to incorporate to the consideration. Though the black areas are present at the edge of the capillary and freejet, we at least can observe a parabolic flow profile within the glass capillary (Figure B.5a) and the gradual growing plug flow profile for the freejet at 5 mm after outlet (Figure S5b). As visible, the maximum velocity at the center part within the capillary amounts to $\nu_{max} = 3.91\text{m/s}$ and shows a parabolic flow profile in

SI: Parallel and perpendicular alignment of anisotropic particles in free liquid micro-jets and emerging micro-droplets.

comparison to the rather plug flow profile for the freejet area at 5 mm after outlet, where the velocity decreased down to $\nu = 3.16\text{m/s}$. Compared to the bigger capillary in Figure B.4, the maximum velocity within the smaller capillary is much higher.

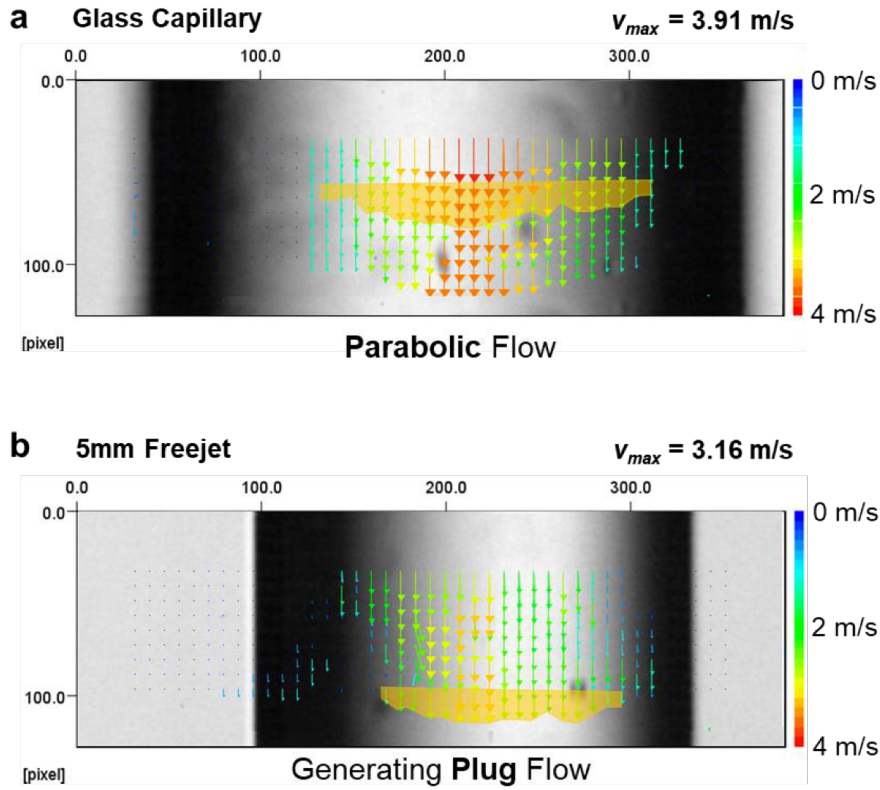


Figure B.5: μ PIV measured flow profiles of water using monodisperse polystyrene tracer particles and a flow rate of $\nu = 750\text{mL/h}$. a) Within a glass capillary of a diameter of $ID = 200\mu\text{m}$ and b) 5 mm after the outlet within the free jet.

SAXS-pattern calculation

In the following we outline the calculation of the scattering patterns of oriented anisotropic particles, such as cylinders and disks, which are dispersed in a solvent. For such two-phase systems consisting of particles (phase "1") with scattering length b_1 and volume fraction ϕ_1 in a solvent (phase "2") of scattering length b_2 and a volume fraction $\phi_2 = 1 - \phi_1$, separated by sharp interfaces, the scattered intensity per unit volume is given by

$$I(q, L, R) = (b_1 - b_2)^2 \rho_N \langle \langle F^2(q, L, R) \rangle \rangle_{L, R} \text{or} [1 + \beta(q, L, R) (\langle Y * q, g(\cdot) \rangle \text{or} - 1) G(q, g)] \quad (\text{B.1})$$

where q is the scattering vector, $\rho_N = N/V$ is the number density of the particles, $F(q)$ the scattering amplitude or Fourier transform of the particle form, L is equal to the length of the cylinder or the thickness of the sheet, R is equal to the cross-sectional radius of the cylinder or the lateral radius of the disk, $Z(q)$ is the lattice factor describing the spatial distribution of the particles, $G(q)$ is the Debye-Waller factor, and

$$\beta(q, L, R) = \frac{\langle\langle F(q, L, R) \rangle\rangle_{L,R}^2}{\langle\langle F^2(q, L, R) \rangle\rangle_{L,R}} \quad (\text{B.2})$$

The effect of the ratio $\beta(q)$ on the scattering intensity is similar to the effect of the Debye-Waller factor $G(q)$, resulting in a decay of the Bragg peak-intensities with increasing scattering vector q . Equation B.1 considers the effect of the particles - via their first and second moment of the particle size distribution - and of the lattice - via the first and second moment of the distribution of lattice points - on the scattered intensity $I(q)$.

The scattering amplitude $F_C(q, L, R)$ for cylindrical particles of cross-sectional radius R and length L can be factorized into

$$F_C(q, L, R) = F_{C\parallel}(q, L)F_{C\perp}(q, R) \quad (\text{B.3})$$

where $F_{C\parallel}(q, L)$ is the longitudinal contribution parallel to the cylinder axis, and $F_{C\perp}(q, R)$ is the contribution from the cross-section of the cylinder. $L = LI_{\parallel}$ is a vector with length L and a direction given by the unit vector parallel to the cylinder axis I_{\parallel} . $R = RI_{\perp}$ is a vector with length R and a direction given by the unit vector perpendicular to the cylinder axis I_{\perp} . The directions are shown in Figure B.6. The longitudinal and cross-sectional contributions for cylinders are given by

$$F_{C\parallel}(q, L) = \frac{\sin(qL/2)}{qL/2} \quad (\text{B.4})$$

$$F_{C\perp}(q, R) = \frac{2J_1(qR)}{qR} \quad (\text{B.5})$$

where $J_1(z)$ is the Bessel function of the first kind.

The structure of disks can be described by their lateral radius R_D and the thickness D as shown in Figure B.6.

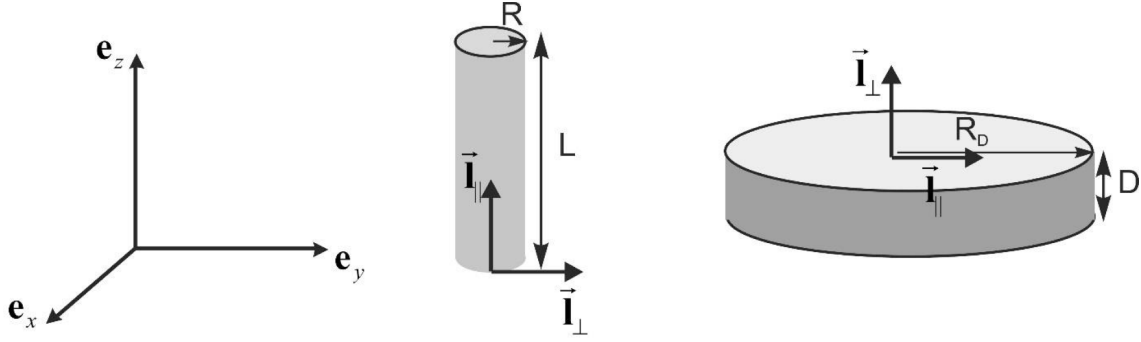


Figure B.6: Different shapes used for SAXS-pattern calculation. Definition of directions for cylinders and disks to calculate the longitudinal and cross-sectional formfactors.

Since disks could equivalently be considered to be short cylinders, where the cross-sectional radius R is larger than the length L , the scattering amplitudes can be derived by substituting $L \rightarrow D$ and $R \rightarrow R_D$ in Equation B.3-B.5 to obtain

$$F_D(q, D, R_D) = F_{D\parallel}(q, R_D)F_{D\perp}(q, D) \quad (\text{B.6})$$

where $F_{D\parallel}(q, R_D)$ is now the contribution in the lateral direction and $F_{D\perp}(q, D)$ is the contribution from the cross-section of the disk. The normal and cross-sectional contributions for disks are given by

$$F_{D\parallel}(q, R_D) = \frac{2J_1(qR_D)}{qR_D} \quad (\text{B.7})$$

$$F_{D\perp}(q, D) = \frac{\sin(qD/2)}{qD/2} \quad (\text{B.8})$$

For the calculation of the averages over the size distribution of lengths L and radii R the scattering amplitudes can be factorized and integrated with respect to each of the variables $X = L, R$. In many cases, the Schulz-Zimm distribution is a useful size distribution function. Then the measured z-averages of the functions $f(q, X)$ are given by

$$\langle f(q, X) \rangle_X = \int_0^\infty f(q, X) X^m h(X) dX \quad (\text{B.9})$$

with

$$h(X) = \frac{(z+1)^{z+m+1} X^z}{\bar{X}^{z+m+1} \Gamma(z+m+1)} \exp \left[-(z+1) \frac{X}{\bar{X}} \right] \quad (\text{B.10})$$

with m the weighting factor for the variable X , the average \bar{X} , and the relative standard deviation $\sigma_m = (z+1)^{-1/2}$. The distribution is normalized such that $\int_0^\infty X^m h(X) dX$.

The weighting factor relates to the measured intensity being the z-average, such that for spheres $m = 6$, for cylinders $m = 2$ for the length, and $m = 4$ for the cross-sectional radius, and for disks $m = 2$ for the thickness and $m = 4$ for the lateral disk radius.

The orientational distribution of the particles can be obtained by averaging the scattering amplitudes $\langle F(q, L, R) \rangle_{L,R}$, $\langle F^2(q, L, R) \rangle_{L,R}$, $\langle F_D(q, D, R_D) \rangle_{D,R_D}$ and $\langle F_D^2(q, D, R_D) \rangle_{D,R_D}$ over a distribution of angles β between the cylinder axis or lateral direction of the disk, l_{\parallel} , and the scattering vector q . The relevant scalar products are $qL = Lq_{\parallel} = qL \cos\beta$, $qR = Rq_{\perp} = qR \sin\beta$, $qD = Dq_{\perp} = qD \cos\beta$, and $qR_D = R_Dq_{\parallel} = qR_D \sin\beta$. The orientational averages are then calculated as

$$\langle \langle F_C(q, L, R) \rangle_{L,R}^2 \rangle_{or} = \int_0^{\pi/2} \langle F_{C\parallel}(qL \cos\beta(\delta)) \rangle_L^2 \langle F_{C\perp}(qR \sin\beta(\delta)) \rangle_R^2 h(\delta) \sin\delta d\delta \quad (\text{B.11})$$

$$\langle \langle F_C^2(q, L, R) \rangle_{L,R} \rangle_{or} = \int_0^{\pi/2} \langle F_{C\parallel}^2(qL \cos\beta(\delta)) \rangle_L \langle F_{C\perp}^2(qR \sin\beta(\delta)) \rangle_R h(\delta) \sin\delta d\delta \quad (\text{B.12})$$

$$\langle \langle F_D(q, D, R_D) \rangle_{D,R_D}^2 \rangle_{or} = \int_0^{\pi/2} \langle F_{D\parallel}(qR_D \sin\beta(\delta)) \rangle_{R_D}^2 \langle F_{D\perp}(qD \cos\beta(\delta)) \rangle_R^2 h(\delta) \sin\delta d\delta \quad (\text{B.13})$$

$$\langle \langle F_D^2(q, D, R_D) \rangle_{D,R_D} \rangle_{or} = \int_0^{\pi/2} \langle F_{D\parallel}^2(qR_D \sin\beta(\delta)) \rangle_{R_D} \langle F_{D\perp}^2(qD \cos\beta(\delta)) \rangle_R h(\delta) \sin\delta d\delta \quad (\text{B.14})$$

Details of this calculation are outlined in ref.[16] of the main publication.

For the calculations we need to specify the orientational distribution of the cylinders and disks, $h(\delta)$, which is defined by the angle δ between a director given by the unit vector n and the direction l_{\parallel} . For the distribution $h(\delta)$ simple approximations can be made which involve Gaussian, Onsager, Boltzmann, or Maier-Saupe distribution functions. These functions are given by

$$h(\delta) = \begin{cases} \exp[-\sin \delta / \bar{\delta}] & , \text{Onsager} \\ \exp[-\delta / \bar{\delta}] & , \text{Boltzmann} \\ \exp[(\cos \delta / \bar{\delta})^2] - 1 & , \text{Maier-Saupe} \\ \exp[-(\delta / \bar{\delta})^2] & , \text{Gaussian} \end{cases} \quad (\text{B.15})$$

with $0 \leq \bar{\delta} \leq \infty$. A value of 0 corresponds to a uniform orientation of all cylinders in the direction of the director n , whereas a value of $\bar{\delta} \rightarrow \infty$ corresponds to an isotropic distribution. If the distribution function is known, the orientational order parameter S defined as

$$S = \left\langle \frac{3 \cos^2 \delta - 1}{2} \right\rangle \quad (\text{B.16})$$

For all scattering patterns a Gaussian-type orientation distribution (Figure B.7) gave the best agreement between experiment and simulation. The structural parameters used for the simulations are summarized in Table B.1-B.3.

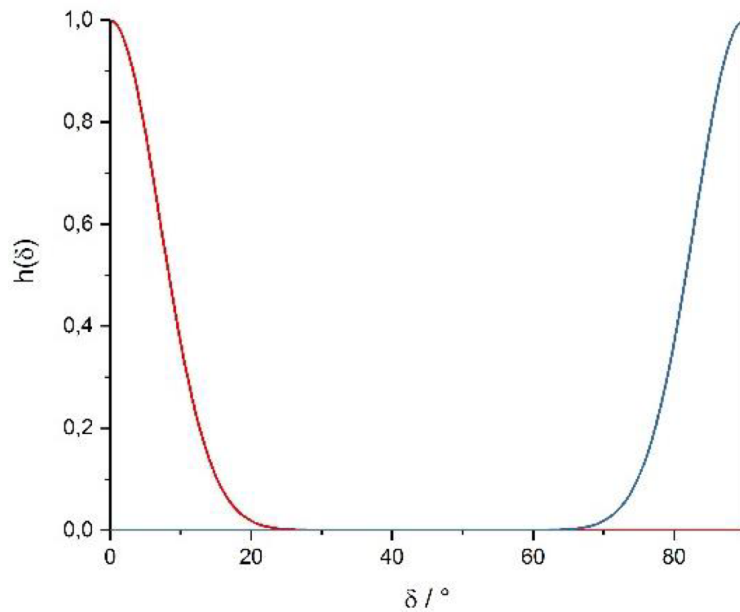


Figure B.7: Gaussian orientational distribution functions. Used for the wormlike micelles and the gold nanorods (red) and the nanoplatelets (blue).

Additionally, 2D-scattering patterns of a pure water microjet with the same diameter and flow rate are shown for the solvent background measurements in Figure B.8 to approve that there were no artefacts in the 2D-scattering patterns of the anisotropic particle jets before.

SI: Parallel and perpendicular alignment of anisotropic particles in free liquid micro-jets and emerging micro-droplets.

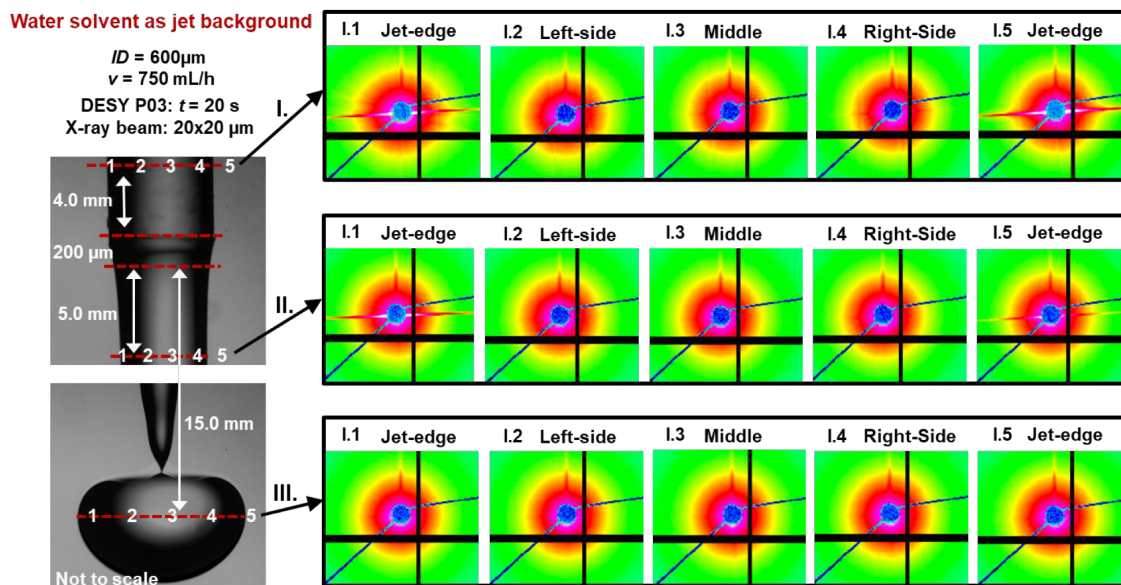


Figure B.8: 2D-scattering patterns of a pure water microjet. (I) On the glass capillary 4 mm before outlet, (II) freejet 5 mm after outlet and (III) droplet region 15 mm after outlet.

Table B.1: Parameters for quantitative calculations in Figure 4.1c and Figure B.9b.

3% w/w Hectorite nanoplatelets	I.1	I.4	IV.4	V.4
Disk radius, R ; nm	300	285	160	260
Relative std. deviation, σ_R	0.1	0.1	0.1	0.1
Layer thickness, d ; nm	1.0	1.0	1.0	1.0
Relative std. deviation, σ_d	0.07	0.07	0.07	0.07
Mean deviation, $d\beta$	10	14	65	10
Orientalional parameter, f	-0.48	-0.46	-0.14	-0.48
Orientalional parameter, S	0.92	0.89	0.20	0.92

SI: Parallel and perpendicular alignment of anisotropic particles in free liquid micro-jets and emerging micro-droplets.

Table B.2: Parameters for quantitative calculations in Figure B.10b.

10% w/w Wormlike micelles	I.1	I.4	IV.4	V.4
Cylinder length, L ; nm	30	20	20	15
Relative std. deviation, σ_L	0.1	0.1	0.1	0.1
Cylinder radius, R ; nm	9	11.5	11.5	12
Relative std. deviation, σ_R	0.07	0.07	0.07	0.07
Unit cell dimensions, a ; nm	42	42	42	42
Radial domain size, D_a ; nm	120	55	55	55
Azimuthal coherence length, D_ψ ; nm	5	48	45	48
Displacement, σ_a ; nm	10	6	8	6
Mean deviation, $d\beta$	2	11	55	12
Orientalional parameter, S	0.98	0.94	0.31	0.93

Table B.3: Parameters for quantitative calculations in Figure B.11b.

Gold nanorods	I.1	I.4	IV.4	V.4
Cylinder length, L ; nm	71.4	71.4	71.4	71.4
Relative std. deviation, σ_L	0.1	0.1	0.1	0.1
Cylinder radius, R ; nm	13	13	13	13
Relative std. deviation, σ_R	0.07	0.07	0.07	0.07
Mean deviation, $d\beta$	65	95	99	35
Orientalional parameter, S	0.23	0.11	0	0.58

Sets of scattering patterns

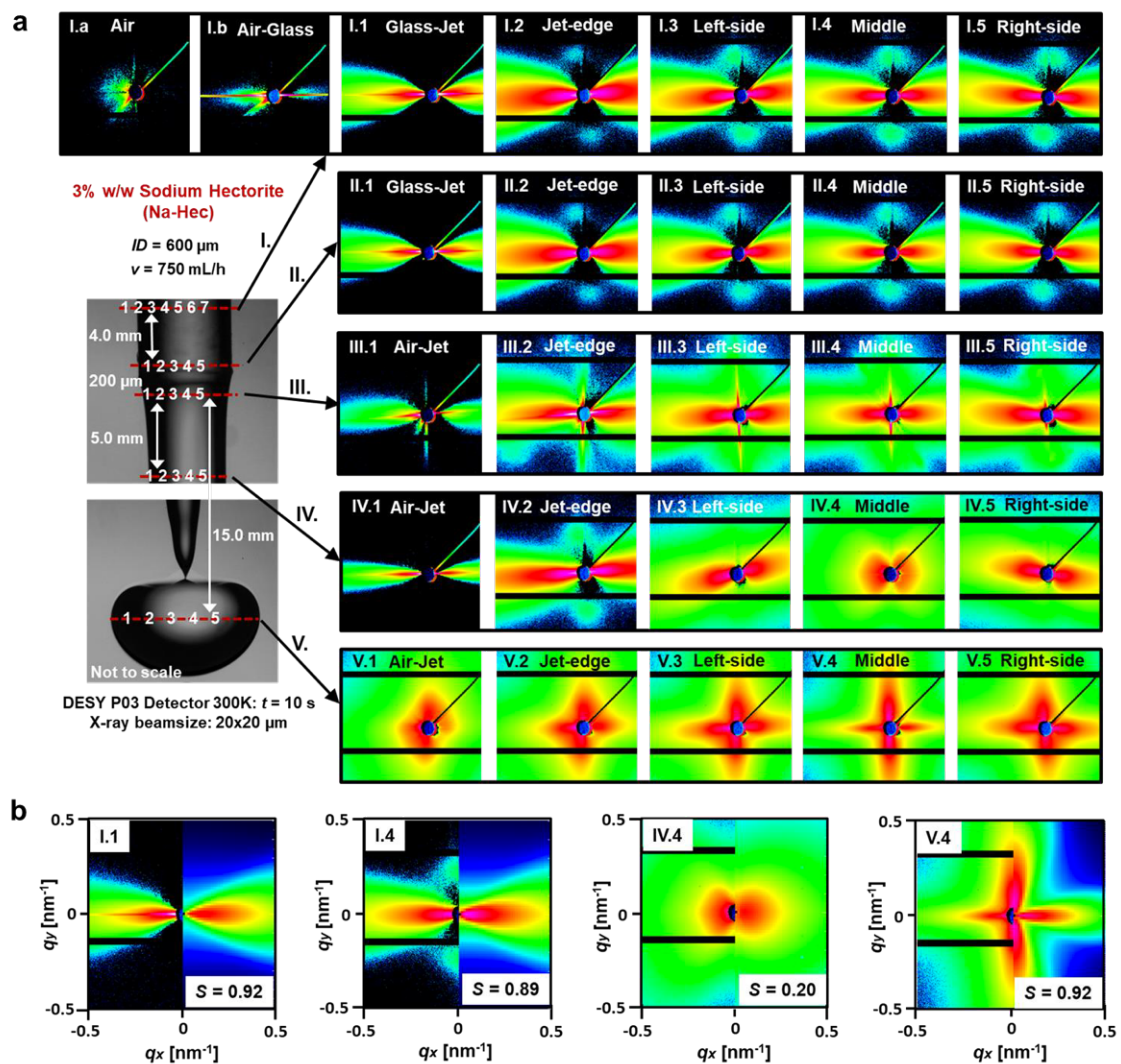


Figure B.9: Sets of measured scattering patterns of the hectorite nanoplatelets. a) At specified scan positions and (b) calculations of scattering patterns as well as their orientation parameter S at four characteristic microjet positions.

SI: Parallel and perpendicular alignment of anisotropic particles in free liquid micro-jets and emerging micro-droplets.

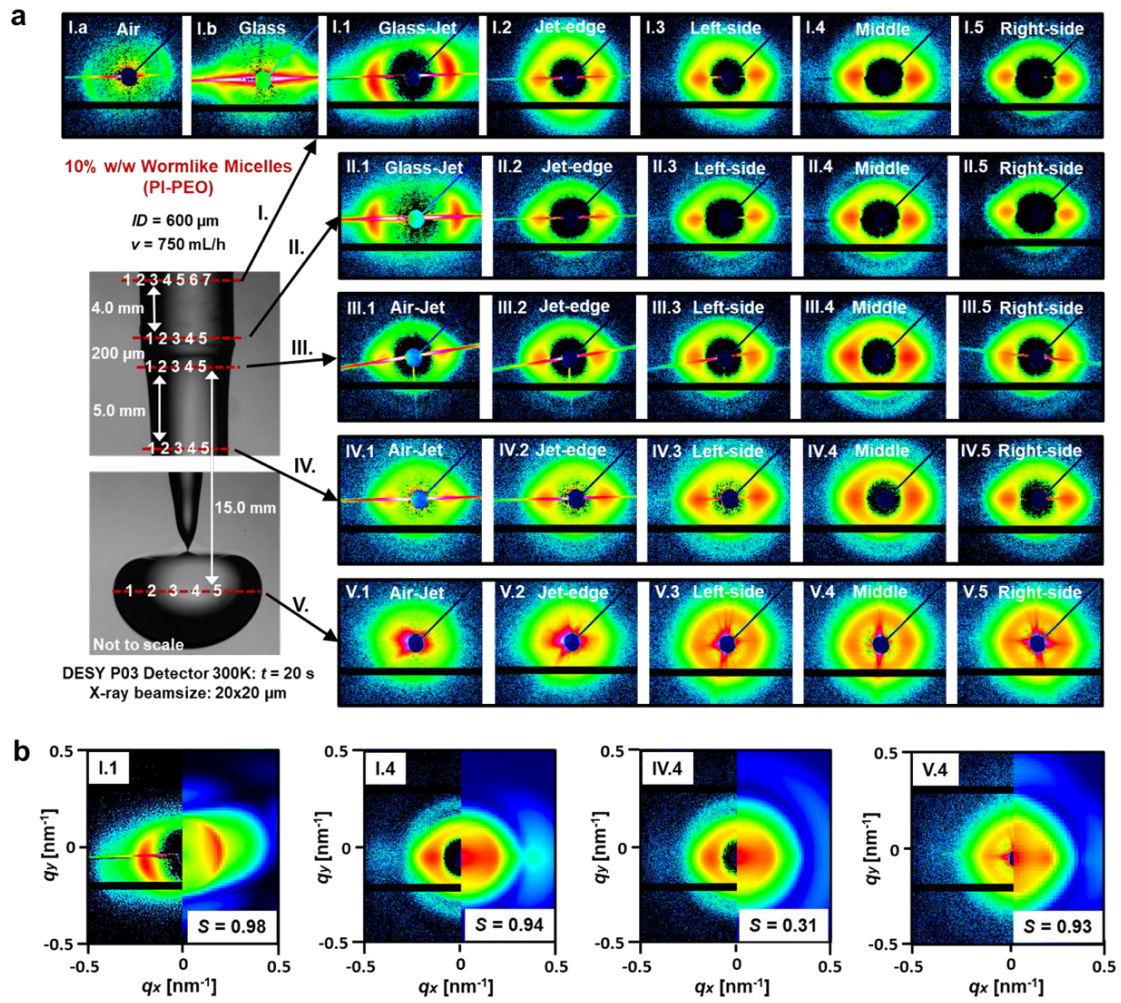


Figure B.10: Sets of measured scattering patterns of the wormlike micelles. a) At specified scan positions and (b) calculations of scattering patterns as well as their orientation parameter S at four characteristic microjet positions.

SI: Parallel and perpendicular alignment of anisotropic particles in free liquid micro-jets and emerging micro-droplets.

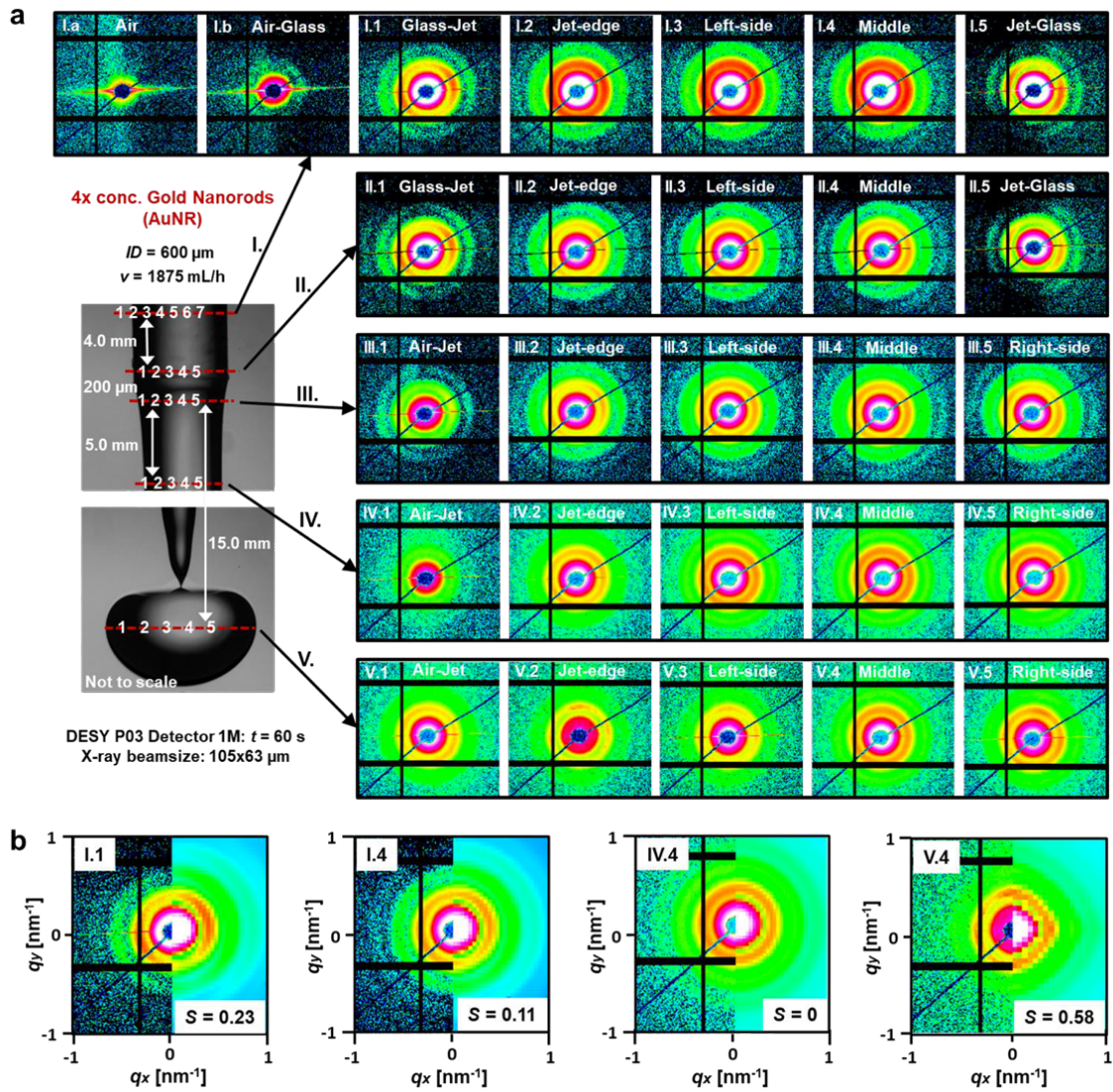
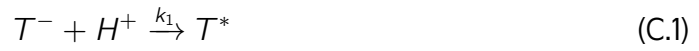


Figure B.11: Sets of measured scattering patterns of the nanorods. a) At specified scan positions and (b) calculations of scattering patterns as well as their orientation parameter S at four characteristic microjet positions.

C. SI: Hydrogelation kinetics measured in a microfluidic device with in-situ X-ray and fluorescence detection.

Reaction kinetics of protonation and self-assembly

The first reaction is the protonation of the negatively charged trisamide (T^-) with a rate constant k_1 , yielding a trisamide T^* with a reduced charge which can undergo self-assembly.



The subsequent self-assembly occurs with a rate constant k_2



where T_2 represents the first dimeric association state. The corresponding rate equations for all four components are

$$\frac{d[T^-]}{dt} = -k_1[T^-][H^+] \quad (C.3)$$

$$\frac{d[H^+]}{dt} = -k_2[T^-][H^+] \quad (C.4)$$

$$\frac{d[T^*]}{dt} = k_1[T^-][H^+] - k_2[T^*]^2 \quad (C.5)$$

$$\frac{d[T_2]}{dt} = k_2[T^*]^2 \quad (C.6)$$

where $[x]$ indicates the concentration of component x . Assuming stationary conditions for the concentration of the intermediate T^* , i.e. $\frac{d[T^*]}{dt} = 0$, allows rewrite the rate equations for the remaining three components as

$$\frac{d[T^-]}{dt} = -k_1[T^-][H^+] \quad (C.7)$$

$$\frac{d[H^+]}{dt} = -k_1[T^-][H^+] \quad (C.8)$$

$$\frac{d[T_2]}{dt} = k_1[T^-][H^+] \quad (C.9)$$

To provide an estimate of the reaction time in a simple stirred reactor, we assume that the initial concentrations are equal, i.e. $[H^+]_0 = [T^-]_0$, such that $\frac{d[T^-]}{dt} = -k[H^+]^2$. For this reaction of second order the reaction half time is equal to $\tau_{1/2} = \frac{1}{2k[H^+]_0}$. With values of 0.001 mol/l (pH 3) and a rate constant of $k = 40000$ mol/l²s we calculate a reaction half time of $\tau_{1/2} = \frac{1}{80} s \approx 12.5$ ms.

Numerical solution in three dimensions

To simplify notations we set $c_1 = [T^-]$, $c_2 = [H^+]$, $c_3 = [T_2]$, and $k_1 = k$. Then the diffusion-advection-reaction equations corresponding to the above reactions is

$$\frac{dc_1}{dt} = D_1 \nabla^2 c_1 - \nu \nabla c_1 - k c_1 c_2 \quad (C.10)$$

$$\frac{dc_2}{dt} = D_2 \nabla^2 c_2 - \nu \nabla c_2 - k c_1 c_2 \quad (C.11)$$

$$\frac{dc_3}{dt} = D_3 \nabla^2 c_3 - \nu \nabla c_3 + k c_1 c_2 \quad (C.12)$$

This set of coupled partial differential equations is numerically solved using a FTCS finite-difference approximation with Gauss-Seidel iteration and simultaneous over-relaxation (SOR) and Chebyshev acceleration [W. H. Press, B. P. Flannery, S. A. Teukolsky, W. T. Vetterling, Numerical Recipes in Pascal, Cambridge University Press, Cambridge, 1989]. The spatial resolution Δx and temporal resolution Δt where typically set to $\Delta x = 2.5 \mu m$ and $\Delta t = 0.2 ms$ for stable FTCS differencing fulfilling the conditions $\frac{D\Delta t}{\Delta x^2}, \frac{\nu\Delta t}{\Delta x}, \frac{k\Delta t}{c} \leq \frac{1}{4}$ for the case of two dimensions (x,y), and $\leq \frac{1}{9}$ for the case of three dimensions (x,y,z).

The boundary conditions at the entrance of the exit channel entrance where set such that BTA enters via the central stream (MC) and the acid via the second outer stream (SC2)

$$c_1(0, y) = \begin{cases} 0 & \text{for } y \geq \frac{w_i}{2} \\ c_1^0 & \text{for } -\frac{w_i}{2} < y < \frac{w_i}{2} \\ 0 & \text{for } y \leq -\frac{w_i}{2} \end{cases} \quad (C.13)$$

$$c_2(0, y) = \begin{cases} c_2^0 & \text{for } y \geq \frac{w_i}{2} + w_b \\ 0 & \text{for } -\frac{w_i}{2} - w_b < y < \frac{w_i}{2} + w_b \\ c_2^0 & \text{for } y \leq -\frac{w_i}{2} - w_b \end{cases} \quad (\text{C.14})$$

where w_i is the width of the central stream containing component T^- and w_b is the width of the buffer stream. We approximate the velocity profile of the microfluidic channel with a square cross-section ($w = h$) by a parabolic profile

$$\nu(y, z) = 2\bar{\nu} \left(1 - \frac{r^2}{w^2} \right) \quad (\text{C.15})$$

where $\bar{\nu}$ is the mean flow velocity and $r = (y^2 + z^2)^{1/2}$ the radial distance from the center of the channel. This set of equations was numerically solved to obtain the concentrations $c_i(x, y, z)$ for a given rate constant k , initial concentrations c_i^0 and diffusion coefficients D_i .

To provide an estimation of the error involved in the radial approximation we consider the exact velocity profile for a rectangular cross-section of width w and height h , which is given by [1]

$$\nu(y, z) = 4\bar{\nu} \sum_{n, \text{odd}} \frac{1}{(\pi n)^3} \left[1 - \frac{\cosh(n\pi \frac{y}{h})}{\cosh(n\pi \frac{w}{2h})} \right] \sin(n\pi \frac{z}{h}) \quad (\text{C.16})$$

where $\bar{\nu} = \frac{h^2 \Delta p}{\eta L}$. The mean flow velocity is then

$$\bar{\nu} = \frac{1}{12} \bar{\nu} (1 - \gamma) \quad (\text{C.17})$$

$$\gamma = \sum_{n, \text{odd}} \frac{192\alpha}{(n\pi)^5} \tanh\left(\frac{n\pi}{2\alpha}\right) \quad (\text{C.18})$$

The maximum flow velocity in the center of the channel ($y = 0, z = \frac{h}{2}$) is given by

$$\nu_{\max} = \frac{1}{8} \bar{\nu} (1 - \beta) \quad (\text{C.19})$$

$$\beta = \sum_{n, \text{odd}} \frac{48 \sin(\frac{n\pi}{2})}{(n\pi)^3 \cosh(n\pi \frac{w}{2h})} \quad (\text{C.20})$$

So for a given flow rate Q we calculate an average velocity $\bar{\nu} = \frac{Q}{wh}$, from which the maximum velocity in the center of the channel in the approximation of a spherical

capillary is $\nu_{max} = 2\bar{\nu}$, whereas for a rectangular channel the value is equal to $\nu_{max} = \frac{3}{2}\bar{\nu}\frac{(1-\beta)}{(1-\gamma)}$. For nearly square cross-sections, as in our case, we have values of $\beta \approx 0.616$ and $\gamma \approx 0.578$, such $\nu_{max} \approx 1.37\bar{\nu}$. Thus, for an exact calculation the maximum velocity in the center of the channel would be $\sim 32\%$ smaller compared to the radial approximation.

Analytical solution in two dimensions

In the following we will consider the rate equations for the case of two dimensions (x, y) , where it is possible to obtain analytical solutions for the concentration profiles. These are used to validate the numerical calculations and to capture the main characteristic features of the concentration profiles and to obtain a more detailed insight into the reaction kinetics occurring under the experimental flow conditions in the microfluidic channel. In two dimensions the rate equations are

$$\frac{dc_1}{dt} = D_1 \nabla^2 c_1 - \nu_x \nabla_x c_1 - \nu_y \nabla_y c_1 - k c_1 c_2 \quad (C.21)$$

$$\frac{dc_2}{dt} = D_2 \nabla^2 c_2 - \nu_x \nabla_x c_2 - \nu_y \nabla_y c_2 - k c_1 c_2 \quad (C.22)$$

$$\frac{dc_3}{dt} = D_3 \nabla^2 c_3 - \nu_x \nabla_x c_3 - \nu_y \nabla_y c_3 - k c_1 c_2 \quad (C.23)$$

We assume laminar flow conditions the y-component of the flow velocity is equal to zero, i.e. $\nu_z = 0$. For Newtonian flows, the flow velocity $\nu_x(y)$ across the stream has a parabolic y-dependence. As the focused stream is confined to a narrow region in the centre of the downstream channel, the flow velocity is approximately constant, independent of the y-position. With velocities in the range of $\nu_x = 1 - 20 \cdot 10^{-3} \text{ m/s}$ and diffusion coefficients in the range of $D = 10^{-9} - 10^{-11} \text{ m}^2/\text{s}$, mass transport in the x-direction is dominated by advection, as apparent from the respective Péclet number, $Pe_x = \nu_x L_x / D \gg 1$, where L_x is of the order of the channel dimension. Under these conditions we have small concentration gradients ∇_x in the x-direction, and the respective terms $D \nabla_x^2 c$ and $\nu_x \nabla_x c$ are small compared to the gradient term in y-direction $D \nabla_y^2 c$, and the sink/source terms $k c_i c_j$ of the chemical reactions. With these assumptions the set of partial differential equations reduces to

$$\frac{dc_1}{dt} = D_1 \nabla_y^2 c_1 - k c_1 c_2 \quad (C.24)$$

$$\frac{dc_2}{dt} = D_2 \nabla_y^2 c_2 - k_{c_1} c_2 \quad (\text{C.25})$$

$$\frac{dc_3}{dt} = D_3 \nabla_y^2 c_3 - k_{c_1} c_2 \quad (\text{C.26})$$

Since the diffusion coefficient of the aggregates is very small, the diffusion term $D_3 \nabla_y^2 c_3$ is negligibly small. If both the concentration gradients ∇_y and the diffusion coefficients $D_{1,2}$ are large, then the diffusion terms dominate the first two rate equations. They are thus decoupled and can be solved analytically to obtain

$$c_1(x, y) = c_1^0 \left[1 + \frac{1}{2} \left\{ \operatorname{erf} \left(\frac{y + \frac{w_i}{2}}{\sqrt{\frac{4D_2 x}{\nu}}} \right) - \operatorname{erf} \left(\frac{y - \frac{w_i}{2}}{\sqrt{\frac{4D_2 x}{\nu}}} \right) \right\} \right] \quad (\text{C.27})$$

$$c_2(x, y) = c_2^0 \left[1 + \frac{1}{2} \left\{ \operatorname{erf} \left(\frac{y - \frac{w_i}{2}}{\sqrt{\frac{4D_2 x}{\nu}}} \right) - \operatorname{erf} \left(\frac{y + \frac{w_i}{2}}{\sqrt{\frac{4D_2 x}{\nu}}} \right) \right\} \right] \quad (\text{C.28})$$

Then the set of equations can be solved for the aggregate concentration to obtain

$$c_3(x, y) = \frac{k_x}{\nu} c_1(x, y) c_2(x, y) \quad (\text{C.29})$$

This is plotted in Fig. C.1 and well reproduces the main features of the experimental data and is used to validate the numerical calculation.

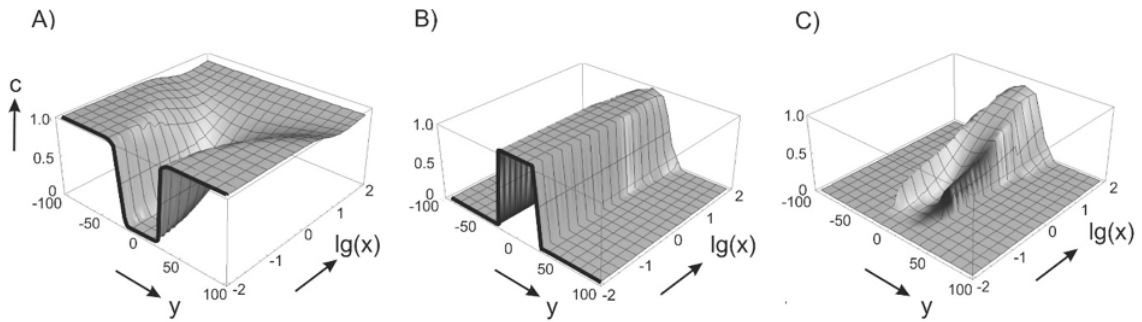


Figure C.1: Concentration profiles calculated from Equation 5.3 for the protons H^+ (A), triply charged BTA^{3-} (B) and BTA assemblies (C) in the downstream channel. $y = 0$ is the position in the middle of the central stream. At the beginning, protons (H^+) and BTA^{3-} have nearly step-function concentration profiles across the channel (y -direction), indicated by the black solid curves, which even out downstream the channel (x -direction). (C) well reproduces the characteristic fluorescence profile observed in the experiments.

Dimensions of the microfluidic channels

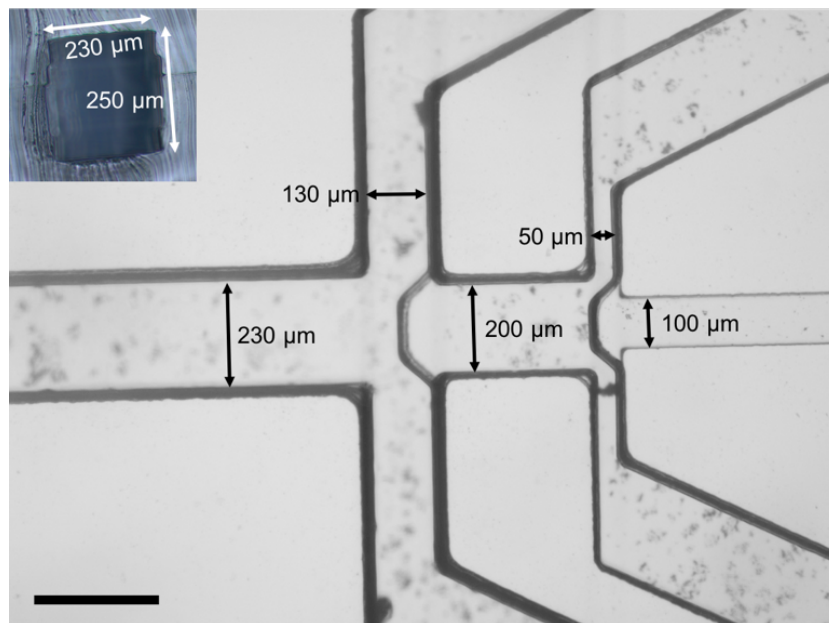


Figure C.2: Microscopy image of the used channel design. The arrows describe all dimensions of each channel part. The inset shows a cross section of the outlet channel with channel dimensions.

Fluorescence intensity scans along the exit channels

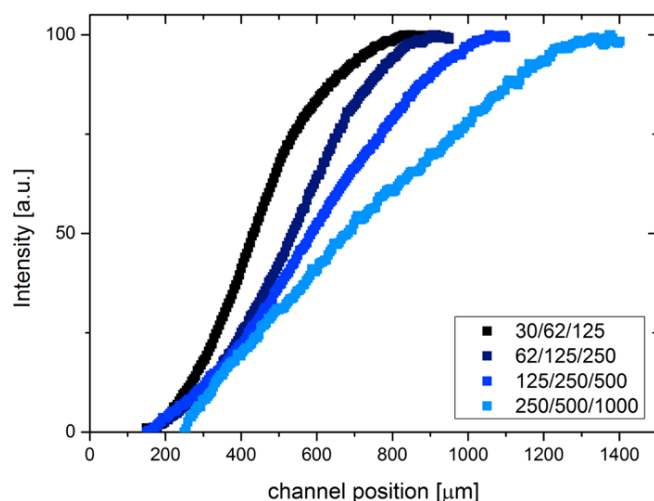


Figure C.3: Intensity distribution along the outlet channel of the BTA assembly process with interdiffusing H^+ without background normalisation of the imbalanced illumination.

SI: Hydrogelation kinetics measured in a microfluidic device with in-situ X-ray and fluorescence detection.

Microfluidic-SAXS setup and scattering curves

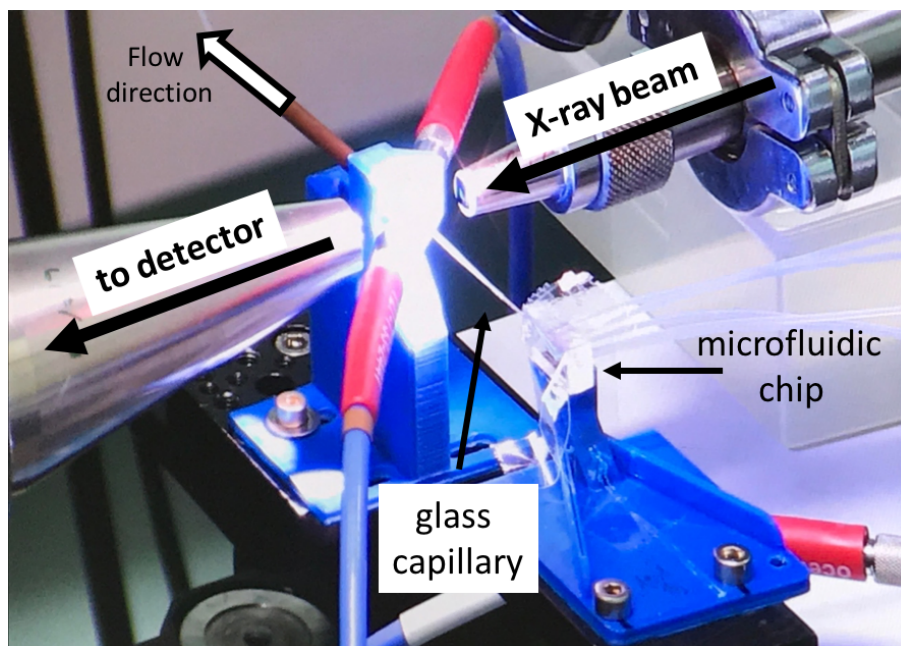


Figure C.4: Photo of the *in-situ* small angle X-ray scattering setup at the in house SAXS system (Ganesh, SAXSLab) in Bayreuth, Germany.

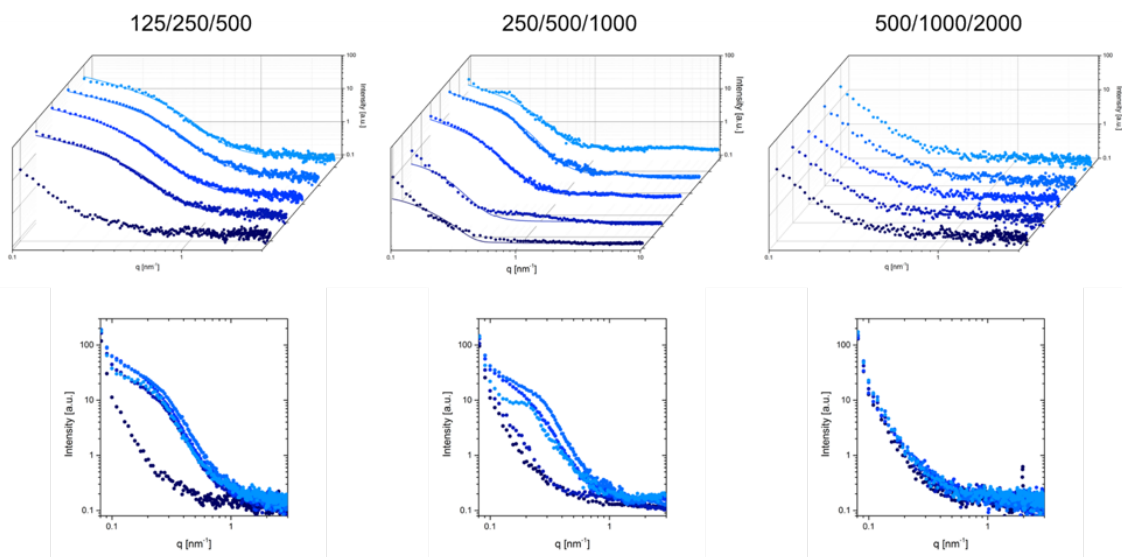


Figure C.5: Position resolved SAXS curves in three-dimensional (top) and two-dimensional (bottom) representation. The different flow rates clearly shift the detection range of the growing BTA nanofibrils.

Cryo-transmission electron microscopy

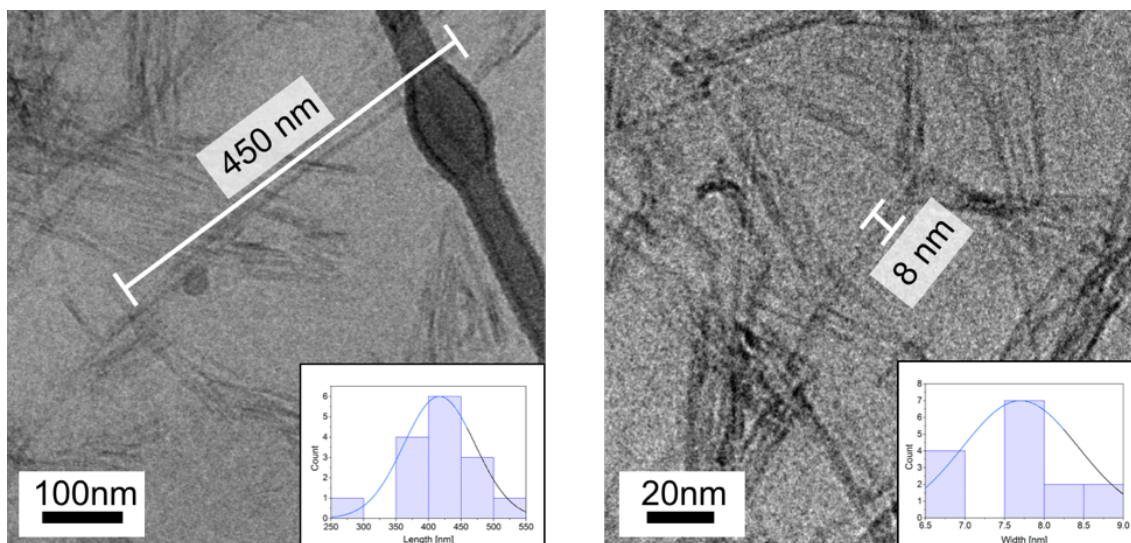


Figure C.6: Cryo-TEM images of the fluorescent BTA nanofibrils out of the microfluidic synthesis. A typical length of about 450 nm is shown in the left picture, the inset shows the size distribution from an example synthesis. The average width of the fibres is about 8 nm, shown in the right image with higher magnification. The inset again is the size distribution.

Fluorescence intensity scans across the exit channel

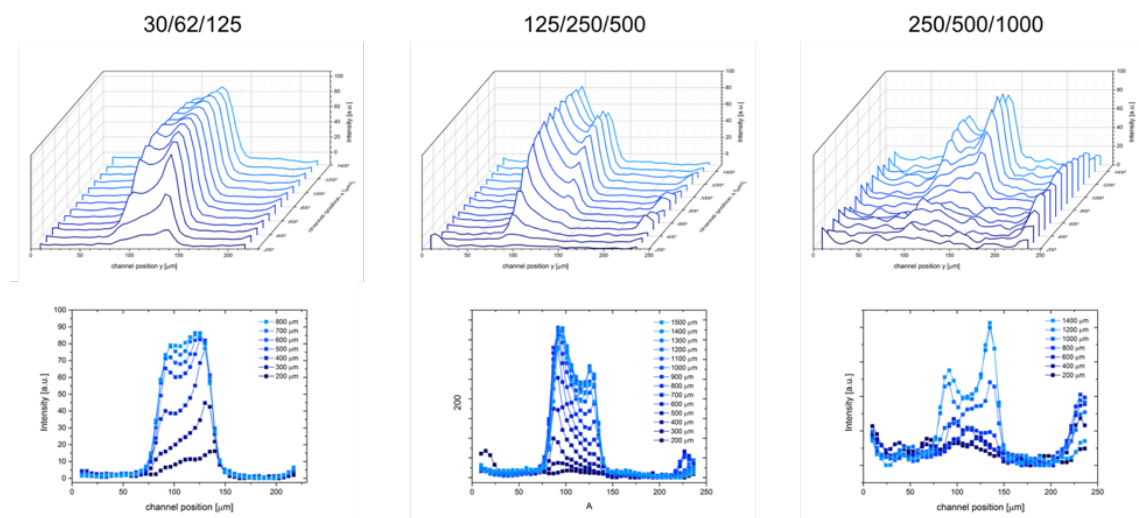


Figure C.7: Observed fluorescence intensity across the channel in $100 \mu\text{m}$ steps for different flow rates. The maximas at both peripheries of the central stream can be seen for each velocity in the three-dimensional (top) and two-dimensional (bottom) plot.

CG5N-Calcium reference experiment

As a reference experiment for a reaction product with a large diffusion coefficient we used the calcium-sensitive dye Calcium-Green-5NTM (CG5N) in combination with calcium chloride to replace BTA and HCl in the main experiment. The green fluorescent reaction product can be used to map the fluorescence downstream the reaction channel. Cascade Blue is used to visualise the different inlet channel streams.

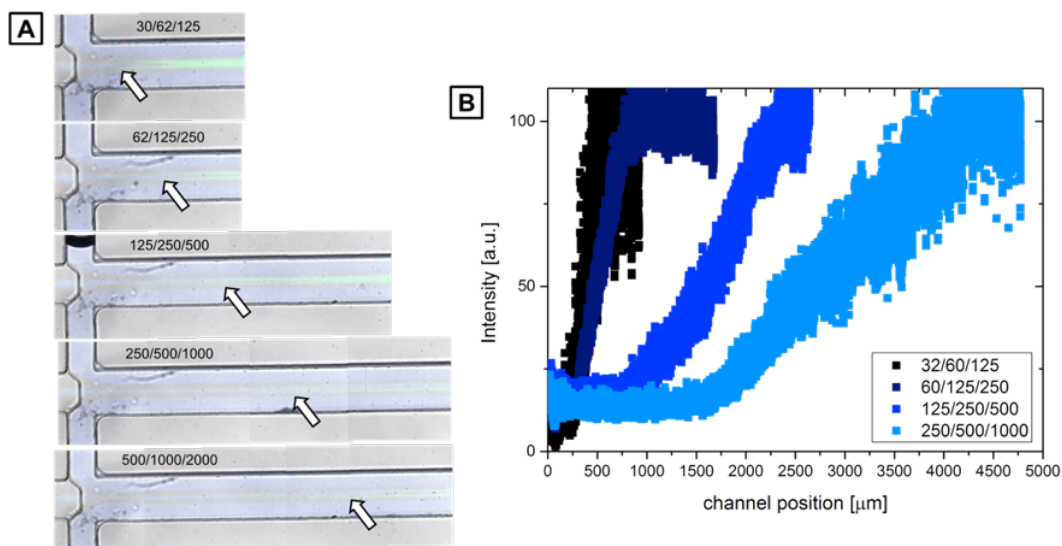


Figure C.8: Two-dimensional CLSM images of the Calcium-Green-5NTM reaction indicating the interdiffusion of calcium-ions shown by green fluorescence at the interface of the central stream. The arrow indicates the region of the first dye-ion interaction. The flow rates are indicated in the form $U_{MC}/U_{SC1}/U_{SC2}$ [$\mu\text{L}/\text{h}$] for each inlet. Averaged intensity along the channel (right). A broader shift of the positions with the same relative intensities to larger downstream channel positions with increasing flow rate can be seen. The introduced solution in the main channel and second side channel is indicated by Cascade Blue showing a blue fluorescence.

Comparing the two-dimensional CLSM images of the CG5N system in Figure C.8 (left) with the fluorescence microscopy images of the BTA assembly, shown in Figure 5.5A, a similar evolution of increasing fluorescent streams along the channel can be seen. In addition, the same shift of the beginning fluorescence to larger downstream channel positions with increasing overall flow rate can be observed.

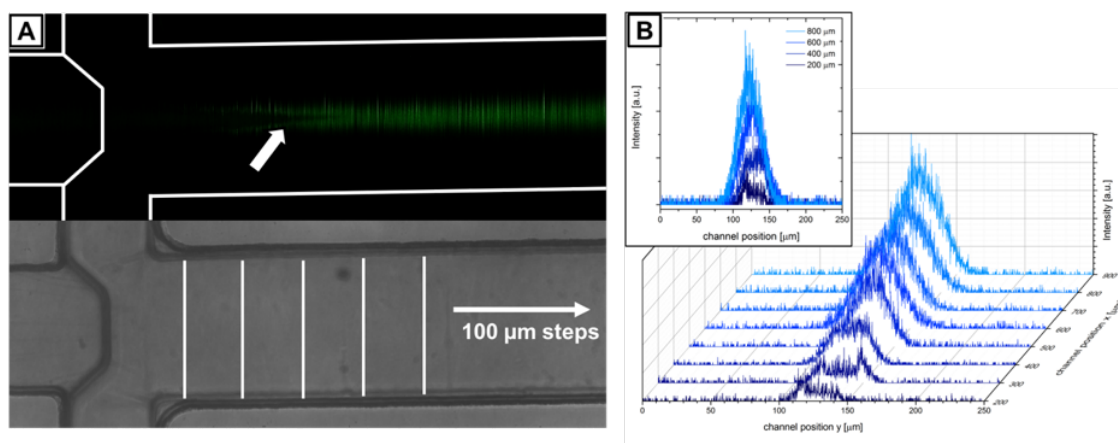


Figure C.9: (A) 2D-CLSM fluorescence (top) and microscopy (bottom) images of the developing fluorescence intensity of CG5N reacting with interdiffusing Ca^{2+} -ions in the exit channel. The flow direction is indicated by the arrow. The vertical lines indicate positions, where the Intensity $I(y)$ was measured across the channel, shown in (B). We observe maxima at both peripheries of the central stream due to reaction of fluorescent dye and calcium ions. The interdiffusion to the centre of the stream is faster than the BTA reaction, shown by a single fluorescence intensity peak.

Figure C.9 shows the fluorescence intensities of the CG5N reaction with interdiffusing Ca^{2+} -ions measured across the downstream channel in steps of $100 \mu\text{m}$ starting $200 \mu\text{m}$ after the channel cross. Only at the beginning a symmetric double peak feature is observed. The peaks quickly merge to a broad central peak with systematically increasing intensity for every consecutive position is observed. The three-dimensional plot shown in Figure C.9B, with a two-dimensional plot of $200 \mu\text{m}$ steps as the insert, supports the assumption of a reaction with a fast diffusing product. Compared to the measured intensity of BTA nanofibril fluorescence in Figure 5.5B, the fluorescent dye system evolves very fast from the symmetric double peak shape to a single Gaussian peak along the downstream channel.

SI: Hydrogelation kinetics measured in a microfluidic device with in-situ X-ray and fluorescence detection.

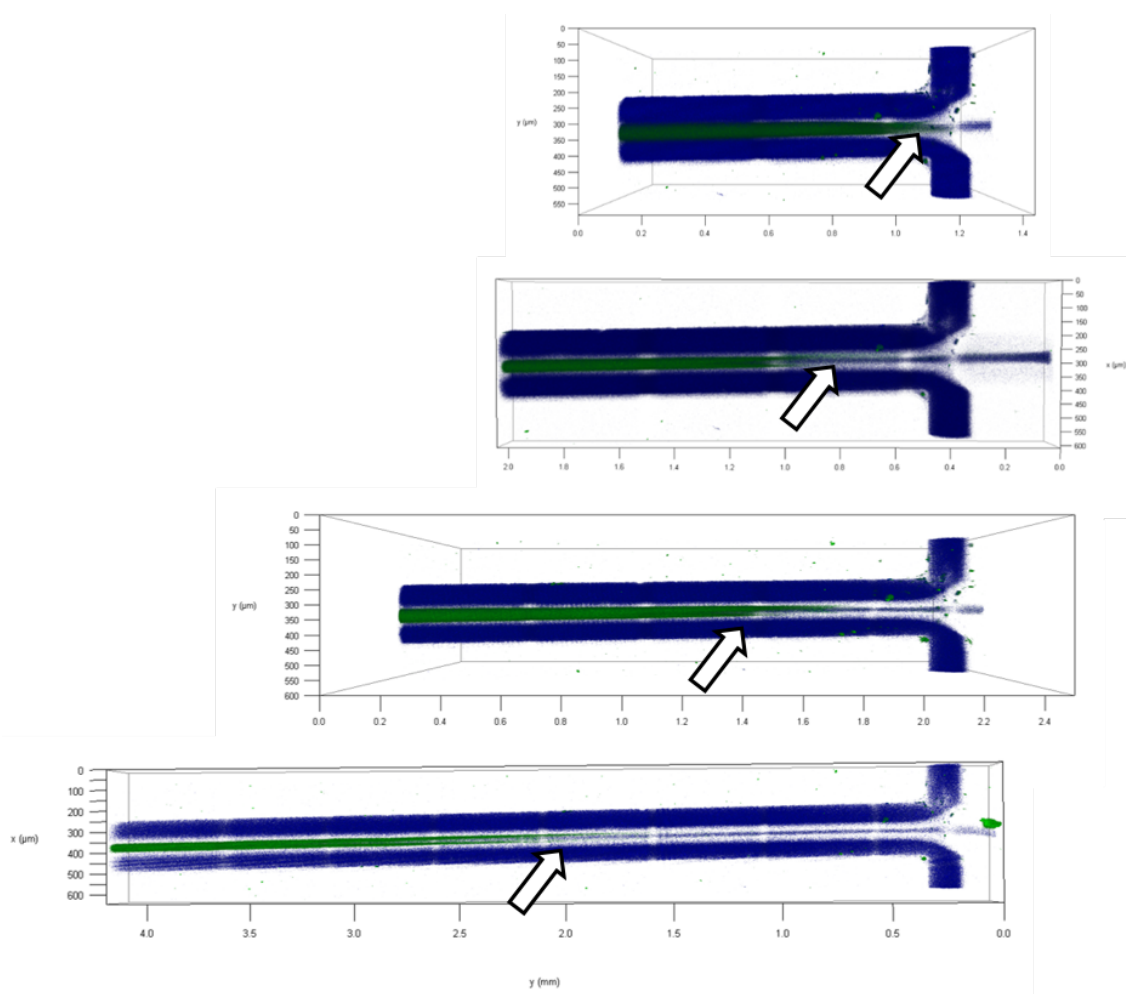


Figure C.10: Three-dimensional CLSM images of the CG5N / Calcium-ion reaction along the outlet channel. The arrow indicates the position of the first fluorescence.

SI: Hydrogelation kinetics measured in a microfluidic device with in-situ X-ray and fluorescence detection.

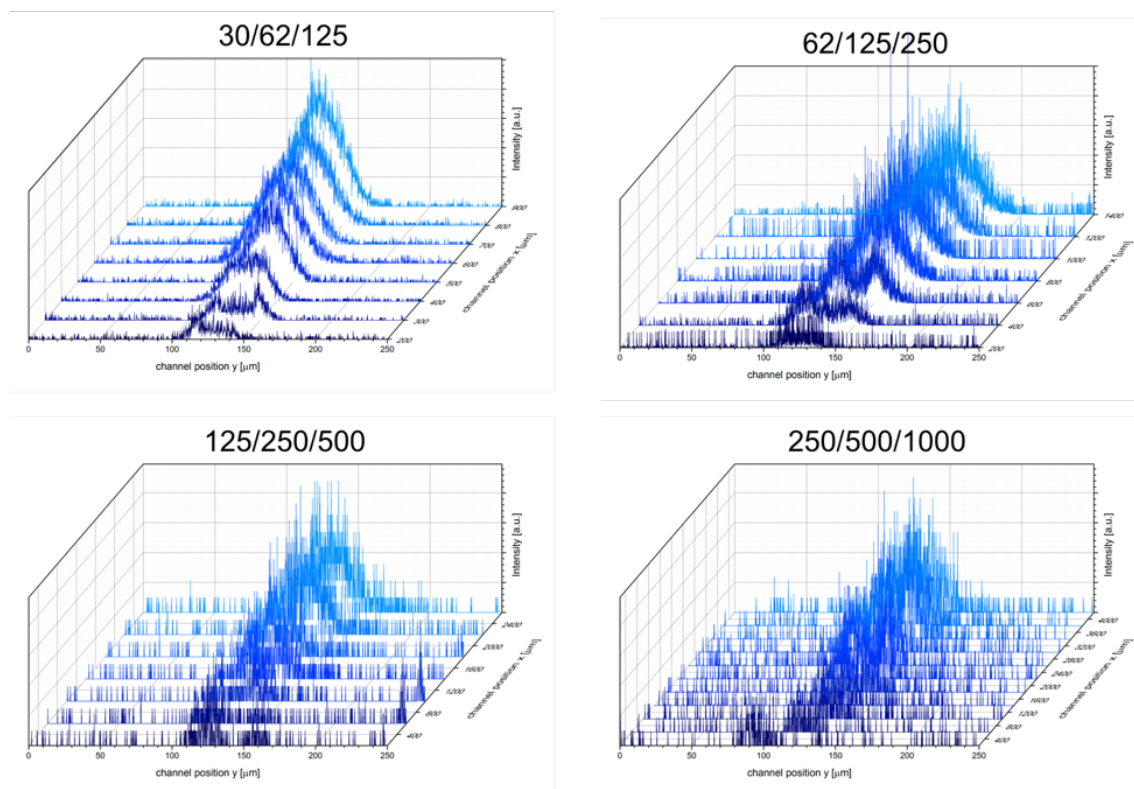


Figure C.11: Three-dimensional position resolved emission spectra across the outlet channel measured in 100 μm steps. The different flow rates heading the graphics show a clear shift of the beginning of the fluorescence along the outlet channel.

[1] H. Bruus, *Theoretical microfluidics*, Oxford University Press, Oxford/New York, 2008.

D. SI: Millisecond CdS nanocrystal nucleation and growth studied by microfluidics with in-situ spectroscopy.

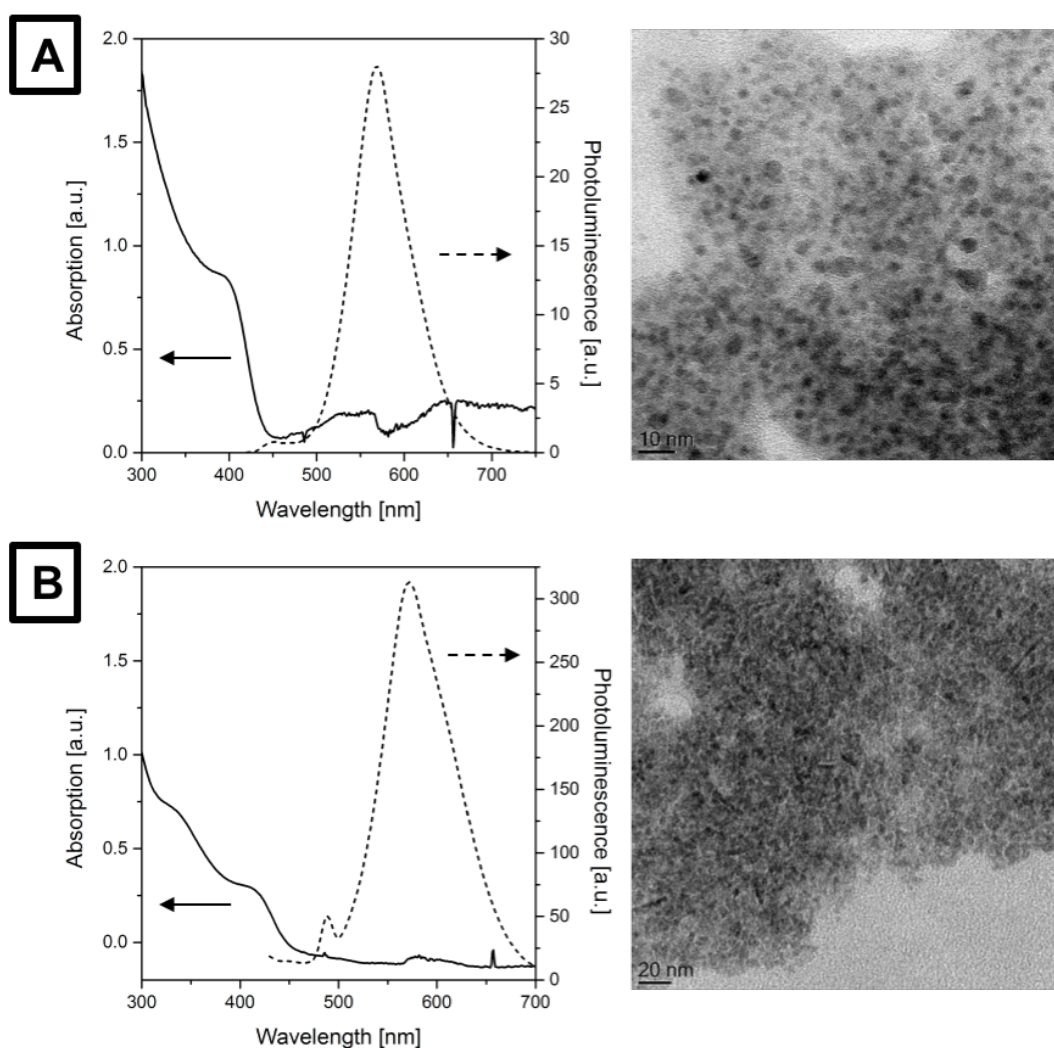


Figure D.1: Absorption (solid line) and emission (dashed line) spectra of the CdS solution, collected out of the microfluidic device and transmission electron microscopy (TEM) analysis of TG (A) and L-cys (B) stabilised nanoparticles.

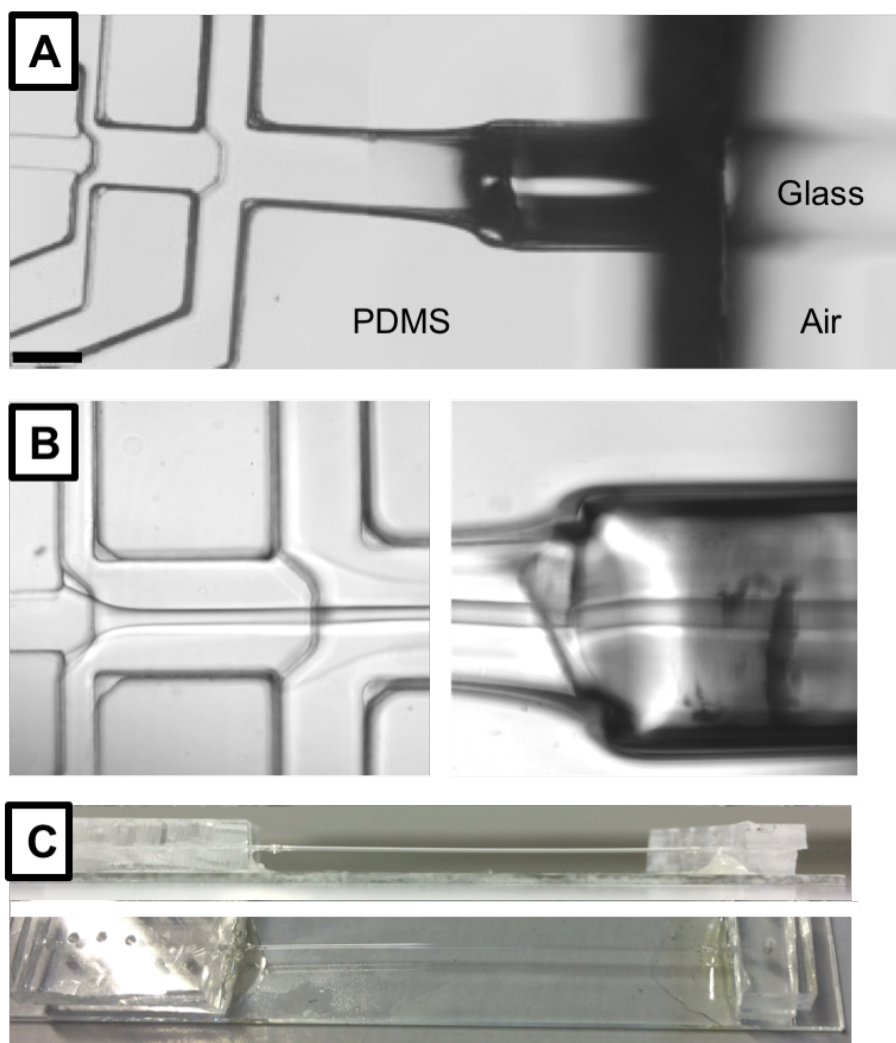


Figure D.2: (A) Optical microscopy image of the PDMS-glass hybrid device. The two mixing crosses with the microfluidic design in the PDMS part, merging the downstream channel with the inserted glass capillary. The cut-off edge of the PDMS is clearly shown by the dark vertical line, with the glass capillary sticking out of the channel. (B) Hydrodynamic flow focusing of the reaction solution streams (left), flowing undisturbed through the changeover from PDMS to glass channel. (C) Photograph of a new PDMS-glass hybrid microfluidic device on a glass-substrate.

SI: Millisecond CdS nanocrystal nucleation and growth studied by microfluidics with in-situ spectroscopy.

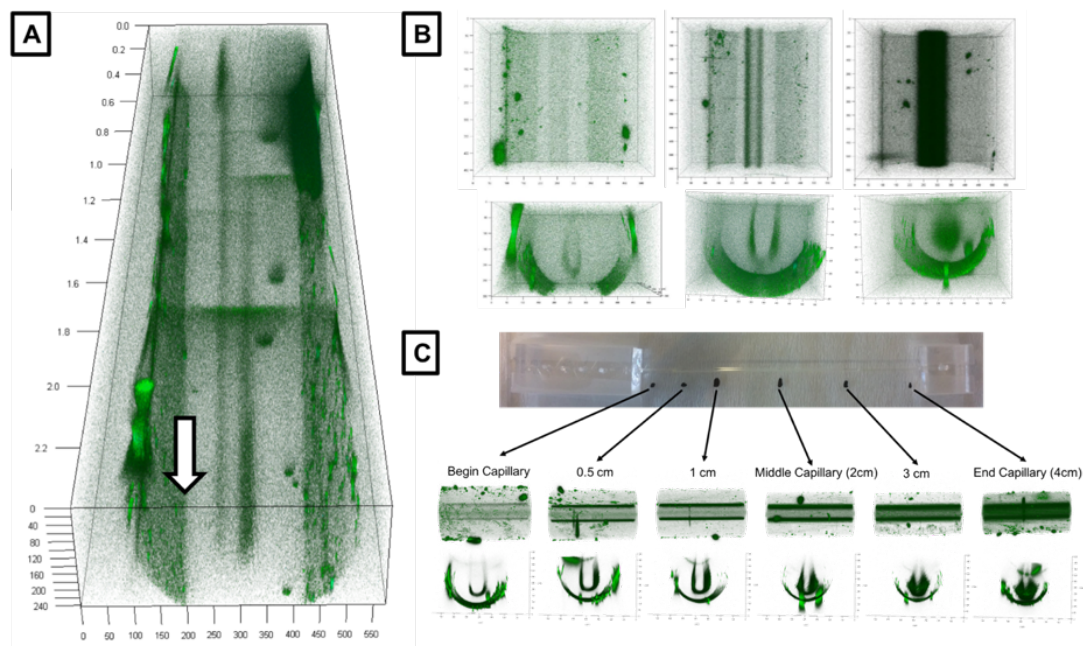


Figure D.3: (A) Three-dimensional reconstruction of a set of CLSM images of the beginning of CdS nucleation and growth fluorescence in the glass capillary after leaving the PDMS device. (B) Single 3D stack images of three positions at the beginning of the capillary (left), the middle of the capillary (center) and the end of the capillary (right) in top (top) and front (bottom) view during a thioglycerol stabilised CdS synthesis. (C) Photograph with according 3D CLSM stack images in top and front view for a L-cystein stabilised CdS synthesis.

SI: Millisecond CdS nanocrystal nucleation and growth studied by microfluidics with in-situ spectroscopy.

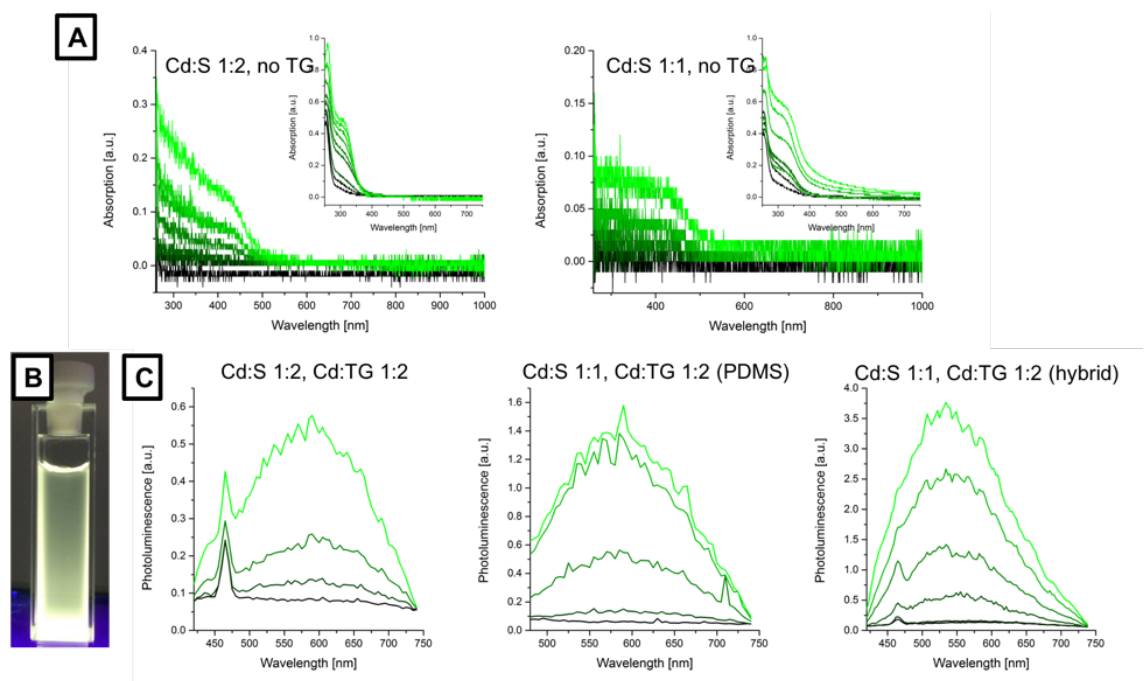


Figure D.4: (A) *In-situ* absorption spectra for CdS synthesis without stabilising agent in comparison to a TG concentration of 1M. The Cd:S ratio was set to 1:2 (left) and 1:1 (right). (B) Photograph of a microfluidic synthesised sample on a UV-lamp, emitting a yellow-green fluorescence. (C) *In-situ* emission spectra for different Cd:S ratios with a constant Cd:TG ratio of 1:2 in PDMS and hybrid microfluidic devices.

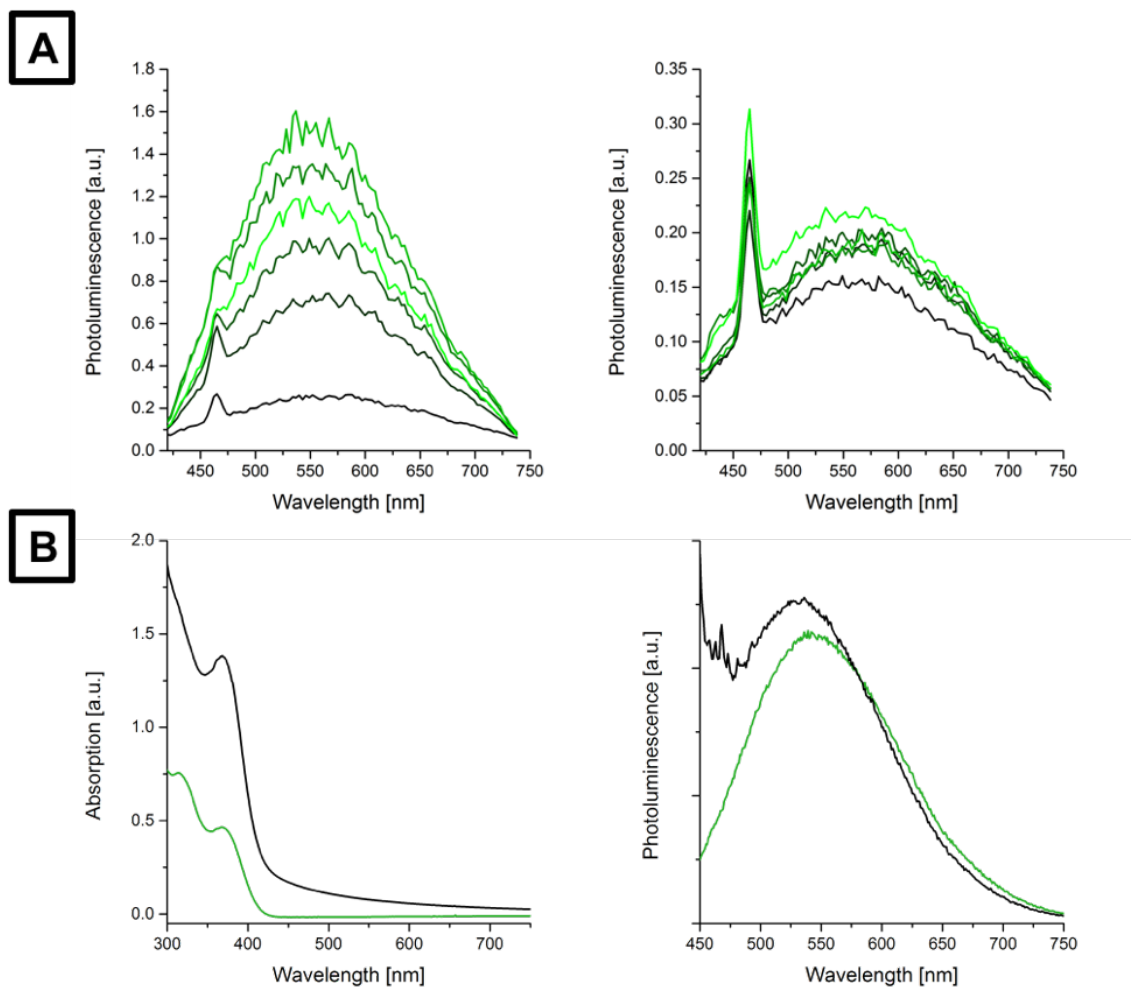


Figure D.5: (A) *In-situ* photoluminescence spectra of a thioglycerol stabilised CdS synthesis with a Cd:S ratio of 1:1, before (left) and after (right) adjusting the pH of the cadmium salt solution by adding NaOH. (B) Final absorption (left) and emission (right) spectra of the CdS solution collected from a microfluidic synthesis, before (black) and after (green) increasing the pH value.

E. SI: Diffusion-limited self-assembly in microfluidics as a platform for structural analysis of anionic conjugated polyelectrolytes.

Raman background spectrum

As the PTHS polymer in solution showed a broad fluorescence in the Raman spectrum using a 532 nm laser, no structure characteristic Raman signals could be investigated. To overcome the problem of overpowering fluorescence due to the laser wavelength being too close to the absorption / emission wavelength of the solution, Raman spectra using a 756 nm laser were recorded. These are shown for water and the dried polymer in Figure E.1.

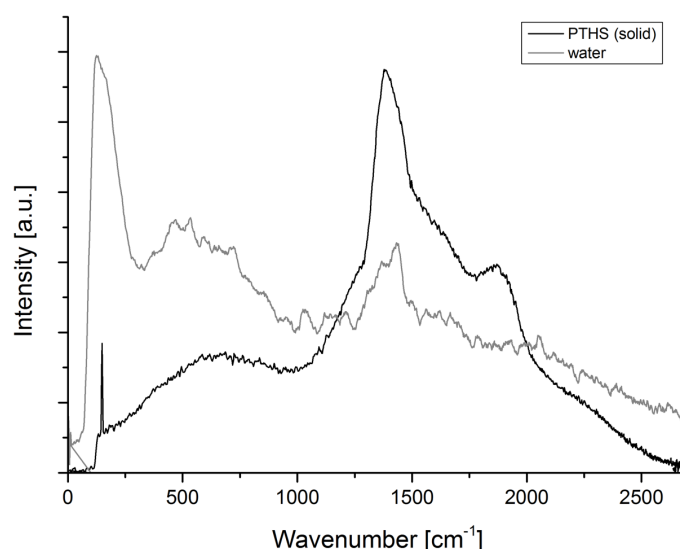


Figure E.1: Raman spectrum of water and the dried polymer PTHS using a 756 nm laser. Weak Raman signals around 1400 cm⁻¹ and 1900 cm⁻¹ can be seen.

As Figure E.1 clearly shows, a characteristic Raman signal for the PTHS polymer can be found between 1400 cm⁻¹ and 2000 cm⁻¹. However, this will be overwhelmed by the signals of the organic solvents in the same region, why even the use of a higher wavelength laser does not lead to a clear tracking of the signal in the scans inside the microfluidic device.

DMF / water interdiffusion in the channel

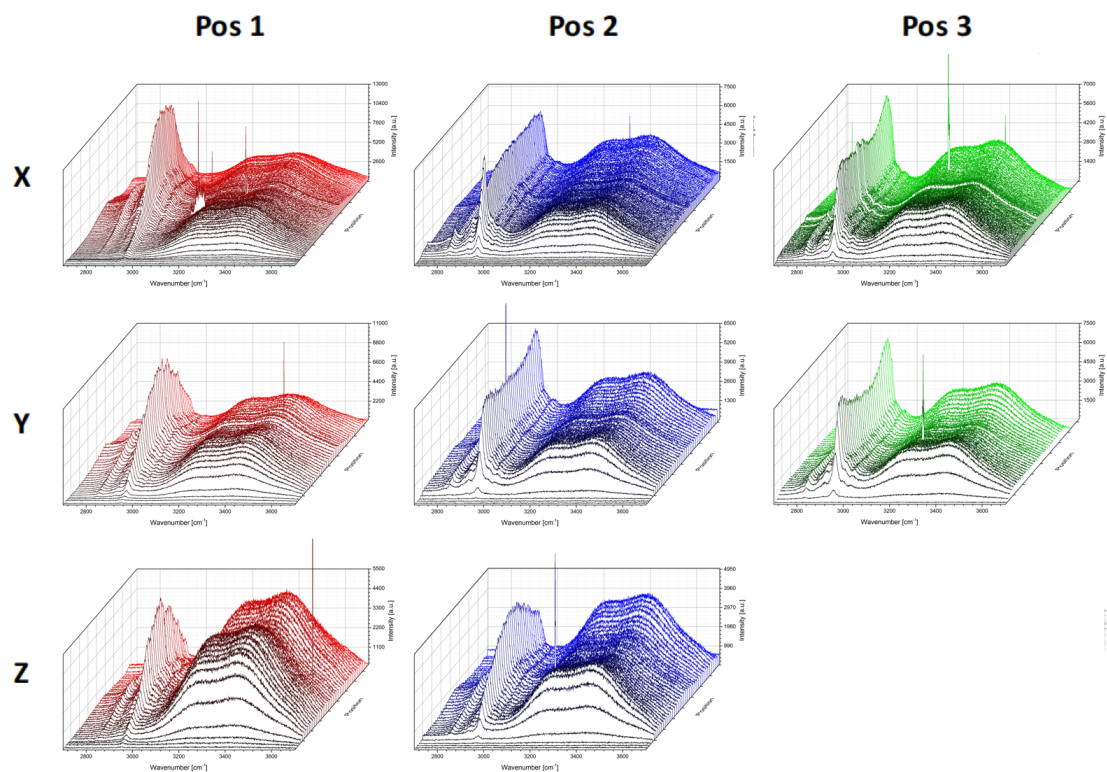


Figure E.2: Confocal Raman spectroscopy scans in 10 μm steps across the channel (edge to edge) for the flow velocities X, Y and Z for DMF as organic solvent without PTHS. Three different positions in 4 mm distances were investigated according to the shown positions along the outlet channel at the beginning (Pos. 1 = 1 mm after mixing cross), the middle (Pos. 2 = 5 mm after mixing cross) and the end (Pos. 3 = 9 mm after mixing cross).

PTHS self-assembly in DMF by adding water

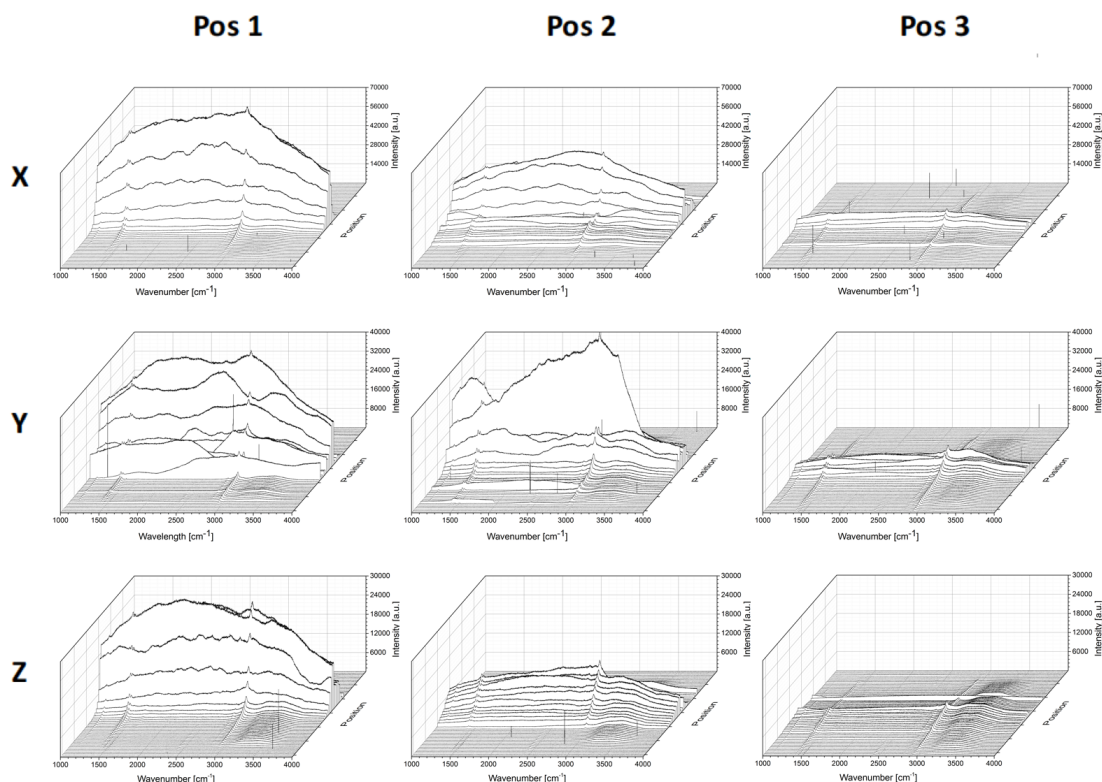


Figure E.3: Confocal Raman spectroscopy scans in 10 μm steps across the channel (edge to edge) for the flow velocities X, Y and Z for DMF as organic solvent with PTHS. Three different positions in 4 mm distances were investigated according to the shown positions along the outlet channel at the beginning (Pos. 1 = 1 mm after mixing cross), the middle (Pos. 2 = 5 mm after mixing cross) and the end (Pos. 3 = 9 mm after mixing cross).

COMSOL Simulations

To obtain a theoretical prediction of the mixing of two miscible solvents (DMSO/Water and DMF/Water) as a function of displacement in the microfluidic chip, COMSOL Multiphysics[®] (v5.3) was employed to determine the volume fraction of either DMSO or DMF in the chip at all locations. The calculation domains were modelled as three dimensional and meshed using a physics controlled extra fine mesh to ensure sufficient accuracy.

The Laminar Flow module was used to simulate fluid flow in the chip, and the wall conditions were set to no slip. The three tiers of inlets had varied flow rates in the three cases as shown in Table 7.2, while the outlet was set to have 0 Pa of applied pressure and suppressed backflow to imitate an open ended capillary. The dynamic viscosity of

the fluid was set as a weighted average based on the volume fraction of each solvent and their respective dynamic viscosity.

This was then coupled with the Transport of Concentrated Species module to simulate the mixing of the two miscible solvents in the chip under convective flow using the Maxwell-Stefan diffusion model at 25°C. The solvent properties are presented in Table E.1, and the tiers of inlets MC, SC1 and SC2 had a volume fraction (DMSO or DMF) of 1, 0.5, and 0 respectively.

Table E.1: Solvent Properties of Water, DMSO, and DMF.

Solvent	Density [kg/M ³]	Molar Mass [g/mol]	Dynamic Viscosity [Pa·s]	Diffusion in Water [m ² /s]
Water	1000	18	$8.90 \cdot 10^{-4}$	
DMSO	1095	78.13	$1.99 \cdot 10^{-3}$	$0.93 \cdot 10^{-9}$
DMF	944	73.1	$8.02 \cdot 10^{-4}$	$0.95 \cdot 10^{-9}$

Figure E.4 shows the COMSOL simulation of the volume fraction of DMF in the channel in combination with water as a mixture during the experiment X (see Table 7.2). Thereby is pure DMF introduced in the main channel, a 50/50 vol. mixture of DMF and water introduced in the first side channel and pure water is fed in the second side channel. The interdiffusion of both solvents can clearly be seen by the decreasing volume fraction of DMF in the centre of the channel, leading to an increasing volume fraction towards the outside. This is clearly visible in the spectra of the volume fraction of DMF as a function of the position in the capillary, in this case measured through the middle from edge to edge, at the same positions the Raman spectra were taken. A broadening of the volume fraction, similar to the broadening of the PTHS fluorescence across the channel can be seen.

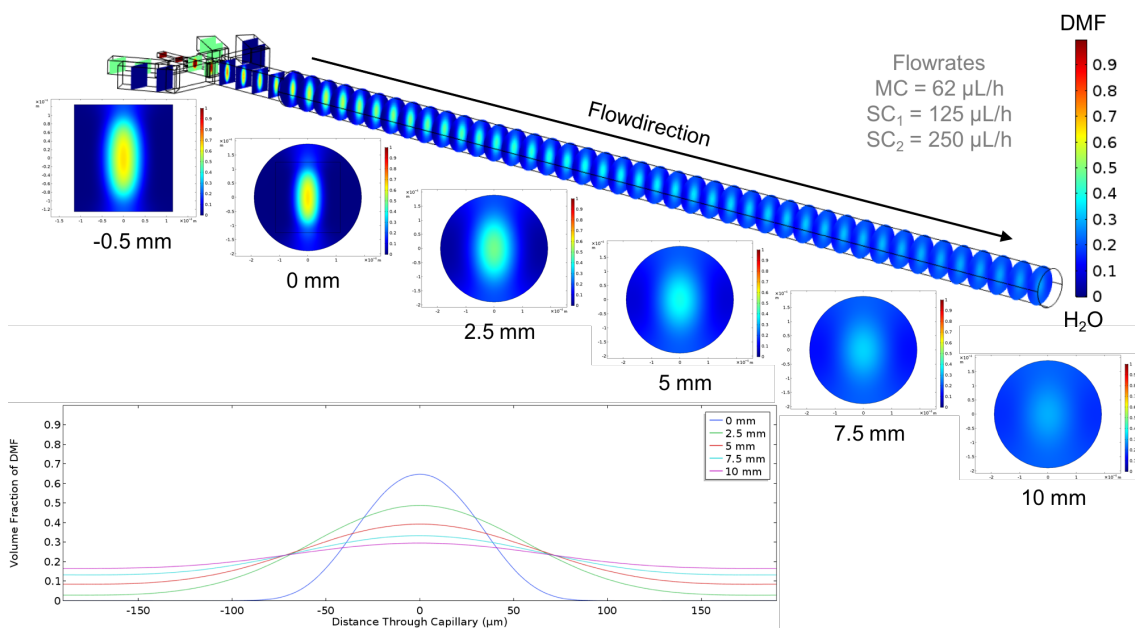


Figure E.4: COMSOL simulation of the experiment *X* with DMF as solvent. Sliced view along the channel with separate simulation cross-sections along the outlet channel directly before and after entering the capillary and in equivalent distances along the channel. The volume fraction of DMF in water can be seen along the channel and in the graph as a function of distance vertically through the channel.

Figure E.5 displays the same volume fraction distribution along the channel in top (upper) and side (lower) view. It can clearly be seen that the hydrodynamic focusing due to the channel geometry results in an ellipsoidal shape (see Figure E.4), resulting in a wider interdiffusion towards the capillary wall in vertical direction than in horizontal direction.

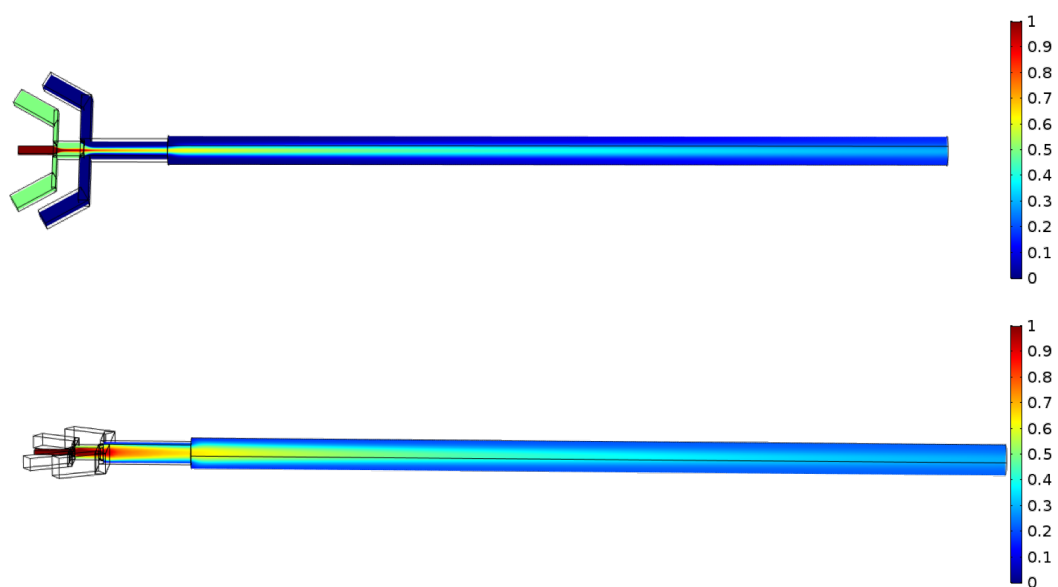


Figure E.5: COMSOL simulations of the experiment X in top (upper) and side (lower) view.

The same simulations for the experiment Y can be seen in Figure E.6 and E.7, as well as for the experiment Z in Figure E.8 and E.9.

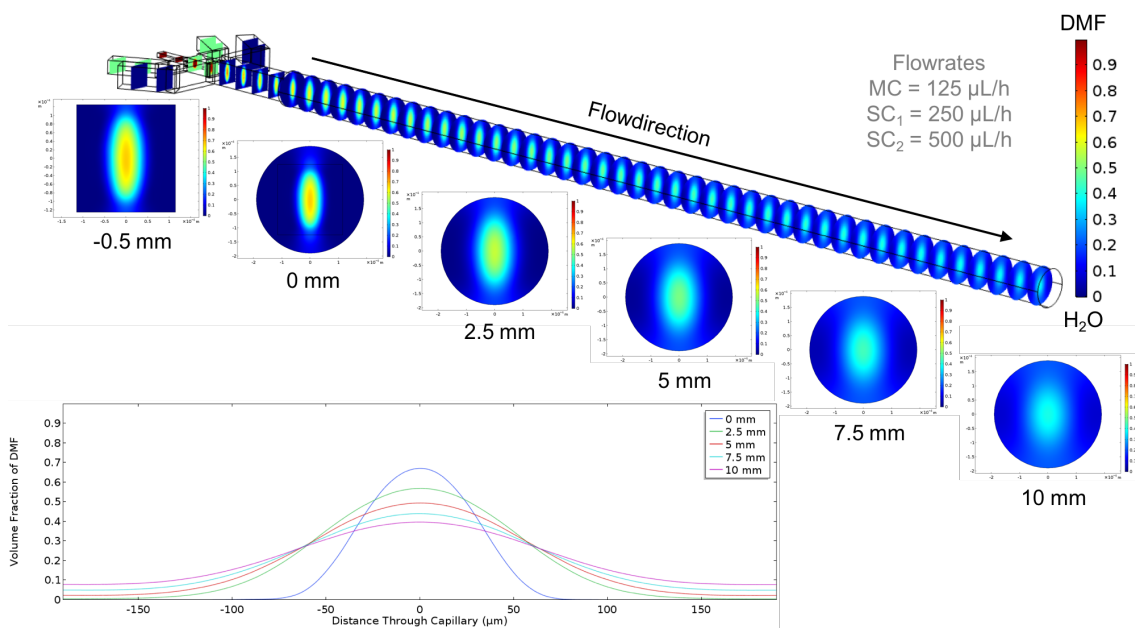


Figure E.6: COMSOL simulation of the experiment Y with DMF as solvent. Sliced view along the channel with separate simulation cross-sections along the outlet channel directly before and after entering the capillary and in equivalent distances along the channel. The volume fraction of DMF in water can be seen along the channel and in the graph as a function of distance vertically through the channel.

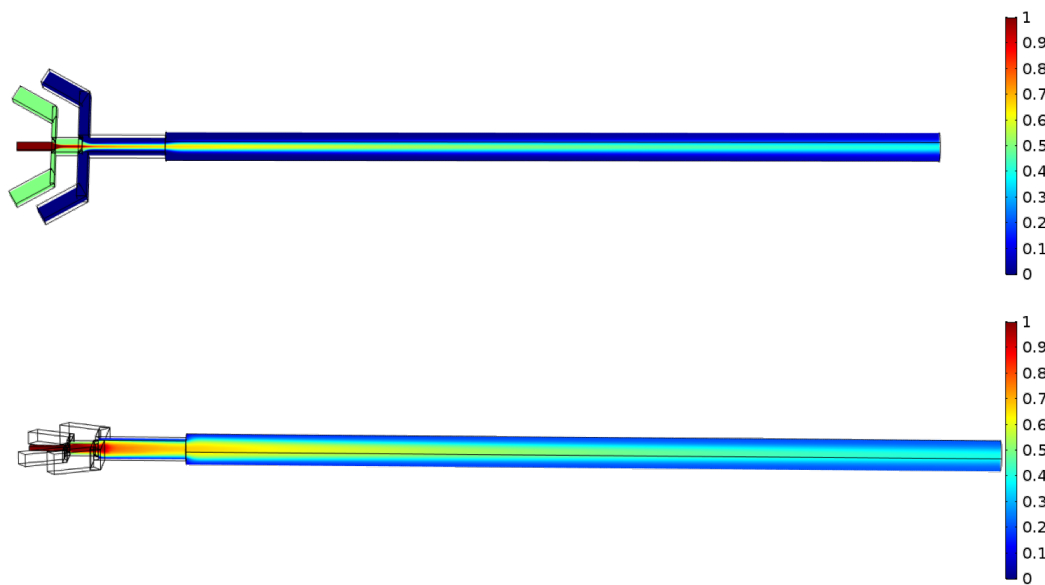


Figure E.7: COMSOL simulations of the experiment Y in top (upper) and side (lower) view.

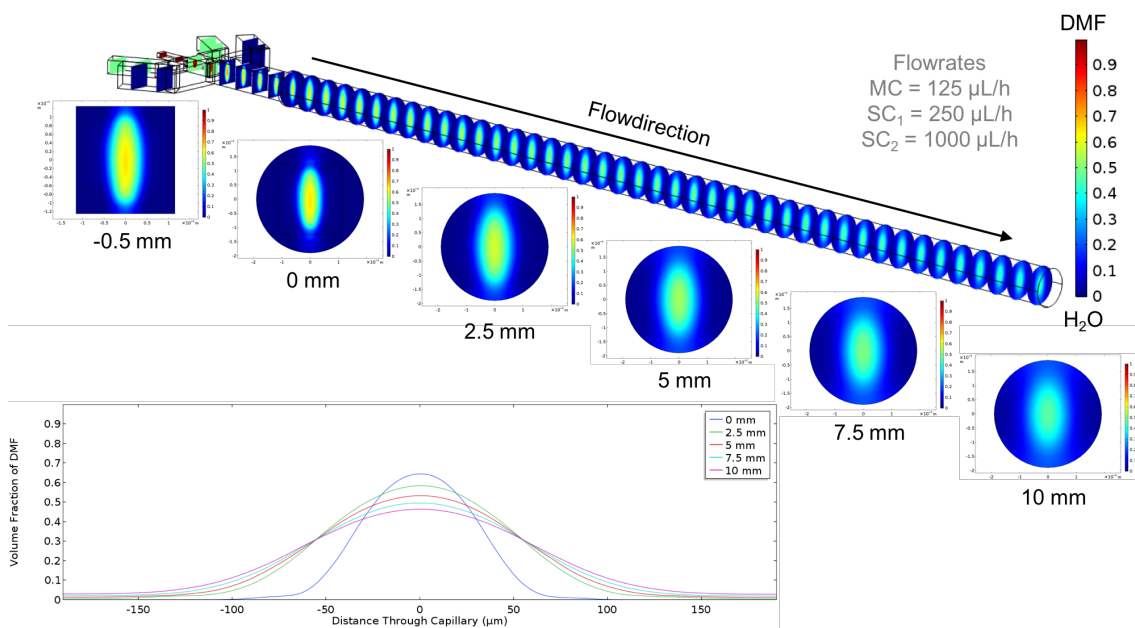


Figure E.8: COMSOL simulation of the experiment Z with DMF as solvent. Sliced view along the channel with separate simulation cross-sections along the outlet channel directly before and after entering the capillary and in equivalent distances along the channel. The volume fraction of DMF in water can be seen along the channel and in the graph as a function of distance vertically through the channel.

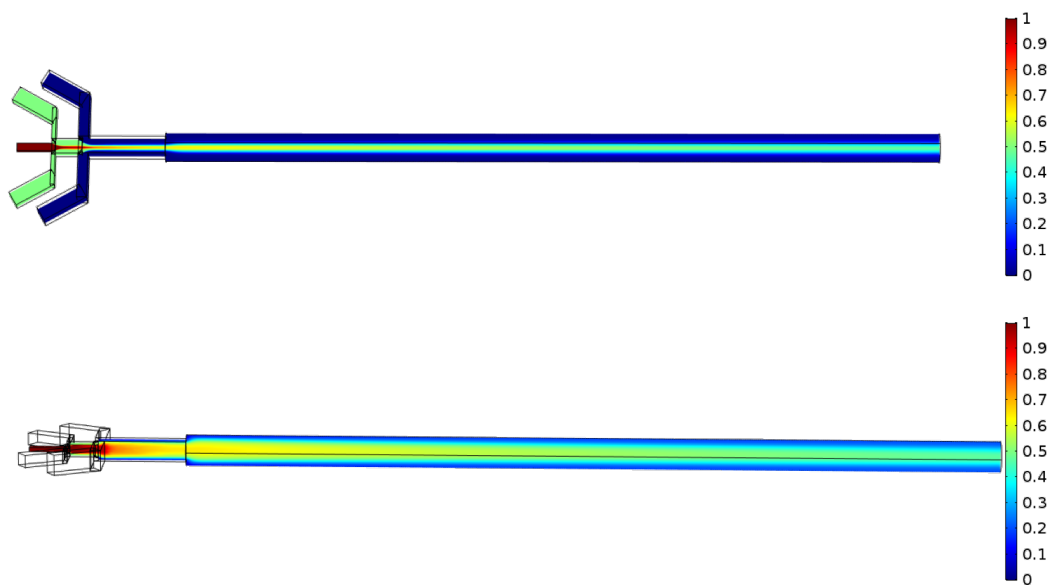


Figure E.9: COMSOL simulations of the experiment Z in top (upper) and side (lower) view.